Kinetics of degradation and exciton quenching in organic light-emitting devices

A DISSERTATION
SUBMITTED TO THE FACULTY OF THE GRADUATE SCHOOL
OF THE UNIVERSITY OF MINNESOTA
BY

John Myers-Bangsund

IN PARTIAL FULFILLMENT OF THE REQUIREMENTS
FOR THE DEGREE OF
DOCTOR OF PHILOSOPHY

Russell J. Holmes, Advisor

June, 2020

© John Myers-Bangsund 2020
ALL RIGHTS RESERVED

Acknowledgments

The work in this thesis would not have been possible, and certainly not enjoyable, without my friends and colleagues in the Holmes group and in the CEMS department. I am grateful to my advisor, Russell Holmes, for his continual support, advice, and his untiring, critical eye. I am grateful to Kyle Hershey for sustained mentorship and collaboration. To Tom Fielitz, for his willingness to explain and discuss just about anything at anytime, and for passing along to me a project that would absorb almost two years of my life but somehow turn into a Nature Materials paper. To my fantastic undergraduate students, Jack Van Sambeek and Trevor Steiner, who carried out countless experiments that would have been impossible on my own. To Robert Newcomb, for collaboration and punctuating my days with foraging and bike shop talk. To Catherine Clark, for constant advice, discussion, and mutual support through the tribulations of grad school. To Nathan Morgan, Ian Curtin, Tao Zhang, Deepesh Rai, Kaicheng Shi, Nolan Concannon, and countless others for all the discussions and conversations over the years which shaped—and served as a reprieve from—my work. And to our collaborators at Dow and DuPont: Wayne Blaylock, Pete Trefonas, Dominea Rathwell, Hong-Yeop (Daniel) Na, Jeong-Hwan Jeon, who discussed and collaborated on my work for four years.

Most of all, I am indebted to my friends, family, and my partner who all supported me and kept me grounded these last five years. Anna, I'll catch up on my baking deficit as soon as this is over.

This work was funded by The Dow Chemical Company and, after a merger and a split, DuPont Electronics and Imaging. Parts of this work were supported by the National Science Foundation (NSF) Program in Solid-State and Materials Chemistry under grant numbers DMR-1307066 and DMR-1708177. I was individually supported by the NSF Graduate Research Fellowship (grant no. 00074041), the University of Minnesota College of Science and Engineering Fellowship, and the Matthew Tirrell First Year Fellowship.

for Anna, who deserves much more than this

Abstract

Organic light-emitting devices (OLEDs) are next-generation, thin film light sources which have significant advantages over conventional display and lighting technologies, including: high contrast, high power efficiency, tunable color, and compatibility with low-cost fabrication techniques on flexible substrates. These attributes have driven the rapid commercialization of OLEDs in mobile phone displays over the last two decades, but OLEDs have yet to gain traction in high brightness applications such as lighting, automotive head lights, imaging light sources, and lasers. In part, this is because OLED performance at high brightness tends to be limited by two processes: reversible efficiency roll-off (where efficiency decreases under high current) and irreversible degradation. Both of these processes are tied to excited state (or exciton) quenching reactions which dissipate energy non-radiatively and can drive chemical reactions within the active layers of an OLED.

In this work, we seek to better understand these limiting phenomena so that they can ultimately be overcome. Our overarching strategy toward this end is to develop and apply combined electrical and optical analysis techniques to decouple efficiency loss pathways. Comparing measurements of electro- and photoluminescence (EL and PL), we unraveled how OLED lifetime depends on the spatial distribution of excited states and charge carriers. We found that multiple kinetic pathways determine the degradation rate, where the emitter radiative efficiency is deteriorated by exciton reactions in the emissive layer, while charge trapping and leakage are aggravated by reactions with charges at interfaces or outside the emissive layer. These methods have allowed us to identify design principles for mixed host emissive layers and molecular screening criteria to accelerate materials development.

These techniques also revealed a surprising result which contradicted conventional models: luminescence quenching can occur even at low electrical bias levels, reducing peak efficiency by more than 20% in some cases. We connect this effect to preferred molecular orientation and net polarization of organic films, and we identify strategies to eliminate this loss pathway. Together, the findings in this work highlight the advantages and limitations of combined electrical and optical characterization of OLEDs. Wider application of these approaches may help researchers more quickly develop new materials and design strategies for efficient and durable OLEDs.

Contents

List of Tables

List of Figures

Abbreviations and Variables

Acronyms

OLED	Organic light-emitting device (or diode)
OPV	Organic photovoltaic
OFET	Organic field-effect transistor
HOMO	Highest-occupied molecular orbital, analagous to valence band
LUMO	Lowest-unoccupied molecular orbital, analagous to conduction band
EL	Electroluminescence, light emission after electrical excitation
PL	Photoluminescence, light emission after excitation by light
EQE	External quantum efficiency
IQE	Internal quantum efficiency
HTL	Hole-transport layer
ETL	Electron-transport layer
EML	Emissive layer
HIL	Hole-injection layer
EIL	Electron-injection layer
M-EML	Mixed host emissive layer
S-EML	Single host emissive layer
IC	Internal conversion
ISC	Intersystem crossing
RISC	Reverse intersystem crossing
EEA	Exciton-exciton annihilation
TTA	Triplet-triplet annihilation
STA	Singlet-triplet annihilation
SSA	Singlet-singlet annihilation

EPQ Exciton-polaron quenching

TPQ Triplet-polaron quenching

SPQ Singlet-polaron quenching

Molecules

The abbreviations and full chemical names of common organic semiconductor molecules are listed below, broadly categorized by their most common usage. These categories are non-exclusive, and many of these molecules can be used for multiple purposes.

Planarizing and hole-injection materials

AQ1250 poly(thiophene-3-[2(2-methoxyethoxy)ethoxy]-2,5-diyl)

PEDOT:PSS poly(3,4-ethylenedioxythiophene) polystyrene sulfonate

HAT-CN Hexaazatriphenylenehexacabonitrile

Hole transport materials

α-NPD N,N′-bis(naphthalen-1-yl)-N,N′-bis(phenyl)-benzidine

TCTA tris(4-carbazoyl-9-ylphenyl)amine

TAPC 4,4′-Cyclohexylidenebis[N,N-bis(4-methylphenyl)benzenamine]

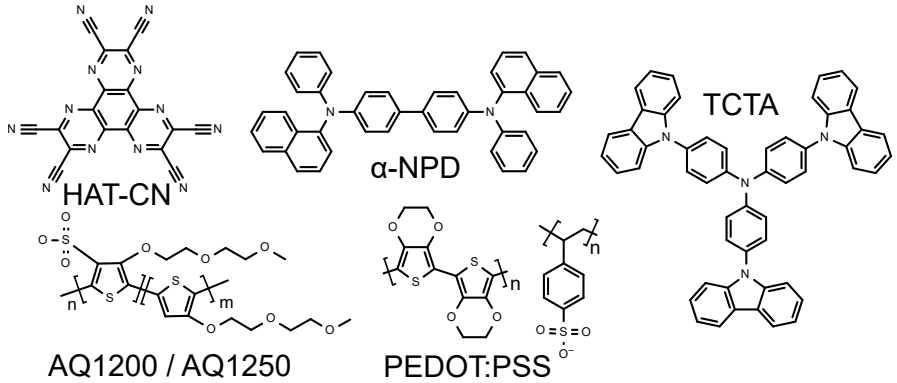

Emitters

4CzIPN 1,2,3,5-Tetrakis(carbazol-9-yl)-4,6-dicyanobenzene

C545T 2,3,6,7-tetrahydro-1,1,7,7,-tetramethyl-1H,5H,11H-10-(2-benzothiazolyl) quinolizino-[9,9a,1gh] coumarin

FIrpic Bis[2-(4,6-difluorophenyl)pyridinato-C2,N](picolinato)iridium(III)

Ir(ppy)$_3$ tris[2-phenylpyridinato-C2,N]iridium(III)

PtTPTBP Pt(II) tetraphenyltetrabenzoporphyrin, also PtTPBP

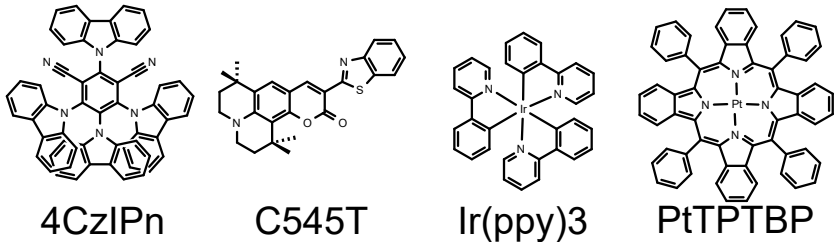

Host materials

BCBP 2,2′-bis(4-(carbazol-9-yl)phenyl)-biphenyl

CBP 4′-bis(N-carbazolyl)-1,1′-biphenyl

CDBP 4,4′-bis(carbazole-9-yl)-2,2′-dimethylbiphenyl

mCBP 3,3′-Di(9H-carbazol-9-yl)-1,1′-biphenyl

mCP 1,3-Bis(carbazol-9-yl)benzene

UGH2 1,4-bis(triphenylsilyl)benzene

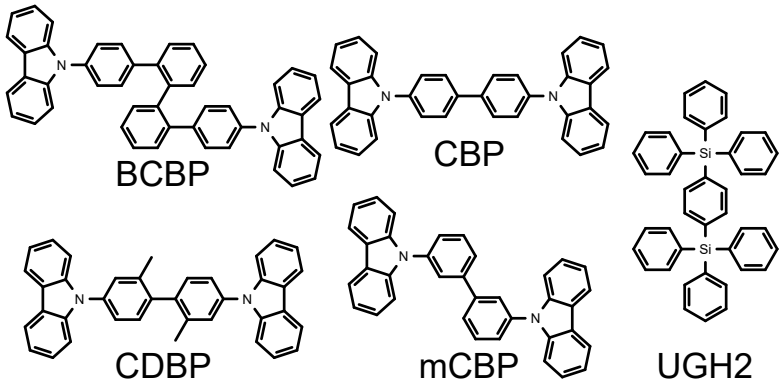

Electron transport materials

3TPYMB Tri[3-(3-pyridyl)mesityl]borane

Alq$_3$ tris-(8-hydroxyquinolate) aluminum

B3PyMPM 4,6-Bis(3,5-di(pyridin-3-yl)phenyl)-2-methylpyrimidine

BAlq bis(2-methyl-8-quinolinolate)-4-(phenylpheno-lato)aluminum

BCP 2,9-dimethyl-4,7-diphenyl-1,10-phenanthroline, or bathocuproine

BPhen 4,7-Diphenyl-1,10-phenanthroline

Liq (8-Hydroxyquinolinato)lithium (electron injection material)

OXD-7 1,3-bis[2-(4-tert-butylphenyl)-1,3,4-oxadiazo-5-yl]benzene

TPBi 2,2′,2"-(1,3,5-benzinetriyl)-tris(1-phenyl-1-H-benzimidazole)

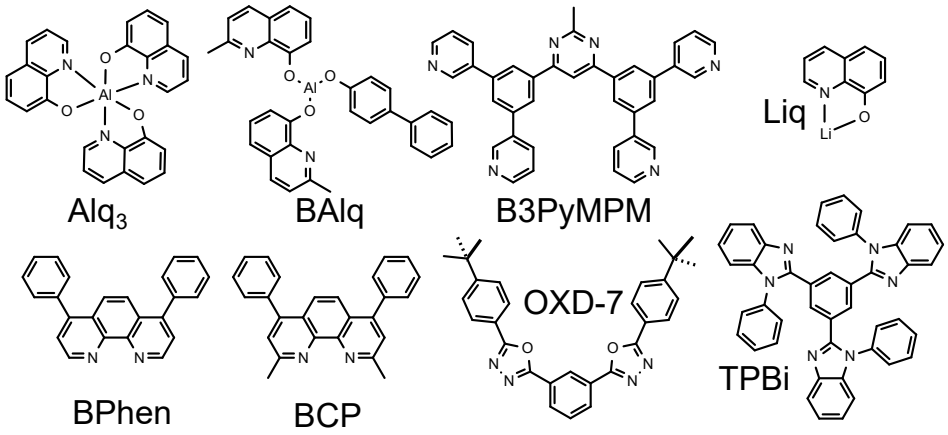

Variables

τ Exciton lifetime

η_{EQE} External quantum efficiency; for OLEDs, the fraction of photons emitted in the forward-viewing direction per injected electron

η_{PL} Photoluminescence efficiency, the fraction of excitons which emit a photon upon relaxation

η_{OC} Outcoupling efficiency, the fraction of emitted photons which are outcoupled to the external environment

χ Radiative spin fraction, the fraction of excitons which are quantum-mechanically allowed to relax radiatively

γ **or** η_{EF} Charge balance factor or exciton formation efficiency

Overview

This thesis seeks to advance understanding of the mechanisms behind degradation and efficiency loss in organic light-emitting devices. To introduce the theory and context of this work, the fundamentals of organic semiconductors are summarized in Chapter 1. Then, an overview of OLEDs—how they work, their design considerations, and what factors affect their efficiency and lifetime—is provided in Chapter 2.

Over the next three chapters, we unravel how OLED lifetime depends on the distribution of excited states and charge carriers (Chapters 3 and 4) and on host excited states (Chapter 5). In Chapter 6, we examine efficiency roll-off and exciton quenching in OLEDs more closely, ultimately identifying how preferred molecular orientation and net polarization of organic films influences device performance. Then, in Chapter 7, we study how efficiency roll-off changes with degradation and what implications this has for device design and lifetime analysis. This thesis concludes, somewhat tangentially, with the demonstration of a novel pattern formation mechanism that occurs during crystallization of organic thin films (Chapter 8). This method could be used to form low-cost, self-assembled scattering layers to increase OLED outcoupling efficiency.

1

Organic semiconductors

This chapter provides an overview of organic semiconductors, focusing on the fundamental physics of bonding, excited states (excitons), electronic transitions, and energy transfer in these materials.

1.1 Bonding and conjugation

Organic molecules are broadly defined as containing carbon-hydrogen bonds; historically, they were classified as originating from living organisms, as they are the basic building blocks for all living matter. Carbon, with its four valence electrons, tends to form covalently-bonded chains and rings, enabling vast structural diversity and, in turn, a wide range of properties. The molecules used in organic optoelectronics share a common structural feature: *conjugation*, where alternating double and single bonds leads to delocalization of electrons across the molecule (Figure 1.1a–e).

In conjugated molecules, the 2s and 2p orbitals of carbon are hybridized to form three sp^2 orbitals, which adopt a trigonal planar configuration, with a remaining unhybridized p_z orbital perpendicular to the sp^2 plane (Figure 1.1e). The sp^2 orbitals form strong σ bonds with neighboring carbon, hydrogen, or other atoms, and the p_z orbital forms a relatively weaker and more diffuse π bond with one of the neighboring p_z orbitals (Figure 1.1f). When an extended chain or ring of alternating π bonds is present in a molecule, the electron cloud will be delocalized across the molecule.

In molecular orbital (MO) theory, bonding of two atomic orbitals leads to two molecular orbitals which are split energetically: the bonding state, which has lower energy than either atomic orbital and hence stabilizes the molecule, and the antibonding state, which has higher energy than either atomic orbital. As depicted in Figure 1.1f, the bonding orbital represents an in-phase superposition of the atomic orbitals and, as a result, the electron probability density is

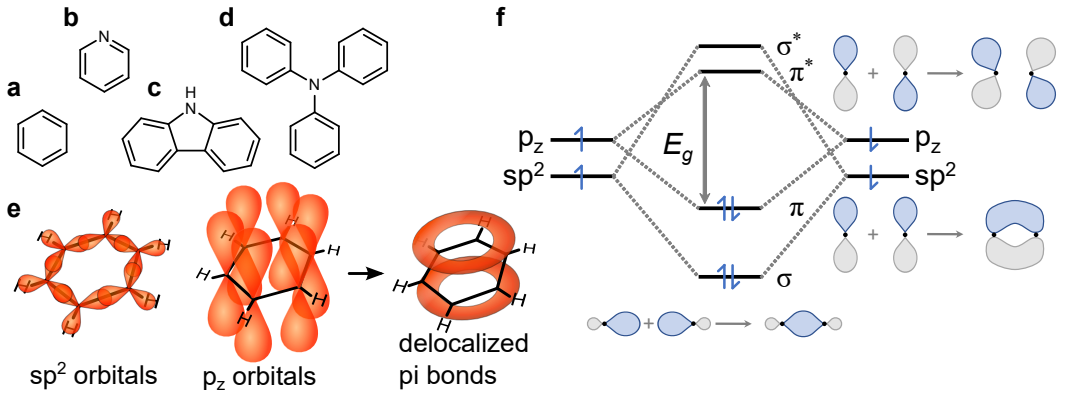

Fig. 1.1. Simple conjugated organic molecules and common building blocks for organic semiconductors: (**a**) benzene, (**b**) pyridine, (**c**) carbazole, and (**d**) triphenylamine. (**e**) Delocalization of π-bonded p_z orbitals in benzene and the trigonal planar geometry of sp^2 hybridized orbitals (WikiMedia Commons).[1] (**f**) Molecular orbital diagram for a C-C double bond, where vertical axis represents energy and arrows represent spin-up and spin-down electrons. The sp^2 orbitals form a σ bond, and p_z orbitals form a π bond. Remaining sp^2 orbitals of each C would bond with a neighboring atom. Optical transitions occur between the HOMO and LUMO, which are separated by the energy gap, E_g. At bottom, middle, and top are illustrations of σ, π, and π^* orbitals, respectively, where the color of the orbital lobes represents their phase.

highest in the internuclear region. The antibonding state represents out-of-phase superposition of the atomic orbitals, leading to electron density being pushed outward, away from the bonding region between atoms.* One way of thinking of the electron density is distributed in these two states is as constructive and destructive interference of the atomic wavefunctions.

Taking the MO diagram in Figure 1.1f, electrons from each atom fill up the MOs, two electrons with anti-aligned spin per state starting at the lowest energy state. In the case of a C-C double bond, the highest occupied molecular orbital (HOMO) is the π orbital and the lowest-unoccupied molecular orbital (LUMO) is the π^* orbital. Due to the Pauli exclusion principle, which states two electrons cannot occupy the same quantum state simultaneously,† optical transitions must occur between a filled and empty state. Generally, absorption of light will occur by exciting an electron from the HOMO to the LUMO or a higher-lying state; emission will occur by an excited electron relaxing from the LUMO to the HOMO. Because π bonds are relatively weak, their energetic splitting is smaller than for σ bonds and the resulting energy gap between π and π^* orbitals is often within the visible range. It is this feature that makes

*To quote Atkins,[2] the energetic splitting between these states "is partly due to the fact that an antibonding electron is excluded from the internuclear region, and hence is distributed largely outside the bonding region. In effect, whereas a bonding electron pulls two nuclei together, an antibonding electron pulls the nuclei apart."

†Pauli exclusion applies to fermions—which are particles with half-integer spin: protons, neutrons, and electrons—and another way of stating this principle is that it is impossible for two fermions to simultaneously have the same quantum numbers (the principal, azimuthal, magnetic, and spin quantum numbers—n, l, m_l, m_s, respectively).

conjugated molecules so useful for interacting with light: conjugation in chlorophyll leads to absorption of blue and red light, driving photosynthesis; absorption in organic solar cells is used to generate electrical current; and in organic LEDs, light is emitted when electrically-generated excited states relax to the ground state.

As a conjugated system is extended, the HOMO-LUMO energy gap generally decreases. From the MO theory perspective, this is can be thought of as π orbitals interacting, leading to further energy splitting and a narrowing of the gap. In the limit of an infinitely extended polymer, the energy difference between bonding states becomes infinitesimal, giving a quasi-continuous band-like structure. This concept, depicted in Figure 1.2, is one of the core concepts for tuning the properties of organic molecules, such as emission wavelength and band gap.*

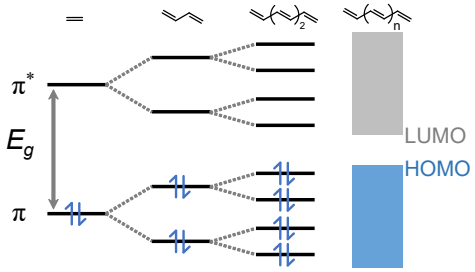

Fig. 1.2. Each additional π bond in an alkene chain causes energy splitting of each molecular orbital, decreasing the HOMO-LUMO gap (E_g). Adapted from ref. [3]

Another simple way to understand the effect of conjugation on energy gap is to treat a conjugated carbon chain as a 1D particle-in-a-box problem, where an electron in a π orbital is confined within the chain of length L. For a polyene chain with n C=C double bonds and $n-1$ single bonds, there will be $2n$ C atoms and $2n$ electrons in n π orbitals. The HOMO-LUMO energy gap can thus be estimated as:†

$$E_{n+1} - E_n = \frac{(n+1)^2\hbar^2\pi^2}{2m_eL} - \frac{n^2\hbar^2\pi^2}{2m_eL} = \frac{(2n+1)\hbar^2\pi^2}{2m_eL} \tag{1.1}$$

where E_{n+1} and E_n are the LUMO and HOMO energy levels, respectively, $\hbar$ is the reduced Planck's constant, m_e is the electron mass, and $L = (2n-1)\cdot l$, where $l \approx 140\,\text{pm}$ is the average C-C bond length. The resulting energy gap vs. chain length dependence is shown in Figure 1.3a. This is clearly a highly simplified approach, but it provides a qualitative rationale for why the energy gap is reduced by extended conjugation. These predicted trends with conjugation extent are observed experimentally for a wide range of molecules, such as the linear

*Of course, there is a large toolbox beyond just conjugation that organic chemists use to tune molecular properties. For instance, heteroatoms—such as N, O, Cl, or F—can be used to disrupt conjugation or donate or withdraw electron density, significantly altering optical and electronic properties. Another strategy is to design molecular conformation, because twisting affects the coupling between different functional groups on a molecule.

†See Atkins, Paula, and Keeler [2, pg. 281].

acenes shown in Figure 1.3b.

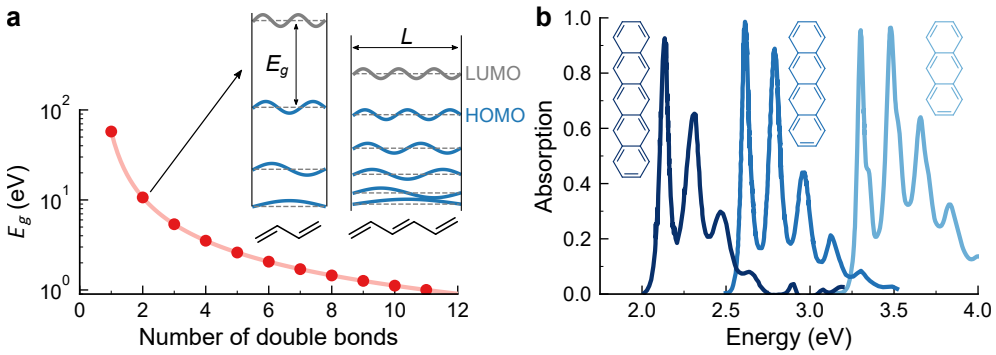

Fig. 1.3. (**a**) Approximate HOMO-LUMO energy gap, E_g, as a function of conjugation length for a alkene chain based on a 1D particle-in-a-box analysis. Inset shows energy levels and wavefunctions for chains with two and three double bonds. (**b**) Absorption of pentacene, tetracene, and anthracene (left to right) in solution, illustrating the how the HOMO-LUMO energy gap is reduced as conjugation is extended.

In the limit of infinite conjugation ($L \rightarrow \infty$), the gap should approach zero, which is precisely the behavior of graphene, which is often considered a zero-gap semi-metal. But it should be noted that a larger molecule does not always translate to a lower energy gap. Conjugation often does not extend across an entire molecule as it can be disrupted by, e.g., sp^3-hybridized carbon or conformational twisting.[4] Because of this, absorption and emission often occur on an isolated portion of a molecule, termed a *chromophore*.[5]

1.2 Excitons

The relaxed configuration of a molecule is the state which minimizes the net energy of its electrons; that is, electrons have fully occupied the lowest energy orbitals, as depicted in Figure 1.1f. The molecule is said to be in an *excited state* when an electron is promoted, either by absorption of light or electrical injection,to the LUMO or a higher-lying state. For organic semiconductors, the excited electron remains Coulombically bound to the positively charged hole which the electron left in its place in the ground state.* This charge-neutral, bound electron-hole pair is called an *exciton*, and it plays a defining role in the optoelectronic properties and device performance of organic semiconductors.

*Holes are positively-charged quasiparticles representing the absence of an electron in a normally filled state

Part of why excitons are so important in organics is because they are stable at room temperature, with relatively long lifetimes ranging from ~0.5 ns to >1 s.[6,7] The binding energy of an exciton is roughly inversely proportional to the dielectric constant, ε_r, of the surrounding medium. Organic semiconductors, which are comprised of low-mass atoms with a small number of orbital shells, have small dielectric constants ($\varepsilon_r \approx 3$) and poor charge screening, resulting in large binding energies of ~0.1–1 eV,[8] well above thermal energy at room temperature ($k_B T \approx 25\,\text{meV}$). Contrast this to inorganic semiconductors, which generally have $\varepsilon_r > 9$ and quite weakly bound excitons which are thermally dissociated at room temperature. These weak and rather delocalized excitons are referred to as Wannier-Mott excitons, whereas the tightly bound excitons in organics—residing on a single molecule—are called Frenkel excitons.

The bound electron and hole can also sit on neighboring molecules, in what is called a charge-transfer (CT) exciton or, more commonly in the OLED literature, an *exciplex*. These CT states have lower binding energies than Frenkel excitons, due to the spatial separation of the charges, and they often serve as an important intermediate state in organic electronics. In OPVs, Frenkel excitons transfer to a CT state, where the electron-hole pair is then dissociated as free carriers which can be collected as photocurrent. In some OLED architectures, holes and electrons are injected electrically, form an exciplex state between two host materials, and then energy transfer to form a Frenkel exciton on an emissive dopant.[9]

The net spin of the exciton electron pair—one residing in the HOMO, the other in the LUMO—influences both the energetics and the allowed transitions of the excited state. Because these electrons sit in separate orbitals, either electron can be spin-up ($|\uparrow\rangle$, $s = +1/2$) or spin-down ($|\downarrow\rangle$, $s = -1/2$), yielding four basis states: $|\uparrow\uparrow\rangle$, $|\downarrow\downarrow\rangle$, $|\uparrow\downarrow\rangle$, and $|\downarrow\uparrow\rangle$. The net spin of the exciton can thus be $S = 0$ or $S = 1$. In Dirac notation, excited states are often expressed as $|S, M_s\rangle$, where S and M_s are the total inherent spin and total spin magnetic quantum numbers, respectively.* There is a single state with $S = 0$, termed

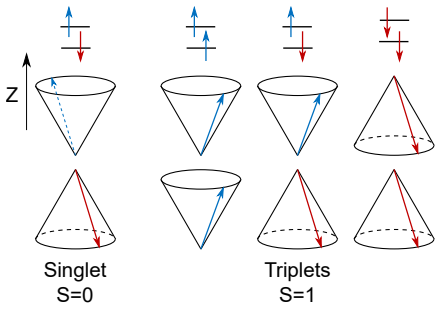

Fig. 1.4. Vector representation of singlet ($S = 0$) and triplet states ($S = 1$).

*S measures the total vector magnitude of the electrons' spins, whereas M_S measures the total z-component.

a *singlet*, which is a superposition of the two $S = 0$ basis states:*

$$|0,0\rangle = \frac{1}{\sqrt{2}}\left(|\uparrow\downarrow\rangle - |\downarrow\uparrow\rangle\right) \tag{1.2}$$

There are $2S + 1 = 3$ degenerate† states with $S = 1$, called *triplets*:

$$\begin{aligned} |1,1\rangle &= |\uparrow\uparrow\rangle \\ |1,0\rangle &= \frac{1}{\sqrt{2}}\left(|\uparrow\downarrow\rangle + |\downarrow\uparrow\rangle\right) \\ |1,-1\rangle &= |\downarrow\downarrow\rangle \end{aligned} \tag{1.3}$$

These states can be visualized as the addition of vectors, as illustrated in Figure 1.4. Though not studied in this thesis, another possible state is the doublet, which occurs in neutral radical molecules and consists of a single unpaired electron in the excited state. Emission from doublet states has recently been exploited for efficient radical emitter OLEDs, where optical transitions occur between the singly-occupied molecular orbital (SOMO) and the HOMO.[10,11]

Triplet excitons generally have lower energy than their corresponding singlet state because the spin-aligned electrons are pushed away from each other by Pauli repulsion (this is, in a sense, magnetic repulsion of the spins and is more generally called the exchange interaction). This increased separation between electrons leads to reduced Coulombic (charge) repulsion and thus lowers the energy of the state.‡

1.3 Electronic transitions

The purpose of an OLED is to efficiently convert electricity into light and vice versa for an OPV. Exciton spin plays a crucial role in these conversion processes as a consequence of the Pauli exclusion principle: because two electrons with the same quantum numbers (and same spin) cannot occupy a state at the same time, a spin flip is needed for a triplet exciton to relax to the ground state. But radiative transitions cannot involve a spin flip because spin is conserved and

*Superposition is necessary here as electrons are indistinguishable, but the $|\uparrow\downarrow\rangle$ and $|\downarrow\uparrow\rangle$ basis states do not satisfy this condition under exchange.

†Because the three states have different angular momenta, these states split energetically under a magnetic field (Zeeman effect).[2] The observation of three spectral lines under a magnetic field was the origin of the term "triplet".

‡Hund's rule of maximum multiplicity is a statement of this phenomenon: a multi-electron system "adopts a configuration with the greatest number of unpaired electrons".[2]

photons carry no spin angular momentum. This means that, to a first-order approximation, only singlets can be optically generated (*absorption*) and emission can only occur during relaxation of singlets (*fluorescence*).

In OLEDs, the spin of electrically-injected charge carriers are uncorrelated; when these charges recombine to form excitons, it is expected statistically that one singlet will be formed for every three triplets. This radiative to non-radiative exciton ratio is often termed the spin fraction, χ, and it limits the maximum achievable internal quantum efficiency of a fluorescent OLED to 25%. Fortunately, this can be overcome in several ways. One of the more common methods is by enhancing spin-orbit coupling—that is, coupling between electron spin and the angular momentum of the orbit—which leads to singlet-triplet mixing, increases the probability of a spin flip, and makes radiative recombination of triplets (*phosphorescence*) weakly allowed. Spin-orbit coupling is stronger in high atomic number elements (high-Z), scaling as Z^4,[2] and because of this, state-of-the-art phosphorescent emitters in OLEDs often contain Pt, Ir, or other heavy-metal cores.[12,13]*

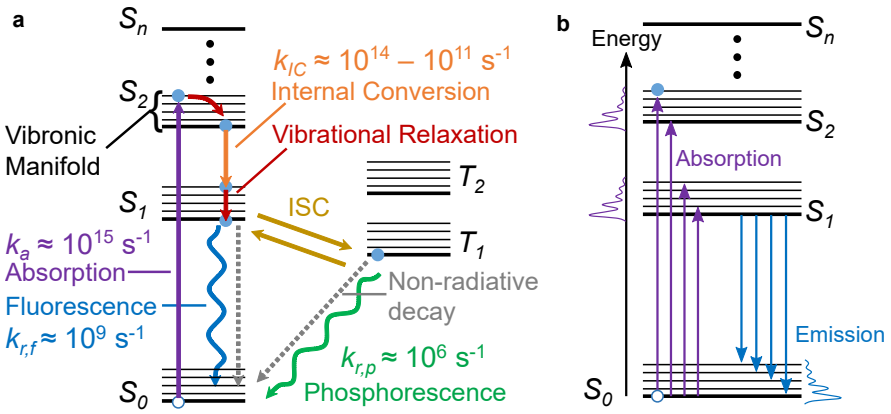

Fig. 1.5. Transition processes and rates in organic semiconductors: (**a**) The ground state (S_0), and n^{th}-order singlet (S_n) and triplet (T_n) levels are shown. Thin black lines represent the vibronic sub-levels for each state. Transition processes shown are absorption, internal conversion, vibrational relaxation, intersystem crossing (ISC), non-radiative decay, fluorescence and phosphorescence. Radiative rate constants are for typical fluorescent and phosphorescent emitters used in OLEDs. (**b**) Schematic of absorption and emission following Kasha's Rule. At left and right are schematic spectra corresponding to the vibronic structure of the excited state and ground state, respectively.

Electronic transitions which occur in organic semiconductors, and their associated rates, are shown in Figure 1.5. Absorption, occurring within ~10^{-15} s, occurs by exciting an electron from

*These emitter molecules usually consist of organic ligands coordinated to a heavy-metal core. Metal-Ligand Charge Transfer states (MLCT) form in these molecules, where the excited state resides on both the metal core and the ligands, and the high energy d-states of the metal atom promote spin-orbit coupling.

the ground state, S_0, to a higher-lying singlet state (S_1 to S_n). The excited electron will then rapidly relax non-radiatively to the lowest energy singlet state available by internal conversion and vibrational relaxation (each occurring over a similar timescale as a molecular vibration, $\sim 10^{-14}$–10^{-11} s). From the S_1 state, the singlet can either relax radiatively (fluorescence) to S_0, relax non-radiatively to S_0, or, if spin-orbit coupling is non-negligible, convert to a triplet by intersystem crossing (ISC). Fluorescence typically occurs over $\sim 10^{-9}$–10^{-7} s, much slower than internal conversion processes, which is why emission from higher-lying singlet states is rarely observed.[14] As mentioned above, intersystem crossing depends strongly on spin-orbit coupling, ranging from $\sim 10^{-8}$–10^{-3} s. Finally, any triplets which form can slowly decay radiatively by phosphorescence ($\sim 10^{-6}$–10^{-1} s), or decay non-radiatively. Approximate timescales for each process are taken from Jaffe and Miller [15].

As a consequence of the short timescale of internal conversion, radiative transitions tend to begin at the lowest vibronic level of the initial state (Kasha's Rule),[16] and can end at any vibronic sub-level of the final state. This results in multiple spectral features for a given transition, where absorption spectra reflect the vibronic structure of the molecular excited states while emission spectra characterize the ground state vibronic structure (Figure 1.5b).

The combination of radiative and non-radiative decay rates (k_r and k_{nr}) determine the exciton lifetime, τ, and the overall photoluminescence efficiency (i.e. exciton-to-photon conversion efficiency) of an emissive molecule (Eqs. (1.4) and (1.5)). These are key parameters in determining the efficiency and kinetic behavior of OLEDs, as discussed further in Chapter 2.

$$\tau = \frac{1}{k_r + k_{nr}} \tag{1.4}$$

$$\eta_{PL} = \frac{k_r}{k_r + k_{nr}} = k_r \tau \tag{1.5}$$

1.4 Organic thin films

The idealized depictions of molecular orbital diagrams and electronic transitions above have implicitly assumed non-interacting molecules. That is, molecules in a vacuum or a dilute solution. In real devices, molecules are condensed in the solid state in thin films, which are held together by van der Waals bonds. These bonds—which are relatively weak compared to the ionic and covalent bonds of inorganic semiconductors—result from dipole-dipole interactions

between molecules, including: induced dipole-induced dipole (London dispersion force), permanent dipole-induced dipole (Debye force), and permanent dipole-permanent dipole (Keesom interaction). Any of these can be active in organic semiconductors films, as many organic molecules have a permanent dipole moment.

Because these intermolecular bonds are weak, the electronic and optical properties of an organic film are often similar to those of an isolated molecule (in other words, the electronic coupling between molecules is small). But the effect of the surrounding medium cannot be neglected. Interactions with neighboring molecules tend polarize and distort a molecule, often leading to broadened and red-shifted emission (see Köhler and Bässler [5, pp. 90–93]). Intermolecular excited states can also form in condensed films, further red-shifting emission and changing the photophysical properties of the film (an example of how this influences OLEDs is discussed in Chapter 5). Interactions between molecules also make possible energy transfer between states, which leads to exciton diffusion and quenching, as discussed in Sections 1.6 and 1.7.

Most organic semiconductors used in OLEDs are amorphous in thin films,* lacking long range, periodic order. The term "amorphous" is sometimes loosely interpreted as meaning the orientation of molecules is completely random, but in practice, organic thin films often show preferred orientation.[20–22] This tendency for molecules to orient in a particular direction has implications for charge carrier mobility,[23] optical properties and light outcoupling efficiency,[22] and mechanical properties.[24]

In this thesis, we will generally assume organic thin films are homogeneous and uniform. When we model the exciton kinetics of an operating device or degradation processes, we will assume that continuous variables can describe these phenomena. And while these assumptions are often needed to make these problems tractable, or at least to reduce the number of unknown parameters, it should be noted that organic films are usually inhomogeneous on the nanoscale. Some researchers have proposed that charge transport in OLEDs is filamentary, occurring along conductive threads which are several molecules wide.[25] It has also been found that emitter molecules—rather than being evenly diluted in the host material—form nanoscopic aggregates which increase exciton diffusion and annihilation processes (see below for more discussion of these processes).[26] Several other researchers have argued that stochastic, 3D models are needed

*At least as-deposited. Some materials, especially those with low glass transition temperature, will crystallize over time or during operation.[17] A few OLEDs have intentionally included crystalline layers to improve outcoupling efficiency or morphological stability.[18,19]

to fully explain charge and exciton transport as well as quenching processes in OLEDs.[27–29] These considerations are beyond the scope of this thesis but should be considered whenever analyzing organic electronic devices.

1.5 Charge carriers

The concentration of thermally excited (intrinsic) charge carriers is negligible in organic semiconductors (unlike conventional inorganic semiconductors). Instead, charge carriers are generated by either electrical injection from conductive contacts, charge transfer from dopants,[30] or dissociation of photogenerated excitons. Free electrons will lie in the LUMO and free holes will lie in the HOMO, which are analogous to the conduction and valence bands of traditional semiconductors. Due to the low dielectric constant of organic materials, molecules nearby an excess electron or hole will rearrange and polarize in response to the charge's electric field, which serves to screen the charge and energetically stabilizing it. This combination of a charge and local distortion is a quasiparticle called a *polaron*.

Charges in amorphous organic semiconductors are typically localized to a single molecule, which is a consequence of the limited electronic coupling and weak intermolecular bonds in organic films. To move, charges must hop between molecules, a discrete process called *hopping transport*. The energetic relaxation of a polaron presents a barrier to hopping, resulting in an Arrhenius behavior for the hopping rate (Marcus theory): $k_{hop} \propto \exp -E_B/k_BT$, where E_B is the energy barrier, T is the temperature, and k_B is the Boltzmann constant.

This contrasts with traditional semiconductors, which show coherent band transport with a delocalized electron wavefunction. Yet, in more ordered or crystalline organic semiconductors, band-like transport can be achieved.[31] In these cases, disorder is limited and greater electronic coupling is achieved by increasing overlap between π orbitals (π–π stacking).

A quick note on terminology: charge carriers will sometimes be called electrons (holes), anions (cations), or negative (positive) polarons. These are all loosely synonyms, with usage depending on field (e.g. anion and cation are more common among chemists, polarons among physicists) and how technical/precise an author is attempting to be. Anion/cation is more specifically referring to a charged molecule, while electrons and polarons refer to the charge carrier itself.

1.6 Energy transfer

Excitons in organic semiconductors can transfer energy to other molecules or available states, a process which can lead to diffusive exciton motion or to non-radiative quenching of excitons. These processes are critical to operation of organic optoelectronic devices and often determine device performance. There are three main ways exciton energy transfer occurs: cascade energy transfer, Förster transfer, and Dexter transfer.[32]

1.6.1 Cascade energy transfer

The cascade process involves exciton relaxation, photon emission, and re-absorption by another molecule. Cascade transfer can occur over long length scales (10–100 nm) but is usually inefficient since it requires high photoluminescence efficiency, strong absorption, and substantial emission-absorption overlap. For most organic optoelectronic devices, this can be neglected.

1.6.2 Förster transfer

Förster transfer, also called Förster resonance energy tranfer (FRET), occurs by non-radiative dipole-dipole coupling where a donor exciton causes an oscillation in the dipole field which excites an acceptor molecule.[33] One analogy often used to explain the FRET mechanism is as energy transfer between transmitting and receiving antennae; another is as emission and re-absorption of a virtual photon. The rate of Förster transfer between two point dipoles separated by distance d can be expressed as:

$$k_F = \frac{1}{\tau}\left(\frac{R_0}{d}\right)^6 \tag{1.6}$$

where τ is the exciton lifetime and R_0 is the Förster radius, defined as the distance where energy transfer is equal to the sum of all other decay rates:

$$R_0^6 = \frac{9\eta_{PL}\kappa^2}{128\pi^5}\int \lambda^4 F_D \sigma_A n^{-4} d\lambda \tag{1.7}$$

where κ^2 is the orientation factor, F_D is the area-normalized emission spectrum of the donor excited state, σ_A is the absorption cross-section of the acceptor molecule, n is the index of refraction of the medium, and λ is wavelength. For a thorough discussion of these parameters,

see Fielitz [34] or Menke and Holmes [32].

While Förster transfer is non-radiative, the radiative properties of the donor and acceptor (η_{PL}, F_D, and σ_A) determine R_0 because they capture the decay rates of the donor and the electronic coupling between the donor and acceptor. The $F_D\sigma_A$ term is an expression of Fermi's Golden Rule and reflects the need for comparable energy states in the acceptor to conserve energy upon transfer. The donor and acceptor states must also have the same spin, so FRET is only possible in singlet excitons or in phosphorescent emitters with significant singlet-triplet mixing. R_0 typically ranges from 1–10 nm, which is relatively long compared to intermolecular spacings which are typically $d < 1\,\mathrm{nm}$.[32]

1.6.3 Dexter transfer

Dexter transfer occurs by direct electron transfer, and thus requires overlap in the electron density of the excited donor and the ground state acceptor molecules. Because of this, Dexter transfer occurs between nearest-neighbors over 0.1–1 nm. The Dexter transfer rate is:[35]

$$k_D = Ke^{-2d/L} \int F_D A_A d\lambda \tag{1.8}$$

where K aggregates quantum-mechanical terms related to the orbital interaction, d is the separation between donor and acceptor molecules, L is the van der Waals radius of the molecules, F_D is the normalized donor emission spectrum, and A_A is normalized acceptor absorption spectrum. Dexter transfer can occur in non-radiative states, and hence excitons with low η_{PL} and triplet excitons can diffuse by this mechanism.[33]

1.7 Exciton quenching

In addition to energy transfer to molecules in the ground state, excitons can transfer energy to molecules which are either in the excited state (other excitons) or ionized (charge carriers or polarons). These processes, termed bimolecular quenching, often serve as loss pathways which lower OLED efficiency as they lead to hot excited states or hot carriers, where the excess energy is then thermalized by internal conversion. Excitons can also be quenched by other means, such as field-induced dissociation.

1.7.1 Exciton-exciton annihilation

Exciton-exciton annihilation (EEA) occurs when one exciton transfers energy to another, with one exciton relaxing to the ground state while promoting the other to a higher excited state (S_n or T_n). The remaining "hot" excited state will then dissipate this excess energy as heat as it relaxes *via* internal conversion to the first excited state. This energy can also be dissipated by cleaving bonds, leading to chemical degradation—this is discussed further in Chapter 2. EEA can occur between singlets (SSA), between a singlet and a triplet (STA), or between two triplets (TTA). In phosphorescent OLEDs, we are only concerned with TTA, as the singlet density is negligible.[36–38] STA can be important in fluorescent or thermally-activated delayed fluorescence OLEDs.[39,40] SSA is usually negligible due to the short exciton lifetimes of singlets.

EEA can likely occur by either Förster or Dexter transfer, as it is often observed in molecules with weakly- or non-radiative triplets. Typically, the rate of EEA is assumed to depend on the squared exciton density: $K = k_{EE} n_{ex}^2$, where k_{EE} is a rate constant which depends on molecular and film properties (such as concentration, aggregation, etc.). In practice, k_{EE} may vary with exciton density,[41] suggesting that this may be a simplified description.

Relatedly, many emitters show significant concentration quenching, where their photoluminescence efficiency decreases as their concentration within a matrix is increased. This is why emitters are often diluted to ~1–15 vol % within a wide-gap host. While there are several mechanisms that can contribute to this, quenching has been shown to scale with d^{-6} (where d is the intermolecular spacing), suggesting a Förster-type EEA process is likely responsible.[42]

EEA is not always detrimental. In fluorescent OLEDs, TTA can be used to upconvert triplets into singlets and surpass the $\chi = 25\,\%$ spin statistical limit.[43,44] This is sometimes referred to as *triplet fusion*. If only singlets are generated during fusion, which can occur in materials where promotion to the upper triplet level is endothermic ($2E_{T_1} < E_{T_n}$),[44] χ can be increased to 62.5 % ($0.25 + 0.75 \cdot 0.5$). To date, this approach has been used in the most efficient commmercial blue OLEDs,[45] as phosphorescent blue emitters still lag in stability.[46]

The inverse of this process is singlet fission, where a singlet transfers energy to form a pair of triplets.[47] This occurs most efficiently in systems which have a triplet energy of less than half the singlet energy. In solar cells, singlet fission can be used to boost photocurrent by generating up to two electrons for every absorbed photon.[48]

1.7.2 Exciton-polaron quenching

Analogously to EEA, exciton-polaron quenching (EPQ, TPQ for triplets) occurs when an exciton transfers energy to a polaron, creating a hot carrier which then dissipates the excess energy as heat. This process can also cleave bonds,[49] leading to degradation. The rate of EPQ is usually expressed as:[38] $K = k_{EP} n_{ex} n_{pol}$, where n_{pol} is the polaron density.* EPQ can likely occur by both Dexter and Förster transfer,[50] and, as such, overlap is needed between the emission spectrum and the absorption spectrum of the polaron (Figure 1.6).

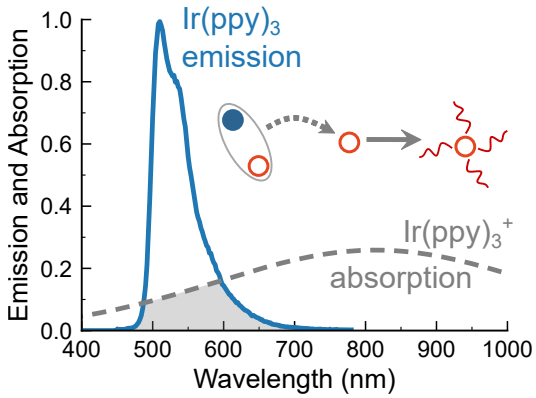

Fig. 1.6. Overlap between emission and cation absorption in $Ir(ppy)_3$. Cation absorption is a gaussian fit to measured absorption in an $Ir(ppy)_3$:MoO_3 film,[51] where electron transfer to MoO_3 ionizes $Ir(ppy)_3$. Inset schematic shows energy transfer—which is made possible by this absorption overlap—from an exciton to a cation (i.e. a hole or positive polaron), leading to heat dissipation from a hot carrier. The absorption scale here is arbitrary and would need to be properly quantified (see Rabe et al. [52]) to estimate the Förster radius between $Ir(ppy)_3$ and its cation.

Cation absorption in organic semiconductors has not been widely reported, but is usually characterized by doping the film with a material which induces charge transfer, generating free charges. In an early study, Rabe et al. [52] demonstrated high-sensitivity cation absorption measurements of S-TAD, a hole transport material. The main conclusion was that the absorption cross-section was too low to efficiently quench excitons. Most subsequent studies have simply looked for relative spectral features, making it difficult to assess whether the cross-sections in other materials are similarly low. Matsushima et al. [51] characterized polaron absorption in m-MTDATA, $Ir(ppy)_3$, 2-TNATA, TPD, Rubrene, alpha-NPD, all with films co-doped with MoO_3. Glaser et al. [53] examined CBP:MoO_3 films with infrared spectroscopy, which is less useful for identifying whether energy transfer can occur for visible emission wavelengths. The cations of carbazole hosts, CBP and mCBP, and several archetypal TADF emitters, such as 4CzIPn, were found to absorb in the visible, suggesting that quenching could occur to any of

*In this formulation, k_{EP} is an effective, time-averaged rate constant that does not capture the spatial dependence of the specific energy transfer mechanism. A 3D kinetic Monte Carlo model is usually employed to capture these spatial effects.[50]

these species.[54] A recent study examined cation absorption of α-NPD, TCTA, BPAPF, and BF-DPB using a $C_{60}F_{48}$ co-dopant.[55] The consensus seems to be, though conclusive evidence of this remains elusive, that Förster-type exciton-polaron quenching is an active loss pathway in many phosphorescent- and TADF-based OLEDs.[28,50]

1.7.3 Electric field-induced dissociation

Excitons can also be directly dissociated by an electric field into a separate electron and hole. These charges can recombine to form an exciton again, or they can leak out of the device. In phosphorescent OLEDs at typical operating conditions, this process has generally been found to be negligible (for fields up to 10^6 V cm^{-1}).[38] It is however possible that field dissociation occurs in these devices, but that charges simply recombine to form an exciton again, resulting in little observable effect on device performance.[56] There are some indications that field dissociation occurs more readily in thermally-activated delayed fluorescence (TADF) emitters, which have excited states with charge transfer character and smaller binding energies, but the magnitude of this process and how much it deteriorates device performance is still unknown.[57] It has also been suggested that electric field dissociation limits efficiency roll-off in fluorescent emitters at the high biases needed for electrically-pumped lasing.[58]

1.8 Summary

The nature of excited states in organic semiconductors—excitons, spin, and the selection rules for transitions between states—have significant impacts on the performance and design considerations of OLEDs. Further, energy transfer and quenching of these states are the underlying mechanisms for efficiency roll-off and degradation of OLEDs, processes which still limit the use of OLEDs in high brightness applications. These issues are summarized in Chapter 2.

2

Organic light-emitting devices

This chapter provides an overview of organic light-emitting devices (OLEDs): the history of their development, the principles of how they work, their design considerations, and what factors affect their efficiency and lifetime.

2.1 A brief history of organic electroluminescence

Electroluminescence (EL) from organic compounds was reported in 1955 by Bernanose [59], and was more famously demonstrated in tetracene crystals in 1963 by Pope, Kallmann, and Magnante [60]. These initial reports showed extremely inefficient EL which required biases of hundreds of volts. Decades of intervening research advanced our fundamental understanding of photophysics in these semiconductors,[61] but broader interest in OLEDs was ignited in 1987 when Tang and VanSlyke [62] demonstrated a ~1% efficient bilayer OLED (NPD/Alq_3). Phosphorescent OLEDs were first demonstrated near the end of the 1990s, enabling efficiencies of ~20%.[12,13,36,63–65]

Pioneer released a car audio console in 1997 with a monochrome passive matrix OLED display, likely the first commercial product containing OLEDs.[66] In 2003, Kodak released the first digital camera with a full-color active matrix OLED (AMOLED) display (the LS633).[67] Nokia released the first (successful) mobile phone with a full-color OLED display, the 6215i,[68,69] in 2006.* OLED displays were brought to prominence by Samsung's Galaxy series in the 2010s,[71] and they have since made their way into every major phone manufacturer's displays. A major reason OLEDs are attractive for displays, and have been so successful in mobile phones, is each pixel provides its own light, eliminating the need for a back-light, as is used in conventional

*The Motorola Timeport P8767, released in 2000, had an "area color" OLED display, meaning red, green, or blue pixels were separated in sections of the display.[70] This phone was withdrawn from the market soon after release because of its low power efficiency, low lifetime, and high cost.[66] The BenQ-Siemens S88 was also released in 2006, slightly before the Nokia 6215i, but BenQ collapsed later that year.[71–73]

liquid crystal displays (LCD). Without a back-light, OLEDs have effectively infinite contrast (black is a "true black", pixels are simply turned off), and they also can have much higher power efficiency (no light is wasted by the LCD filtering process).

While these commercial advances were made, academic research continued to push forward our understanding of the physics of light outcoupling,[74] efficiency roll-off,[75] and degradation in OLEDs.[46] New, heavy-metal-free strategies to achieve high efficiency and surpass spin statistical limits were also developed and explained: delayed fluorescence from triplet-triplet annihilation, where two triplets fuse to generate a singlet;[76] thermally activated delayed fluorescence (TADF), where a low singlet-triplet energy gap leads to significant reverse intersystem crossing (2012);[77] and doublet emission from a neutral radical (2015).[11] Around 2010, researchers also started to realize that emitter dipoles were not necessarily isotropically oriented,[22,78,79] which has since been exploited to improve outcoupling efficiency by designing emitters with preferential horizontal orientation.

Together, these advances have given us a comprehensive understanding of how OLEDs work and have provided a slew of design strategies to further optimize efficiency. But a number of challenges still remain. Efficiency roll-off at high electrical biases due to exciton quenching still limits performance in high brightness automotive and imaging applications. Blue phosphorescent (and TADF) emitters have not yet been incorporated in a commercial display because of their poor stability.[45,80] Even beyond blue emitters, device lifetime is notoriously difficult to predict. In fact, operational stability has been largely empirically optimized—to admirable success, as lifetimes for green and red devices have reached over 10^6 h at standard operating conditions[46]—but the underlying mechanisms of device degradation remain difficult to unravel. This lack of understanding in turn slows down materials discovery, because even closely related molecules can show drastic differences in lifetime (see Chapter 5 for a case study of this effect).* These issues of efficiency roll-off and degradation are also fundamental challenges to the effort to developing an electrical-injection organic laser. While the first ever organic EL laser was demonstrated in 2019,[81] considerable optimization is needed to develop this device into a scalable, efficient, and durable product fit for applications.

*Other challenges not focused on in this thesis include color purity and outcoupling strategies which are scalable and don't contribute to pixel cross-talk.

2.2 Structure and operation

The earliest demonstrations of organic electroluminescence consisted of a single organic semiconductor layer sandwiched between two conductive contacts.[59,60] In this simple structure, electrons and holes are injected by the contacts when an electrical bias is applied, they recombine to form excitons, the excitons decay to emit light, and then some fraction of the emitted photons escape the device into the external medium. These fundamental steps for light emission are illustrated schematically in Figure 2.1.

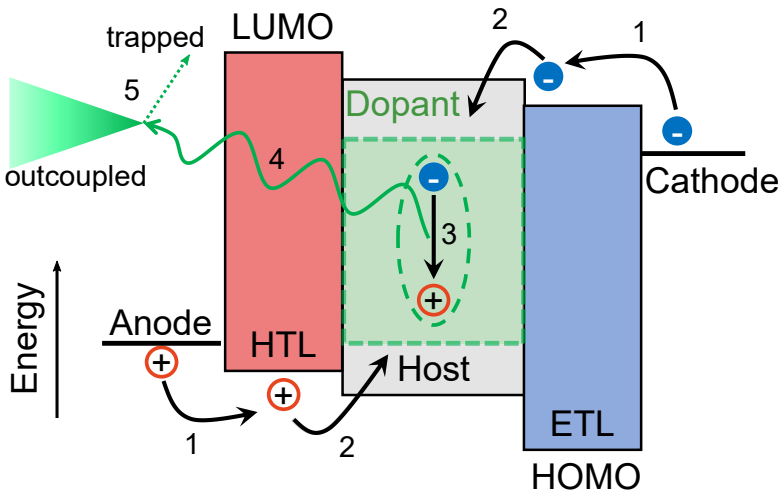

Fig. 2.1. Schematic of energy levels and each step of the light emission mechanism of an OLED: (1) electrons and holes are injected from the cathode and anode, respectively; (2) holes move along the HOMO level of the hole transport layer and electrons move along the LUMO level of the electron transport layer, arriving at the emissive layer; (3) charges recombine to form excitons; (4) a fraction of excitons relax radiatively; and (5) a fraction of emitted photons are outcoupled from the device, while the rest remain trapped (or couple to loss pathways) within the device.

For photons to escape an OLED, one or more of the electrodes must be transparent (Figure 2.2a–b). In "bottom-emitting" OLEDs, light emission occurs through the transparent bottom contact (closest to the substrate), usually indium tin oxide (ITO) or some other transparent conductive oxide (TCO). In "top-emitting" OLEDs, light emission occurs through the transparent top electrode, usually a thin metal layer or ITO. Less commonly, both contacts can be transparent, allowing for emission from both sides. The OLEDs studied throughout this thesis are all bottom-emitting structures with the anode (hole-injecting) contact on the bottom and the cathode (electron-injecting) contact on the top.

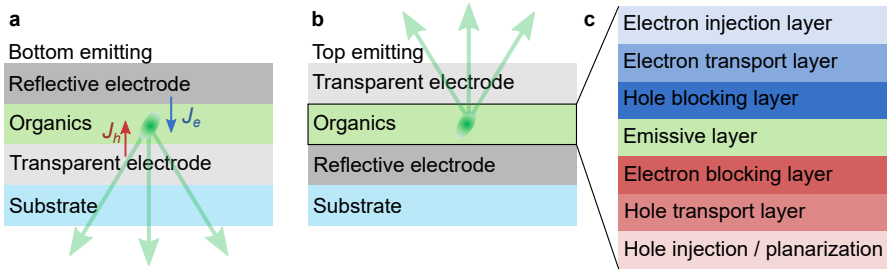

Fig. 2.2. Basic OLED architectures: (**a**) Bottom-emitting architecture where emission occurs through the substrate side of the architecture. The transparent electrode is usually ITO. Red and blue arrows show hole and electron current (J_h and J_e), respectively. (**b**) Top-emitting architecture where emission occurs through the top transparent electrode, usually a thin metal layer or ITO. (**c**) Typical organic layer structure for commercial OLEDs, including charge injection, transport, and blocking layers to efficiently move charge to and confine charge within the emissive layer.

Since the demonstration of tetracene EL in 1963,[60] device structures have grown more complicated and advanced to achieve high efficiency and stability. State-of-the art OLEDs are almost always multi-layer stacks (Figure 2.2c),* often consisting of an emissive layer (EML) surrounded by charge injection, transport, and blocking layers.

Injection layers serve to adjust the work function of the contacts to more closely align with the HOMO and LUMO of the organic layers. Typical hole injection layers (HIL) include MoO_3, HAT-CN, CuPc, PEDOT:PSS, and Plexcore AQ1250. The latter two are spin-coated conductive polymers which also serve to planarize the step edges and surface roughness in patterned ITO contacts, reducing the probability of electrical shorts. Electron injection layers (EIL) usually consist of Li or Cs due to their shallow work functions; most commonly, the EIL is a thin (0.5–3 nm) layer of LiF or Liq.[82–84] (See Abbreviations for full molecular names.)

Charge transport layers (CTL generally, HTL for holes, ETL for electrons) are selected to have relatively high charge carrier mobilities for their respective carrier, minimizing voltage drop across the layer. CTLs can also be doped with oxides, metals, or molecular charge-transfer dopants to further increase their conductivity and improve power efficiency.[85–87] CTLs also play two other roles: spacing the EML from the electrodes to optimize outcoupling efficiency,[74] and improving yield by reducing electrical shorts (for this reason, commercial ETLs are often >100 nm thick).

Blocking layers are selected to have high triplet energies (or high singlet energies in fluorescent devices), which are greater than the triplet energy of the emissive guest to confine excitons

*Ironically, these refined multi-layer structures were thrown out the window in the breakthrough demonstration of an electrically-pumped organic laser in 2019, which used a very simple single-layer structure (plus some thin charge injection layers) to avoid the problematic charge accumulation that occurs at organic heterointerfaces.[81]

within the emissive layer, and deep HOMO or shallow LUMO levels to prevent hole or electron leakage from the EML.

Finally, the emissive layer often consists of an emissive dopant (also called the *emitter* or the *guest*) diluted in a wide energy gap host. The host:guest structure serves to confine excitons on the guest, reduce concentration quenching by spacing guest molecules apart, and modify charge transport.[88]

2.3 Device performance and characteristics

2.3.1 Current-voltage and luminance

OLEDs show diode-like current-voltage characteristics (Figure 2.3) due to their charge-selective contacts and transport layers. Below the turn-on voltage (region 1, usually $\lesssim 2\,\mathrm{V}$), carriers have insufficient energy to overcome the injection barriers at the contacts. The current density through an efficient OLED in this region is quite low ($J \lesssim 10^{-5}\,\mathrm{mA\,cm^{-2}}$) and reflects a combination the geometric capacitance of the device and leakage current (from pinholes and shorts). In region 2, slightly above the turn-on voltage, current sharply increases. Current here is injection limited, increasing exponentially as the applied bias overcomes the injection barriers, and predominantly reflects recombination current (electrons and holes annihilating, preferably by forming excitons and emitting light). The current-voltage slope reduces into a power-law dependence in region 3 at biases 1–2 V above turn-on, where injection is no longer limiting and instead accumulated charge in the device limits the current (space charge limited current).[61]

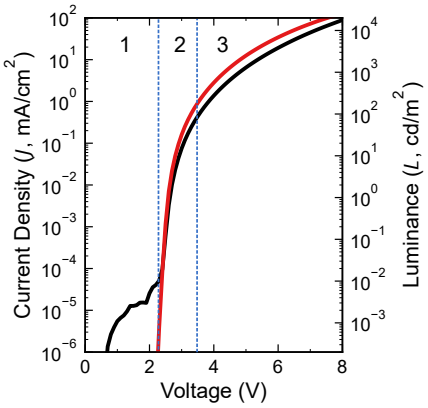

Fig. 2.3. Current-voltage (black curve) regimes and luminance (red curve) characteristics: (1) capacitive curent below turn-on, (2) injection-limited current, and (3) space-charge limited current.

2.3.2 External quantum efficiency

In this work, the primary efficiency metric we are concerned with is the external quantum efficiency (η_{EQE} or EQE),* which is the number of photons which escape to the external medium divided by the number of injected electrons (photons out over electrons in). The EQE can in turn be expressed as the product of component efficiencies representing each step required to convert injected charge carriers to extracted photons (Figure 2.1):[12,91]

$$\eta_{EQE} = \eta_{EF}\chi\eta_{\tau}\eta_{PL}\eta_{OC} \tag{2.1}$$

η_{EF} is the exciton formation efficiency, or the fraction of injected electrons which form an exciton on an emitter molecule. This term is discussed in more detail in Section 2.3.3.

χ is the radiative spin fraction, discussed in Section 1.2, which is typically unity for phosphorescent and TADF emitters and $1/4$ for fluorescent emitters in the absence of triplet fusion.[43,92]

η_{PL} is the photoluminescence efficiency of the emitter (i.e. the exciton-to-photon conversion efficiency). This term takes into account the influence of the device microcavity on the radiative rate (the Purcell effect).[74] In most state-of-the-art emitters, η_{PL} approaches unity.[65]

η_{τ} is the fraction of excitons that recombine *via* the natural lifetime as opposed to bimolecular quenching (EEA or EPQ).[41,91] This factor is usually thought to be near unity at low biases near peak EQE and then falls off at high bias, contributing to efficiency roll-off. η_{τ} is discussed further in Section 2.4 and chapters 6 and 7.

η_{OC} is the outcoupling efficiency, i.e. the fraction of emitted photons which escape into the external medium. For bottom-emitting OLEDs, η_{OC} is often estimated at ~20% based on simple ray optics, taking into account the index of refraction of the organic layers which determines the angle for total-internal reflection ($\eta_{OC} \approx 1/(2n^2)$.[93,94] This term is by far the limiting factor for most OLEDs, but it can be overcome by a variety of strategies such as designing emitters with horizontal orientation or including scattering layers to extract waveguided light.[94] Accurate calculation of η_{OC}, taking into account waveguiding and surface plasmon modes at the cathode interface, requires a transfer matrix formalism coupled with the assumption that emitters behave as classical dipoles (Figure 2.4).[74] The relative importance of each of these modes

*For a comprehensive overview of various efficiency metrics and measurement approaches for thin film LEDs, see refs. [89, 90].

depends on the layer thicknesses, indices of refraction of each material, emitter dipole orientation, and the emission color. Coupling to the surface plasmon mode is more dominant when the emissive dipoles are located less than ~40 nm from the reflective cathode (Figure 2.4b), whereas waveguiding is more significant when the organic layers are more than ~200 nm thick.

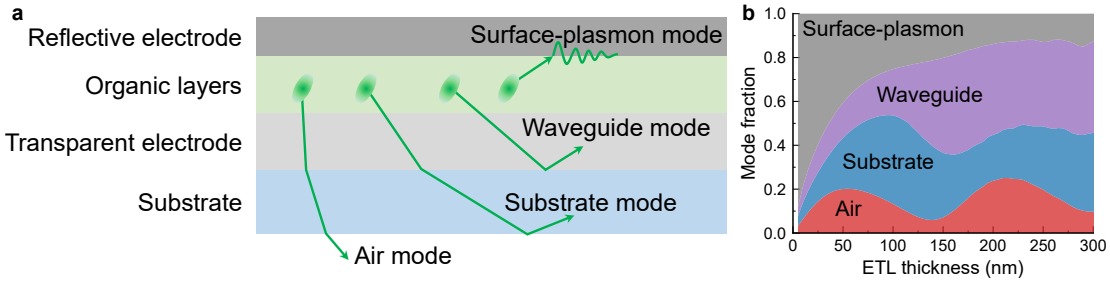

Fig. 2.4. Optical modes in an OLED: (**a**) Schematic showing the primary modes for light coupling in an OLED. The **air mode** is light which escapes to air, the **substrate mode** represents totally-internally reflected light within the substrate, the **waveguide mode** represents light trapped within the ITO and organic layers, and the **surface-plasmon mode** represents evanescent coupling of the emitter dipole to the surface-plasmon modes at the organic/metal interface. (**b**) Calculated mode distribution as function of electron transport layer (ETL) thickness for an OLED with the structure: Glass/ITO (100 nm)/TCTA (100 nm)/TPBi:Ir(ppy)$_3$ (8%, 10 nm)/TPBi (x nm)/Al (100 nm).

Taking all of these terms together, the peak efficiency of state-of-the-art phosphorescent OLEDs is generally limited by the outcoupling efficiency, resulting in $\eta_{EQE} \approx 20\%$ for isotropic emitters, up to $\eta_{EQE} \approx 30\%$ for an oriented emitter, and over 50% for OLEDs with scattering layers.[95]

We note that other terms can be envisioned to capture possible loss pathways, such as the exciton confinement efficiency,[96] to capture if excitons leak out of the EML. In any case, formulating EQE into separate components is always an approximation based on assumptions about which factors limit performance, and this approach is limited by our ability to reliably measure or calculate each parameter. Nonetheless, Eq. (2.1) helps to guide our thinking about where energy is lost within an OLED.

2.3.3 Exciton formation and charge balance

In this thesis, we will generally avoid the conventional terminology of the "charge balance factor", γ, and replace it with a more general exciton formation efficiency, η_{EF}. Charge balance is typically cast as the efficiency of charge carrier recombination in the emissive layer, competing with carrier leakage.[46,96] In contrast, we take η_{EF} to represent the efficiency of forming excitons

on an emissive molecule, which can be reduced by both the introduction of non-radiative recombination centers and charge leakage (Figure 2.5).[97,98] The reason for this formulation is that neither charge leakage nor non-radiative recombination can be readily measured. By grouping both factors in one term, their combined value can be isolated by separately quantifying all other efficiency terms (which can all be routinely measured or simulated).

The exciton formation efficiency can be defined quantitatively in terms of the recombination current on emitter molecules (J_{rec}) and the injected current (J_{inj}) or the competitive leakage (J_{leak}) and non-radiative recombination currents (J_{nr}). These currents cannot be readily measured, but they can be simulated using a drift-diffusion or other charge transport model:

$$\eta_{EF} = \frac{J_{rec}}{J_{inj}} = \frac{J_{rec}}{J_{rec} + J_{nr} + J_{leak}} \tag{2.2}$$

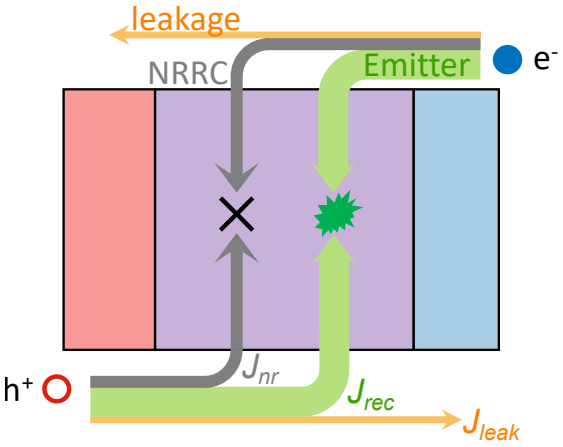

Fig. 2.5. Charge recombination and loss pathways: Injected holes and electrons can either (1) recombine to form an exciton on an emitter molecule (with current J_{rec}),[a] (2) recombine on a non-radiative recombination center (J_{nr}), or (3) leak out of the emissive layer to recombine in a transport layer or at the electrodes (J_{leak}).

[a] Charges can also recombine to form host excitons. We assume that the exciton transfer efficiency from host to guest is unity here, but this could in principle introduce another loss pathway.

Charge leakage can sometimes be experimentally observed by transport layer emission, but this is only qualitative due to unknown quenching within the transport layer. Direct measurements of charge and exciton leakage, and hence η_{EF}, have been carried out using thin strips of fluorescent and phosphorescent sensitizers at either end of the emissive layer.[96] This approach is more quantitative but requires accurate knowledge of the η_{PL} of each sensitizer and assumes no quenching occurs at either sensitizer. Care must also be taken to avoid site saturation. In the absence of these types of extensive characterization, η_{EF} or γ are often used as fudge factors to account for deviations in the peak EQE from the calculated outcoupling efficiency and measured photoluminescence efficiency. One way in which this sloppy sort of quantification can go wrong is detailed in Chapter 6.

2.4 Efficiency roll-off

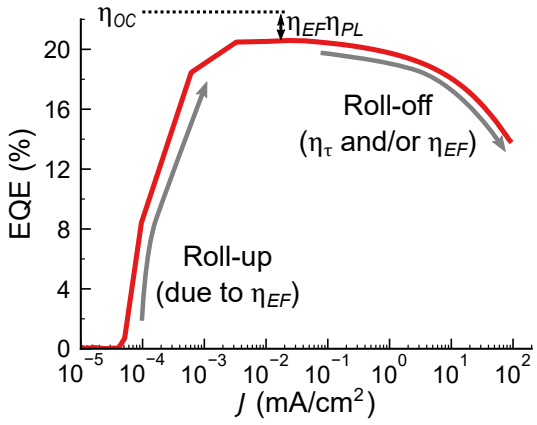

Fig. 2.6. Example of EQE roll-up and roll-off: Between roughly 10^{-4} mA cm^{-2} and 10^{-3} mA cm^{-2}, EQE is limited by leakage current and "rolls-up" to the peak EQE of ~20%. The peak EQE for this phosphorescent OLED is primarily limited by η_{OC} but can also be reduced by non-unity η_{PL} and η_{EF}. Above ~10^{-1} mA cm^{-2}, EQE begins to decline ("roll-off"). Roll-off is primarily attributed to reductions in η_τ due to bimolecular quenching, but charge leakage (η_{EF}) can also contribute.

As shown in Figure 2.6, the EQE of an OLED, and the component efficiencies which make up EQE, are not generally constant with electrical bias. At low biases near turn-on, EQE is initially low, likely due to charge leakage,* and then quickly rises to reach a saturation value which is typically fairly flat between $J \approx 10^{-3}$–10^{-1} mA cm^{-2}. This region, which coincides with the injection-limited region of the current-voltage characteristics, is called the "roll-up". The peak EQE after the roll-up is ideally limited only by η_{OC}, but in practice some combination of non-unity η_{PL} and η_{EF} may also lower EQE at this bias level. As current density is increased above some threshold (typically $J \approx 10^{-1}$–10^{1} mA cm^{-2}), EQE begins to reversibly decline below the peak value, a process which is called "roll-off" (referred to as "droop" in the inorganic LED literature).

Coarsely, we can think of the roll-up as being limited by η_{EF}, the peak EQE being limited by η_{OC}, and the roll-off being limited by η_τ. The bimolecular quenching processes (EEA and EPQ) which lower η_τ can be treated kinetically as chemical reactions which consume excitons. For phosphorescent OLEDs, which have a large intersystem crossing rate and negligible singlet exciton density, the competing "reactions" an exciton can undergo can be expressed with the rate equation for triplet exciton density (n_T):

$$\frac{dn_T}{dt} = G + D\frac{\partial^2 n_T}{\partial x^2} - \frac{n_T}{\tau} - k_{TP} n_T n_{pol} - k_{TT} n_T^2 \tag{2.3}$$

*Though, as discussed in Chapter 6, exciton quenching near turn-on could also influence this roll-up behavior.

The polaron quenching term used here, $k_{TP}n_T n_{pol}$, captures the average behavior of electron and hole quenching. The quenching rate constants for electrons and holes can be separated by fabricating single-carrier devices with charge-selective contacts.[38] We can then define η_τ as the magnitude of the natural decay term (n_T/τ) divided by the sum of all other consumption terms:

$$\eta_\tau = \frac{n_T/\tau}{n_T/\tau + \frac{1}{2}k_{TT}n_T^2 + k_{TP}n_T n_{pol}} = \frac{1/\tau}{1/\tau + \frac{1}{2}k_{TT}n_T + k_{TP}n_{pol}} \tag{2.4}$$

Or, to account for spatial variations in exciton density ($n_T(x)$) and polaron density ($n_{pol}(x)$), the average η_τ for the device can be obtained by integrating over the emissive layer:

$$\eta_\tau = \frac{\int_{EML} n_T/\tau dx}{\int_{EML} n_T/\tau + \frac{1}{2}k_{TT}n_T^2 + k_{TP}n_T n_{pol} dx} \tag{2.5}$$

Similar formulations for η_τ could be made for fluorescent or TADF OLEDs, but a second, coupled differential equation for singlets would be needed, adding terms for intersystem crossing, singlet-triplet annihilation, field quenching, etc.

The origin of efficiency roll-off at high current densities is made clear by Eq. (2.4). TTA and TPQ are second order processes, proportional to n_T^2 and $n_T n_P$, respectively. Because both triplet density and polaron density are roughly proportional to current density, these terms increase much more sharply with current density than the first order natural decay process.

η_τ is usually thought to be the dominant roll-off pathway at moderate to high current densities,[41] but other processes can also contribute to roll-off. At the extremely high biases ($\gtrsim 1\ \mathrm{A\,cm^{-2}}$) needed for electrical injection lasing, Joule heating can become a limiting factor because the non-radiative rate increases at high temperature.[58] Charge leakage is also expected to increase, lowering η_{EF}, as the applied biases begin to exceed the charge confining energy barriers.[99]

2.5 Degradation

The efficiency roll-off processes described in the previous section are mostly reversible: reduce the applied bias and the EQE recovers to its initial value. But, over time, EQE can be reduced irreversibly due to environmental exposure, morphology changes, and/or chemical reactions. These competing processes of device degradation are often broadly classified as either *extrinsic*

mechanisms—such as exposure to heat, air, or moisture, or the inclusion of impurities)—or *intrinsic* mechanisms which occur unavoidably due to operation of the device itself. Intrinsic degradation is usually manifest as chemical or morphological changes within the device. The same mechanisms that cause efficiency roll-off (EEA and EPQ) are also thought to be responsible for most intrinsic degradation,[97] as the excess energy from a bimolecular annihilation event can be sufficient to dissociate bonds.[100]

In early studies,[101,102] device lifetime was limited by extrinsic degradation due to exposure to moisture and oxygen. OLEDs operated in ambient conditions rapidly show growth of "dark spots", areas of the device which are non-emissive (Figure 2.7). Dark spots form due to oxidation of the cathode and formation of gas bubbles which delaminate the cathode,[102] and can fortunately be easily avoided by encapsulating devices in an inert atmosphere. Devices in this thesis are encapsulated in a N_2 glovebox with cover glass lids sealed onto the substrate with UV-curable epoxy. Encapsulation of this sort is sufficient for lifetime testing in ambient conditions over several weeks, but the water vapor transmission rate of epoxy is too high to be effective for long term use. In practical applications, which must survive years of use, OLEDs are packaged with multilayer barrier layer structures as well as getter materials which can absorb and trap moisture and oxygen.[103]

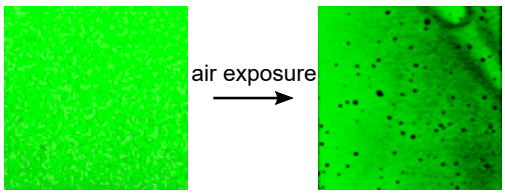

Fig. 2.7. Pristine pixel (left) and dark-spot formation after exposure to moisture (right).

While there is still room to optimize the cost and performance of barrier layers, the focus of this thesis is on intrinsic degradation, which remains less well understood and difficult to predict. The subsequent sections summarize the typical time dependence of intrinsic luminance loss, the chemical and morphological pathways underlying intrinsic degradation, and the kinetics of these degradation reactions.

2.5.1 Typical luminance loss behavior

When operated at a constant current, the luminance (EL intensity) of OLEDs generally shows a roughly stretched exponential decay over time:[104]

$$L(t)/L(0) = \exp\left(-(t/\tau)^{\beta}\right) \tag{2.6}$$

Eq. (2.6) is purely phenomenological with no basis in degradation mechanism and many devices deviate from this functional form. But it can be useful for fitting lifetime data and extrapolating approximate lifetime values (Figure 2.8a). OLED lifetime is usually defined as the time t_x that it takes for the luminance to decline to $x\%$ of the initial value (e.g. t_{50} when the brightness has degraded by half, see Figure 2.8a). Lifetime values are quoted at a range of percentages of luminance loss; for industrial purposes, lifetimes are often quoted at t_{97} (3% luminance variation is the approximate threshold the human eye can detect), t_{95}, or t_{90} based on the specific demands of a given product. In academic papers, lifetimes are generally lower—due to the lower intrinsic stability of materials in the public domain and also, perhaps, less stringent control over material purity—and it is common to quote t_{50} or t_{70}.

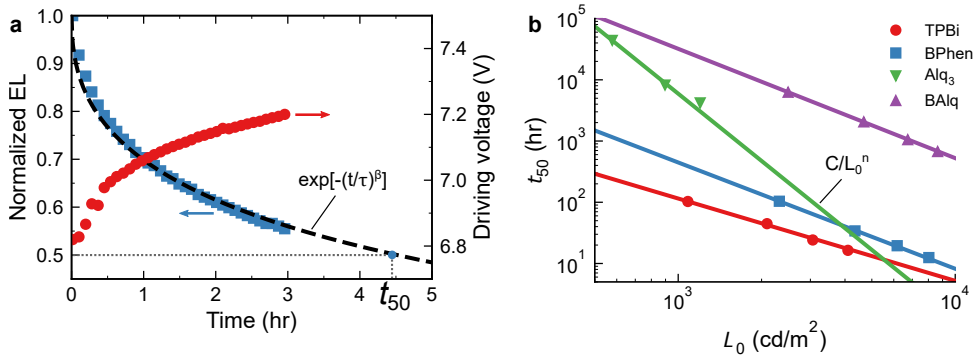

Fig. 2.8. (**a**) Example OLED lifetime data, showing a decrease in EL intensity (luminance) and rise in driving voltage when operated at constant current. Dashed line shows stretched exponential fit for extrapolating the approximate t_{50} lifetime. (**b**) Example accelerated testing data for extrapolating lifetime at low luminance. Data is taken from Meerheim et al. [105] for a red phosphorescent OLED with different ETLs. The acceleration factor (n, slope on the log-log plot), differs between the ETLs reflecting changes in degradation mechanism.

Many state-of-the-art OLEDs are prohibitively long lived ($t_{50} > 10^5$ h) at display- and lighting-relevant brightness (100–1000 cd m^{-2}),[46] so accelerated testing methods are needed to characterize their lifetime. Commercially, accelerated testing is often done at elevated humidity (typically 80% r.h.), elevated temperature (typically ~50 °C),[106] and high brightness. High humidity is meant to test failures in packaging, increasing temperature accelerates degradation reactions (which have Arrhenius rate constants),[46,106] and increasing brightness accelerates bimolecular-quenching-induced defect reactions.* Of these parameters, increasing brightness is the most straightforward (as it doesn't require climate control), and it usually leads to an inverse

*Brightness and temperature effects are coupled in the absence of active cooling because of increased Joule heating at high brightness.[106]

power law scaling of lifetime:[104]

$$t_x = C / L_0^n \tag{2.7}$$

Beyond its usefulness for lifetime extrapolation, this scaling relationship can also provide qualitative insight into the degradation mechanism.[97] For example, Meerheim et al. [105] found that devices with different ETLs had different exciton distributions and considerably different acceleration factors (the log-log slope, n—see Figure 2.8b), reflecting changes in degradation kinetics. Again, extracting physical meaning from this scaling relationship is difficult, as numerous factors are bundled in the device lifetime. But one example of the type of insight that can be gleaned for luminance scaling is discussed in Chapter 3.

2.5.2 Morphological degradation

One form of intrinsic degradation is morphological changes which occur as a consequence of, or which are accelerated by, device operation. Often, changes in morphology occur due to metastability of amorphous films,[17] exposure to high temperature,[107] and/or Joule heating during device operation at high luminance.[46] Examples include crystallization, phase segregation, and interdiffusion between layers. Crystallization can lead to substantial film roughness and in turn causes cathode delamination and increased leakage.[108] Phase segregation of a doped film over time can lead to aggregation and concentration quenching of the emitter and decreased mobility of the film.[42,46] Interdiffusion between layers can have devastating effects on charge balance and leakage by reducing charge confinement.[109] Nonetheless, morphological changes can largely be avoided by selection of materials with high glass transition temperature, and by employing mixed layers.[46,110,111] For example, altering dopant concentration can stabilize an amorphous layer and decrease film aggregation.[17,109]

2.5.3 Chemical degradation

In well-optimized material systems, intrinsic degradation of OLEDs is almost always associated with chemical reactions within the organic semiconductor active layers.[46,112] These chemical reactions can occur when an excited state has sufficient energy to dissociate a bond, splitting a molecule into fragments. An example reaction pathway of the hole transport material, TCTA, is shown in Figure 2.9.

As Figure 2.9 illustrates, energy from electrical pumping promotes molecules to the excited

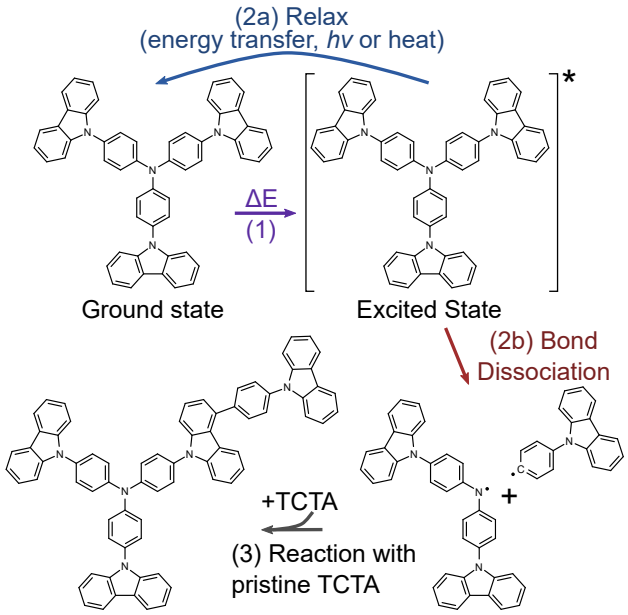

Fig. 2.9. Fragmentation and degradation reaction scheme of TCTA: (**1**) A ground-state TCTA molecule is promoted to the excited state by energy from optical or electrical excitation (ΔE). In the vast majority of excitations, the energy of the excited state is dissipated by (**2a**) relaxation to the ground state (transferring energy to another state, emitting light, or releasing heat). But occasionally, after perhaps tens of millions of excitations,[97] excess energy is dissipated by (**2b**) bond dissociation. The most prevalent fragments form when one of the central C–N bonds breaks (of the triphenylamine group). (**3**) Radical fragments from (2b) can then react with pristine TCTA molecules to form larger-molecular-weight products. Fragments and secondary products proposed by Scholz, Walzer, and Leo [113] based on LDI-TOF-MS analysis.

state when a device is operated. In the vast majority of these events, the excited molecule will simply relax to the ground state by transferring energy to another state, emitting a photon, or releasing heat. Each emitter molecule is excited tens of thousands of times an hour,* and after perhaps tens of millions of these excitations,[97] the energy of the excited state will be dissipated by breaking a bond.

Bond cleavage can result in either two radicals (uncharged species, each with an unpaired electron) or two charged fragments (an anion and a cation). These radicals and charged species can persist in the film,[46,98] or participate in further reactions, forming larger complexes with neighboring molecules.[46,113] These fragments and secondary reaction products, called *defects*, generally have different energy levels and photophysical properties than the pristine materials.[46,49,97,114,115] For instance, larger complexes from secondary reactions will likely have a greater extent of conjugation (Figure 2.9, step 3), and their energy levels will be red-shifted compared to the pristine molecule. Once formed, defects can deteriorate device performance by: (a) quenching luminescence (if the defect's triplet energy is lower than the pristine emitter),[6,116,117] (b) trapping charges (if the defect has a shallower HOMO or deeper LUMO than the host or guest),[118–120] (c) serving as a radiative or non-radiative recombination centers that

*Number of excitations is estimated as $n_T c_{mol} t/(\tau\rho)$, where $n_T \approx 5\times10^{16}\,\mathrm{cm}^{-3}$ is the exciton density, c_{mol} is the molar doping percentage, t is the operation time, $\tau \approx 1\,\mu\mathrm{s}$ is the exciton lifetime, and $\rho \approx 10^{21}\,\mathrm{cm}^{-3}$ is the molecular concentration.

bypass the emitter,[46,98,121] or some combination of the above. These mechanisms are illustrated in Figure 2.10.

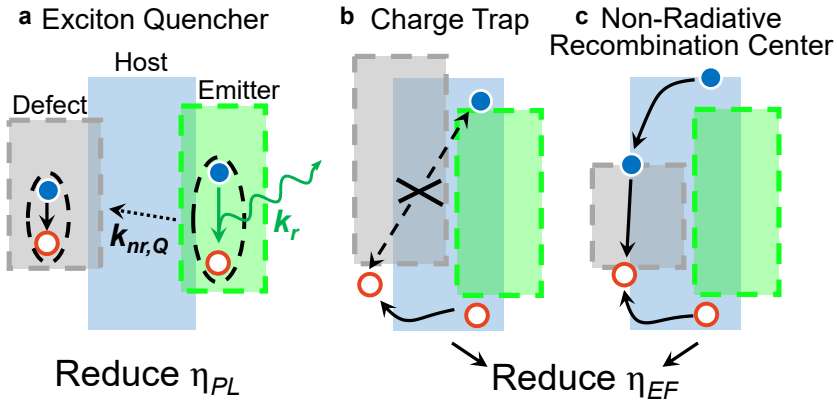

Fig. 2.10. Energy level schematic illustrating three proposed mechanisms by which a defect can deteriorate OLED performance: (**a**) Luminescence quenching by exciton transfer of an emitter triplet to the non-emissive triplet level of a defect with a small triplet energy. This increases the non-radiative rate (by $k_{nr,Q}$), reducing η_{PL}; (**b**) charge trapping by a defect with a shallower HOMO than the emitter, which can prevent exciton formation, lower mobility, and increase driving voltage;[116] and (**c**) recombination center, which bypasses the emitter and can be weakly radiative or non-radiative.[116,121]

Again, the formation of defects occurs in only a minuscule fraction of total excitations. But even small concentrations of defects can dramatically reduce device efficiency. Using a simple differential equation model for degradation, Giebink et al. [97] estimated that degradation of as little as 0.1% of molecules could reduce efficiency by 50%. These small concentrations make it exceedingly difficult to directly measure degradation reaction products, but significant progress has been made using mass spectrometry techniques. Perhaps the most widely applied is Laser Desorption/Ionization Time-of-Flight Mass Spectrometry (LDI-TOF-MS), which can be used directly on full devices.[113,114,117] Comparing mass spectra before and after degradation, researchers have been able to identify fragments which only form during device degradation and which become more prevalent at higher levels of degradation.[46,114] (This method is covered in more detail in Section 5.3.)

In one recent example, Jeong et al. [114] identified fragments which form in blue phosphorescent OLEDs based on the emitter $Ir(dmp)_3$ and an mCBP host (Figure 2.11a). They then used density functional theory (DFT) to calculate the HOMO, LUMO, and triplet energy levels of radical, ionized, and neutral forms of the fragments (Figure 2.11b). In their neutral and ionized forms, most fragments were found to be inert: they had non-trapping energy levels and triplet energies larger than the emitter. However, in their radical form, almost every fragment

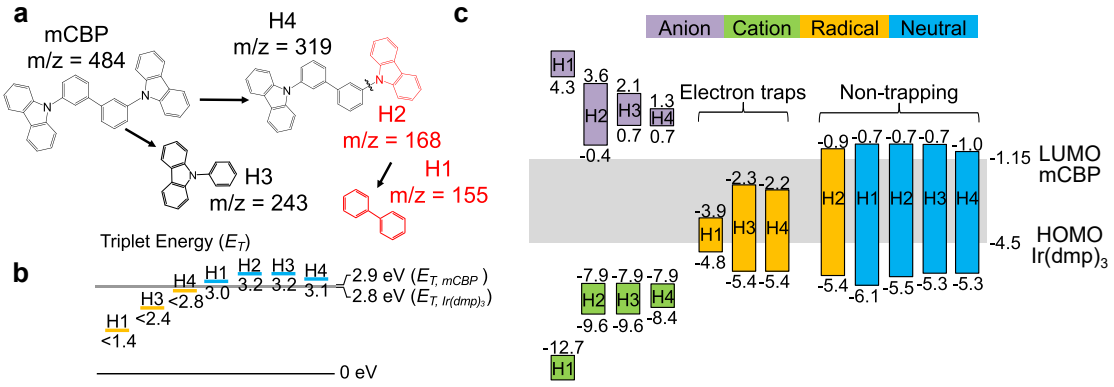

Fig. 2.11. (**a**) Fragmentation pathways for the carbazole host mCBP. (**b**) HOMO, LUMO, and triplet energy levels of ionized, radical, or neutral molecular fragments from (a) and (b). Adapted from Jeong et al. [114].

is predicted to act as an electron trap and an exciton quencher. This analysis demonstrates how even small-molecular weight fragments can be detrimental to device performance.

2.5.4 Degradation kinetics and modeling

Defect formation, being tied to device operation, is fundamentally driven by the presence of charge carriers (polarons) and excitons.* In limited cases, molecules can become unstable in the charged state alone.[46] For example, the oxygen bond in Alq_3 has been found to directly dissociate under a hole-only current.[122,123] More often, excitons and the energy they carry are involved in fragmentation of molecule. The energy from an exciton can either directly break a bond, or—what is more likely—the energy can transfer to another exciton or polaron during bimolecular annihilation and promote it to a higher energy state. This "hot" excited state or carrier holds roughly twice the energy of a T_1 exciton, easily in excess of the bond dissociation energy,[100,112] and can dissipate this energy by cleaving a bond. From this standpoint, the phenomenon of EQE roll-off is thought to be mechanistically tied to degradation in OLEDs. That is, the same bimolecular quenching processes that dictate EQE roll-off have some small probability of forming a defect.[97,112]

It should be noted that defects do not necessarily need to involve bond dissociation. Recently, formation of aggregates (such as dimers, trimers, etc.) of transport and host materials has been identified as another active pathway for degradation.[6,121,124,125] These aggregates

*This type of degradation is somtimes called "Coulombic",[116] since it scales with the amount of charge passed through the device.

are formed primarily by exciton-polaron interactions at emissive layer/transport layer interfaces where substantial charge accumulation occurs.[121] Weak, red-shifted emission has been observed from these aggregates, and thus they can act as weakly radiative luminescence quenchers (Figure 2.10c).

In early work, Giebink et al. [97] evaluated the hypothesis that bimolecular quenching events cause degradation using a multi-scale, coupled differential equation model to describe defect formation. In this approach, the differential equation for exciton density, with dynamics at the microsecond timescale (t), is solved at the steady-state and then input into the longer-timescale (t') defect formation equation and numerically integrated. Note that Eq. (2.8) is identical to Eq. (2.3) except for diffusion is ignored and an additional term for defect quenching ($-k_{nr,Q}n_T Q$) is added:

$$\frac{dn_T}{dt} = G - \frac{n_T}{\tau} - k_{nr,Q}n_T Q - k_{TP}n_T n_{pol} - k_{TT}n_T^2 \tag{2.8}$$

$$\frac{dQ}{dt'} = k_{QF,TT}n_T^2 + k_{QF,TP}n_T n_{pol} \tag{2.9}$$

where Q is the defect density, $k_{nr,Q}$ is the defect quenching rate constant, $k_{QF,TT}$ is the TTA-induced defect formation rate constant, and $k_{QF,TP}$ is the TPQ-induced defect formation rate constant. The exciton generation rate, G, was calculated by Giebink et al. assuming Langevin recombination and a simple polaron dynamics equation (see ref. [97] for more details).

This model provides reasonable fits to degradation data over a range of initial luminances, providing some support to the notion that bimolecular quenching reactions are involved in degradation. But the large number of free (and unverifiable) parameters,* in addition to assumptions placed on charge and exciton distributions within the device, makes it difficult to come to strong mechanistic conclusions. By varying the hypothetical defect formation reaction, Giebink et al. [97] used the model to argue that TPQ-induced degradation was dominant. Yet later studies of similar devices from the same group suggested that TTA-induced degradation was responsible.[100,126] These conflicting findings point to the challenging ambiguities of modeling OLED degradation with limited observable quantities. As a veteran industrial researcher put it:

*Scholz et al. [46] described this work as using "a mathematical model with several arbitrary parameters and assuming an otherwise unsubstantiated mechanism of electroluminescence loss"

> Considering the multitude of experimentally unsupported assumptions about distribution and dynamics of charge carriers and excited states required for such models, it is doubtful that reliable mechanistic conclusions can be reached based on fitting operational characteristics to some models.
>
> – D.Y. Kondakov
> *The Role of Homolytic Reactions in the Intrinsic Degradation of OLEDs*, pg. 232.[116]

This model of degradation was first presented by Giebink et al. [97] in 2008, and it has been widely applied since then without much further sophistication (other than to add more free parameters).[100,126] We will use the basic framework of this model to guide our intuition and analysis of the degradation kinetics studies described in Chapters 3 and 4, but one major goal of this thesis is to develop a deeper understanding of degradation mechanisms. Toward this end, we have focused on developing experimental techniques which give us access to more observable quantities which can be compared against, and used to refine, these existing models.

2.5.5 Characterizing degradation

OLED lifetime testing is generally carried out under constant current density conditions. Most often, characterization of lifetime consists solely of measuring EL over time with a photodetector and voltage rise with a source measure unit. Changes in EL, when operating at a fixed current density, reflect changes in EQE. But how the various components of efficiency (e.g. η_{EF}, η_{PL}) change with degradation cannot be resolved with only measurements of EL. This limits our ability to assess the mechanisms and kinetics of degradation.

To access more information into device degradation, several groups have tracked changes in PL simultaneously (Figure 2.12).[116,127,128] We have further developed this technique, both in instrumentation and analysis of results, to allow for more quantitative decoupling of EL and PL losses. These advances are described in Chapters 3 and 4 and specifics of the measurement refinement are included in Appendix C. We also show in Chapter 5 how PL measurements can be used to isolate the influence of singlet and triplet excitons on degradation and to aid materials screening. In Chapter 7, we use measurements of PL from devices in on- and off-states to gain information into degradation-induced changes in η_τ.

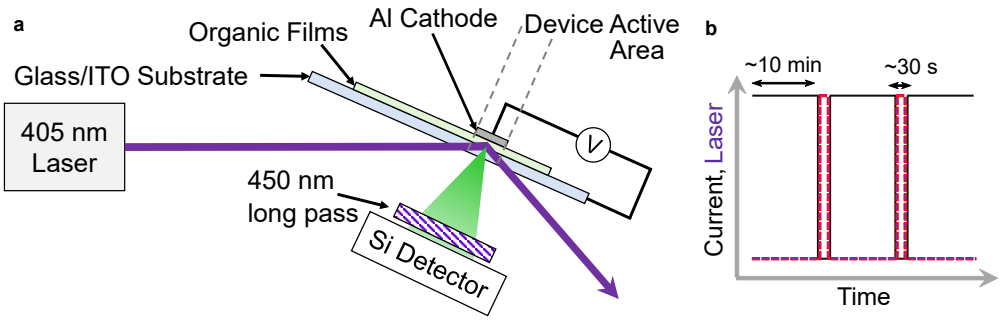

Fig. 2.12. (**a**) Schematic of decoupled EL and PL degradation measurement. A $\lambda = 405\,\mathrm{nm}$ laser illuminates the device at an incident angle of ~45°. The laser selectively pumps the emitter, the photoluminescence of which is passed through a $\lambda = 450\,\mathrm{nm}$ long pass filter (to remove scattered laser light) and collected with a Si detector. (**b**) Approximate measurement timing, where constant current is applied for ten minute intervals—measuring EL throughout—separated by ~30 s measurements of PL with the pump laser.

3

Lifetime scaling with recombination zone width

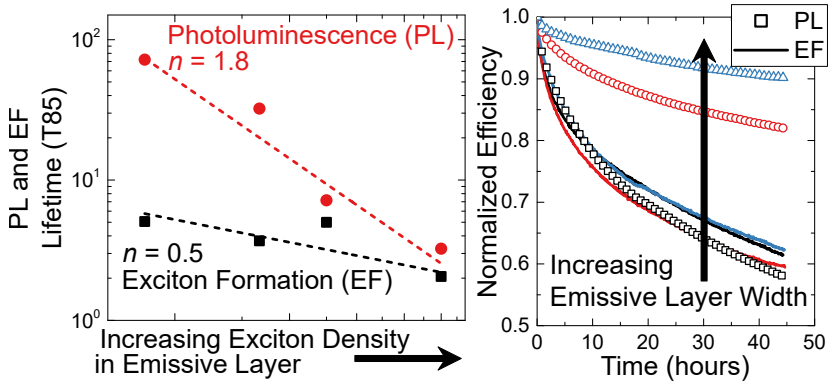

Separate degradation mechanisms determine photoluminescence and exciton formation stability

Degradation in OLEDs is generally driven by reactions involving excitons and polarons. Accordingly, a common design strategy to improve OLED lifetime is to reduce the density of these species by engineering the emissive layer to achieve a broad exciton recombination zone. Here, the role of exciton density on device degradation is analyzed in a mixed host emissive layer (M-EML) architecture which exhibits a broad recombination zone. To gain further insight into the dominant degradation mechanism, losses in the exciton formation efficiency and photoluminescence (PL) efficiency are decoupled by tracking emissive layer PL during device degradation. By varying the starting luminance and M-EML thickness, the rate of PL degradation is found to depend strongly on recombination zone width and hence exciton density. In contrast, losses in exciton formation depend only weakly on the recombination zone, and thus may originate outside of the emissive layer. These results suggest that the lifetime enhancement observed in M-EML devices reflects a reduction in the rate of PL degradation. Moreover, the varying roles of excitons and polarons in degrading the PL and exciton formation efficiencies suggest that kinetically distinct pathways drive OLED degradation, and that a single degradation mechanism cannot be assumed when attempting to model device lifetime.

3.1 Introduction

Improving operational stability is one of the key challenges facing further commercial development of organic light-emitting devices (OLEDs) for large-area displays and solid state lighting applications.[46] Previous work has shown that intrinsic degradation in OLEDs is driven by chemical reactions mediated by both excited molecules (excitons) and charged molecules (polarons).[17,46,49,97,112,115] One general strategy to improve lifetime, therefore, is to reduce the density of these species by expanding the exciton recombination zone (RZ). A broad RZ can be achieved by engineering the emissive layer architecture to balance charge transport and injection. To this end, graded- and step-doping profiles,[126,129–131] mixtures and gradients of multiple host materials,[132–139] and double emissive layers[85,140,141] have been shown to yield a broad and centered RZ, and consequently to improve exciton confinement, charge balance, efficiency, and lifetime. Here, we study degradation in a mixed host emissive layer (M-EML) architecture, in which hole- and electron-transport materials are uniformly mixed with an emissive guest. The use of a mixed emissive layer has been shown to reduce the roll-off in external quantum efficiency observed under high current injection and increase lifetime. Indeed, while a favorable trend between device lifetime and RZ width has been well-documented,[126,129,137,142,143] the specific role the RZ plays in degradation kinetics remains an active area of investigation. Prior work has proposed that the RZ, by establishing charge and exciton densities, plays a role in determining the formation of both exciton quenchers and non-radiative recombination centers.[97,126]

In this work, the overall degradation in device electroluminescence (EL) is decoupled in terms of corresponding reductions in the efficiencies of exciton formation (η_{EF}) and radiative recombination (i.e. photoluminescence (PL) efficiency, η_{PL}).[91,125,127,128,144] Specifically, we find that a systematic increase in the RZ width for an M-EML OLED leads to a sharp reduction in the rate of degradation of η_{PL}. The exciton formation efficiency is less sensitive to reductions in M-EML width, suggesting that the exciton density may not as strongly dictate degradation in η_{EF}, potentially indicating a greater role for factors outside the emissive layer. These results provide diagnostic insight into the source of device instability, and reveal new details regarding the kinetics of degradation.

3.2 Theory

During constant current operation, losses in electroluminescence (EL) intensity occur due to reductions in the external quantum efficiency (η_{EQE}), which can be expressed as:[12,91]

$$\eta_{EQE} = \chi \eta_{EF} \eta_{PL} \eta_{OC} \eta_{\tau} \tag{3.1}$$

where χ is the spin fraction, η_{PL} is the outcoupling efficiency, and η_{τ} is the fraction of excitons that recombine via the natural lifetime, representing the degree of bimolecular quenching at a given current density.[41,91] Here, we replace the conventional charge balance factor, γ, with a more general exciton formation efficiency, η_{EF}. Charge balance is typically cast as the efficiency of charge carrier recombination in the emissive layer, competing with carrier leakage.[46,96] In contrast, we take η_{EF} to represent the efficiency of forming excitons on an emissive molecule, which can be reduced by both the introduction of non-radiative recombination centers and charge leakage.[97,98] It has previously been argued that η_{PL} and η_{EF} will be the primary contributors to luminance loss,[46,125] while χ, η_{OC} , η_{τ} will only vary negligibly during device degradation.[91] Changes in η_{OC} could occur in the event of significant shifts in the recombination zone position, but the broad RZ present in M-EML devices reduces this effect. In addition, η_{τ} is expected to increase during degradation due to reduced exciton density. Previous work has found, however, that this increase is small unless testing above 10,000 cd m^{-2}.[91] The potential error introduced by these simplifying assumptions is discussed in Section 3.5 and in Chapter 7. Therefore, at any point during the degradation, the normalized device EL can be written as:

$$\frac{\eta_{EQE}(t)}{\eta^0_{EQE}} = \frac{\eta_{EF}(t)}{\eta_{EF}(0)} \frac{\eta_{PL}(t)}{\eta_{PL}(0)} \tag{3.2}$$

Eq. (3.2) suggests that a simultaneous measurement of device electroluminescence (yielding $\eta_{EQE}(t)$) and photoluminescence (yielding $\eta_{PL}(t)$) permits the extraction of the exciton formation efficiency as a function of time. The direct connection between the photoluminescence intensity and η_{PL} assumes that absorption of the emissive layer is constant, changes in photoluminescence intensity come from an increase in the non-radiative rate, and that there is substantial overlap between the RZ and the optically generated exciton profile. Previous work found a direct correspondence between the reduction in PL intensity and exciton lifetime with degradation,[91] supporting the first two assumptions. The validity of the latter assumption is discussed

at the end of this work.

3.3 Recombination zone and device characteristics

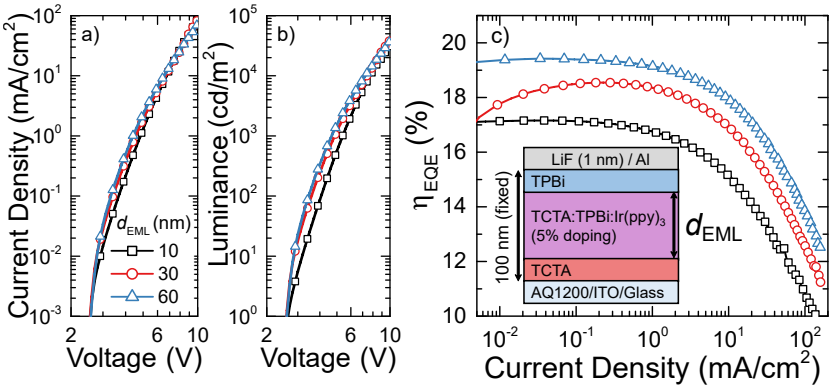

Fig. 3.1. (**a**) Current density vs. voltage, (**b**) luminance vs. voltage, and (**c**) external quantum efficiency (η_{EQE}) vs. current density for devices with M-EML thicknesses (d_{EML}) of 10, 30, and 60 nm. Inset: Device architecture of interest, where the HTL and ETL thickness are equal to each other and the total HTL/EML/ETL thickness is fixed at 100 nm.

To systematically study the effect of RZ width on degradation, we selected an architecture (inset in Figure 3.1c) with a recombination zone which spans entire emissive layer,[145] allowing the M-EML thickness, d_{EML}, to be taken as a proxy for RZ width. In principle, this permits the exciton density in the emissive layer to be tuned by changing d_{EML}. The current density-voltage-luminance characteristics and external quantum efficiency for devices with emissive layer thicknesses of 10 nm, 30 nm, and 60 nm are shown in Figure 3.1. As d_{EML} is increased from 10 nm to 60 nm, the peak efficiency increases gradually from (17 $\pm$ 1)% to (19 $\pm$ 2)% and the onset of the efficiency roll-off is pushed to higher current densities (Figure 3.1c). This change in roll-off is consistent with an increase in recombination zone width, which leads to a reduced exciton density and reduced severity of bimolecular quenching processes.[38,146]

To experimentally confirm that the RZ spans the majority of the M-EML in this architecture, we used a sensitizer-doped-strip approach.[126,133] In this method, illustrated in Figure 3.2, thin layers of a near-infrared phosphorescent sensitizer are deposited at different locations across the emissive layer. The sensitizer is selected to have spectrally-separated emission from the primary emitter, Ir(ppy)$_3$, and a lower triplet energy to ensure Ir(ppy)$_3$ excitons are efficiently transferred to the sensitizer. Excitons within about a Förster radius, R_0, of the strip will be quenched, thereby reducing the EL intensity from the Ir(ppy)$_3$ peak and increasing the EL intensity of the

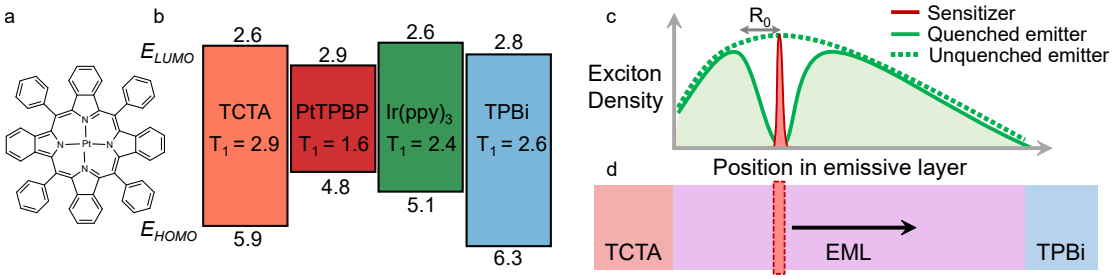

Fig. 3.2. (**a**) Molecular structure of the NIR sensitizer, PtTPTBP. (**b**) Energy level schematic of materials used in recombination zone measurement devices. The HOMO and LUMO of PtTPTBP are from Perez et al. [147]. (**c**) Schematic of recombination zone measurement, showing that emitter (Ir(ppy)$_3$) excitons are quenched within a Förster radius, R_0, of the sensitizer strip. (**d**) Illustration of the position of the thin doped sensitizer strip within the device.

sensitizer peak. The spatial resolution of this technique is limited by the thickness of the strip and R_0, so higher resolution can be achieved by minimizing the overlap between the primary emitter's emission spectrum and the sensitizer's absorption (Figure 3.3). The spatial variation of the exciton density on Ir(ppy)$_3$ is then estimated by comparing the relative outcoupling-corrected sensitizer emission:*

$$n_{ex}(x) \propto \int EL_{PtTPTBP}(\lambda, x)/\eta_{OC}(\lambda, x)d\lambda \tag{3.3}$$

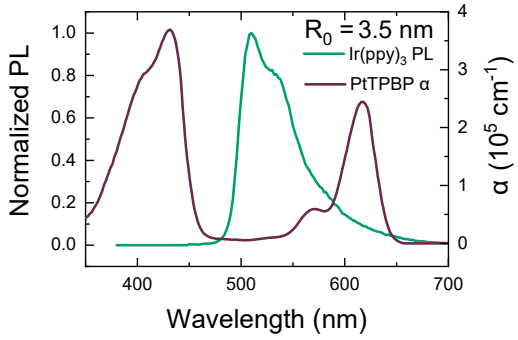

Fig. 3.3. Absorption of PtTPTBP and emission of Ir(ppy)$_3$ used to calculate the Förster radius between these molecules.

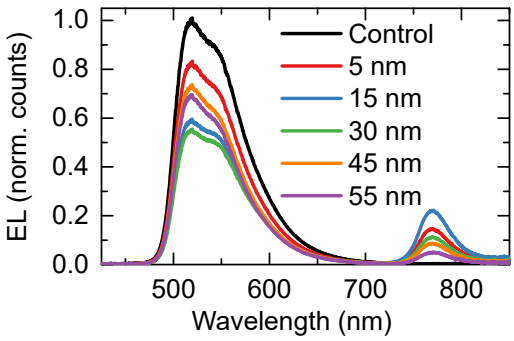

Fig. 3.4. EL spectra (counts normalized) for sensitized devices with d_{EML} = 60 nm at a current density of 1 mA cm^{-2}. Sensitizer-doped strips are centered at 5, 15, 30, 45, and 55 nm from the HTL.

*Note that normalization to the un-sensitized control device is unnecessary, as these corrections fall out as constant prefactors in this relative measurement. In some other reports, the sensitizer emission is normalized to the primary emitter's peak for each device, which is not a valid comparison because the emitter's peak is quenched by the sensitizer. In other words, this approach double counts excitons on the sensitizer.

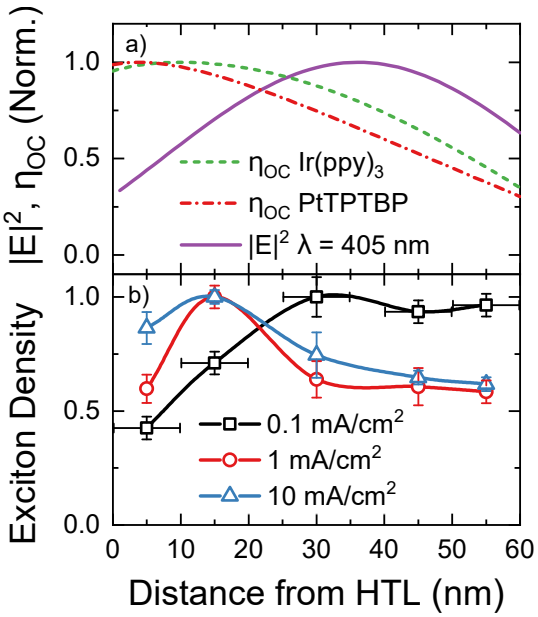

Fig. 3.5. (**a**) Electric field profile of the PL pump (λ = 405 nm, incident angle = 45°) and the spectrally weighted outcoupling efficiency for Ir(ppy)$_3$ and PtTPBP emission. (**b**) Normalized exciton density profiles for 0.1, 1, and 10 mA cm^{-2}. Solid lines are guides to the eye. Error bars in position represent the width of the dopant strips and the Förster radius between Ir(ppy)$_3$ and PtTPTBP (3.5 nm). Error bars in relative exciton density represent standard deviations taken from a minimum of four samples

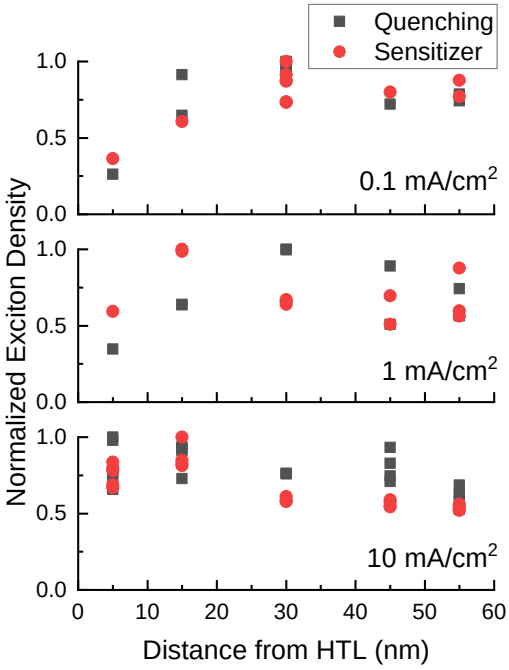

Fig. 3.6. Comparison of sensitizer and quenching-based measurements of the recombination zone at 0.1 mA cm^{-2}, 1 mA cm^{-2}, and 10 mA cm^{-2}.

The electroluminescence spectra of sensitized devices are shown in Figure 3.4. The outcoupling of PtTPTBP emission, calculated using an optical transfer matrix and power dissipation model (shown in Figure 3.5a),[74,148,149] drops by a factor of three across the emissive layer. Normalizing the sensitizer EL by the outcoupling profile, the exciton density is found to remain above 60% of the peak across the entire 60 nm M-EML at a current density of 10 mA cm^{-2} (Figure 3.5b). As current density increases from 0.1 mA cm^{-2} to 10 mA cm^{-2}, the peak of the RZ migrates from the ETL side to the HTL side of the M-EML. These findings are consistent with other reports for similar device architectures,[133,145] and confirm that d_{EML} is a good proxy for RZ width.

One issue with this measurement is that we observe substantial sensitizer quenching at current densities above ~1 mA cm^{-2}, evidenced by the roll-off in PtTPTBP EL relative to Ir(ppy)$_3$ for all sensitized device (Figure 3.7). This could have the effect of slightly flattening the extracted recombination zone at high bias, as sensitizers located near the peak of the RZ will

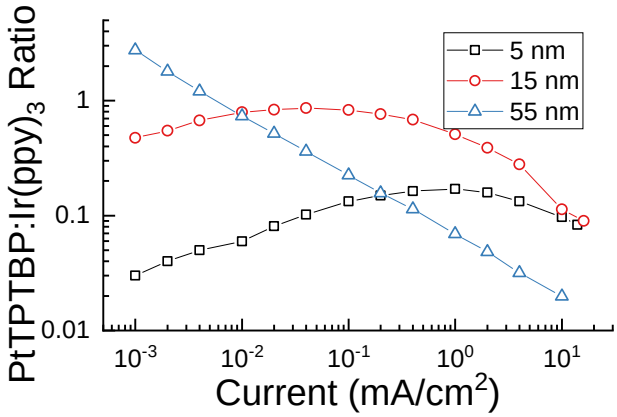

Fig. 3.7. Ratio of sensitizer to primary emitter EL (PtTPTBP:Ir(ppy)$_3$) for sensitizers at 5 nm, 15 nm, and 55 nm from the HTL/EML interface. The roll-off at high current densities in the 5 nm and 15 nm devices indicates sensitizer quenching.

experience more quenching. A method which should avoid this issue, introduced by Erickson and Holmes [133], compares quenching of the primary emitter electroluminescence by taking ratios of sensitized and non-sensitized EL:*

$$n_{ex}(x) \propto 1 - \frac{\int EL_{Ir(ppy)_3}(\lambda, x)d\lambda}{\int EL_{Ir(ppy)_3,unquenched}(\lambda)d\lambda} \tag{3.4}$$

These methods yield generally similar results, as shown in Figure 3.6, indicating that sensitizer quenching does not substantially impact the extracted recombination zone over this range.† Most importantly to the present study, the conclusion still holds that the RZ spans the majority emissive layer.

3.4 Lifetime scaling with recombination zone and luminance

The reduction in device EL over time is shown in Figure 3.8a for devices having emissive layer thicknesses of 10, 30 or 60 nm at an initial luminance of $L_0 = 3000\,\mathrm{cd\,m^{-2}}$, with the corresponding decays in PL and η_{EF} shown in Figure 3.8b. The EL lifetime increases by approximately a factor of 3 in increasing the thickness from 10 nm to 60 nm, and nearly all this enhancement can be attributed to a reduced rate of PL degradation. No trend with thickness is apparent in the η_{EF} decays shown in Figure 3.8b, which are all within typical device-to-device variation. In contrast, the PL decays show a dramatic separation with thickness. We also note that a reduction

*Outcoupling correction is less straightforward here, as the position of the sensitizer will change the average η_{OC} of the primary emitter.

†Sensitizer molecules with shorter exciton lifetimes could be employed to further limit quenching issues

in η_{EF} dominates the overall degradation rate in the 30 nm and 60 nm thick M-EML devices, but is comparable to PL losses in the 10 nm M-EML device. These results suggest that reduced degradation in emissive layer PL efficiency may be the primary reason for enhanced stability in M-EML architectures, as compared to their single-host counterparts with narrower recombination zones.[132] Moreover, the combination of improved efficiency roll-off and PL lifetime with an increased RZ width, and thus decreased exciton density, provides further evidence of a link between exciton quenching events and the degradation of PL efficiency.[112] Losses in η_{EF}, however, appear to be relatively insensitive to exciton density.

To further confirm the link between exciton density and PL loss, the exciton density was approximately matched between these architectures by scaling the starting luminance by the ratio of the M-EML thicknesses. Shown in Figure 3.9, the PL degradation is nearly identical for devices with d_{EML} = 10, 30, and 60 nm operated at luminances of 1000 , 3000 , and 6000 cd m^{-2}, respectively. Exciton formation efficiency losses, on the other hand, are rapidly accelerated as luminance is increased. At long times, the PL degradation slows slightly with increasing M-EML thickness, and this is attributed to the large differences in exciton formation efficiency losses. The exciton density does not remain matched over the course of the entire test due to these differences in η_{EF} losses, and consequently the formation rate for exciton quenchers will be reduced at long times in devices with larger d_{EML}. This observation of matched PL losses under scaled luminance has been reproduced under a range of scaled luminances from 330 cd m^{-2} to 15,000 cd m^{-2} (Figure 3.9). Despite comparable exciton densities in the emissive layer, exciton formation efficiency losses differ substantially, and appear to scale with increased luminance and current density. Increased current density would result in a larger polaron density in the transport layers

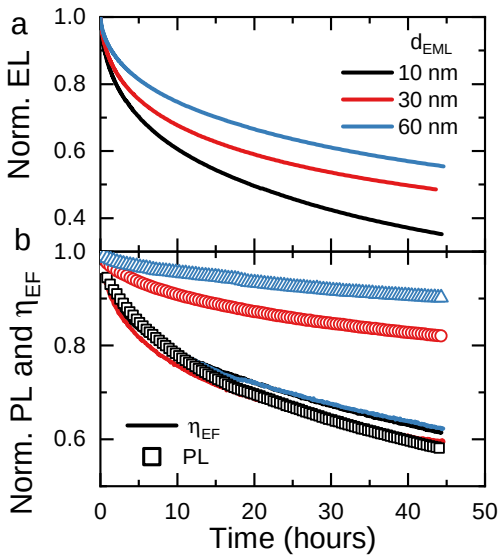

Fig. 3.8. (**a**) Normalized EL intensity for 10, 30, and 60 nm M-EML devices operated at an initial luminance of 3000 cd m^{-2}. The current densities for these tests were 7.2, 6.4, and 6.0 mA cm^{-2}, respectively. (**b**) Decoupled PL (symbols) and exciton formation efficiency losses (η_{EF}, solid lines) corresponding to the curves in (**a**).

and could lead to an increase in the rate of defect formation mediated by unstable cationic or anionic molecules.[112] Alternatively, the trend with luminance could be explained as an increase in interfacial photodegradation of the cathode or anode due to device electroluminescence.[150–152]

To further validate the results in Figure 3.8, the degradation behavior of these devices was measured across a range of initial luminances. Since the RZ spans the entire M-EML thickness, as demonstrated in Section 3.3, the exciton density at a given luminance is inversely proportional to the EML thickness ($N \propto 1/d_{EML}$). In this sense, tuning the thickness of the M-EML is analogous to accelerated aging under increased initial luminance, and might be expected to show a similar scaling relationship. OLED lifetime has been widely observed to follow a $1/L_0^n$ relationship,[104] where L_0 is the initial luminance, and n is the acceleration factor, a device specific parameter typically between 1-2. For these devices, $n = 1.8 \pm 0.1$ for the t_{50} of EL and is independent of M-EML thickness (Figure 3.16). As shown in Figure 3.10a, the degradation in PL and η_{EF} for a 60 nm M-EML show similar acceleration behavior as a function of luminance, with $n = 1.8$ and $n = 1.75$, respectively. Comparable slopes are seen for 10 nm and 30 nm M-EML devices (see Figure 3.16).

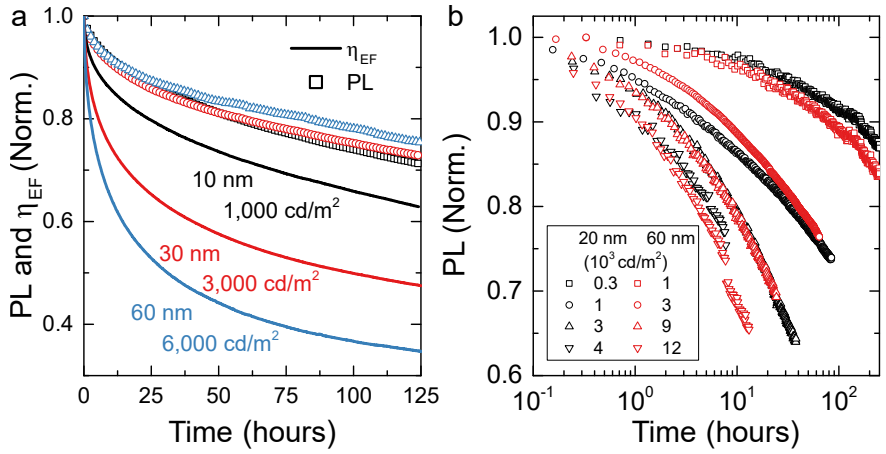

Fig. 3.9. **a** Decoupled losses in PL (symbols) and η_{EF} (solid lines) for 10, 30, and 60 nm M-EML devices operated at initial luminances of 1000, 3000, and 6000 cd m^{-2}, respectively. The current densities for these tests were 2.0, 6.0, and 12 mA cm^{-2}, respectively. Scaling the initial luminance by the emissive layer thickness results in an approximately matched exciton density and similar timescales for the PL loss. **b** PL loss for 20 nm and 60 nm M-EML devices operated at luminances scaled by the M-EML thickness (333 cd m^{-2} vs. 1000 cd m^{-2}, 1000 cd m^{-2} vs. 3000 cd m^{-2}, etc.). Good agreement is seen across all luminances, further supporting the hypothesis that recombination zone width and hence exciton density determine PL loss.

However, when scaled by $1/d_{EML}$, as displayed in Figure 3.10b, η_{EF} and PL show distinct scaling behavior. While PL t_{85} shows a slope of $n = 1.9 \pm 0.3$, almost identical to the

slope under luminance acceleration, η_{EF} t_{85} shows a much shallower slope of $n = 0.5 \pm 0.2$ (decreasing to $n = 0.3 \pm 0.3$ at $L_0 = 10{,}000\,\mathrm{cd\,m^{-2}}$). This raises several important implications. First, the nearly identical slopes for PL in Figure 3.10a,b provide further evidence that PL losses in this system are determined by the exciton density and the width of the recombination zone, and imply that there is a direct scaling law between recombination zone width and PL lifetime. While polarons can generally play a role in PL degradation,[128,153] it is unlikely that polaron density scales identically with both luminance and d_{EML}, implying that degradation may be dominated by a single exciton driven or an exciton-exciton annihilation driven degradation mechanism in this system. Second, the shallow dependence of η_{EF} t_{85} on RZ width (and hence exciton density) shown in Figure 3.10b suggests that excitons play a less significant role in η_{EF} degradation. Notably, the difference in scaling with L_0 and d_{EML} for η_{EF} t_{85} suggests that multiple degradation mechanisms comprise the total η_{EF} loss.

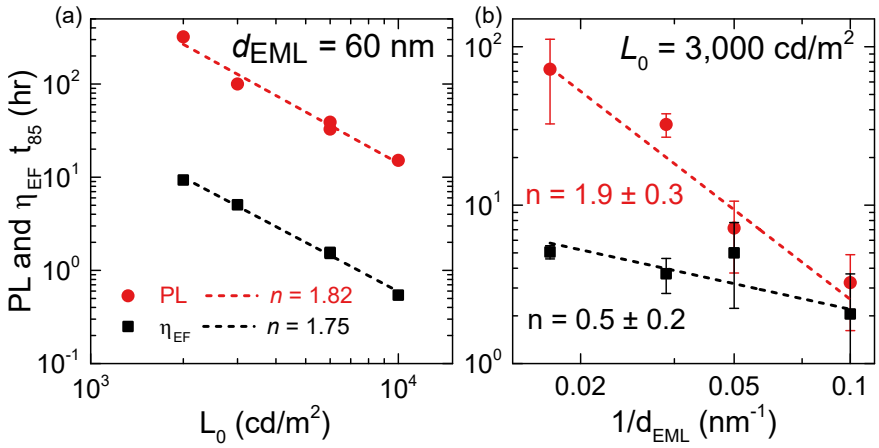

Fig. 3.10. Lifetime scaling with luminance and emissive layer width: **a** t_{85} lifetime for PL and η_{EF} plotted against initial luminance for the 60 nm M-EML. The acceleration factor, n, is approximately 1.8 in both cases. **b** t_{85} for PL and η_{EF} plotted against $1/d_{EML}$ for devices tested at an initial luminance of 3000 cd m^{-2}. A similar power law relationship is observed, and the analogous acceleration factor is $n = 1.9 \pm 0.3$ for PL, nearly identical to the luminance acceleration factor. For η_{EF}, a much shallower factor of $n = 0.5 \pm 0.2$ is observed, suggesting a separate degradation mechanism. Error bars represent standard deviations calculated over at least four measurements across at least two separate device sets.

Exciton formation loss is typically attributed to the accumulation of non-radiative recombination centers in the emissive layer,[98,115,116] and has been linked to exciton-polaron interactions.[125] We interpret the d_{EML}-dependent increase in η_{EF} degradation (Figure 3.10b) to reflect the generation of non-radiative recombination centers by an exciton-mediated process consistent with these reports. However, this mechanism alone cannot account for degradation in η_{EF},

as the scaling with L_0 is much steeper (Figure 3.10a). This contrasting behavior suggests that a second mechanism which is independent of emissive layer exciton density governs η_{EF} losses. As discussed above, this behavior is consistent with degradation mediated primarily by polarons or photodegradation of the cathode or anode interface,[150–152] and thus may originate outside of the emissive layer.

These findings have implications for efforts to model OLED lifetime. Previous modeling attempts have often assumed that the same defect population responsible for exciton quenching was also responsible for non-radiative recombination of charge carriers, and that this population resided entirely in the emissive layer.[97,126] Defect populations external to the emissive layer have been considered, but only for the purposes of fitting voltage rise.[100] Other work has argued that triplet-polaron quenching increases during degradation due to trapped charge in the emissive layer.[119] In all cases, the generation of defects is proposed to proceed via bimolecular quenching processes, either triplet-triplet annihilation or triplet-polaron quenching.[29] While these treatments have yielded reasonable fits of the overall degradation behavior, they are unable to capture the behavior observed here. Exciton formation and PL degradation would be expected to trend together within these formalisms, whereas Figure 3.10b shows clearly distinct scaling behavior. Our results thus show that losses to η_{PL} and η_{EF} originate from kinetically distinct mechanisms. Moreover, the weak dependence of η_{EF} on exciton density indicates that defects external to the emissive layer may play an important role in luminance loss, and should be considered in future modeling attempts.

It is important to note that defects that serve as non-radiative recombination centers could have suitable energetics to serve as exciton quenchers, and vice versa.[46] However, the differing scaling behavior observed here indicates that the exciton quenchers formed in the EML are likely inefficient non-radiative recombination centers for charge carriers.

3.5 Analysis of measurement error

> [The] quantitative interpretation of photoluminescence measurements in terms of the quenching contribution to the overall loss of electroluminescence efficiency is **hindered by the generally unavoidable differences in spatial distributions of quenchers and excited states in the electroluminescence and photoluminescence experiments**: Whereas electroluminescence is typically tied to some interface and distributed unevenly within an emissive layer, photoluminescence results from the mostly uniform excitation of an emissive layer. Considering that the distribution of quenchers is likely to be nonuniform ... **it follows that the quantitative relationship between the extents of photoluminescence and electroluminescence quenching processes is generally not known**.
>
> – D.Y. Kondakov
> *The Role of Homolytic Reactions in the Intrinsic Degradation of OLEDs*.[116]

In extracting η_{EF}, we assume that the measured PL intensity is representative of the device-relevant η_{PL} which helps determine the electroluminescence efficiency (Eq. (2.1)). This assumption may begin to break down in wide emissive layer architectures in which the optically and electrically generated exciton profiles are challenging to match.[116,125] In such cases, the measured PL intensity will be a convolution of the spatial dependences of the recombination zone, the electric field profile of the λ=405 nm pump, and the outcoupling efficiency. The dependence of outcoupling on position for $Ir(ppy)_3$ and PtTPTBP emission and the electric field profile of the λ=405 nm pump at 45° from normal incidence were calculated using an optical transfer matrix and power dissipation model (shown in Figure 3.5a).[74,148,149] As shown in Figure 3.5a,b, the RZ and $\eta_{OC}(x)$ of $Ir(ppy)_3$ peak on the HTL side of emissive layer, and the electric field profile of the pump peaks at 35 nm from the HTL. Qualitatively, the substantial overlap of these profiles suggests that error may be minimal in these devices.

To quantify the measurement error introduced by this mismatch, we employ a basic defect quenching model, similar to the treatment of Giebink et al. [97], and compare our measured PL loss with the device relevant η_{PL} loss. First, we assume that the optically-generated triplet

exciton density, $n_{ex,opt}$, can be described by the rate equation:

$$\frac{dn_{ex}}{dt} = G_T(x) - \frac{n_T(x)}{\tau} - K_{Qn}Q(x)n_{ex}(x) \tag{3.5}$$

where $G_{ex}(x)$ is the optical generation profile of excitons due to the pump laser, and is proportional to the electric field profile, $|E(x)|^2$, which is calculated using a transfer matrix formalism and shown in Figure 3.5a.[154] The natural exciton lifetime, τ, is assumed to be 0.6 µs.[41] K_{Qn} is the exciton quenching rate constant, and $Q(x)$ is the spatially dependent concentration of exciton quenchers. $Q(x)$ is taken to be proportional either to the recombination zone (i.e. the electrically-generated exciton density, $n_{ex,el}(x)$) or the recombination zone squared ($n^2_{ex,el}(x)$), to compare two possible exciton quencher formation mechanisms: a single exciton forms an exciton quencher, or exciton-exciton annihilation forms an exciton quencher. We do not consider the possibility of an exciton-polaron annihilation pathway for forming exciton quenchers, as the resulting error would likely be within these bounds.

At steady-state, Eq. (3.5) can be rearranged to solve for the exciton density:

$$\frac{dn_{ex}}{dt} = \frac{G_{ex}(x)}{\frac{1}{\tau} + K_{Qn}Q(x)} \tag{3.6}$$

The photoluminescence intensity that is detected in our measurement will simply be the integral of the exciton density multiplied by the radiative rate, $k_r(x)$, and weighted by the spatially-dependent out-coupling efficiency ($\eta_{OC}(x)$). $k_r(x)$ and $\eta_{OC}(x)$ are calculated using a dipole power-dissipation model (shown in Figure 3.11b),[74] and are both weighted by the photoluminescence spectrum of $Ir(ppy)_3$.

$$\begin{aligned} PL &= \int_{EML} k_r(x)\eta_{OC}(x)n_{ex,opt}(x)dx \\ &= \int_{EML} \frac{k_r(x)\eta_{OC}(x)G(x)}{1/\tau + K_{Qn}Q(x)}dx \end{aligned} \tag{3.7}$$

The results of this analysis are shown in Figure 3.12. We find that in the case of a unimolecular quencher formation process ($Q(x) \propto n_{ex,el}(x)$), the measurement underestimates PL efficiency loss by ~1% at t_{85} (when the PL efficiency has reached 85% of its initial value). In the case of a bimolecular quencher formation process ($Q(x) \propto n^2_{ex,el}(x)$), the underestimate is

~3%. It is important to note that these errors are within typical device-to-device variations, but with less judicious device design they can increase substantially. For example, increasing the electron transport layer (ETL) thickness from 20 to 40 nm was found to triple the measurement error in the 60 nm M-EML due to a substantial shift in $|E(x)|^2$ towards the ETL (assuming no change in RZ position). In any device with a wide emissive layer or inhomogeneous RZ or $|E(x)|^2$, the overlap between the electric field profile of the pump and the recombination zone should be carefully considered.

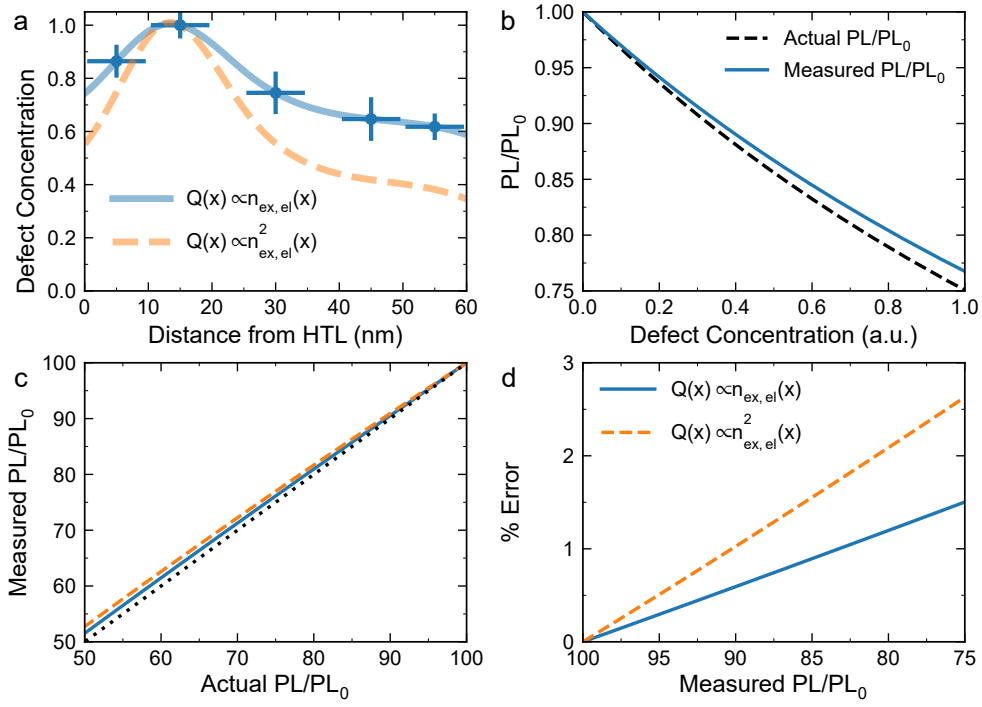

Fig. 3.12. (**a**) Hypothetical spatial dependences of the defect density assuming defects are generated by a unimolecular process (single exciton, $Q(x) \propto n_{ex,el}(x)$) or a bimolecular process (exciton-exciton annihilation, $Q(x) \propto n^2_{ex,el}(x)$). These profiles are based on a spline of the measured recombination zone ($n_{ex,el}$) at a current density of 10 mA cm^{-2} (see Figure 3.5)). (**b**) The measured and actual normalized PL efficiency (PL/PL_0) as a function of the product of the quenching rate constant and the exciton quencher concentration $K_{QN}Q$ for a $n^2_{ex}(x)$ degradation mechanism. The "actual" PL efficiency is the effective PL efficiency experienced by electrically generated excitons in the recombination zone. (**c**) Measured PL/PL_0 as a function of actual PL/PL_0 and (**d**) relative error in the measured PL/PL_0 for the two defect generation scenarios.

By assuming a unimolecular (single-exciton-induced) defect formation process, we find the PL measurement underestimates actual η_{PL} loss by <1% for degradation up to $PL/PL_0 = 85\%$. In the case of a bimolecular process (i.e. exciton-exciton annihilation induced defect formation),

the error remains <3% up to PL/PL_0 = 85%. It is worth noting that the model used here does not consider exciton diffusion nor the possibility of a large transfer radius between the defect and $Ir(ppy)_3$, which would likely serve to broaden the effective defect profile and hence reduce measurement error. These error estimates therefore represent upper bounds, and are within typical device-to-device variations. Nonetheless, this analysis underscores the importance of considering the optical design of a device architecture before attempting to quantitatively decouple PL and η_{EF} losses.

We also consider the accuracy of the assumption that η_{OC} is constant during degradation. In the absence of changes in optical constants, molecular orientation, or substantial crystallization, the primary mechanism for η_{OC} loss is recombination zone migration.[46] Evidence of RZ migration during degradation has been observed in several cases,[155,156] and is generally attributed to changes in injection properties on either side of the EML.[151] While we do not track RZ position during degradation, we assess the limits of η_{OC} changes due to RZ movement. In the most extreme case, the RZ would be a delta function moving from the position of highest outcoupling efficiency (24.7%) to lowest (15.3%), or vice versa, resulting in a 38% relative change in outcoupling efficiency. In practice, the recombination zone will have a substantial width. We considered the error introduced by migrating a Gaussian RZ with full width at half maximum ranging from 10 to 60 nm. For a narrow RZ, η_{PL} could fall from 23% to 16% if the RZ fully migrated from the HTL side to the ETL side. For a wide RZ similar to that measured here, however, η_{PL} only falls from 23% to 22%. Losses to η_{OC} can therefore be neglected in devices with a narrow emissive layer or broad RZ. These calculations are discussed in more detail in the Supporting Information (Fig. S5).

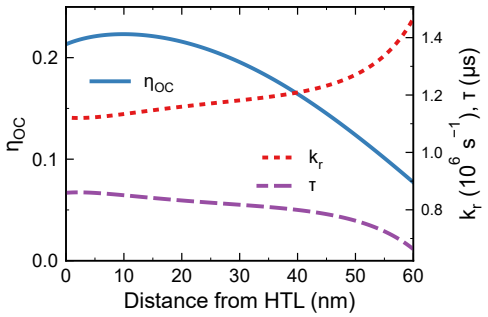

Fig. 3.11. Spatial dependence of outcoupling efficiency, radiative rate, and exciton lifetime in a 60 nm M-EML device

Finally, we revisit the assumption that changes to η_τ, which represents bimolecular quenching (Eq. (2.1)), are negligible. By employing a bimolecular quenching model and previously measured rate constants,[41] we find that η_τ increases 2.7% by 50% of the initial luminance (EL

t_{50}) for a 10 nm M-EML operated at 3000 cd m^{-2} (Figure 3.14). This effect is reduced in devices with a thicker d_{EML} due to the lower initial exciton density, but is not large enough to alter the conclusions of this work. Degradation-induced changes in η_τ are discussed in more detail in Chapter 7.

3.6 Conclusions

In conclusion, we find that broadening the recombination zone (RZ) sharply reduces the rate of PL degradation, showing a similar scaling relationship as with initial luminance variation, and confirming that PL degradation is strongly dependent on exciton density. However, losses in the exciton formation efficiency (η_{EF}) show a weaker dependence on RZ width, suggesting that η_{EF} losses are less sensitive to exciton density and may partly originate outside of the M-EML in this system. Notably, the different dependences of PL and exciton formation efficiency loss on RZ width provide clear evidence that kinetically distinct pathways drive OLED degradation, and that a single degradation mechanism cannot be assumed when attempting to model device lifetime. These results highlight the capability of decoupled measurements of PL and η_{EF} losses to yield useful diagnostic insight into the source of device instability and shed light on the kinetics of degradation and the nature of defects.

3.7 Methods

Organic light-emitting devices with active areas of 25 mm^2 were fabricated on glass substrates pre-patterned with a 150-nm-thick anode layer of indium tin oxide (ITO, Xinyan). Substrates were solvent-cleaned and exposed to UV-ozone ambient. Devices consisted of a 60-nm-thick hole injection layer (HIL) of poly(thiophene-3-[2[(2-methoxyethoxy)ethoxy]-2,5-diyl)(AQ1200, Sigma Aldrich), a TCTA (TCI America) hole-transport layer (HTL), a mixed-host emissive layer (M-EML) consisting of a 47.5 vol.% TCTA, 47.5 vol.% TPBi (Lumtec) and 5 vol.% of the green phosphorescent emitter Ir(ppy)$_3$(Lumtec), a TPBi electron-transport layer (ETL), and a LiF (1 nm)/Al (100 nm) cathode. When varying the M-EML thickness (10 nm, 30 nm, 60 nm), the HTL and ETL thicknesses are varied equally to maintain a total device thickness of 100 nm. The HIL is spin-cast in a N_2 glovebox and annealed for 30 minutes at 150 °C. The remaining layers are deposited by vacuum thermal evaporation at a

base pressure $< 7 \cdot 10^{-7}$ Torr and a rate of 0.3 nm s^{-1}.

Efficiency measurements were taken with an Agilent 4155C parameter analyzer and a large area photodiode (Hamamatsu S3584–08). Electroluminescence spectra were collected with an Ocean Optics HR4000 spectrometer. The electrically generated exciton profile (i.e. the RZ) of the 60-nm-thick M-EML was measured using a sensitizer doping method as described previously,[126,133] with 2-nm-thick strips doped with 2 vol. % PtTPTBP centered at 5, 15, 30, 45, and 55 nm from the HTL. Inclusion of the strip had negligible impact on device current density–voltage characteristics (shown in Figure 3.15). The RZ was extracted from electroluminescence spectra by normalizing the photon flux emitted from each sensitizer strip by the spectrally-weighted outcoupling efficiency for PtTPTBP emission at that position in the device.

During degradation of the M-EML devices, the decay in PL from the emissive layer is collected in tandem with EL by intermittently turning off the applied current and illuminating the device with a $\lambda = 405$ nm continuous-wave (CW) laser (Coherent OBIS LX). The CW laser is incident at an angle of 45° and the PL is collected through a $\lambda = 450$ nm long pass filter to prevent detection of scattered pump laser light. The pump wavelength is chosen so that only the emissive guest is excited. The laser spot diameter is ~1 mm, and hence averages over ~3% of the total device area. Current is applied for 10 minutes between PL measurements, which take ~20 s. This intermittency in current has no discernible effect on degradation rate, and no laser-induced degradation was observed after over 500 repetitions of the laser measurement cycle on a non-operating device.

3.8 Acknowledgments and Contributions

The work presented in this chapter was originally published in:

J. S. Bangsund, K. W. Hershey, and R. J. Holmes. “Isolating Degradation Mechanisms in Mixed Emissive Layer Organic Light-Emitting Devices”. *ACS Applied Materials & Interfaces* 10.6 (2018), pp. 5693–5699. DOI: 10.1021/acsami.7b16643

Kyle W. Hershey was a co-author of this work, assisting with development of the EL-PL decoupling measurement set-up and analysis of changes in η_τ. This work was funded by The Dow Chemical Company. I was supported by the National Science Foundation Graduate Research Fellowship under grant no. 00039202. We acknowledge useful discussions with Dr. D. Wayne Blaylock, Dr. Peter Trefonas, Mr. Hong-Yeop Na, and Dr. Dominea C. K. Rathwell.

3.9 Supplemental details

3.9.1 Code for spatial overlap error

Below, the code used to calculate error in the PL measurement due to spatial mismatch is included. These calculations produced the data in Figures 3.11 and 3.12. To run this code, you will need the transfer matrix and dipole emission calculation packages, available at github.com/jsbangsund/oledpy.

```
from oledpy.dipole_emission import ThinFilmArchitecture
import numpy as np
##### Define layer structure
layers = [
     {'name':'SiO2'     ,'d':0   ,'doping':1,'coherent':0},
     {'name':'ITO'      ,'d':100,'doping':1,'coherent':1},
     {'name':'PEDOT'    ,'d':60 ,'doping':1,'coherent':1},
     {'name':'TCTA'     ,'d':20 ,'doping':1,'coherent':1},
     {'name':'TCTA-TPBi-Irppy','d':60
      ↪  ,'doping':[0.475,0.475,0.05],'coherent':1,'active':1},
     {'name':'TPBi'     ,'d':20 ,'doping':1,'coherent':1},
     {'name':'Al'       ,'d':100,'doping':1,'coherent':1},
     {'name':'Air'      ,'d':0   ,'doping':1,'coherent':0},
]
dipole_positions = np.arange(0,1.01,0.01)
# Define wavelengths of interest
wavelengths = np.arange(450,676,5)
PL = np.genfromtxt('ref_data/Irppy3.pl',skip_header=5,delimiter='\t')
PL_interp = np.interp(wavelengths,PL[:,0],PL[:,1])/wavelengths
arch_MEML = ThinFilmArchitecture(
    layer_dict_list = layers,
    dipole_positions = dipole_positions,
    vac_wavelengths=wavelengths,pl_spectrum=PL_interp)
arch_MEML.load_nk(df_nk=df_nk)
arch_MEML.run_attribute_checks()

##### Calculate outcoupling
arch_MEML.show_wavelength_progress_bar=True
custom_u = np.hstack((np.arange(0,0.75,0.005),
```

```
                        np.arange(0.75,1,0.001),
                        np.arange(1+0.001,2,0.002),
                        np.arange(2,10,0.1)))#,np.arange(30,100,1)
arch_MEML.init_pds_variables(custom_u=custom_u)
arch_MEML.tau = 1.2e-6
arch_MEML.PLQY = 0.95
arch_MEML.k_r = arch_MEML.PLQY / arch_MEML.tau
arch_MEML.k_nr = 1/arch_MEML.tau - arch_MEML.k_r
arch_MEML.summarize_device()
# Calculate k_r(x), tau(x) for given intrinsic rates
arch_MEML.tau = 1.3e-6
arch_MEML.PLQY = 0.95
arch_MEML.k_r = arch_MEML.PLQY / arch_MEML.tau
arch_MEML.k_nr = 1/arch_MEML.tau - arch_MEML.k_r
arch_MEML.purcell_factor()
##### Calculate optical field
import tmm # https://pypi.org/project/tmm/
theta0 = 45
lam_vac = 404 #nm
degree=np.pi/180
layers = [ 'Air','SiO2', 'ITO' ,'PEDOT' ,
           'TCTA'  ,'TCTA-TPBi-Irppy' ,'TPBi', 'Al', 'Air']
doping = [ 1, 1  ,  1  ,  1    ,
            1      ,[0.475,0.475,0.05]   ,  1,    1,   1]
d_list = np.array([0,0,   100 ,  60  ,  20 ,   60 ,   20  , 100, 0])
powerDensity = 5 #mW/cm2
layer = 5 # EML
fig,ax=plt.subplots(figsize=(4,3))
n_list = tmm.load_nk(layers,doping,lam_vac,df_nk)
coh_tmm_data = tmm.coherent_tmm('s',n_list, d_list,
                            theta0*degree, lam_vac)
position = np.arange(0,1.01,0.01) * d_list[layer]
position_full = tmm.position_resolved(
    layer,position,coh_tmm_data,powerDensity=powerDensity)
G_ex = position_full['G']
##### Calculate spatial overlap error
from scipy.signal import argrelextrema
from scipy.interpolate import LSQUnivariateSpline
# measured RZ @ 10 mA/cm2
```

```
RZx = np.array([-5,5,15,30,45,55]) # nm from HTL/EML interface
RZy = np.array([0.7,0.86439,1,0.74546,0.64679,0.6178])
RZerr = np.array([0,0.06196,0.05,0.08,0.08213,0.05])
x_interp = position
# Spline for interpolating in calculation
knots = [12,26]
spline = LSQUnivariateSpline(RZx, RZy,knots,k=3) # k is polynomial order
RZ_smooth = spline(x_interp)
x = position
k_r = arch_MEML.kr_effective_spatial
tau = arch_MEML.tau_effective_spatial
eta_OC = arch_MEML.wavelength_averaged_eta_out
# This KQ array spans a range of defect density (degree of degradation)
# With a model for degradation, this can be mapped to a time axis
KQ = 10 ** np.arange(3,8,0.05)
KQ = np.insert(KQ,0,0)
# Error here is calculated for defect generation proportional
# to the RZ or proportional to the RZ squared (i.e. TTA)
PL_RZ = np.trapz((k_r * G_ex * eta_OC)
                 / (1/tau + KQ.reshape(-1,1)*RZ_smooth), x,axis=1)
PL_RZ2 = np.trapz((k_r * G_ex * eta_OC)
                  / (1/tau + KQ.reshape(-1,1)*RZ_smooth**2), x,axis=1)
PL_actual = np.trapz((k_r * RZ_smooth * eta_OC)
                     / (1/tau + KQ.reshape(-1,1)*RZ_smooth), x,axis=1)
PL_actual2 = np.trapz((k_r * RZ_smooth * eta_OC)
                      / (1/tau + KQ.reshape(-1,1)*RZ_smooth**2), x,axis=1)
# Normalize to max
PL_RZ /= np.amax(PL_RZ)
PL_RZ2 /= np.amax(PL_RZ2)
PL_actual /= np.amax(PL_actual)
PL_actual2 /= np.amax(PL_actual2)
# Calculate error
error = (PL_RZ-PL_actual)/PL_actual * 100
error2 = (PL_RZ2-PL_actual2)/PL_actual2 * 100
```

3.9.2 Limits on η_{OC} changes with degradation

The analysis in this chapter assumes that the outcoupling efficiency, η_{OC}, is constant during degradation. This assumption has been made previously,[46,91,125] but may become less accurate in wide emissive layer devices where η_{OC} varies substantially across the EML. In some cases, the recombination zone has been found to migrate during degradation,[96,156,158] presumably due to changes in charge injection and transport. While we do not monitor RZ migration during our measurement, we assess here the limits of changes to η_{OC} due to RZ migration. For simplicity, we calculate changes for an RZ with a gaussian spatial dependence. By calculating the average η_{OC} for a given RZ ($\eta_{OC,avg} = \int_{EML} \eta_{OC}(x) n_{RZ}(x) dx / \int_{EML} n_{RZ}(x) dx$) We find that the absolute change in $\eta_{OC,avg}$ is less than 1% for a RZ similar to our measured RZ moving to the EML/ETL interface, as shown in Figure 3.13. This assumes no narrowing of the RZ. In the worst case, a 38% relative change in $\eta_{OC,avg}$ occurs when a δ function recombination zone moves from the region of peak outcoupling efficiency to the EML/ETL interface.

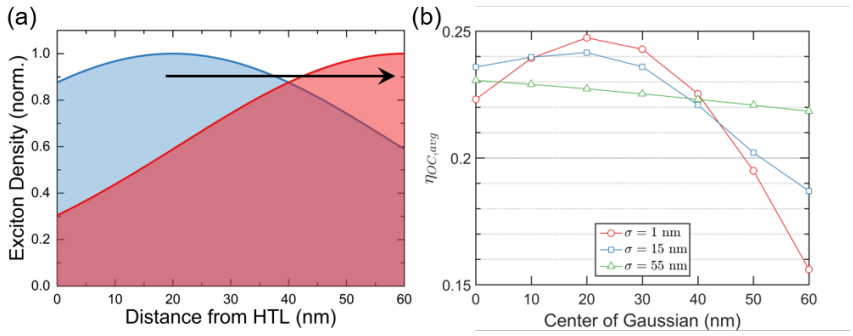

Fig. 3.13. (**a**) Example RZ migration for a gaussian moving from 20 nm and 60 nm (at center) with a variance of $\sigma = 55$ nm, similar to the measured RZ profile in this work. This migration would reflect less than a 1% absolute drop in η_{OC}. (**b**) The average outcoupling efficiency for gaussian RZ profiles as a function of the center position with variances of 1, 15, and 55 nm. For a thin RZ (1 nm variance) the effects of RZ migration are dramatic, with a relative change in η_{OC} of 38% in the most extreme case. For a thick RZ, however, the relative change is less than 5%.

3.9.3 Changes in bimolecular quenching

The analysis in this chapter also assumes that bimolecular quenching is constant during degradation. However, the steady-state exciton density monotonically decreases during degradation at a constant current density, and therefore the fraction of excitons that are deactivated via exciton-exciton annihilation and exciton-polaron annihilation are expected to decrease over time. To

assess the limits on error introduced by these changes, we employ a previously applied model and measured rate constants for CBP:Ir(ppy)$_3$ devices.[91] Modifying Eq. (3.5) to include bimolecular quenching gives:

$$\frac{dn_{ex}}{dt} = G_{ex}(x) - \frac{n_{ex}(x)}{\tau} - k_{TT}n_{ex}^2 - k_{TP}n_{ex}n_{pol} \tag{3.8}$$

where k_{TT} is the triplet-triplet annihilation rate constant, taken as 7.1×10^{-12} cm^3 s^{-1}, k_{TP} is the triplet-polaron quenching rate constant, taken as 3.3×10^{-13} cm^3 s^{-1}, and n_{pol} is the polaron density, taken as 10^{15} cm^{-3}. The natural lifetime efficiency, η_τ, is then simply the term for excitons consumed by the natural lifetime divided by the sum of all other consumption terms:

$$\eta_\tau = \frac{n_{ex}/\tau}{n_{ex}/\tau + \frac{1}{2}k_{TT}n_{ex}^2 + k_{TP}n_{ex}n_{pol}} \tag{3.9}$$

We assume the only time varying components of Eq. (3.9) are τ (which changes due to reductions PL efficiency) and n_{ex}. We calculate the time dependent exciton density from the electroluminescence decay curve as $n_{ex}(t) = n_{ex}(0) \cdot \eta_{EQE}(t)/\eta_{EQE,0}$, where $n_{ex}(0)$ is approximated from the luminance assuming a flat recombination zone and a flat outcoupling efficiency of 20%. During degradation, we assume a decrease to our measured PL intensity reflects an increase in the non-radiative rate and a decrease in the natural lifetime, τ, which is supported by previous work.[91] Conceptually, we are bundling the term representing exciton quenching defects in Eq. (3.5) ($-k_{Qn}Qn_{ex}$) into the non-radiative rate. Therefore, we can extract the time dependence of the natural lifetime as $\tau(t) = \tau(0) \cdot \eta_{PL}/\eta_{PL,0}$. For a 10 nm M-EML operated at 3000 cd m^{-2}, we find that η_τ increases 2.7% at 50% of the initial luminance, as shown in Figure 3.14. This small change is not sufficient to change the conclusions of the main text.

3.9.4 Supplemental figures

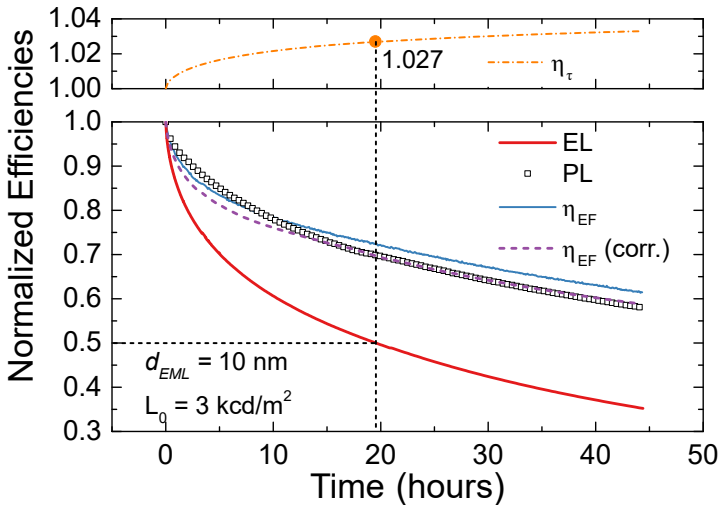

Fig. 3.14. Complete decoupling of efficiencies for a 10 nm M-EML device operated at 3000 cd m^{-2}. Bimolecular quenching is reduced over time, resulting in an increase in η_τ by 2.7% at 50% of the initial luminance (marked by an orange circle). This factor is used to calculate the corrected η_{EF} (purple dashed line), which is modestly decreased.

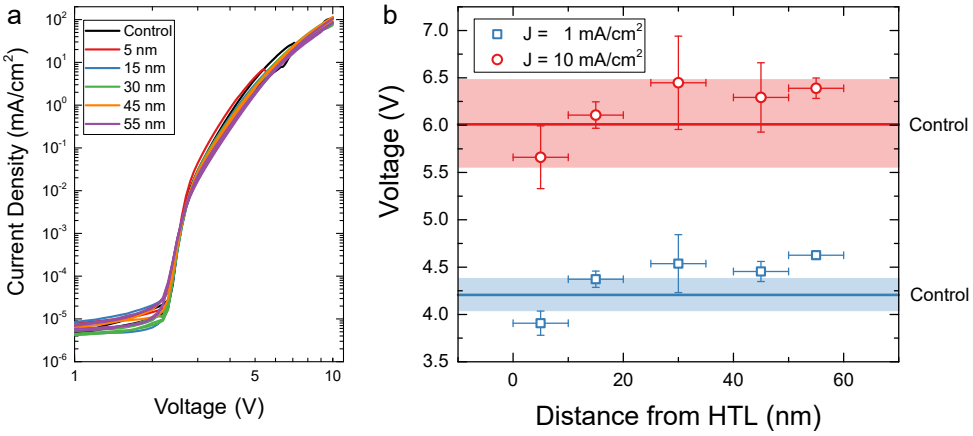

Fig. 3.15. (**a**) Current density-voltage characteristics for 60 nm M-EML devices as a function of sensitizer strip position in nm from the HTL. (**b**) Voltage at current densities of 1 and 10 mA cm^{-2} as a function of sensitizer strip position. At 10 mA cm^{-2}, the average voltage for each strip position is within the standard deviation of the control device (shaded region).

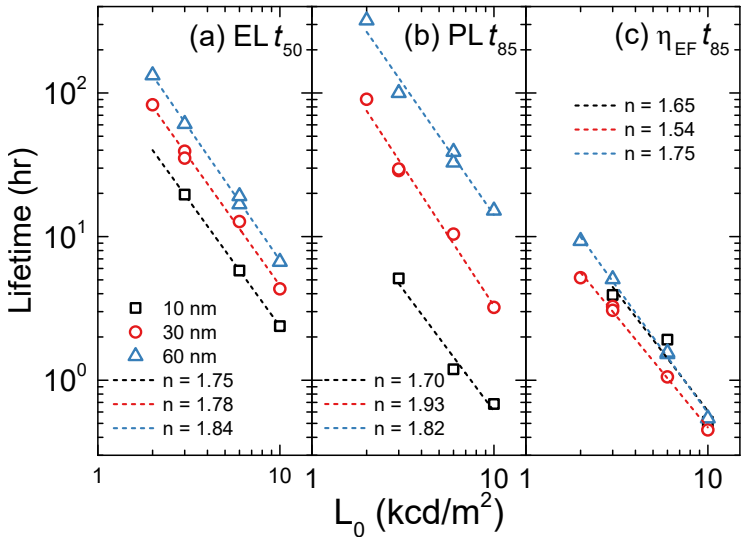

Fig. 3.16. (**a**) EL t_{50} lifetime, (**b**) PL t_{85} lifetime, and (**c**) η_{EF} t_{85} lifetime for M-EML devices with emissive layer thicknesses of 10 nm, 30 nm, and 60 nm.

4

Balancing recombination zone position and width

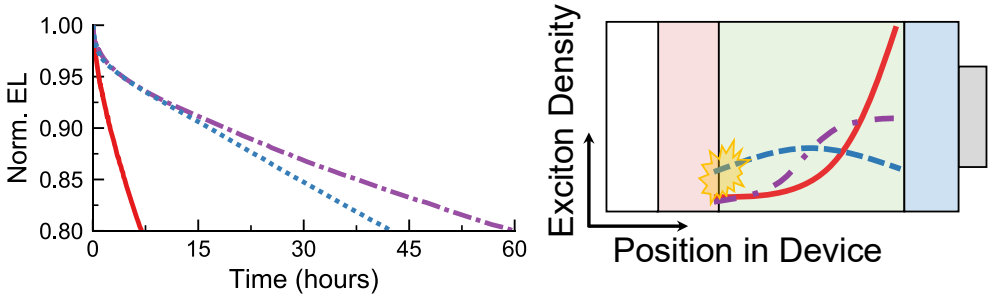

Excitons near interfaces accelerate degradation

Improved stability is realized in phosphorescent organic light-emitting devices (OLEDs) by adding a wide energy gap host material to an ambipolar emissive layer. While the resulting structure contains two host materials, this device differs from conventional mixed-host OLEDs that combine hole- and electron-transporting hosts. Here, charges are transported primarily along the ambipolar host and the emitter, and the addition of the wide energy gap host serves to tune the charge injection and transport characteristics of the emissive layer. This approach offers tuning of both the exciton recombination zone width and position. By decoupling overall device degradation into the photostability of the emitter and the exciton formation efficiency, the detailed role of the wide energy gap host in improving performance is elucidated. Unlike conventional mixed-host OLEDs, where mixing tends to increase recombination zone width and overall device stability, mixing in this system reduces the recombination zone extent while improving stability. This enhancement is explained in terms of a trade-off between bulk and interfacial degradation, with the recombination zone being pushed away from an interface, reducing the overall width but improving stability. We find that the lifetime can be improved by 50% by balancing this observed trade-off between bulk and interfacial degradation.

> There is no doubt that carrier densities have a major influence on device efficiency [and] lifetime... Considering that excitons of some OLED materials appear more effective in initiating deleterious chemical reactions, it is obvious that controlling distributions of charge carriers can be used to suppress some degradation mechanisms. The improvement or even the inhibition of charge injection at certain interfaces may therefore be essential for a lifetime improvement in OLEDs, where charged molecules and subsequently formed excitons tend to react and form charged traps or nonradiative recombination centers.
>
> – Scholz et al. [46], pg. 8471
> *"Degradation Mechanisms and Reactions in Organic Light-Emitting Devices"*, 2015

4.1 Introduction

Several studies of operational stability in organic light-emitting devices (OLEDs) have suggested that exciton density-driven processes are responsible for overall device degradation.[46,97,112,116,157] Consequently, substantial work has sought to reduce exciton density in the OLED emissive layer by engineering the exciton recombination zone (RZ). The RZ is the spatial extent of exciton formation in an OLED, and its width determines the exciton density for a given luminance, setting the rate of emissive layer degradation.[126,157] Previous studies have found that device lifetime can be enhanced by maximizing the RZ width.[126,129,132,157] In conventional mixed- and graded-emissive layer (EML) devices, electron- and hole-transporting hosts are mixed to achieve high charge balance and a wide RZ.[132,159–162] The absolute position of the RZ is also important, as proximity to a transport layer interface can exacerbate degradation,[6,91,121,163] or influence exciton confinement and charge balance.[96,155,163] In cases showing interfacial degradation, the RZ is typically pinned at the degrading interface. Avoiding both bulk and interface degradation suggests a trade-off between increased RZ width for reduced exciton density and the need to avoid stressing unstable interfaces.

In this work, we demonstrate an unconventional mixed-EML approach to improve device stability that combines an ambipolar charge-transporting host with a wide energy gap host. The use of a wide-energy gap host as an additive provides an advantage of simplifying the host pair selection process. A wide-gap host is less likely to act as a charge trap or introduce an exciplex

state which could change the exciton formation mechanism, quench the emitter excitons or introduce unwanted spectral features. Varying the EML composition permits tuning of the exciton RZ width and position, and an optimization of device stability. This system illustrates a trade-off between bulk and interfacial degradation as lifetime is not optimized for devices with the broadest RZ, in contrast to conventional mixed-EML OLEDs.[164–166] It is further interesting to note that the stability of an ambipolar host material can be enhanced through the addition of a wide energy gap host which modulates charge transport and the RZ in the EML.

Here, devices are constructed using two proprietary host materials supplied by DuPont Electronics and Imaging, designated Host A and Host B. While we cannot disclose the chemical structures of these host materials, we provide characterization of the molecular energy levels and optical and electrical properties of both Host A and Host B, which should allow these results to be reproduced in other materials systems displaying similar properties. In commercial devices manufactured by DuPont, devices based on a uniform host mixture show improved lifetimes up to $t_{90} = 8.6\,\text{h}$ (i.e. the time to 90% of initial luminance) at an initial luminance of $L_0 = 15{,}000\,\text{cd}\,\text{m}^{-2}$, compared to $t_{90} = 1.3\,\text{h}$ and $t_{90} = 4.2\,\text{h}$ for devices containing only Host A or Host B, respectively. It is worth noting that these lifetimes are reported at an extreme luminance condition used for rapid commercial screening.

4.2 Effect of mixed host composition on performance

Figure 4.1a shows the molecular orbital energy levels for the active materials of interest. The highest occupied molecular orbital (HOMO) energy levels for TCTA, TPBi, and Ir(ppy)_3 are obtained from literature ultraviolet photoelectron spectroscopy (UPS) measurements.[167,168] The HOMO levels for Host A and Host B were calculated from the oxidation potential in cyclic voltammetry (CV) measurements, and corrected using established relationships between CV and UPS measurements.[167] The lowest unoccupied molecular orbital (LUMO) levels of TCTA and Ir(ppy)_3 are taken from literature inverse photoelectron spectroscopy (IPES) measurements,[169] while all others are calculated from the reduction potential in CV measurements, and again corrected using prior work comparing CV and IPES measurements.[170] The optical energy gaps for each material are shown in Figure 4.1a as dashed lines relative to the HOMO level ($E_g = 3.5\,\text{eV}$ for Host A and $E_g = 3.0\,\text{eV}$ for Host B, Figure 4.5b). The triplet energy levels (labeled T_1) are also shown in Figure 4.1a. The triplet energy levels for Host A and Host

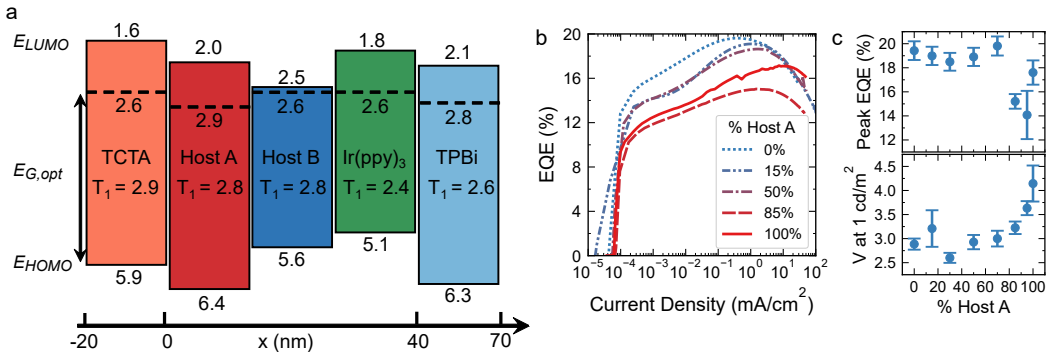

Fig. 4.1. (**a**) Energy level schematic showing the highest occupied molecular orbital (HOMO), lowest unoccupied molecular orbital (LUMO), and triplet energy levels for the materials used in this study. The dashed line indicates the optical energy gap relative to the HOMO level. The x-axis denotes the layer thicknesses used in the devices of interest, as a function of distance from the HTL/EML interface. (**b**) External quantum efficiency (EQE) as a function of current density for various EML compositions. (**c**) Peak EQE and turn-on voltage (at 1 cd m^{-2}) as a function of percent host A in the EML (ignoring emitter concentration). Error bars represent standard deviations taken over at least four separate pixels.

B were estimated from low temperature phosphorescence (Figure 4.5a), while those for the other materials were taken from literature.[35,171–173] Despite having differences in energy gap and fluorescence energy, Host A and Host B have similar triplet energies. It is worth noting that the energy levels of Host B reside entirely within those of Host A, and Host A and B do not form an emissive exciplex, as confirmed from measurements of mixed film photoluminescence (PL) and bilayer device (ITO/Host A/Host B/LiF/Al) electroluminescence (EL).

The dependence of the external quantum efficiency and driving voltage on EML composition is shown in Figure 4.1b-c. Relative to a device with an EML of Host B and Ir(ppy)$_3$, the addition of the wide energy gap Host A has minimal impact on EQE at moderate concentrations, only leading to a reduction in efficiency at compositions greater than 70% Host A (defined relative to the total host composition). Likewise, the turn-on voltage to achieve 1 cd m^{-2}, shown in Figure 4.1c, is relatively constant up to 70% Host A. The power efficiency at 1000 cd m^{-2} is minimally impacted over this range, decreasing slightly from 37 ± 1 lm/W for 0% Host A to 34 ± 2 lm/W for 50% Host A (Figure 4.6). As Host A composition is increased above 70%, the turn-on voltage increases from ~3 V to ~4.2 V, leading to a corresponding decrease in power efficiency to 25 ± 4 lm/W. This increase in turn-on voltage is attributed to a reduction in the efficiency of charge injection and transport upon adding Host A to the EML, reflecting, in part, the difference in molecular orbital energy levels.

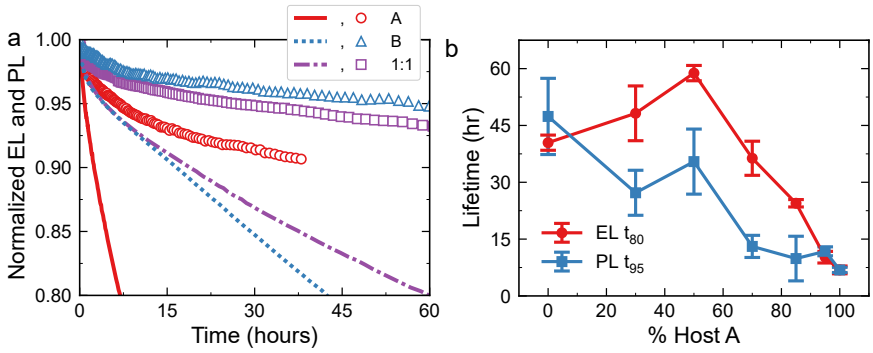

Fig. 4.2. (**a**) Normalized electroluminescence (EL, lines) and photoluminescence (PL, symbols) decay curves for devices having an emissive layer (EML) consisting of host A, host B, or a uniform mixture of host A and host B (1:1). The initial luminance is 5000 cd m^{-2} in all cases, with an operating current density of approximately 8 mA cm^{-2}. (**b**) EL lifetime (t_{80}) and PL lifetime (t_{95}) as a function of percent host A in the EML (ignoring emitter concentration). EL lifetime is maximized at a host composition of 50% host A, whereas the PL lifetime is longest at a host composition of 100% host B. Error bars represent standard deviations taken over at least four separate pixel lifetimes.

Figure 4.2 shows the dependence of device lifetime on EML composition, with mixed architectures showing superior stability to those based on single-host EMLs containing only one of the hosts and Ir(ppy)$_3$. Interestingly, the stability of devices based on Host B ($t_{80} = 40 \pm 2$ h), is improved upon adding Host A ($t_{80} = 59 \pm 2$ h for an EML containing a 1:1 mixture of the two hosts), despite devices based on an EML of Host A:Ir(ppy)$_3$ showing a short lifetime ($t_{80} = 7$ h). In contrast, the degradation in PL efficiency is slowest for devices with an EML of Host B:Ir(ppy)$_3$ ($t_{95} = 48 \pm 10$ h), with mixed host devices showing faster PL degradation (Figure 4.2b). In previous work, PL stability has been found to scale with exciton density, with devices having the widest RZ showing the longest PL lifetime.[157] Here, this suggests that the RZ is widest in devices containing an EML of Host B:Ir(ppy)$_3$, yet that the overall EL lifetime is not optimized by maximizing RZ width. This observation may indicate that RZ position changes with composition, leading to a trade-off between bulk degradation within the EML and interface degradation adjacent to the EML.[6,91,121] In order to probe this hypothesis, the RZ extent is measured directly.

4.3 Recombination zone and charge transport

The RZ for devices containing 0%, 50%, and 100% Host B (defined relative to the total host composition) were measured using a δ-doped sensitizer approach.[174] This is similar to the methods described in Chapter 3, except instead of co-doping the sensitizer, discontinuous layers

(nominally 0.1 nm thick) of the near-infrared phosphor Pt (II) tetraphenyltetrabenzoporphyrin (PtTPTBP) were deposited at various locations in the EML. Thin, discontinuous strips were used to limit concentration quenching, minimize the impact of the sensitizer on the electrical properties of the device, and make device fabrication easier. Excitons residing on $Ir(ppy)_3$ within a Förster radius of the sensitizer ($R_0 = 3.5$ nm, see Figure 3.3) are quenched, leading to emission from PtTPTBP and a reduction in the intensity of $Ir(ppy)_3$ emission. To summarize the analysis presented in Section 3.3, the ratio of EL from $Ir(ppy)_3$ between sensitized and control devices (denoted β) reflects the fraction of electrically generated excitons which are not quenched by the sensitizer, i.e. which recombine on $Ir(ppy)_3$ molecules more than a Förster radius away from the sensitizer strip. Therefore, $(1-\beta)$ reflects the local exciton density quenched by the sensitizer strip (Eq. (3.4)).[146] By translating this sensitizer across the emissive layer, $(1-\beta)$ reflects the relative exciton population profile across the EML. This measurement is found to agree within error with RZ probes based off of an outcoupling corrected sensitizer EL approach.[100,155,157] The area-normalized exciton population map resulting from this measurement for each architecture is shown in Figure 4.3a, with the associated EL spectra included in Figure 4.7. Devices based on an EML of Host A have the highest exciton density of all three architectures, with a narrow RZ peaked at the ETL interface. Those based on an EML of Host B show the widest recombination zone, that is nearly flat across the EML. The uniform mixture EML device shows an intermediate behavior with a narrower RZ than Host B that is also shifted away from the HTL/EML interface.

The shift in RZ width and position can be understood by considering how the addition of Host A to the EML changes injection and charge transport. Both injection and transport are assessed in single-carrier devices fabricated for compositions of 0%, 50%, and 100% Host B. The current density-voltage characteristics for hole-only (HOD) and electron-only (EOD) devices are shown in Figure 4.3b-c. In both cases, devices based on Host B show larger currents than those based on Host A. The addition of Host A to Host B reduces both the hole- and electron-currents, suggesting Host B and the phosphorescent guest remain the dominant transporting phase, even in mixtures. Thus, the observed shift in device stability and RZ position reflect a favorable adjustment in the transport properties of the EML upon adding Host A. These results, taken together with the RZ measurements, indicate that adding Host A to the EML serves to preferentially frustrate the transport and injection of electrons in the EML. While Host A also impacts hole transport, the net impact is to reduce the electron concentration in the EML and

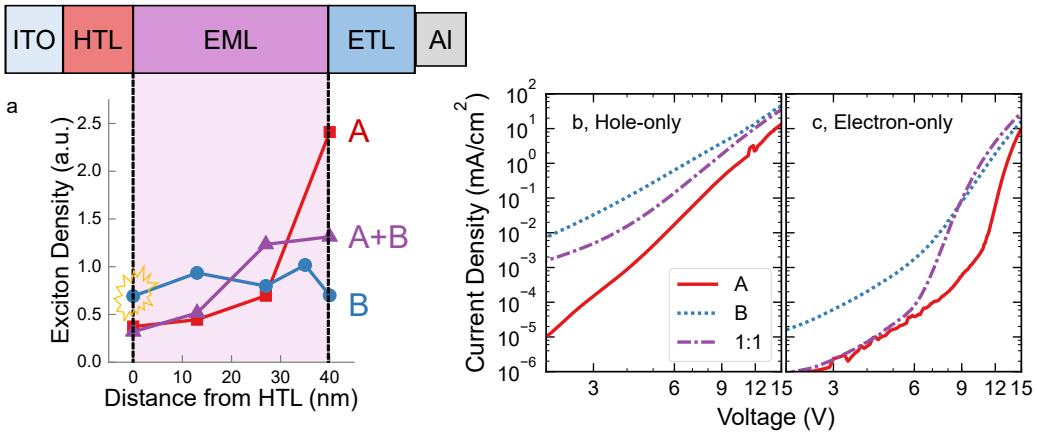

Fig. 4.3. (**a**) Area-normalized exciton density profiles extracted from electroluminescence spectra of devices with δ-doped exciton quenching layers. The host B device shows the broadest recombination zone (RZ), whereas the host A device shows an RZ pinned at the emissive layer (EML)/electron-transport layer (ETL) interface. The uniform, 1:1 mixture of host A and host B shows intermediate behavior and has a reduced exciton density at the hole-transport layer (HTL)/EML interface. (**b**) Current density- voltage characteristics for hole-only devices and (**c**) electron-only devices with EMLs consisting of host A, host B, and a 1:1 mixture of host A and host B. Structures described in Section 4.5.

shift the RZ towards the EML/ETL interface.

The trend in measured RZ width is consistent with expectations based on the PL stability behavior in Figure 4.2b, where a narrower RZ leads to greater exciton density and directly accelerates PL degradation. The observed increase in the overall EL stability of the mixture, despite its reduced RZ width and PL stability, suggests that the EL stability is limited by the position of the RZ. Specifically, the exciton density in the 100% Host B device is only higher than the uniform mixture near the HTL/EML interface. This suggests that the HTL/EML interface is sensitive to exciton density and limits the overall stability of the wide RZ, 100% Host B device.

To further confirm that the lifetime enhancement upon mixing is driven by reduced interfacial degradation and not differences in intrinsic or morphological stability of the EML, devices were fabricated with a 10-nm-thick EML. A thin EML helps to minimize variations in RZ position and width between devices, making more uniform the role of degradation at the HTL/EML interface. For these devices, the ETL thickness is increased to 50 nm to center the electric field profile of the $\lambda = 473$ nm pump laser in the EML (Figure 4.8). All other layers have the same thicknesses as the 40-nm-thick EML devices. The peak external quantum efficiency of these devices is 14 ± 1 % for all three EML architectures (Figure 4.9). The EL and PL lifetimes for devices operated at $L_0 = 5000\,\mathrm{cd\,m^{-2}}$ are shown in Figure 4.4. Devices with an EML

containing Host B and a 1:1 mixture of Host A and Host B are found to have nearly identical lifetimes with EL $t_{80} = 3.1 \pm 0.3$ h for Host B and $t_{80} = 3.4 \pm 0.4$ h for the mixture, and PL $t_{95} = 0.6 \pm 0.1$ h for Host B and $t_{95} = 0.9 \pm 0.4$ h for the mixture. This behavior suggests that the intrinsic and/or morphological stability is the same for devices based on Host B and the uniform mixture, providing further evidence that stability differences for the 40-nm-thick EML devices stem from differences in RZ position. Devices containing an EML of Host A:Ir(ppy)$_3$ still show a shorter lifetime in both EL and PL, likely due to the narrow RZ of these devices which is heavily peaked at the ETL interface.

Taken together with the RZ measurements, these thin EML device results indicate that the HTL/EML interface is sensitive to exciton density and limits the overall stability of the 100% Host B device. This interfacial exciton sensitivity is likely due to an accumulated density of polarons at the interface, leading to exciton-polaron annihilation driven degradation processes, such as host or transport layer aggregate formation, as have been reported previously.[6,121] The addition of Host A to the EML moves the RZ away from this interface in 40-nm-thick EML devices, reducing the exciton density at this interface and increasing the EL stability. It is worth noting that the ETL/EML interface can also contribute to degradation, and degradation at this interface could limit stability in other materials systems. In these cases, we expect that a wide energy gap host which selectively frustrates hole transport and injection would provide similar stability improvements. In a general sense, this approach could improve the reliability of existing host materials that have desirable properties but are limited by non-optimum recombination zone profiles. Importantly, this method does not require a re-engineering of transport and blocking layers or the development of entirely new materials to realize the desired RZ. Use of a wide-gap host is advantageous since it is less likely to act as a charge trap or introduce an exciplex state which could change the exciton formation mechanism, quench the emitter, or introduce unwanted spectral features. In this way, a wide gap host can tune the

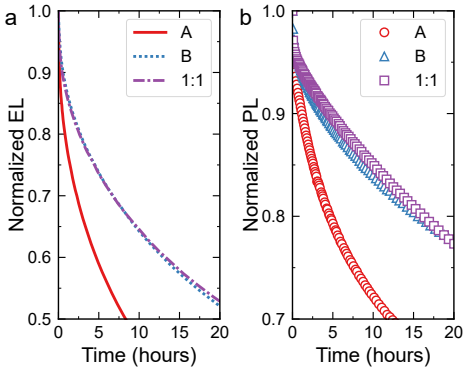

Fig. 4.4. Normalized (**a**) electroluminescence (EL) and (**b**) photoluminescence (PL) decays for devices with a 10-nm-thick emissive layer (EML) operated at $L_0 = 5000\,\mathrm{cd\,m^{-2}}$. Devices consisting of host B and a uniform mixture show identical EL and PL lifetimes, indicating that when differences in recombination zone (RZ) position and width are reduced, the stability of these two devices is identical.

mobility and recombination zone of a device without impacting the emission spectrum or the exciton formation mechanism. From a design perspective, the wide-gap host should have a deeper HOMO and shallower LUMO than the other host and emitter, preventing charge trapping or exciplex formation, and addition of the wide-gap host to the EML at low to moderate concentrations should have minimal impact on turn-on voltage.

4.4 Conclusion

In this work, increased device lifetime is demonstrated in an unconventional mixed-host architecture that combines wide energy gap and ambipolar hosts. Based on measurements of the exciton recombination zone, the wide energy gap host serves to frustrate electron injection and transport in the emissive layer, allowing the position and width of the recombination zone to be controlled. Notably, lifetime is improved upon mixing despite a reduction in both recombination zone width and PL stability. The overall increase in stability is shown to result from shifting the RZ away from an unstable interface. This work offers a new strategy to manage the position of the recombination zone, allowing the trade-off between bulk and interfacial degradation to be balanced and hence optimize lifetime.

4.5 Methods

4.5.1 Device fabrication

Devices with an active area of 25 mm^2 were fabricated on glass substrates pre-patterned with a 150-nm-thick anode layer of indium tin oxide (ITO, Xinyan). Substrates were cleaned with solvents followed by exposure to ambient UV-ozone. A AQ1250 hole-injection layer (Sigma Aldrich) was spin-cast on the ITO anode, followed by a hole-transport layer of TCTA (TCI America). The emissive layer consisted of Host A, Host B, or a mixture of the two hosts, and a constant emitter loading of 15 vol.% $Ir(ppy)_3$ (Lumtec). The remaining 85 vol.% of the EML consisted of mixture compositions of 0%, 5%, 15%, 30%, 50%, 70%, 85%, and 100% Host A by volume. An electron-transport layer of TPBi (Lumtec) was deposited over the EML, followed by a 1 nm LiF/ 100 nm Al cathode. The full device architecture was: ITO / AQ1250 (70 nm) / TCTA (20 nm) / EML (40 nm) / TPBi (30 nm) / LiF (1 nm) / Al (100 nm). The HIL was spin-cast in a N_2 glovebox and annealed for 30 minutes at 150 °C. The remaining layers were deposited

by vacuum thermal evaporation at a base pressure $< 7 \cdot 10^{-7}$ Torr and a rate of 0.3 nm s^{-1}. Devices were encapsulated with epoxy and a cover glass in a N_2 glovebox. PtTPTBP, used for recombination zone sensing experiments, was purchased from Frontier Scientific.

4.5.2 Single-carrier device architectures

The layer structure for electron-only devices (EOD) was ITO (150 nm)/Al (10 nm)/LiF (1 nm)/TPBi (20 nm)/EML (100 nm)/TPBi (20 nm)/LiF (1 nm)/Al (100 nm). The layer structure for hole-only devices (HOD) was ITO (150 nm)/AQ1250 (70 nm)/TCTA (20 nm)/EML (100 nm)/TCTA (20 nm)/MoOx (10 nm)/Al (100 nm). All emissive layers were doped with 15 vol. % $Ir(ppy)_3$.

4.5.3 Device efficiency and stability characterization

Efficiency and luminance measurements were taken with an Agilent 4155C parameter analyzer and a large area photodiode (Hamamatsu S3584–08), assuming Lambertian emission for luminance calculations. Electroluminescence (EL) spectra were collected with an Ocean Optics HR4000 spectrometer. Unless otherwise noted, device lifetimes were characterized at an initial luminance of 5000 cd m^{-2} using a Keithley 26XX to source device current and to measure device EL from a Hamamatsu S2281 photodiode. Photoluminescence (PL) was measured periodically during degradation by temporarily removing the current and optically pumping the device using a $\lambda = 473$ nm laser (Coherent OBIS). The PL signal was passed through a 500 nm long pass filter to prevent detection of stray laser light. This method has been previously described and has been shown to introduce no further degradation to devices or influence the electrical lifetime.[91]

4.5.4 Cyclic voltammetry measurements

Host A and B were dissolved in N,N-dimethylformamide at a concentration of ~1 mM, with 0.1 M tetrabutylammonium tetrafluoroborate as the supporting electrolyte. A Pt counter electrode, Pt working electrode with an area of 0.3 mm2, and an Ag/Ag+ reference electrode were used, and measurements were calibrated with a ferrocene standard. TPBi was measured in acetonitrile.

4.6 Acknowledgments and Contributions

The work presented in this chapter was originally published in:

J. S. Bangsund, K. W. Hershey, D. C. K. Rathwell, H.-Y. Na, J.-H. Jeon, P. Trefonas, and R. J. Holmes. “Improved Stability in Organic Light-Emitting Devices by Mixing Ambipolar and Wide Energy Gap Hosts”. en. *Journal of the Society for Information Display* 27.7 (2019), pp. 434–441. DOI: 10.1002/jsid.761

This work was an equal effort with Kyle W. Hershey. Co-authors from DuPont Electronics and Imaging (Dr. Peter Trefonas, Mr. Hong-Yeop Na, Mr. Jeong-Hwan Jeon and Dr. Dominea C. K. Rathwell) provided the host materials and preliminary devices, performed quantum chemical calculations, and discussed the work. We acknowledge the group of C. Daniel Frisbie for the use of their potentiostat and Yan Wang for providing training and assistance in cyclic voltammetry.

Funding and support for this work was provided by DuPont Electronics and Imaging. I was supported by the National Science Foundation Graduate Research Fellowship under Grant No 00039202.

4.7 Supplemental Figures

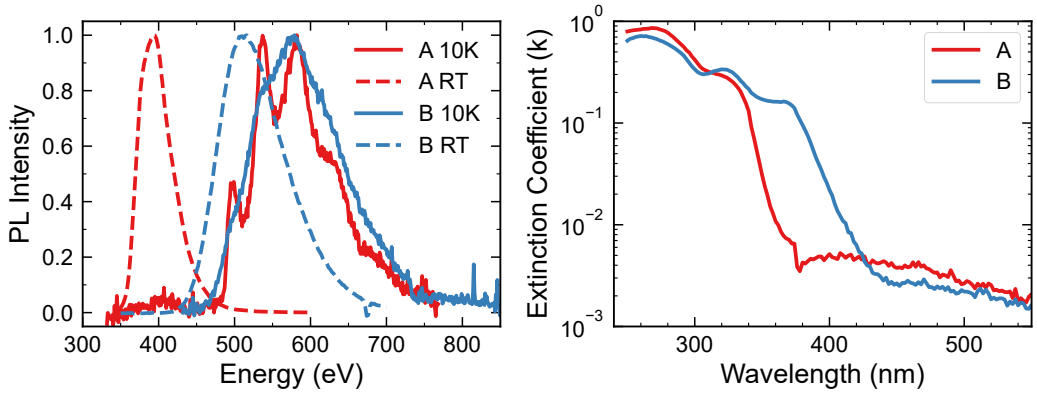

Fig. 4.5. (Left) Fluorescence (at room temperature, RT) and phosphorescence (at 10 K) of Host A and Host B, measured from 60-nm-thick films on Si substrates. (Right), Extinction coefficient, k, for Host A and Host B, measured using spectroscopic ellipsometry on 60-nm-thick films on glass.

The accuracy of the decoupled EL and PL decay lifetime measurements presented in the main text depend on an understanding of the overlap between the recombination zone and the

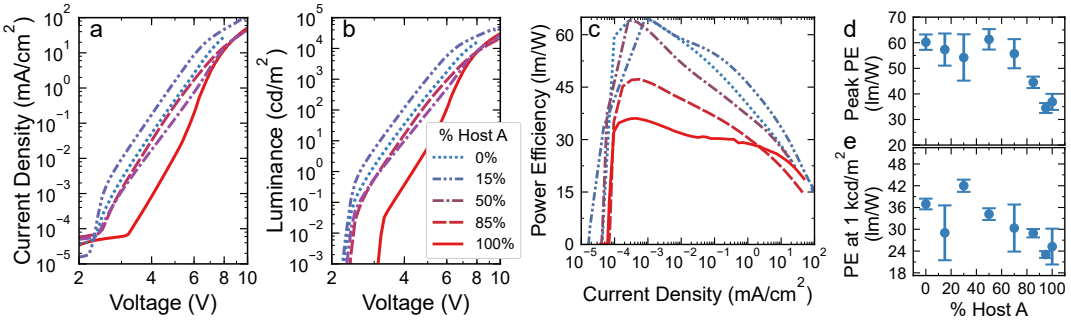

Fig. 4.6. (**a**) Current-voltage, (**b**) luminance-voltage, and (**c**) power efficiency characteristics for devices with various mixed host compositions. (**d**) peak power efficiency and (**e**) power efficiency at 1000 cd m^{-2} as a function of host composition. Peak power efficiency stays relatively constant up to 50% Host A, and then begins to diminish due to the increased electron injection barrier.

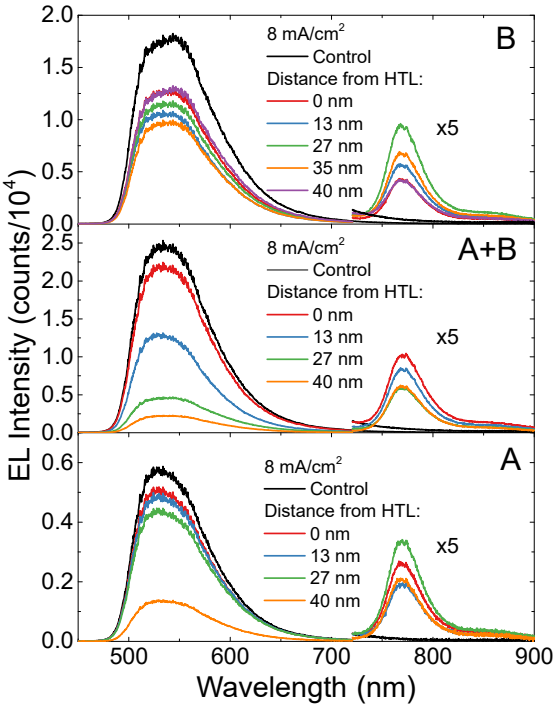

Fig. 4.7. Electroluminescence (EL) spectra of sensitizer-strip devices used to extract recombination zone extent, where control devices have no sensitizer strip, and all other devices have a 0.1 nm strip of PtTPTBP located at 0, 13, 27, 35, or 40 nm from the HTL/EML interface. Spectra are collected for emissive layers consisting of Host B, Host A, and a uniform mixture of Host B and Host A. The $\lambda = 770$ nm peak has been magnified by 5x for visibility.

electric field profile of the $\lambda = 473$ nm pump laser. Figure 4.8 shows the electric field profile for the two device EML thicknesses used. The field profile shows almost no variation as a

function of host composition. A strong overlap in the photon absorption profile, related to $|E|^2$ for the PL measurement and the electrical recombination zone is important to ensure the same PL is representative of the device degradation. In Figure 4.8a, a slight preference is seen towards the HTL side of the EML, though the profile is relatively well balanced. For devices using Host A, where the RZ is peaked heavily at the ETL, the measurement may underestimate PL degradation. However, Host A shows the most dramatic PL loss, and hence the overall trend will not be affected. For 10-nm-thick EML devices, the EML is sampled uniformly, with a nearly flat electric field profile (Figure 4.8b).

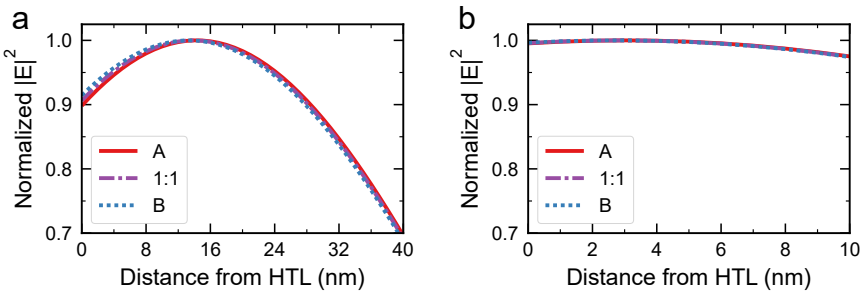

Fig. 4.8. Optical field intensity profile in the EML as a function of composition for (**a**) 40-nm-thick EML and (**b**) 10-nm-thick EML devices. The electric field is calculated for the s-polarized $\lambda = 473$ nm laser at an incident angle of 45° using a transfer matrix formalism.

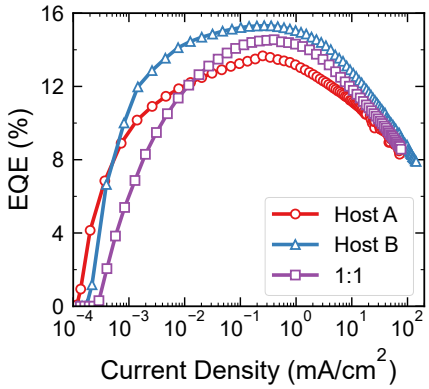

Fig. 4.9. External quantum efficiency (EQE) as a function of current density for devices with a 10-nm-thick EML.

5

Role of host excited states in degradation

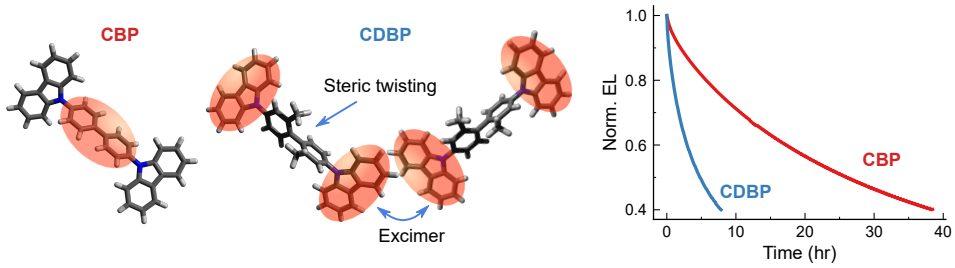

Steric twisting leads to excimer formation which in turn reduces device lifetime.

Host-guest structures are used in most state-of-the-art organic light-emitting devices (OLEDs), where host molecules serve to dilute guest molecules, transport charge, and confine excitons on the guest. Hosts are often critical to achieving high efficiency and stability, yet predicting and understanding the effect of host properties on device stability is a persistent design challenge which slows the discovery of new OLED materials. Closely related host molecules, which differ only by several functional groups, often show drastically different degradation behavior. Here, we explore this observation for the archetypical carbazole hosts CBP and CDBP. While devices based on these hosts show similar efficiencies, CDBP-based devices show a tenfold lower lifetime than CBP devices when paired with phosphorescent or fluorescent emitters. Using optically- and electrically-pumped degradation tests, mass spectrometry, compositional analysis and low-temperature phosphorescence spectroscopy, the lifetimes of devices containing CDBP are shown to correlate with the formation of intermolecular triplet excimer states. These findings suggest that candidate host molecules should be screened for excimer formation, as host excimers may aggravate device degradation and lower device stability.

5.1 Introduction

Organic light-emitting devices (OLEDs) have become an established display technology, finding especially broad commercialization for mobile applications.[46,122,176] Despite this, further adoption of OLEDs could be realized with additional improvements in molecular and device design for long operational lifetime. The OLED emissive layer (EML) frequently contains two molecular systems, mixing a highly luminescent guest at low concentration with a host that serves to space guest molecules to maximize luminescence efficiency, and may also serve to transport charge and excitons.[46,65,177] Host selection is often made based on the electronic and excitonic energy levels in order to maximize exciton confinement on the guest.[178,179] This has led to a wide range of host materials being realized via chemical functionalization with a range of singlet and triplet energies.[88,177,180] While improved exciton confinement frequently leads to enhanced device efficiencies, trends in degradation are often not as clear.[121,181] Indeed, seemingly small changes in host molecular structure can lead to significant changes in device stability, likely reflecting changes in nanoscale packing, morphology, and/or intermolecular interactions.[4,121,180,182,183]

Among the most widely studied hosts are those containing carbazole moieties, which have been widely implemented in phosphorescent OLEDs and OLEDs based on thermally activated delayed fluorescence (TADF).[88] Carbazoles perform well as host materials due to their typically ambipolar charge transport properties and high triplet energies, which ensure effective guest exciton confinement.[88] Two archetypical carbazole hosts are CBP[64,184] and CDBP.[178] These similarly structured hosts, which differ by only two methyl groups, show a stark contrast in device stability. Here, we consider the degradation of OLEDs based on the archetypal green phosphorescent emitter, $Ir(ppy)_3$, paired with each host. We find that the reduced lifetime of devices based on CDBP is related to the tendency of CDBP to form triplet excimers. Since carbazole hosts are often susceptible to excimer formation,[180,185] these findings could inform

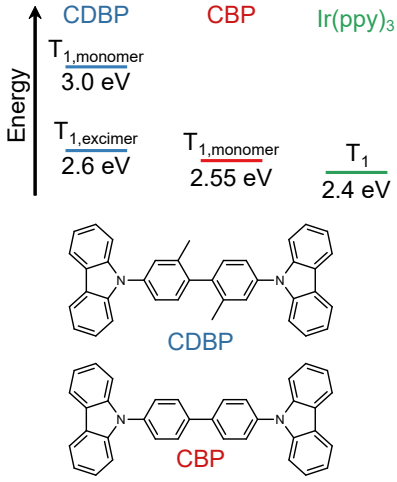

Fig. 5.1. Triplet energy level schematic of CDBP and CBP relative to the green phosphor, $Ir(ppy)_3$, and molecular structures of both hosts.

molecular screening criteria for developing more stable host materials.

5.2 Lifetime scaling with luminance

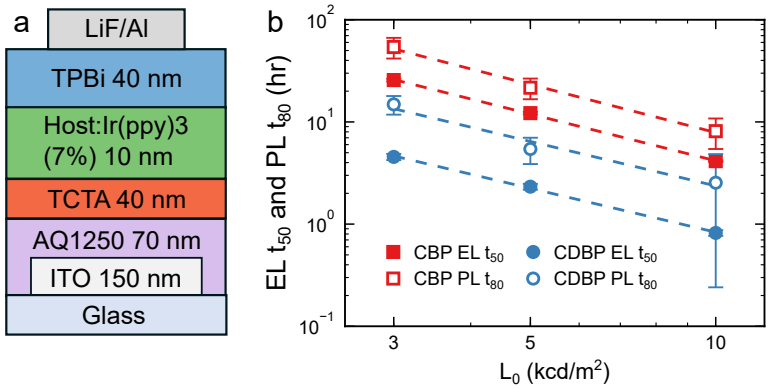

Fig. 5.2. (**a**) Device architecture. (**b**) EL t_{50} and PL t_{80} vs. initial luminance for devices based on each host.

The molecular structures of CBP and CDBP and their triplet energy levels relative to $Ir(ppy)_3$ are shown in Figure 5.1. Figure 5.2a shows the device architecture used in this work. To characterize the stability for devices based on each host, simultaneous measurements of degradation in device EL and photoluminescence (PL) were made as a function of initial luminance. Here, PL measurements were taken every 10 min during a lifetime test by turning off current and illuminating the device with a $\lambda = 405$ nm laser which selectively pumps the emitter. A low laser power is used (<5 mW cm^{-2}) to ensure photo-induced degradation is negligible, and a thin emissive layer (10 nm) minimizes spatial mismatch between the optical and electrical excitation profiles (see Chapter 3).[157] With these considerations, measured reductions in PL intensity accurately reflect losses in emitter PL efficiency resulting from EL degradation. Figure 5.2b shows the dependence of the EL and PL lifetimes on initial luminance (L_0). The t_{50} lifetime is defined as the time required for a device to degrade to 50% of the starting EL intensity under constant current density. Similarly, t_{80} refers to the time required for the photoluminescence (PL) to reach 80% of the initial intensity. Both EL and PL in CDBP-based devices decay as much as 10 times faster than in CBP-based devices under similar degradation conditions. However, the same power-law behavior with similar acceleration factors ($n \approx 1.5$, where n is the exponent in $t_{50} \propto L_0^{-n}$) was observed for both hosts. This

suggests that while degradation is accelerated in the CDBP case, similar kinetic pathways are likely responsible for the reduction in lifetime.[104,105,157,175]

5.3 Molecular fragmentation

To examine potential differences in intrinsic molecular stability for each host, our collaborators at DuPont carried out bond dissociation energy (BDE)* calculations using B3LYP, basis set (6-31G*) and Gaussian 16 software. BDEs were calculated for ground state configurations (shown in Figure 5.3), while dihedral C-C bond angle calculations were performed in ground and excited states.[153,186,187] The C-N bond was found to be weakest in both hosts, in agreement with previous results.[187] The C-N BDE is almost identical in both hosts (81.75 kcal/mol for CBP and 81.28 kcal/mol for CDBP),[112,187] while the central C-C bond energy was slightly higher for CBP (112.5 kcal/mol for CBP and 107.7 kcal/mol for CDBP). As typically the weakest bond determines molecular stability,[112] these results suggest that CDBP is not intrinsically less stable than CBP from a chemical perspective. To confirm these calculations, we investigated of molecular fragmentation via Laser Desorption Ionization Time-of-Flight Mass Spectrometry (LDI-TOF-MS). Prior application of this technique to OLEDs has allowed more detailed investigations of degradation pathways.[113,114,188,189]

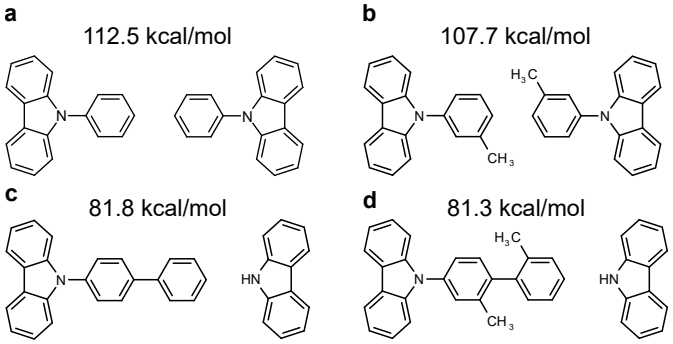

Fig. 5.3. Bond dissociation energies and fragment molecular structures for the central C-C bond in (**a**) CBP and (**b**) CDBP, and for the C-N bond in (**c**) CBP and (**d**) CDBP.

In a LDI-TOF-MS measurement, an intense UV laser is used to volatilize the organic thin film layers, which are then collected by a mass spectrometer. The laser itself will break apart some molecules, leading to fragment peaks even in pristine (undegraded) devices. For this reason, the fragment peak intensities are compared before and after degradation to identify which fragments, and the approximate quantity of these fragments, are produced by device

*No, not *that* BDE

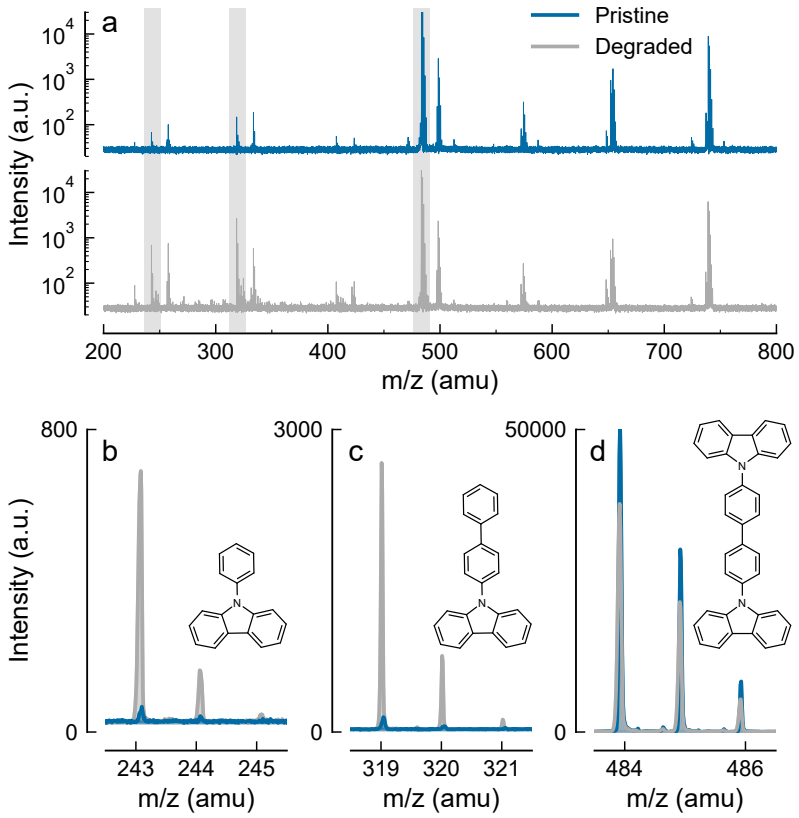

Fig. 5.4. LDI-TOF-MS of pristine and degraded CBP devices: (**a**) Full mass spectra for pristine and degraded (to 10% of L_0) CBP-based devices. (**b**)–(**d**) Zoomed view of primary fragment peaks: (**b**) CBP moleculed cleaved at the central C-C bond (243 amu), (**c**) CBP molecule cleaved at the C-N bond (319 amu), (**d**) the full CBP molecule (484 amu). The three peaks for each fragment reflect the isotopic distribution of each molecule.

degradation. Example spectra are shown in Figure 5.4, showing a clear increase in two CBP fragments with a corresponding decline in the peak intensity of the whole CBP molecule.

Here, results from LDI-TOF-MS on degraded devices are consistent with BDE calculations and previous reports,[187] with the most abundant fragments forming by cleavage of the weak C-N bond in both CBP and CDBP. Primary results are summarized in Figure 5.5. Fragmentation in the two hosts differs only subtly: CBP shows slightly higher formation of fragments cleaved at the C-C bonds (Figure 5.5a,b), and the ratio of C-N cleaved fragment peak to the pristine molecule peak in CDBP is higher than for CBP (Figure 5.5b,d). These differences may reflect the excited state localization in each host, where the CDBP excited state resides on the carbazole group (possibly accelerating C-N bond scission) and the CBP excited state resides primarily on the biphenyl, near the central C-C bond.[4] Overall, these results confirm that both CDBP and

CBP degrade primarily via cleavage of C-N bonds.

Taken together, the results of Figures 5.2 and 5.5 suggest that CBP and CDBP share a common primary degradation mechanism. Why, then, are these same processes accelerated in CDBP devices? A notable difference between these hosts is that CDBP forms a triplet excimer state, while CBP does not.[4,180,185] In other words, the first excited triplet state in CDBP is delocalized across adjacent molecules, while that of CBP is a localized triplet residing on a single molecule. Bagnich et al.[4] have argued that excimer formation is caused by rotation of the center C-C bond in CDBP, which decreases coupling between the end carbazole groups, moves the excited state to the ends of the molecule, and consequently allows greater orbital overlap between neighboring carbazole groups, where the excimer can form.[4,180,185] While it has been speculated that excimers are detrimental to stability,[180] this connection has not been demonstrated experimentally.

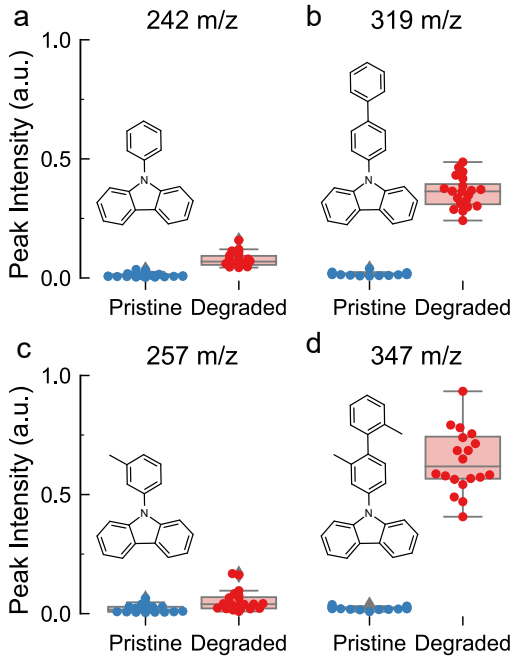

Fig. 5.5. Integrated peak intensities of pristine and degraded CBP devices for fragments with masses of (**a**) 242 amu and (**b**) 319 amu, and of CDBP devices for fragments with masses of (**c**) 257 amu and (**d**) 347 amu.

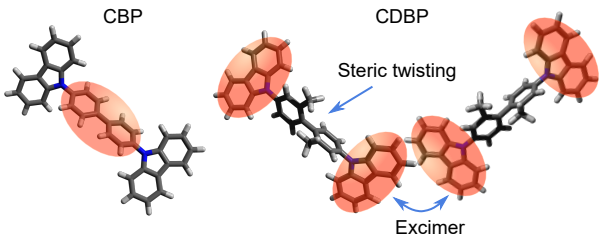

Fig. 5.6. 3D structure of CBP (left) and CDBP (right). In CBP, the central biphenyl group is planarized and the triplet excited state is localized along the biphenyl (illustrated with the shaded area). The methyl groups in CDBP induce steric twisting which disrupts delocalization in the biphenyl and moves the excited state to the carbazole ends of the molecule. This leads to a higher triplet energy in the dilute limit, but when the triplet state can interact with neighboring molecules it can form a lower energy excimer triplet. Adapted from ref. [4]. 3D structure files were downloaded from chemspider.com and the final images were rendered with Avogadro and POV-ray.

5.4 Host triplets and excimers

As excimer formation relies on intermolecular interactions, excimers are less likely to form in dilute films. The formation of the excimer in CDBP could therefore be frustrated by diluting with CBP; if the excimer is responsible for the instability of CDBP devices, the lifetime of dilute CDBP devices should equal that of pure CBP devices. To first assess the composition dependence of excimer formation, low-temperature phosphorescence spectroscopy was carried out on films of CDBP in UGH2. UGH2 acts as a transparent matrix for CDBP, permitting changes in phosphorescence to be attributed to changes in excimer formation. Low temperature measurements of phosphorescence have been previously used to identify the CDBP triplet excimer.[185] Figure 5.7a shows phosphorescence spectra for films of 5, 10, 20, 30, 50 and 100 vol.% CDBP in UGH2. Looking at the most dilute films, the CDBP monomer triplet phosphorescence is defined by two peaks centered at wavelengths of $\lambda = 412$ nm and $\lambda = 440$ nm. In the neat film, triplet excimer emission is characterized by a single broad feature centered at $\lambda = 473$ nm.[4] The CDBP monomer peaks fall in intensity as the concentration is increased from 5% to 20% CDBP, with the onset of excimer formation occurring above ~10% CDBP. Figure 5.7b shows increasingly intense excimer emission is observed above 20% CDBP, with mostly excimer emission observed for CDBP concentrations $\geq$50%.

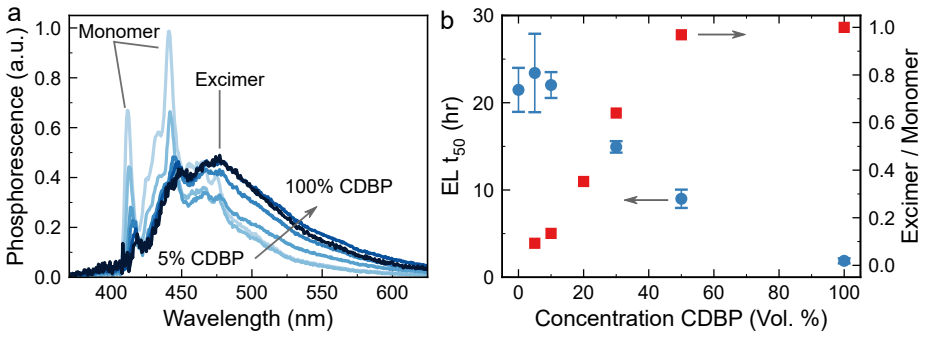

Fig. 5.7. (**a**) Phosphorescence spectra at 10 K of thin films of CDBP doped in UGH2 as a function of concentration. (**b**) EL t_{50} for $L_0 = 3000\,\mathrm{cd\,m^{-2}}$ in CBP:CDBP mixed host devices (blue circles). Excimer to monomer signal ratio extracted from the phosphorescence intensity in (**a**) at wavelengths of $\lambda = 525$ nm and $\lambda = 412$ nm (red squares). The onset of excimer signal >10% CDBP corresponds well with the decrease in lifetime.

With an understanding of the concentration of CDBP required to form excimers, OLEDs were constructed based on a mixed host emissive layer of CDBP and CBP. EQE and electrical characteristics for these devices are shown in Figure 5.8. The peak EQE decreases slightly

as CDBP is added to the emissive layer, from 16% for 0% CDBP (100% CBP) to 14% for 100% CDBP devices. A more pronounced change in the efficiency is observed at higher current density, where pure CDBP devices show more severe efficiency roll-off. This behavior may indicate reduced recombination zone width in pure CDBP due to differing tranport and injection properties.[146] Interestingly, pure CBP and CDBP devices show quite similar current-voltage behavior (Figure 5.8a), while intermediate concentrations (10 - 50 % CDBP) show higher current. It is not entirely clear why this happens, but it suggests that the mixtures have more balanced injection and transport of holes and electrons. Speculating any further is difficult without more detailed knowledge of charge transport and injection barriers in each of these hosts; such data is unavailable for CDBP, which has been studied less extensively than CBP.

Regardless, the slightly lower EQE in CDBP-rich mixtures cannot fully explain the up-to-tenfold lower lifetime compared to CBP. To estimate how much of this accelerated degradation can be attributed to differences in efficiency, recall that $t_x \propto L_0^{-n}$. When efficiency roll-off is small, L_0 is proportional to current density (J), and J is in turn inversely proportional to EQE. We can thus estimate that efficiency differences would account for a ~60% larger lifetime in CBP devices.*

$$\frac{t_{50,CBP}}{t_{50,CDBP}} \approx \left(\frac{J_{0,CDBP}}{J_{0,CBP}}\right)^n \approx \left(\frac{EQE_{0,CBP}}{EQE_{0,CDBP}}\right)^n \approx \left(\frac{10.5}{14.5}\right)^{1.5} \approx 1.6 \tag{5.1}$$

where efficiencies for each device are taken at ~3000 cd m^{-2}. Another possibility is that recombination zone is narrowed in CDBP, increasing exciton and polaron densities and, in turn, accelerating degradation. But to explain the 10× difference in lifetime, the recombination zone width would have to be ~3× larger in CBP, which seems implausible given the already thin emissive layers employed here. This estimate is based on the scaling relationship established in

*To be clear, this is a coarse approximation at best; scaling of lifetime with luminance and current are not rigorously identical. Here, devices are operated at the same nominal luminance, but differences in charge balance or quenching lead to different efficiencies and current densities. In less efficient devices, the higher current density likely corresponds to a larger polaron density, which will accelerate exciton-polaron-induced degradation.

Chapter 3 ($t_x \propto L_0^{-n} d_{RZ}^m$) and the assumption that n and m are both ~1.5:

$$\frac{t_{50,CBP}}{t_{50,CDBP}} \approx \frac{L_{0,CDBP}^n d_{RZ,CBP}^m}{L_{0,CBP}^n d_{RZ,CDBP}^m} \approx \frac{EQE_{0,CBP}^n d_{RZ,CBP}^m}{EQE_{0,CDBP}^n d_{RZ,CDBP}^m}$$
$$\Rightarrow \frac{d_{RZ,CBP}^m}{d_{RZ,CDBP}^m} \approx \left(\frac{t_{50,CBP}}{t_{50,CDBP}} \cdot \frac{EQE_{0,CDBP}^n}{EQE_{0,CBP}^n} \right)^{-m} \tag{5.2}$$

Figure 5.7b shows the dependence of EL t_{50} lifetime on mixed emissive layer composition for $L_0 = 3000\,\mathrm{cd\,m^{-2}}$. Devices containing $\leq$10% CDBP show nearly identical lifetime behavior to devices containing only CBP. Above the threshold of ~10% CDBP, the lifetime falls sharply. The concentration onset of the excimer feature correlates well with the steep reduction in device lifetime, suggesting that the presence of CDBP excimers accelerates degradation in these mixed-host devices. Other potential explanations for the lower stability of CDBP (e.g. if CDBP were chemically less stable or the CDBP source material introduced an impurity) would most likely show a monotonic linear dependence of lifetime on concentration. The distinct concentration threshold behavior observed here makes these alternatives seem unlikely.

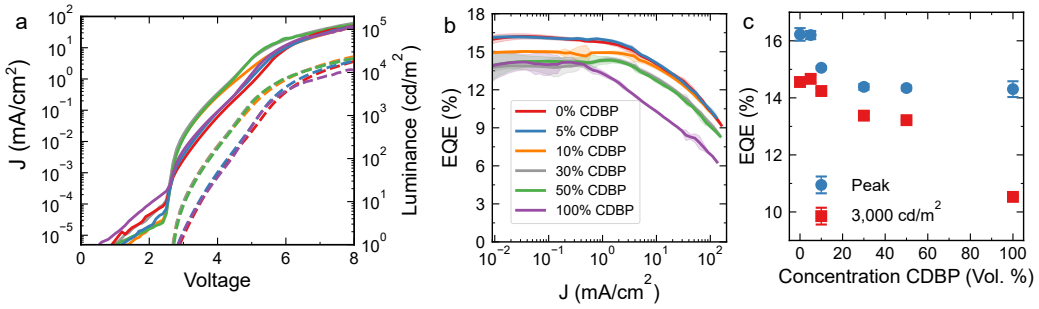

Fig. 5.8. (**a**) Current density and luminance as a function of voltage, (**b**) EQE as a function of current density, and (**c**) peak EQE and EQE at 3000 cd m^{-2} for various mixed-host compositions of CBP and CDBP.

To further confirm the role of the triplet excimer state in degradation, we performed optically-pumped degradation of devices containing a fluorescent (C545T) or phosphorescent ($Ir(ppy)_3$) emitter (Figure 5.9). Comparing these emitters allows the effect of host triplets on stability to be isolated. Fluorescent emitters have negligible intersystem crossing; hence, there is negligible generation of triplets under optical pumping of C545T and the host triplet state will not be populated. Phosphorescent emitters, on the other hand, have a large intersystem

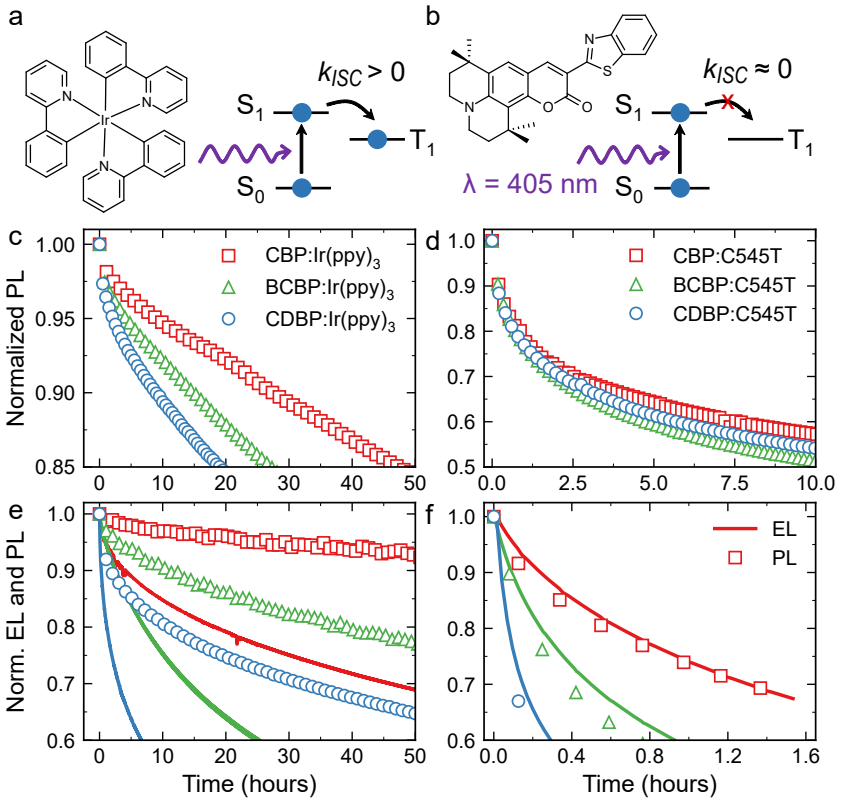

Fig. 5.9. Optical and electrical degradation to isolate the role of host triplets: (**a**) Molecular structure of the phosphorescent emitter, Ir(ppy)$_3$, and schematic showing that triplets are generated during optical pumping due to non-zero intersystem crossing. (**b**) Molecular structure of the fluorescent emitter, C545T, and schematic showing that negligible triplet formation occurs during optical pumping due to vanishing intersystem crossing. (**c**)–(**d**) Show normalized PL decays during optically-pumped degradation ($\lambda = 405$ nm) of devices with (**c**) Ir(ppy)$_3$ and (**d**) C545T doped in each host. (**e**)–(**f**) Show normalized EL and PL decays during electrically-pumped degradation of devices with (**e**) Ir(ppy)$_3$ and (**f**) C545T doped in each host. Ir(ppy)$_3$ devices were degraded at $L_0 = 1000\,\mathrm{cd\,m^{-2}}$ and C545T devices were degraded at $L_0 = 500\,\mathrm{cd\,m^{-2}}$. Optical degradation of (**c**) Ir(ppy)$_3$ and (**d**) C545T devices used pump fluences of ~400 mW cm^{-2} and ~10.000 mW cm^{-2}, respectively.* BCBP is discussed in Section 5.5.

crossing rate (k_{ISC}) and optical pumping will generate a large triplet population which can back transfer to the host triplet state endothermically or exothermically after triplet-triplet annihilation produces a high energy triplet. In the absence of host triplets, the stability of devices containing CBP and CDBP is nearly identical (devices with a C545T emitter in Figure 5.9d). In contrast, when host triplets are present, CDBP:Ir(ppy)$_3$ devices shower much lower PL stability under optical pumping than CBP:Ir(ppy)$_3$ devices. Further, when triplets are introduced to the C545T devices via electrical pumping, devices with a CDBP host again show significantly lower stability than those with CBP (Figure 5.9e-f). Combined with Figure 5.7, these results strongly support the conclusion that the triplet excimer of CDBP accelerates

degradation, as devices are only destabilized when the excimer state is populated.

Given this correlation, there are several theories that could explain the role of the excimer in device degradation. Previous reports have observed an increased excited-state lifetime for excimer triplet states compared to the monomer.[180] The longer lifetime of excimer states could increase the probability of annihilation events as the exciton density is proportional to lifetime.[190] We measured the triplet lifetime of each host by varying the delay time between the laser pulse and spectrum acquisition. The triplet lifetimes of both hosts are within error ($\tau \approx 950$ ms, Figure 5.10), invalidating this explanation. CDBP does show a faster and more non-linear (super-exponential) decay at short times, an effect which has been reproduced with multiple measurements on several films, possibly suggesting a higher rate of triplet-triplet annihilation.* As such, it is possible that the triplet diffusivity is higher in CDBP, which would increase the triplet-triplet annihilation rate and accelerate degradation.[26,46] Further studies should consider if the host triplet diffusivity impacts degradation by measuring the triplet lifetime and triplet diffusion length.[191]

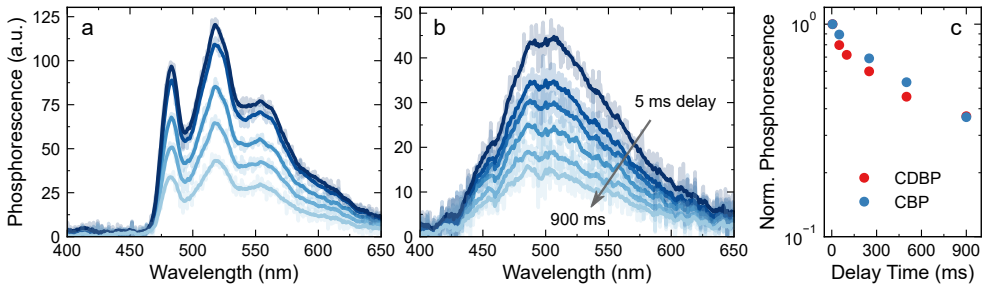

Fig. 5.10. Phosphorescence spectra at 10 K for (**a**) CBP and (**b**) CDBP as a function of delay time from the laser pulse (delays are 5, 50, 100, 250, 500, and 900 ms). (**c**) Normalized integrated phosphorescence as a function of delay time, revealing a similar triplet exciton lifetime of $\tau \approx 950$ ms for both hosts.

Alternatively, it is possible that the localization of the excited state is responsible for the observed stability difference. Since the excimer state in CDBP is localized to the end carbazole groups,[4] excess energy given off during relaxation of hot excited states may be concentrated closer to the weakest bond (C-N).[100] It is also possible that the position of the excimer state

*Another possible source of this effect would be if CDBP had higher absorbance than CBP, yielding a larger excited state density. In fact, the opposite is true,[185] but differences in intersystem crossing rate between the hosts could also play a role here (k_{ISC} has not been reported for these hosts, to my knowledge). In any case, a more thorough spectroscopic study, where excited state densities are well-quantified, would be needed to resolve these conflicting explanations.

allows it to more easily exchange energy with nearby excited states, increasing TTA and accelerating degradation. The more centrally located excited state of CBP, in contrast, may be shielded from neighboring triplets and thus have lower TTA. Given that other carbazole derivatives also exhibit similar excimer formation behavior, the conclusions from this study may apply more generally to other systems.[185] Therefore, this work suggests that additional screening for excimer formation should be considered in OLED host design.

5.5 Next steps

Going forward, these effects should be reproduced across a wider range of host materials to further confirm whether this is a useful screening tool. It is possible that whether the host triplet is an excimer or not is irrelevant, and instead some other property of the triplet is important—the lifetime, the proximity of the excited state to weak bonds, or the ability of the excited state to energy transfer to nearby molecules. Each of these properties could go hand in hand with excimer formation, but they are not necessarily conditional on one another. To this end we examined several other carbazole hosts over the course of this study, including BCBP, which shows intermediate behavior between CBP and CDBP (shown in Figure 5.9). The optical degradation data suggests that BCBP's triplet is involved in degradation as well, but we see no clear evidence of excimer formation: the phosphorescence emission is broad and featureless (without the vibronic features characteristic of most monomer emission), but upon dilution in polystyrene the peak simply narrows and blue-shifts (Figure 5.11). The triplet lifetime of BCBP is comparable to, if marginally longer than, CBP's, a small enough difference that it is unlikely to explain the lifetime trends.

This result does not necessarily contradict the argument that CDBP's triplet excimer state accelerates degradation, but it does suggest that the conclusion should be broadened: host triplets are involved in degradation, and the properties of these triplet states (whether they are excimers or not) can influence device lifetime. In future work, conformational twisting, the location of the triplet excited state, and the bond energies of BCBP and other carbazole-based hosts should be studied further and correlated with device lifetime.

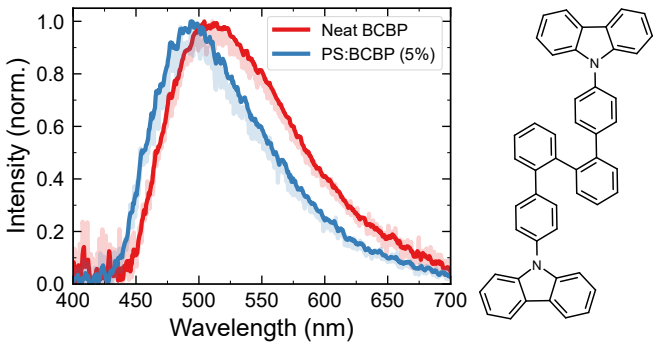

Fig. 5.11. Triplet spectra of neat and dilute BCBP (5 wt.% in polystyrene) and molecular structure of BCBP.

5.6 Conclusions

In summary, we identify the origin of lifetime differences for OLEDs based on two carbazole hosts with similar molecular structures. The accelerated degradation in CDBP-based devices (relative to CBP) correlates with the formation of host excimer states, highlighting the importance of host molecule triplet states and exciton localization in device degradation. Using LDI-TOF-MS, we show that the lifetime reduction does not correspond with the formation of new fragment molecules. Instead, the presence of excimer states appears to accelerate degradation of CDBP via the same C-N bond cleavage which occurs in CBP. These conclusions are confirmed by selectively exciting the triplet state with optically-pumped degradation tests and by frustrating excimer formation by diluting CDBP in CBP. Based on these findings, candidate molecules should be screened for excimer formation early in the design of an OLED stack. This work reinforces the importance of understanding bimolecular interactions in hosts, as they can ultimately drive the degradation of OLEDs.

5.7 Methods

Devices were constructed on pre-patterned indium-tin-oxide (ITO)-coated glass substrates (Xin Yan). Substrates were cleaned by sequentially sonicating in tergitol, distilled water, and acetone, followed by rinsing in boiling isopropanol. Substrates were treated with UV-ozone ambient for 15 minutes before a planarizing hole-injection layer of Plexcore AQ1250 (Sigma Aldrich) was spun-cast in a N_2 glovebox and annealed for 30 minutes at 150 °C. The remaining organic and metal layers were deposited by high vacuum thermal evaporation at a rate of 0.1–0.3 nm s^{-1}: a 40-nm-thick HTL of TCTA, followed by a 10-nm-thick EML composed of the host and 7 vol.

% $Ir(ppy)_3$, and a 40-nm-thick ETL of TPBi. Finally, the cathode consists of 0.5 nm of LiF followed by 100 nm of Al, shadow-masked to define a device area of 0.25 cm^2. Devices for optical degradations used a 20-nm-thick EML, with an emitter of either $Ir(ppy)_3$ or C545T and an otherwise identical architecture. Devices were encapsulated in an N_2 glovebox with a glass cover slide and UV cured epoxy.

Measurements of device external quantum efficiency (EQE) were performed using a Hamamatsu S3584-08 calibrated photodiode and an Agilent 4155C parameter analyzer, assuming Lambertian emission for luminance calculations. Emission spectra were collected with a Princeton Instruments FERGIE spectrometer. Low temperature measurements of film phosphorescence were carried out in a Janis CSS-150 Optical Cryostat at 10 K, using a N_2 laser with a wavelength of $\lambda = 337$ nm (repetition rate of 0.5 Hz) to pump the sample. The spectrometer was triggered to measure phosphorescence 5 ms after each laser pulse with an integration window of 1000 ms. Each spectrum was averaged over ~100 pulses. The spectrometer exposure is synchronized with the laser using a Hewlett Packard 8114A pulse generator. Laser Desorption Ionization Time-of-Flight Mass Spectrometry (LDI-TOF-MS) was performed using an Applied Biosystems-Sciex 5800 MALDI-TOF/TOF on degraded and undegraded devices.[112–114,192] Devices were degraded to 10% of initial luminescence to improve fragment signal.

5.7.1 LDI-TOF-MS

Immediately prior to LDI-TOF-MS characterization, the epoxy sealed cover of each device was removed, the cathode was delaminated using scotch tape, and substrates were secured with copper tape to the target plate. Copper tape grounded the samples by contacting the ITO electrodes in each device to the steel sample plate.

Six spots were scanned on each device using Reflector Mode to achieve low mass resolution, at a machine defined laser intensity of 4200 (a.u.), laser pulse rate of 404 Hz, and detector multiplier voltage of 0.72. Note that these parameters are likely to vary widely between instruments. The laser intensity was set by inspecting the fragment signal and isotopic distributions of materials. This laser intensity further allowed for the resolution of fragments while minimizing potential fragment formation during laser ablation. Areas with evident surface features were avoided, as was overlapping scanning. Each sub-spectrum consisted of 200 laser pulses, and each final spectrum consisted of 4000 laser pulses. Both the CBP (484 m/z) and CDBP (511 m/z) peaks were checked for mass accuracy after instrument internal calibration. Each scan was

processed by integrating around peaks of interest, using a 5 amu window around the peak of highest signal to account for isotopic distributions.

Comparing degraded and undegraded devices permitting detection of fragments arising from laser ablation from those resulting from device degradation. The ratio of fragment to host molecule before and after degradation was also compared.

5.8 Acknowledgments and Contributions

The work presented in this chapter is reproduced with the permission of AIP Publishing from:

R. Newcomb, J. S. Bangsund, K. W. Hershey, D. C. K. Rathwell, H.-Y. Na, J.-H. Jeon, P. Trefonas, and R. J. Holmes. "Role of Host Excimer Formation in the Degradation of Organic Light-Emitting Devices". *Applied Physics Letters* 116.6 (2020), p. 063302. DOI: 10.1063/1.5124802

This work was largely carried out by Robert Newcomb, performing the majority of the device fabrication, lifetime testing, and LDI-TOF-MS measurements. I built the optical degradation and lifetime measurement set-ups used in this work, helped analyze data and write the manuscript, and conceived of the optical degradation approach (Figure 5.9) to decoupling the influence of singlets and triplets. This project was initiated by Kyle W. Hershey, who performed the preliminary lifetime and optical degradation experiments.

This work was funded by DuPont Electronics and Imaging. I was supported by the National Science Foundation Graduate Research Fellowship under grant no. 00074041. Mass spectrometry was performed at The University of Minnesota (UMN) Department of Chemistry Mass Spectrometry Laboratory (MSL), supported by the Office of the Vice President of Research, College of Science and Engineering, and the Department of Chemistry at UMN, as well as through NSF Grant No. CHE-1336940.

6

Sub-turn-on exciton quenching

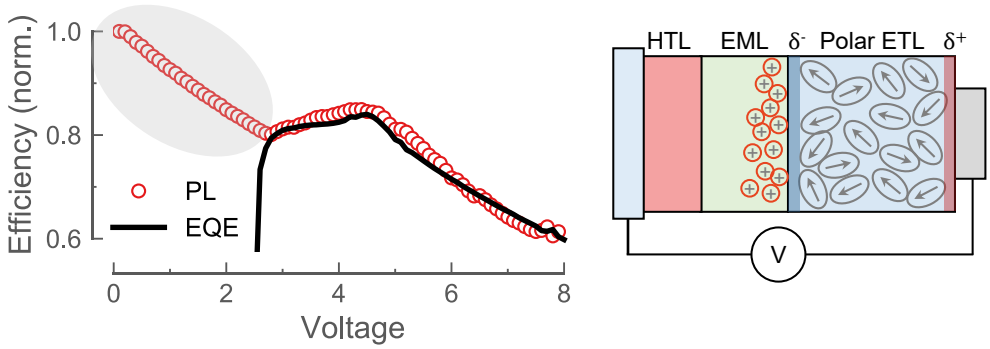

Luminescence quenching occurs at biases below device turn-on due to orientation polarization

The efficiency of organic light-emitting devices (OLEDs) is often limited by roll-off, where efficiency decreases with increasing bias. In most OLEDs, roll-off primarily occurs due to exciton quenching, which is commonly assumed to be active only above device turn-on. Below turn-on, exciton and charge carrier densities are often presumed to be too small to cause quenching. Using lock-in detection of photoluminescence (PL), we find that this assumption is not generally valid; in fact, luminescence can be quenched by >20% at biases below turn-on. We show that this low-bias quenching is due to hole accumulation induced by intrinsic polarization of the electron transport layer (ETL). Further, we demonstrate that selection of non-polar ETLs or heating during deposition minimizes these losses, leading to efficiency enhancements of >15%. These results reveal design rules to optimize efficiency, clarify how ultrastable glasses improve OLED performance, and demonstrate the importance of quantifying exciton quenching at low bias.

6.1 Some context

> **If the data you get seems weird, don't panic.**
>
> Also? Don't... erase it or obfuscate it. It might be something is weird, it might be something is cool, you might have done something wrong... But there is always something to learn.
>
> - Prof. Sarah Tuttle, @niais

The seeds of this project were planted in early 2018 when I noticed a weird feature in my data, something that I couldn't easily rationalize and seemed inconsistent with my basic assumptions of how OLEDs work. I had just finished building a new set-up that measured PL while biasing an OLED—removing electroluminescence (EL) using a lock-in amplifer—and the first data I collected showed a decline in PL at a bias of ~0 V, well below the device turn-on voltage:

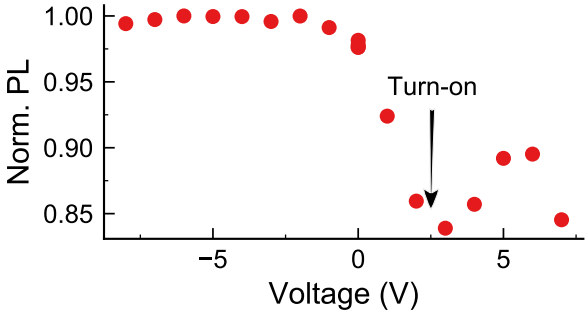

Fig. 6.1. Preliminary bias-dependent PL data showing quenching below device turn-on. Device had a 10 nm TCTA:TPBi M-EML with a 45 nm TPBi ETL (see Figure 3.1 for full structure).

Why was this data so surprising? As discussed in Section 1.7, PL quenching in organic semiconductors can generally occur by three pathways: 1) electric field-induced dissociation, 2) energy transfer between two excitons, or 3) energy transfer from an exciton to a charge carrier. It is clear from above that no quenching occurs even at large reverse biases—so (1) is not active here—and it is widely assumed that both exciton and charge densities are negligible prior to turn-on, meaning that (2) and (3) should also be inactive. Based on these assumptions, the conventional picture for efficiency loss in OLEDs (shown in Figure 6.2) is this: at low biases, bimolecular quenching (i.e. (2) and (3) above) is negligible and some combination of outcoupling efficency and charge balance limit EQE; at moderate to high biases, bimolecular quenching increases in magnitude, causing the efficiency to decrease ("roll-off").

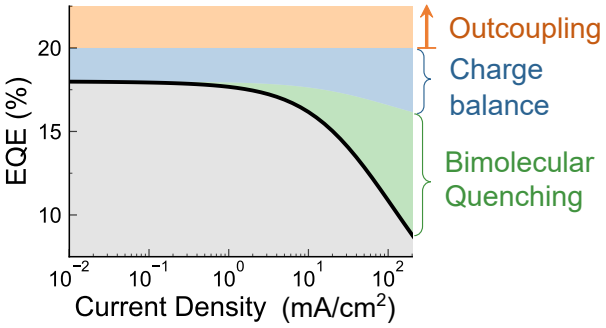

Fig. 6.2. Conventional model for efficiency loss contributions. Outcoupling efficiency (typically ~20%) is roughly independent of bias and is the main limiting factor for efficiency overall. Charge balance also lowers EQE at low-bias, often estimated at around 80-90% at peak EQE,[41,194] and sometimes thought to roll-off at high biases.[99,174] Bimolecular quenching losses are only appreciable above moderate current densities (>1 mA cm^{-2}).

The results in Figure 6.1 are clearly incompatible with the picture in Figure 6.2. But I was much more skeptical, at the time, of my data—this was after all a new measurement that I hadn't yet validated—than the model and assumptions behind quenching in OLEDs that have been applied almost universally.* My first thought was that this was an artifact, so I tried varying anything I could think of: pump power, wavelength, and chopping frequency; detection optics and electronics; and comparing lock-in and oscilloscope detection. But the effect was persistent and present to varying degrees in every device I tested.

Eventually, when I failed to come up with a satisfying explanation, I moved on and convinced myself that the effect wouldn't undermine what I was trying to measure in the first place: how bimolecular quenching changes with degradation. For this project, discussed in Chapter 7, I was comparing PL in an OLED in on and off states. I figured that all quenching processes present in the on state would be captured by this measurement, so it was somewhat irrelevant how this quenching was distributed with bias.† It took another year—in part because I stopped interrogating and trying to understand this feature, in part because I was too attached to the established model for OLED quenching—for me to realize that this effect was too important to ignore.

In this chapter, I will lay out why this effect occurs, why it is important, how it changes our understanding of what determines efficiency in OLEDs, and how to control it.

*As it happens, the mechanism behind this effect, clarified in this chapter, has been understood for at least a decade.[195] These findings have been relatively niche within the field, however, and the potential impact of this effect has not been broadly appreciated nor been demonstrated. When I first heard of SOP—relayed by Tom Fielitz who by chance had talked to Prof. Hisao Ishii at a Materials Research Society conference back in 2016—I thought it was a weird curiosity but didn't really grasp how it could affect device performance.

†This assumption also turned out to be incorrect. As shown in this chapter, quenching can occur even at reverse biases.

6.2 Introduction

While organic light-emitting devices (OLEDs) have been successfully commercialized in mobile displays, their performance at high brightness is still limited by efficiency roll-off and degradation,[46,75] hindering their viability for lighting, automotive, and outdoor applications.[196] Frequently, these detrimental processes are driven by bimolecular reactions such as exciton-polaron quenching (EPQ) and exciton-exciton annihilation (EEA). Of these, quenching by charge carriers (i.e. EPQ) has often been found to be the dominant mechanism.[28,49,197] The density of charges within an OLED therefore plays a critical role in device performance, and higher densities have been correlated with reduced lifetime and increased roll-off.[164,198–200]

It is typically assumed that EPQ and EEA processes are negligible at biases below the threshold for device turn-on,[28,38,41,75,99] as the exciton density in this regime is vanishingly small and the polaron density in organic semiconductors is negligible in the absence of charge injection. However, large charge densities can be injected into the device even at biases below the built-in voltage due to spontaneous orientation polarization (SOP).[201,202] A common phenomenon in organic thin films, SOP is the spontaneous ordering of permanent, molecular dipole moments (PDMs) leading to a net polarization. In a device, the polarization charge from SOP leads to the accumulation of charge carriers, typically holes, adjacent to the polar layer.[203] While it has been speculated that this SOP-induced hole density can quench excitons and accelerate degradation,[201] direct quantification of these effects has been limited. Only recently has it been appreciated that SOP can cause exciton quenching in fluorescent emitters.[57]

Here, we directly quantify exciton quenching due to SOP-induced hole accumulation in archetypical phosphorescent OLEDs. We find that SOP leads to quenching of photoluminescence by 20–35% at biases below device turn-on, reducing peak device efficiency by >15%. We show that failing to account for this effect can lead to incorrect conclusions about exciton and charge kinetics and the factors that govern device efficiency. Further, we demonstrate that this effect can be nearly eliminated by heating during deposition or by selecting materials with negligible SOP. These findings underscore the importance of considering SOP during materials selection and device fabrication strategies to minimize these losses.

6.3 Measuring quenching *via* lock-in PL

A variety of approaches have been taken to quantify quenching in OLEDs. Perhaps the most common is to fit EQE roll-off to an exciton kinetics model with little or no supporting characterization.[39,75,129,204,205] This suffers from a few obvious drawbacks: any quenching at peak EQE cannot be isolated without assumptions about charge balance, and the result depends strongly on what simplified model for charge carrier (polaron) density is chosen.

Another method is fitting kinetics models or simple exponential lifetimes to transient electroluminescence;[41,146] this data is much richer than EQE and should, in principle, capture all quenching processes in a device. However, the EL decay often reflects a convolution of quenching and delayed recombination from residual charges,[41] leading to the same limitations of simplified charge models. Transient EL is also typically taken at relatively large biases to generate sufficient signal, making it difficult to probe quenching at low biases.

A more comprehensive, and labor-intensive, approach is occasionally taken by combining complementary techniques such as EQE roll-off fitting, steady-state PL quenching in single-carrier devices to measure exciton-polaron quenching, and transient photoluminescence to measure exciton-exciton annihilation.[38,41] This significantly increases confidence in fitted rate constants, but it still has shortcomings. For instance, measuring quenching in single-carrier devices still relies on a simplified model of polaron density, and the layer structure is necessarily different than the device of interest, leading to differences in charge injection, transport, and accumulation.

The most powerful method available for quantifying quenching is simultaneous EL and PL measurements, where a background bias is used to vary charge and exciton densities in device-relevant conditions. This is commonly achieved by measuring transient PL with a short laser pulse in a device held under a longer voltage pulse.[99,174,197] Here, we opt for a steady-state PL approach: we excite the EML with a chopped $\lambda = 405$ nm laser and measure PL from the DC-biased device with a lock-in amplifier. This wavelength selectively pumps $Ir(ppy)_3$, so that only the relative PL efficiency of the emitter is probed (see Figure 6.3a). Lock-in detection excludes any background EL from the PL measurement, allowing relative PL changes due to exciton quenching to be isolated (see Section 6.8 and Figure 6.3b). This approach has been used previously to quantify efficiency roll-off mechanisms in light-emitting devices based on

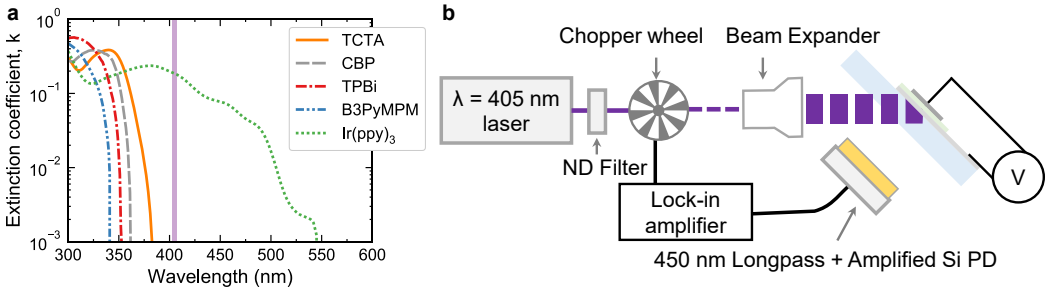

Fig. 6.3. (**a**) The extinction coefficient, measured with spectroscopic ellipsometry, for TCTA, CBP, TPBi, B3PyMPM, and $Ir(ppy)_3$. The $\lambda = 405\,nm$ pump laser, shown for reference in the shaded purple box, selectively pumps $Ir(ppy)_3$ and no other materials in the device stack. The hole-injection layer, AQ-1250, is non-emissive and spatially separated from the emissive layer, so excitation of this layer does not interfere with the PL measurement. (**b**) The pump laser is attenuated with a neutral density (ND) filter, chopped, and spatially expanded. The incident angle is ~45°. The resulting photoluminescence is filtered through a 450 nm longpass filter and collected with an amplified Si photodiode. The photoluminescence signal is measured with a lock-in amplifier, which removes the background EL signal. See Materials and Methods in the main text for a complete description of the equipment and measurement parameters.

quantum dots and metal-halide perovskites.[206,207] One advantage of the steady-state photoluminescence approach over transient PL techniques is that it is more amenable to automation and allows voltage sweeps to be made rapidly with fine step sizes.*

Aside from selective pumping of the emitter, the most important considerations of this measurement are chopping frequency and pump power. Pump power should be kept as small as possible—to minimize photogenerated charge and exciton density, as well as light-induced changes in device performance—while still large enough to achieve a signal to noise ratio of at least 10. The selection of chopping frequency is important for rejecting noise sources, such as the power line frequency. Total noise will often be lower at higher frequencies due to reduced $1/f$ noise. In some devices, the pump laser induces transient changes in the conductivity which can introduce artifacts by causing oscillations in EL that are in phase with the chopped PL and thus captured by the lock-in amplifier. In these cases, a high chopping frequency can be used to bring these effects to steady-state so they can be effectively rejected (see Figure 6.18). These factors are discussed in more detail in Section 6.8.

*The transient technique does hold an advantage in that it can provide additional insight into the quenching mechanism, as TTA and TPQ will have different effects on the functional form of the decay.

6.4 Comparing polar and non-polar electron transport materials

To determine whether SOP-induced hole accumulation influences exciton quenching, comparison devices were fabricated incorporating polar (i.e. exhibiting SOP) and non-polar electron transport layers (ETL). We selected two widely studied materials: TPBi as the polar ETL and B3PyMPM as the non-polar ETL (molecular structures shown in Figure 6.4a).[201] TPBi has a permanent dipole moment (PDM) of 2.01 D and a giant surface potential (GSP) slope of 40–70 mV nm^{-1},[203,208] which is a figure-of-merit for the magnitude of SOP. B3PyMPM has a larger PDM of 4.29 D but its GSP slope is almost negligible, only ~3 mV nm^{-1}.[201] The small magnitude of SOP in B3PyMPM films has been attributed to a strong intermolecular interaction which leads to anti-parallel alignment of PDMs, canceling out the overall polarization.[20]

Devices contained a 10-nm-thick emissive layer (EML) of the archetypical carbazole host, CBP, and the green phosphorescent emitter, Ir(ppy)$_3$ (schematic in Figure 6.4a), both of which are non-polar.[20] Aside from the ETL, all layers in these devices were shared and deposited in the same run.

The dependence of the normalized PL intensity on applied voltage is shown in Figure 6.4c for devices with ETL thicknesses of 50 nm for TPBi and 47 nm for B3PyMPM. The bias-dependence is markedly different for the two ETLs. Photoluminescence from devices containing TPBi is reasonably flat from -4 V to -2 V; as the voltage is increased above -2 V, the PL declines steeply, reaching 65% of the initial value by +2 V. This reduction arises due to EPQ with holes which accumulate in the EML as a result of the polarized ETL, a claim that is proven below. In contrast, devices based on B3PyMPM show negligible quenching of PL until the device turns on at +2 V (the decline in PL observed under reverse biases is likely due to quenching from leakage current). Above +2 V, the reduction in PL from the B3PyMPM devices reflects conventional bimolecular quenching and roll-off behavior. Interestingly, the PL from TPBi devices increases for biases between +2.5 V to +4 V. This roll-up in PL coincides with device turn-on (i.e. the sharp onset of luminance at +2.5 V in Figure 6.4c), likely reflecting a reduction in hole concentration in the EML due to recombination with injected electrons. Similar behavior, where EPQ is reduced with increasing bias, was recently predicted for comparable CBP:Ir(ppy)$_3$ devices with a drift-diffusion model.[209]

To understand the potential impact of sub–turn-on exciton quenching on device performance, we compare the dependence of both the normalized PL and the device internal quantum

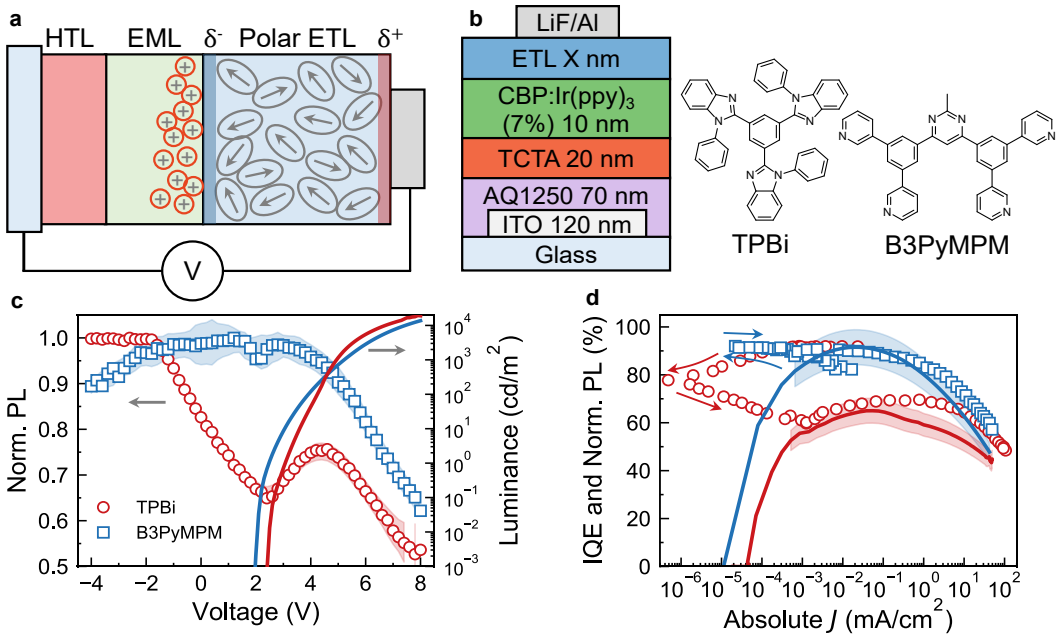

Fig. 6.4. Comparison of polar and non-polar ETL device performance. (**a**) Schematic of SOP-induced hole-accumulation. Preferred orientation of permanent dipole moments (PDMs) in the ETL (denoted as arrows) leads to net polarization sheet charges on each side of the ETL (δ^- and δ^+). (**b**) Device schematic and molecular structures of TPBi (polar ETL) and B3PyMPM (non-polar ETL). (**c**) Normalized photoluminescence (PL, symbols) and luminance (lines) as a function of voltage for devices with TPBi (red circles) and B3PyMPM (blue squares) ETLs with thicknesses of 50 nm and 47 nm, respectively. Shaded regions are 95% confidence intervals of the mean weighted by Student's t factor. (**d**) Internal quantum efficiency (IQE, lines) and normalized lock-in PL data (symbols) as a function of absolute current density for devices with a B3PyMPM or TPBi ETL. To allow direct comparison with IQE, normalized PL data is multiplied by $\eta_{PL} = 92\%$, the intrinsic PL efficiency of $Ir(ppy)_3$ at this doping concentration.[42] Arrows indicate the sweep direction for the PL data, where the change in direction is due to negative photocurrent.

efficiency (IQE) on current density (J). The IQE, which is the electron-to-photon conversion efficiency, is calculated by dividing the measured external quantum efficiency (EQE) (Figure 6.19) by the simulated optical outcoupling efficiency for each architecture ($\eta_{OC} = 18.8\%$ for B3PyMPM and 24.1% for TPBi, see Section 6.8). The IQE reaches near unity (~92%) in the B3PyMPM devices, almost identical to the intrinsic photoluminescence efficiency ($\eta_{PL} \approx 92\%$) of $Ir(ppy)_3$ at this doping concentration.[42] In the TPBi devices, IQE reaches only 70%. This difference in peak IQE is almost entirely explained by the PL quenching at low biases (Figure 6.4d). When the TPBi device initially turns on, the IQE at $J = 10^{-3}$ mA cm^{-2} is 56% and nearly equivalent to the normalized PL at the same bias (61%). The PL and IQE then rise with a similar slope between $J = 10^{-3}$ mA cm^{-2} and 10^{-1} mA cm^{-2}. These similarities indicate that IQE is predominantly limited by exciton quenching at low to moderate biases (<10^{-1} mA cm^{-2})

and that charge balance is near unity.* This finding stands in contrast to, and calls into question, the common practice of ascribing lower-than-expected peak EQE values to charge balance or electrical losses.[41,194]

Above $J = 10^{-1}$ mA cm^{-2}, the PL and IQE curves begin to diverge, with the IQE showing a steeper roll-off than PL in all devices. This may indicate that charge balance losses contribute to roll-off at higher current densities,[99,174] but error due to spatial mismatch between the recombination zone and the electric field of the pump laser could also contribute (see Section 3.5).[157] In any case, the majority of roll-off in both devices arises from exciton quenching.

6.4.1 Probing hole accumulation with displacement current

We next sought to further confirm that the observed sub–turn-on exciton quenching is due to hole accumulation from the orientation polarization of the ETL. A key feature of thin films exhibiting SOP is that their surface potential scales with film thickness.[201,202] In a device, this leads to a linear dependence of the hole-injection voltage on the thickness of the polar layer (note that the interface charge is constant with film thickness). This dependence was investigated here by fabricating TPBi and B3PyMPM devices with a range of ETL thicknesses (d_{ETL}). Actual ETL thicknesses for TPBi devices were 33 ± 1 nm, 50 ± 1 nm, and 68 ± 1 nm; those for B3PyMPM devices were 32 ± 1 nm, 47 ± 1 nm, and 64 ± 1 nm.

Displacement current measurements (DCM) were used to measure the hole-injection voltage (V_{inj}) and the injected charge density. DCM is a widely-applied capacitance-voltage-type measurement useful for evaluating charge injection and accumulation in OLEDs.[195] This approach involves applying a triangular voltage waveform to the device and measuring the response current, which is a combination of the displacement and conduction currents. At low to moderate sweep rates ($\lesssim 100$ V s^{-1}), charge accumulation in the device can be considered to be quasi-static, and in this regime the measured current is predominantly displacement current. Because the displacement current is proportional to the apparent device capacitance, this measurement is sensitive to increases in charge density within the device and changes in the charge distribution.[195,201,210]

To illustrate how DCM works, an example measurement and corresponding analysis is shown in Figure 6.5; a complete discussion of the method is included in Section 6.8. A DCM

*The roll-up in efficiency in the narrow range of biases near turn-on is still likely limited by charge balance.[41]

scan begins at reverse biases, where the device is fully depleted; here, the current is proportional to the geometric capacitance of the entire device. As the sweep moves to biases above the hole-injection voltage—which is determined by the polarization and thickness of each layer in the device—holes traverse the non-polar layers and begin to accumulate at the non-polar/polar interface. At this point, only the polar layers behave as a dielectric, and the apparent capacitance (and current) increase to reflect the reduced thickness of the capacitive layer. By integrating the current above hole injection, we can directly calculate the SOP-induced hole density, σ_h.

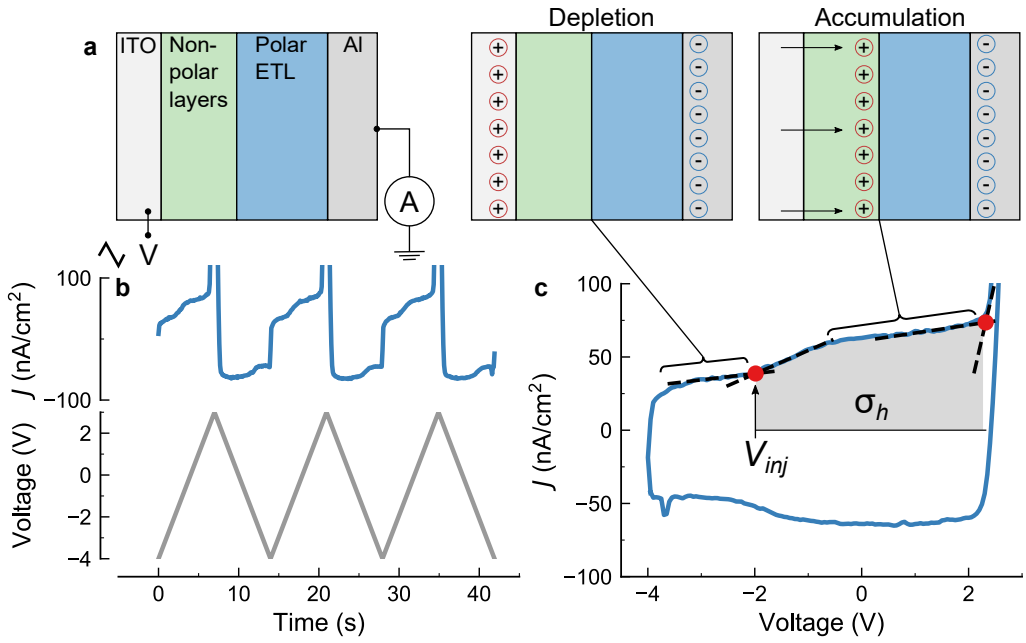

Fig. 6.5. Example displacement current measurements and analysis. (**a**) Electrical schematic (left) of device with a voltage supplied at the anode and current is measured out of the cathode. The middle schematic shows the fully depleted device, below V_{inj}, and the right schematic shows hole accumulation at the non-polar/polar interface above V_{inj}. (**b**) Example measurement, where a triangle voltage wave is applied (bottom) and the resulting current is measured (top). (**c**) Example analysis, where the injection and threshold voltages are identified by the intersection of linear fits. The charge density, σ_h, is measured by integrating the current from V_{inj} to V_{th}.

V_{inj} is assigned based on the onset of slope change in the DCM curve (see dashed vertical lines in Figure 6.6a), which is when the capacitance of the device (and the accumulated charge density) begins to increase. Increasing the thickness of the TPBi ETL shifts the hole-injection voltage from -0.08 ± 0.25 V for d_{ETL} = 33 nm to about -3.00 ± 0.32 V for d_{ETL} = 68 nm (Figure 6.6a), as expected for an ETL showing SOP.[195,201] No shift of V_{inj} is discernible when

increasing thickness of the B3PyMPM ETL (Figure 6.6b), confirming that B3PyMPM is non-polar. Comparing the DCM data to PL measurements, we see that the onset of the PL roll-off coincides exactly with the hole-injection voltage. This result provides strong support for the conclusion that hole accumulation induced by SOP of the ETL is responsible for exciton quenching prior to turn-on.

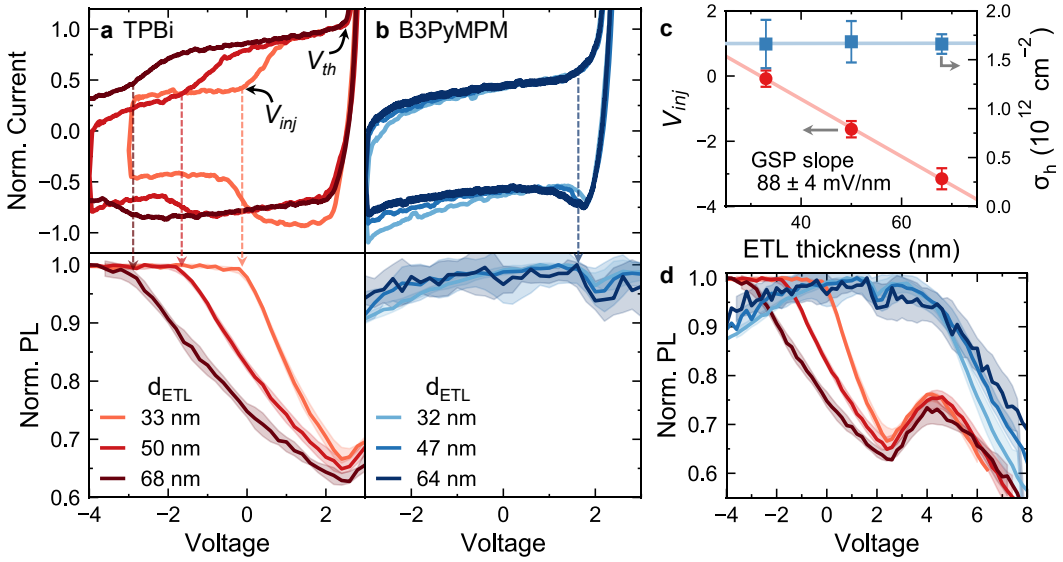

Fig. 6.6. Displacement current and lock-in PL measurements for various ETL thicknesses: (**a**) Displacement current measurements (DCM) (top) and lock-in PL measurements (bottom) as a function of applied voltage for different thicknesses (d_{ETL}) of the TPBi ETL. For visualization clarity, current is normalized to the value at 2 V (raw data shown in Figure 6.20). The onset of the roll-off in PL intensity coincides with the hole-injection voltage (denoted with dashed arrows). (**b**) The same measurements for a B3PyMPM ETL, which show no discernible shift in hole-injection voltage or quenching of PL prior to device turn-on. (**c**) V_{inj} and hole sheet density (σ_h) for TPBi devices extracted from the DCM curves in (**a**). Error-bars represent standard deviations over at least three pixels. (**d**) Full voltage dependence of lock-in PL data for devices with an ETL composed of TPBi or B3PyMPM. Colors correspond to the legends in (**a**) and (**b**). Shaded regions are 95% confidence intervals of the mean weighted by Student's t factor based on measurements of at least three pixels.

For comparison purposes, the giant surface potential (GSP) slope (m_{GSP}) can also be extracted from these measurements based on the slope of V_{inj} vs. d_{ETL} (Figure 6.6c). We measure a GSP slope of $88 \pm 4\,\mathrm{mV\,nm^{-1}}$, which is double the $43\,\mathrm{mV\,nm^{-1}}$ value reported by Noguchi et al. [203], but agrees reasonably with an earlier report of $\sim 70\,\mathrm{mV\,nm^{-1}}$.[208] This value of m_{GSP} corresponds to an interface charge density of $\sigma_h = 2.5\,\mathrm{mC\,m^{-2}}$.* Consistent with m_{GSP}, the

*$\sigma_h = \varepsilon_{r,ETL}\varepsilon_0 m_{GSP}$ if no other layers are polar;[203] assuming $\varepsilon_{r,ETL} \approx 3.2$, then $\sigma_{h,GSP} = 3.2 \cdot 8.854 \times 10^{-12}\,\mathrm{F\,m^{-1}} \cdot 88\,\mathrm{mV\,nm^{-1}} = 3.2 \cdot 8.854 \times 10^{-3}\,\mathrm{mC\,mV^{-1}\,nm^{-1}} \cdot 88\,\mathrm{mV\,nm^{-1}} = 2.5\,\mathrm{mC\,m^{-2}}$

integral of the DCM curves yields $\sigma_h = 1.6 \pm 0.2 \times 10^{12}\,\mathrm{cm}^{-2}$ (or $2.6\,\mathrm{mC\,m}^{-2}$), which is independent of d_{ETL} (Figure 6.6c). This value is again about twice as large as previous reports for TPBi ($\sim 1.1\,\mathrm{mC\,m}^{-2}$),[203] but it is still well below the theoretical maximum charge density based on the PDM of TPBi (i.e. when the PDMs are all perfectly aligned in the out-of-plane direction, $\sigma_{h,max} = 5.2 \times 10^{12}\,\mathrm{cm}^{-2} = 8.3\,\mathrm{mC\,m}^{-2}$).*

The variability in these reported values for m_{GSP} and σ_h could arise from differences in the initial surface (α-NPD in ref. [203] and 1-TNATA in ref. [208], compared to CBP:Ir(ppy)$_3$ here) or other deposition conditions, such as the deposition rate or the substrate temperature. Notably, the substrate temperature is usually not monitored and could depend on deposition chamber; the role of this parameter is discussed in the next section.

Figure 6.6d shows the full voltage dependence of PL for both TPBi and B3PyMPM devices. Normalized PL at device turn-on (2.5 V) are nearly within error for the different ETL thickness, which is expected as the interface charge is constant with film thickness. The slight monotonic decrease in PL at this point for higher ETL thicknesses (from ~67% for d_{ETL} = 33 nm to ~63% for d_{ETL} = 68 nm) is consistent with a SOP-induced charge density that is expected to be peaked at the EML/ETL interface.[213] That is, the peak in the optical field of the pump laser moves towards the EML/ETL interface as ETL thickness is increased (Figure 6.22), leading to more overlap between the optically generated exciton population and the charge density.

6.5 Eliminating polarization by heating during deposition

Fabricating OLEDs at elevated temperatures has recently been shown to improve efficiency and lifetime; these enhancements were attributed to the formation of ultrastable glasses and it was hypothesized that increased rigidity in these dense glasses suppressed non-radiative decay.[214] TPBi served as the host and ETL in these devices, and the devices fabricated above room temperature showed increased exciton lifetime, consistent with reduced exciton quenching. Considering that molecular orientation has been shown to be tunable with deposition temperature,[21] it is plausible that these results simply reflect reduced SOP and hence reduced hole accumulation within the device. Notably, the reported increases in peak efficiency (14-28%) and exciton lifetime (15-17%) achieved by this method are similar to those from using a non-polar ETL

*$\sigma_{h,max} = pN/V$,[211] where p is the PDM and N/V is number of molecules per volume. Note that p has units of Debye, which is defined as $\mathrm{D} \equiv \frac{10^{-21}\,\mathrm{C\,m}}{c}$, where c is the speed of light. For TPBi, N/V is estimated at $\sim 1.2 \times 10^{21}\,\mathrm{cm}^{-2}$ based on the correlation between density and molecular weight from Xiang et al. [212].

(10% increase in peak EQE and 20% increase in PL at 0 V, see Figure 6.19 and Figure 6.4c).

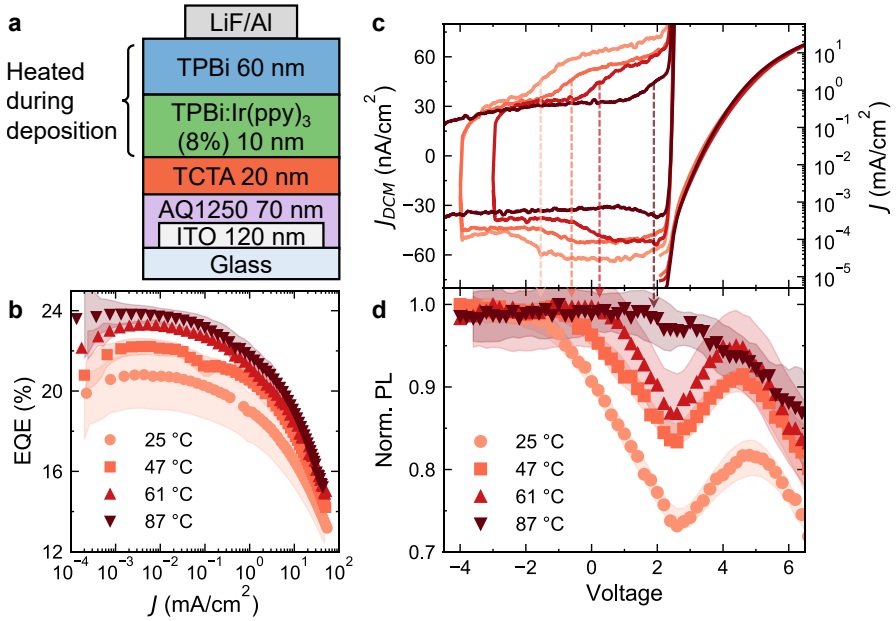

Fig. 6.7. Device performance and PL measurements for heated depositions of TPBi. (**a**) Device structure, where substrates are heated during deposition of the EML and ETL but are kept at room temperature for all other layers. (**b**) EQE as a function of current density for devices deposited at 25 °C, 47 °C, 61 °C, and 87 °C. EQEs are outcoupling-corrected to account for d_{ETL} variations (see Table 6.1). (**c**) DCM curves and (**d**) corresponding PL data at low biases for the same deposition temperatures. The right axis in (**c**) shows the conduction current density above device turn-on, showing that heating during deposition negligibly influences electrical characteristics. The shaded regions in (**b**) and (**d**) are 95% confidence intervals of the mean weighted by Student's t factor based on measurements of three to six separate pixels.

To assess this possibility, we made devices with a similar structure to that used by Ràfols-Ribé et al. [214] (see Figure 6.7a and Section 6.8) and varied the substrate temperature during deposition of the EML and ETL from 25 °C to ~107 °C. Peak EQE increases sharply at elevated deposition temperature and eventually saturates at ~23.5% above 70 °C, showing a (18.1±0.5)% enhancement at ~61 °C compared to 25 °C.* Over this range, the current-voltage characteristics are within error (Figure 6.7c and Figure 6.21), suggesting that heating does not significantly influence charge transport properties.

This enhancement in EQE is similar in magnitude to the previous report, but the trend differs: instead of reaching an optimum near 66 °C,[214] EQE here is monotonic over the entire temperature range. This distinction is important because the density of vapor-deposited glasses

*see Figure 6.7b and Figure 6.21, the median peak EQE increased from (19.7±0.4)% at 25 °C to (23.3±0.5)% at ~61 °C

is generally maximized when the substrate temperature is near 85% of the glass transition temperature (T_g) in Kelvin,[21] which is ~65 °C here given T_g = 124 °C for the TPBi host.[177] If glass density predicted efficiency, then EQE should be peaked at ~65 °C and decline at higher temperatures. Another mechanism must then be responsible for the enhanced efficiency.

It is worth noting that the difference in these EQE trends is not necessarily contradictory. The device used by Ràfols-Ribé et al. [214] contained a horizontally-oriented emitter, $Ir(ppy)_2(acac)$, which showed reduced outcoupling efficiency at high temperatures due to a shift to more isotropic or vertically-oriented transition dipole moments (TDMs), which are less preferential for outcoupling. This reduction in η_{OC} is likely responsible for the observed optimum (both EQE and calculated η_{OC} fell by ~8% from their peak by 90 °C),[214] whereas our devices contain $Ir(ppy)_3$, which should show no reduction in η_{OC} since its TDMs are already isotropic.[211]

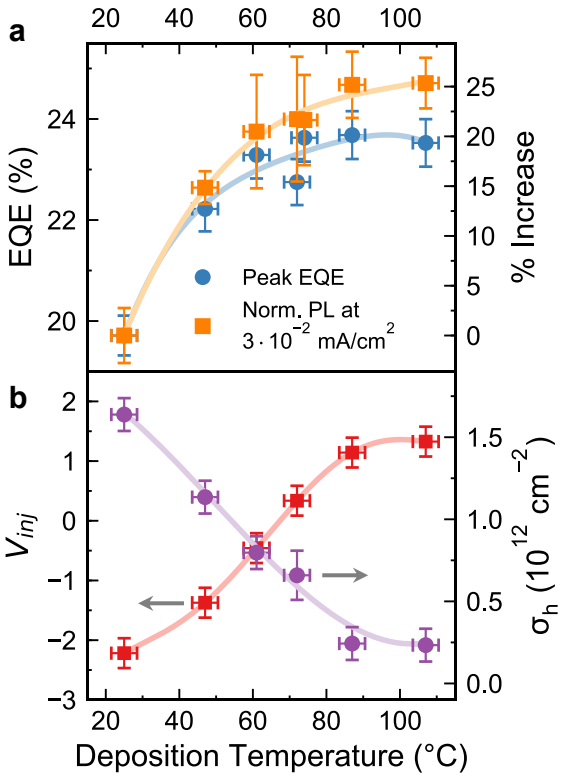

Fig. 6.8. Temperature dependence of peak EQE, PL, hole-injection voltage, and charge density. (**a**) Peak EQE and normalized PL extracted near the peak EQE—at $J = 3 \times 10^{-2}$ mA cm^{-2}—as a function of deposition temperature. The right axis gives the percentage increase of both variables, showing good agreement. EQEs are outcoupling-corrected (see Table 6.1, raw data in Figure 6.21). The 107 °C device had a 70 nm ETL, resulting in a correction factor of 12%. (**b**) Hole-injection voltage, V_{inj}, and injected hole sheet density at turn-on, σ_h, extracted from DCM as a function of deposition temperature. Solid lines are guides-to-the-eye. Y-axis error bars are 95% confidence intervals of the mean weighted by Student's t factor based on measurements of three to six separate pixels.

The rise in EQE is accompanied by an increase in the hole-injection voltage and a commensurate shift in the onset of PL roll-off to higher voltages (Figure 6.7c,d). Further, the

amount of quenching at device turn-on (~2.5 V) decreases monotonically at higher temperatures (Figure 6.7d). At biases near peak EQE ($J = 3 \times 10^{-2}$ mA cm^{-2}), the normalized PL is (20.5±1.1)% higher in devices fabricated at ~61 °C than at 25 °C, remarkably similar to the enhancement in peak EQE (Figure 6.8a). The agreement between EQE and PL holds across all temperatures for a range of biases (Figure 6.23), only breaking down above ~6 V (~1 mA cm^{-2}), when, as mentioned above, charge balance roll-off or spatial mismatch effects could become more significant.[157] These reductions in PL quenching are mirrored by reductions in the SOP-induced hole sheet density from ~1.6×10^{12} cm^{-2} at 25 °C to ~0.2×10^{12} cm^{-2} at 107 °C (Figure 6.8b).

Taken together, these concurrent changes in PL quenching and hole-injection confirm that heating during deposition reduces or even eliminates spontaneous orientation polarization in TPBi, thereby reducing the concentration of holes in the emissive layer. Exciton quenching is thus reduced, increasing the exciton lifetime and device efficiency. Further, the close agreement between EQE and PL demonstrates that the efficiency enhancement results almost entirely from reduced exciton-polaron quenching.

Nonetheless, these relative measurements of PL cannot rule out increases in the intrinsic η_{PL}, which would uniformly boost PL intensity and EQE independent of bias. To remove this ambiguity, we evaluated whether heating during deposition impacts exciton kinetics in TPBi:Ir(ppy)$_3$ (8 vol.%) films on glass, outside of a device such that holes cannot be injected from electrodes. The exciton lifetime (τ), measured using PL transients (see Section 6.8), shows a slight linear increase with deposition temperature (Figure 6.9).* Relative to 25 °C films, τ increases by only ~2.6% at ~67 °C and ~3.8% at ~90 °C, further demonstrating that suppressed non-radiative decay due to the higher density of the glass cannot explain the observed efficiency increases of >15%. Additionally, because τ does not peak at the temperature of maximum glass density (~0.85 T_g, 65 °C), this trend is more likely due to reduced impurity incorporation at elevated temperature.[215]

It is worth noting that Ràfols-Ribé et al. [214] reported that exciton lifetime explained most but not all of the efficiency enhancement, and the remaining increase was tentatively assigned to charge balance improvements. Based on our results, it seems likely that this discrepancy arises from the measurement of exciton lifetime being taken on an unbiased OLED, which does not fully capture the quenching processes which occur at peak EQE.

*Recall that η_{PL} is proportional to τ, i.e. $\eta_{PL} = k_r \tau$ where k_r is the radiative rate

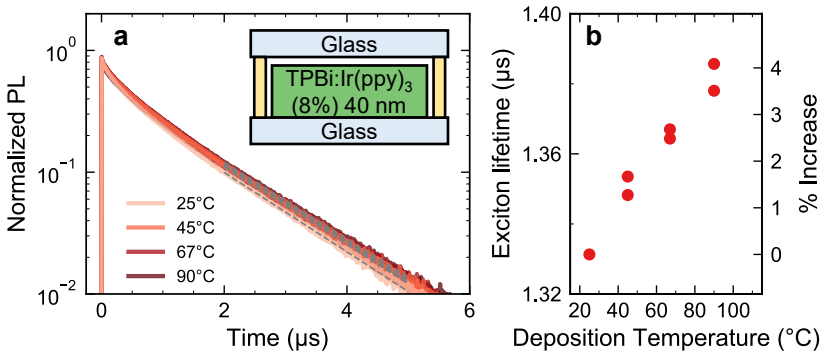

Fig. 6.9. Exciton kinetics vs. deposition temperature. (**a**) Transient PL decays of TPBi:Ir(ppy)$_3$ (8 vol.%) films outside of a device (no SOP-induced holes present). Films are deposited on glass and encapsulated with UV-cured epoxy and cover glass (see inset). Dashed gray lines are exponential decay fits to extract the exciton lifetimes in (**b**). Decays are fit from 2–5 μs to avoid non-linearities from triplet-triplet annihilation at short times.

6.5.1 Effects of heating on degradation

Heating during deposition could also influence device stability. For instance, reduced SOP-induced hole accumulation at high temperatures could lower the rate of exciton-polaron-mediated degradation,[46,49] while ultrastable glass formation can improve intrinsic photostability.[216] Ràfols-Ribé et al. [214] argued this latter effect was responsible for an observed 86%–500% enhancement in electrical lifetime which was peaked at substrate temperatures near 0.8-0.85 T_g.

We sought to reproduce this finding and better understand how heating influences stability by comparing degradation under optical and electrical pumping. We photodegraded TPBi:Ir(ppy)$_3$ films on glass, outside of a device to avoid the potential influence of SOP-induced hole density within the emissive layer (λ = 405 nm laser, ~1 W cm^{-2}). Films heated at 45–60 °C showed a (43±16)% enhancement in lifetime relative to room temperature films (Figure 6.10a).* A similar increase in photostability also occurs for films within a device (λ = 405 nm laser, ~20 W cm^{-2}, see Figure 6.10b). These devices were degraded at open-circuit (~2 V at this illumination intensity), meaning that SOP-induced holes were accumulated during the

*Increasing from $t_{70} = (7.7 \pm 2.0)$ hr at 25 °C to $t_{70} = (11 \pm 3)$ hr at 45 °C

test. Because the enhancement is similar,* we infer that SOP-induced hole density does not substantially accelerate photodegradation† in these devices and that ultrastable glass effects may be responsible for this improvement.[216] Still, the magnitude of this enhancement is much smaller than that reported in ref. [214] and other studies of photostability in ultrastable glasses.[216,218]

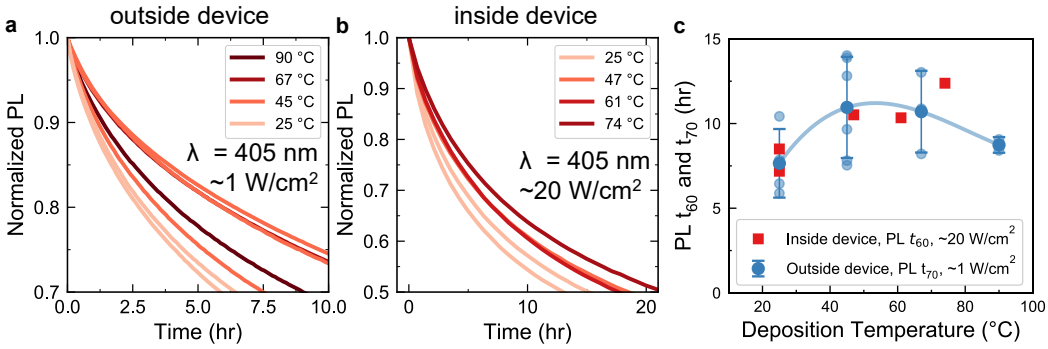

Fig. 6.10. Optical degradation as a function of deposition temperature. Normalized PL intensity as a function of time and deposition temperature for optically-pumped degradation ($\lambda = 405$ nm) of (**a**) TPBi:Ir(ppy)$_3$ films on glass (i.e. outside of a device, pump power ~1 W cm^{-2}) and (**b**) TPBi:Ir(ppy)$_3$ devices from Figure 6.7a (pump power ~20 W cm^{-2}). (**c**) Extracted PL t_{60} and t_{70} lifetimes (time to reach 60% and 70% of the initial PL intensity) for optically-pumped degradation from (**a**) and (**b**). Line is a guide to the eye and error bars are standard deviations over >3 tests. Devices are not contacted during degradation, and hence are degraded at open-circuit conditions under which both photogenerated carriers and SOP-induced holes will be present in the device.

In contrast, the lifetime under electrical pumping shows no enhancement and instead declines slightly as temperature is increased (initial luminance of $L_0 = 1000$ cd m^{-2}, Figure 6.11). This discrepancy suggests that electrical and optical stability are limited by different factors in our devices. Because exciton and charge densities are likely lower in heated devices, due to their higher efficiency and reduced SOP, degradation reactions dictated by exciton and charge kinetics are unlikely to explain this deviation.[49,97] One possibility is that processing-dependent impurities limit the electrical stability and depend on deposition temperature. For instance, impurities from the vacuum chamber—such as residual gases, vacuum grease, and resins—can be incorporated in the device during deposition and lower lifetime,[219,220] an effect which becomes more significant for longer deposition times and lower deposition temperatures.[215] The

*Note that the similar magnitude of PL lifetime inside and outside of a device, despite a 20× difference in pump power, is likely due to cavity-induced reductions in the exciton lifetime, which in turn reduces exciton density and the degradation rate.[217] Morphological effects could also contribute, since the films outside of a device have a free upper surface which makes it easier for molecules to rearrange and aggregate.

†We also tested photostability under forward and reverse bias (Figure 6.24) to directly compare the effect of SOP-induced hole density within an identical device. In the absence of SOP-induced holes (under reverse bias), PL stability is slightly increased, but the enhancement is nearly within error.

fabrication procedure or even the specifics of the deposition tool may therefore critically impact lifetime, and could explain the disagreement with ref. [214]. In ref. [214], devices are deposited using a shutter system to grow each condition in a single run, in descending order of temperatures; we grew each temperature in a separate run in increasing order. These results indicate that while ultrastable glass layers show improved photostability, the benefit to electrical lifetime can be complicated by other factors. Future work should focus on isolating how various processing conditions impact lifetime for devices which are heated during deposition.

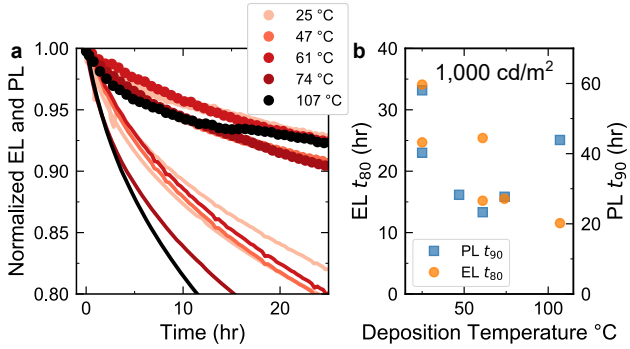

Fig. 6.11. Electrical degradation vs. deposition temperature. (**a**) Normalized EL (solid lines) and PL (circles) as a function of time and (**b**) EL t_{80} and PL t_{90} lifetimes for electrically-pumped degradation at $L_0 = 1000\,\mathrm{cd\,m^{-2}}$. Current density varied proportionally to the efficiencies reported in Figure 6.21h, in the range of $1.3\,\mathrm{mA\,cm^{-2}}$ to $1.5\,\mathrm{mA\,cm^{-2}}$. The current is turned off every 10 minutes to measure PL with a $\lambda = 405$ nm laser (~$5\,\mathrm{mW\,cm^{-2}}$).

6.6 Modeling exciton quenching

We next carried out exciton kinetic modeling to 1) better understand how measured SOP-induced charge density quantitatively relates to measured exciton quenching and 2) to estimate how exciton quenching and charge density vary spatially in these devices. We model the steady-state triplet exciton density, n_T, near device turn-on (~2.5 V), allowing for diffusion and triplet-polaron quenching with holes accumulated due to SOP. At this bias, the hole density should mostly reflect the SOP-induced population and the electrically generated exciton density is small enough to neglect exciton-exciton annihilation processes. The rate equation for n_T in these conditions is:

$$\frac{dn_T}{dt} = G + D\frac{\partial^2 n_T}{\partial x^2} - n_T\left(\frac{1}{\tau} + k_{TP}n_h\right) \tag{6.1}$$

where x is the out-of-plane spatial coordinate, D is the triplet exciton diffusivity, τ is the cavity-modified exciton lifetime,[74] k_{TP} is the triplet-polaron quenching rate constant, n_h is the SOP-induced hole density, and G is the exciton generation rate. It is commonly assumed that SOP-induced holes are concentrated within a few nanometers of the polar layer.[213,221] For simplicity, we assume n_h decays exponentially with width w from the EML/ETL interface in CBP:Ir(ppy)$_3$ devices (Figure 6.4a). The magnitude of n_h is set by the hole density measured using DCM assuming holes only accumulate within the emissive layer. n_h is then calculated with coordinates in the appropriate reference frame (based on exponential decay from either the HTL/EML interface or the EML/ETL interface) as:

$$n_h = \sigma_h \frac{e^{-x/w}}{\int_0^{d_{EML}} e^{-x/w} dx} \tag{6.2}$$

where σ_h is the measured hole sheet density (Figures 6.6 and 6.7) and d_{EML} is the EML thickness (10 nm). When simulating PL, G is calculated using the transfer matrix formalism.[154] Under electrical excitation, we assume that G (i.e. the recombination zone) has the same functional form as n_h, as the recombination probability will be highest where the hole density is large. Eq. (6.1) is then solved numerically, applying reflecting boundary conditions ($dn_T/dt = 0$) at each interface of the emissive layer. The normalized PL can then be calculated by dividing the outcoupled photon flux when holes are present (at the turn-on voltage, $V = 2.5$), by the outcoupled photon flux when no holes are accumulated in the device (at $V = -3$):

$$PL_{norm} = \frac{PL(V = 2.5)}{PL(V = -3)} = \frac{\int \eta_{OC} k_r n_T(n_h) dx}{\int \eta_{OC} k_r n_T(n_h = 0) dx} \tag{6.3}$$

where k_r is the cavity-modified radiative decay rate and η_{OC} is the outcoupling efficiency, both integrated over the PL spectrum of Ir(ppy)$_3$ and calculated using a classical dipole emission model assuming isotropic dipole orientation.[74] In calculating EQE, we assume that both charge balance and the spin fraction are unity, which is supported by the results in Figure 6.4d. In other words, every injected charge forms an exciton which can decay radiatively. EQE is then simply equal to the outcoupled photon flux divided by the exciton generation rate. This is equivalent to

the outcoupled radiative decay rate divided by the total decay rate:[41,74]

$$EQE = \frac{\int \eta_{OC} k_r n_T dx}{\int \left(G + D\frac{\partial^2 n_T}{\partial x^2}\right) dx} = \frac{\int \eta_{OC} k_r \tau^* \left(G + D\frac{\partial^2 n_T}{\partial x^2}\right) dx}{\int \left(G + D\frac{\partial^2 n_T}{\partial x^2}\right) dx} = \frac{\int \eta_{OC} \eta_{PL}^* \left(G + D\frac{\partial^2 n_T}{\partial x^2}\right) dx}{\int \left(G + D\frac{\partial^2 n_T}{\partial x^2}\right)}$$
$$= \frac{\int \eta_{OC} k_r n_T dx}{\int [k_r + k_{nr} + k_{TP} n_h] n_T dx} \tag{6.4}$$

where τ^* is the modified exciton lifetime, taking into account the Purcell factor and EPQ, and $\eta_{PL}^* = k_r \tau^*$ is the modified photoluminescence efficiency.

For the CBP:Ir(ppy)$_3$ device in Figure 6.4a, the normalized PL is ~66% and EQE = 13.4% (IQE $\approx$ 57%) near turn-on at ~2.5 V (Figure 6.4c). Minimizing the difference between these measured values and the output of Eqs. (6.3) and (6.4) allows us to identify the feasible region for the unknown parameters (D, k_{TP}, and w). Figure 6.12a-c shows contour plots of parameter combinations which give solutions within 2–6% of the measured PL and EQE values. Notably, the best-fit k_{TP} value of $5 \pm 1 \times 10^{-13}$ cm^3 s^{-1} is independent of the other two parameters and agrees well with previous reports.[38,41,146] The diffusivity and hole distribution width are dependent on one another. When the exciton diffusion length ($L_D = \sqrt{D\tau}$) is low, the model can only simultaneously match PL and EQE when the charges are distributed across at least half the emissive layer ($w > 4.5$ nm). But at higher diffusivities, a wider range of charge distributions can describe the data, and when L_D >8 nm, holes are confined within ~1 nm of the EML/ETL interface in the best solutions. Given the uncertainty in our measurements, hole distributions from 1–10 nm wide would be reasonably consistent with our data in this high-diffusivity limit (Figure 6.12c). In other words, the close agreement we see between measured EQE and quenching in PL can only be described by our model when either excitons, holes, or both species are distributed across at least 40% of the emissive layer. This result is expected, based on the mostly uniform optical generation profile (Figure 6.22).

Without direct characterization of either of these parameters, we favor a scenario between these two extremes, such as the solution shown in Figure 6.12d, where charges are moderately distributed within 2-3 nm of the EML/ETL interface ($w = 3$ nm) and excitons are modestly diffusive with $L_D = 3.9$ nm ($D = 2 \times 10^7$ nm^2 s^{-1}). This magnitude of L_D is supported by

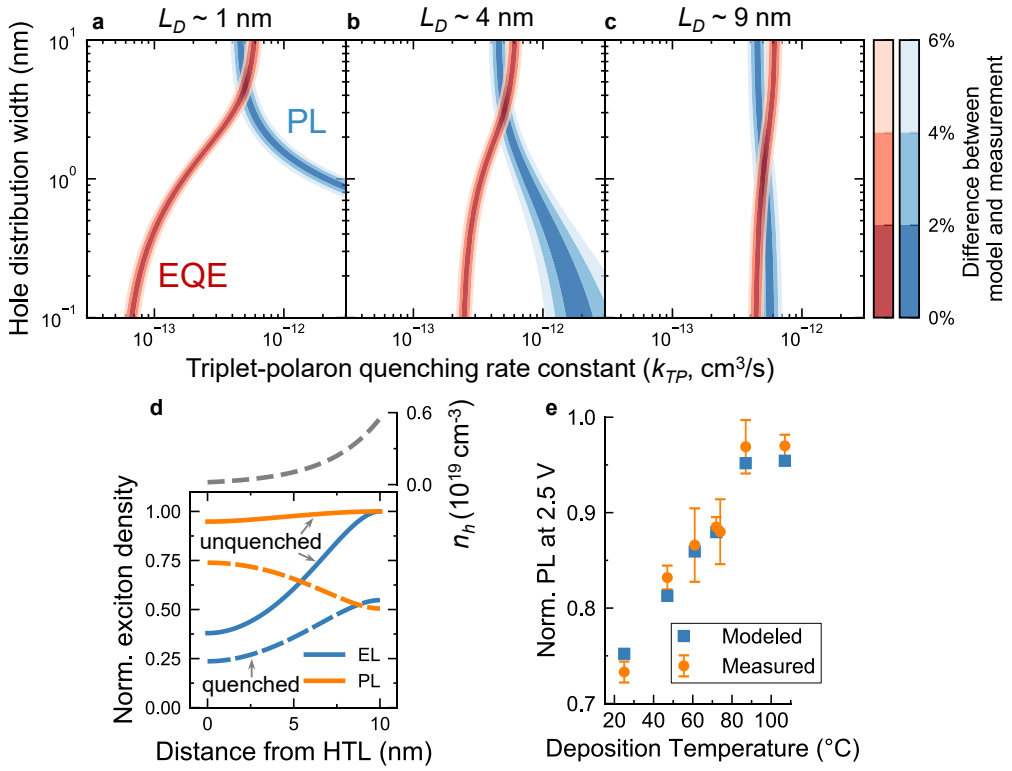

Fig. 6.12. Modeling SOP-induced exciton quenching under electrical and optical pumping. (**a**)–(**c**) Contour plots of the percent difference between modeled and measured EQE (red) and PL (blue) as a function of input parameters for the CBP:Ir(ppy)$_3$ device in Figure 6.4a. The hole distribution width (w) characterizes exponential decay ($e^{-x/w}$) from the EML/ETL interface. Diffusivities are ((**e**)–(**h**)) $D = 1.4 \times 10^6$ nm^2 s^{-1}, (**b**) $D = 2.2 \times 10^7$ nm^2 s^{-1}, and (**c**) $D = 1 \times 10^8$ nm^2 s^{-1}. (**d**) Hole (n_h, top) and exciton density (n_T, bottom) of one plausible solution for the CBP:Ir(ppy)$_3$ device in Figure 6.4a. n_T with and without hole quenching is shown in solid and dashed lines, respectively. Solution parameters: $D = 2 \times 10^7$ nm^2 s^{-1} ($L_D \approx 3.9$ nm), $k_{TP} = 5 \pm 1 \times 10^{-13}$ cm^3 s^{-1}, and $w = 3$ nm. (**e**) Modeled and measured PL at turn-on (2.5 V) as a function of deposition temperature for the TPBi:Ir(ppy)$_3$ device in Figure 6.7a. The measured charge densities in Figure 6.8 are the only model inputs which vary with temperature. Temperature independent parameters are: $D = 2 \times 10^7$ nm^2 s^{-1}, $k_{TP} = 3 \pm 1 \times 10^{-13}$ cm^3 s^{-1}, and $w = 4$ nm (exponential decay from HTL/EML interface).

measurements of Ir(ppy)$_3$ in a BCP host which yield an estimated L_D of 4-9 nm depending on intermolecular spacing.[222]* This should be investigated further, as recent simulation-based estimates of L_D in CBP:Ir(ppy)$_3$ are only 1-2 nm at these doping concentrations.[223] In practice, these values could be raised by aggregation or clustering of Ir(ppy)$_3$ molecules.[27,190,224]

*Note that very little direct characterization of dilute Ir(ppy)$_3$ diffusion has been reported. This particular report uses thin (0.5 nm) layers of neat Ir(ppy)$_3$ separated by layers of BCP with varied thickness.[222] How these numbers translate to dilute diffusion within a host is unclear.

Qualitatively, this estimated spatial extent of the charge distribution is supported by measurements of PL quenching for different EML thicknesses. When the EML thickness is increased from 10 nm to 30 nm, the low-bias PL quenching is reduced by ~3×, from ~20% to ~7% (Figure 6.13). This suggests that little or no quenching occurs in the additional 20 nm of the 30-nm-thick EML and thus SOP-induced hole accumulation is mostly localized within 10 nm of the EML/ETL interface.

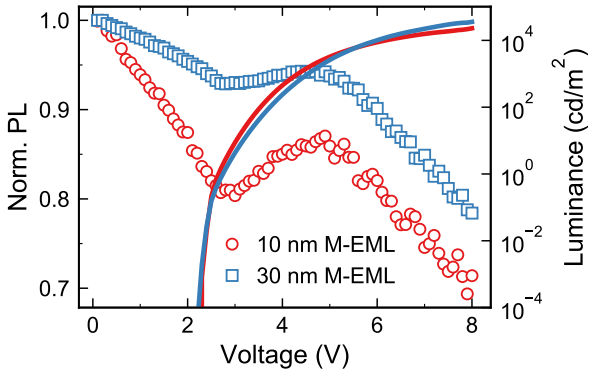

Fig. 6.13. Effect of EML thickness on PL quenching. Devices have a TCTA:TPBi:Ir(ppy)$_3$ M-EML with the same structure as in Chapter 3. PL is pumped with a $\lambda = 405$ nm laser chopped at 3 kHz.

It is also possible that the distributed charge density predicted by our model is an artifact of its simplified description of exciton-polaron quenching (EPQ). EPQ can occur either by nearest-neighbor interactions or by long-range Förster transfer,[28,50] which requires overlap between the emission spectrum of the emitter and the absorption spectrum of the cation. The typical Förster radius for phosphorescent emitters has been estimated at 2–3 nm,[50] similar to the hole distribution width extracted here. If Förster-type EPQ is active here, a narrower charge distribution could be consistent with our results. Nonetheless, a confined charge density would also result in heightened quenching under electrical excitation, which should lead to a larger discrepancy between PL and EQE than we observe.

We next modeled the temperature dependence of quenching in TPBi:Ir(ppy)$_3$ devices (Figure 6.7). Since the host is polar in this device, unlike CBP,[20] we assumed that holes would be concentrated near the hole-transport layer (HTL)/EML interface. A fraction of these holes may be accumulated within the HTL, but these are unlikely to quench excitons because 1) they are spatially separated from the EML and 2) TCTA cations show very weak absorption in the emission range of Ir(ppy)$_3$,[55] suggesting that energy transfer from Ir(ppy)$_3$ to TCTA$^+$ should be inefficient. For these reasons, we continue to assume that all holes are accumulated in the emissive layer and that they decay exponentially from the HTL/EML interface. To model the

temperature dependence, we input the measured temperature-dependent charge densities from Figure 6.8b and keep all other parameters constant. As shown in Figure 6.12e, the modeled and measured PL ratios agree within error across the full range of temperatures, indicating that the independent measure of charge density (from DCM) can fully explain the observed changes in quenching.

The best-fit k_{TP} value of $3 \pm 1 \times 10^{-13}$ cm^3 s^{-1} is ~40% lower than in CBP:Ir(ppy)$_3$ devices, which reflects the higher IQE and less severe PL quenching in the TPBi:Ir(ppy)$_3$ devices (~27% reduction in PL near turn-on compared to a ~35% reduction in CBP:Ir(ppy)$_3$). This lower degree of exciton-polaron quenching has several possible explanations: 1) a portion of the hole density is accumulated within the HTL, where holes cannot efficiently quench excitons; 2) if holes residing on TCTA can quench excitons, they would have a different characteristic k_{TP} due to their different absorption characteristics and spatial separation from the emissive layer; or 3) the host (TPBi vs. CBP) could modify the interaction between excitons and charges, changing k_{TP}. We favor the first scenario, which is supported qualitatively by the slight lag between the start of hole-injection voltage (Figure 6.7c) and the onset of PL roll-off (Figure 6.7d). In other words, holes accumulate within the device (presumably in the HTL) before exciton-polaron quenching is observed. This contrasts with the CBP:Ir(ppy)$_3$ devices in which these two processes occur in lockstep (Figure 6.6a).

6.7 Discussion

These findings underscore the importance of carefully considering hole accumulation at biases below device turn-on when quantifying exciton quenching. While several groups have shown that quenching can occur at surprisingly low current densities,[174,197,225] the assumption that no quenching occurs prior to device turn-on has been widely applied, usually because of a lack of a convenient method to characterize quenching in this regime. More importantly, many previous studies of exciton quenching did not look at reverse biases,[99,174,197] which, depending on ETL thickness and polarization (and the resulting hole-injection voltage), can be necessary to fully quantify quenching. In other words, using the PL intensity or lifetime of an unbiased OLED is not necessarily a valid reference point, when holes can be accumulated in the device even at 0 V (or at the open circuit voltage).

> [The] charge balance term is also frequently used in a much broader and nonquantitative manner, lumping together various mostly not understood or not quantified effects such as efficiency variation due to quenching of excited states by charge carriers.
>
> – Scholz et al. [46], pg. 8471
> *"Degradation Mechanisms and Reactions in Organic Light-Emitting Devices"*, 2015

As a result, deviations in efficiency from optical simulations in many studies may have been incorrectly ascribed to other mechanisms, such as the charge balance factor (electrical losses).[194] Because many conventional electron transport materials exhibit SOP (such as BPhen, BCP, Alq_3, BAlq),[201] these sub–turn-on quenching effects are likely widespread in the literature. In work from our own group, a charge balance factor of ~80% was extracted based on kinetic modeling of steady-state and transient electroluminescence measurements.[41] The devices used by Hershey and Holmes [41] are similar to those in Figure 6.4, except they contain a BPhen ETL. Here, PL near peak EQE is quenched to ~75% by holes accumulated due to SOP. It therefore seems likely that charge balance of similar state-of-the-art OLEDs is closer to unity than previously thought.

The holes responsible for quenching excitons here most likely reside on $Ir(ppy)_3$ molecules, as $Ir(ppy)_3$ has a shallower HOMO than CBP, TPBi and TCTA, leading to hole trapping. This is supported by kinetic Monte Carlo (kMC) simulations which found that holes in a CBP:$Ir(ppy)_3$ device spend >95% of the time on $Ir(ppy)_3$ molecules (41).[27] The absorption spectrum of the $Ir(ppy)_3{}^+$ cation has also been shown to overlap with $Ir(ppy)_3$ emission,[51] indicating that energy transfer, i.e. quenching, can occur from excitons to polarons in $Ir(ppy)_3$. Further, as mentioned above, quenching by TCTA cations should be inefficient.[55]

This work also provides more clarity for the mechanism of enhanced efficiency in OLEDs containing ultrastable glasses. The primary conclusion drawn by Ràfols-Ribé et al. [214] is that ultrastable glasses reduce non-radiative decay and thereby increase the effective photoluminescence efficiency ($\eta_{PL,eff}$); they speculate that the concentration of exciton traps is reduced or that the increased density of ultrastable glass suppresses thermal relaxation. While our results confirm that $\eta_{PL,eff}$ is increased due to the heated deposition (if $\eta_{PL,eff}$ is defined to capture

bimolecular quenching losses), they point to a different mechanism responsible for this enhancement: reduced exciton-polaron quenching with holes which accumulate in the device due to polarization of the ETL. Consequently, the generality of improving device performance with heated deposition is less broad than previously thought: devices containing non-polar hosts and ETLs will not show the same benefits from this method. Our results do not, however, exclude the possibility that non-polar ETLs could experience a lifetime enhancement from heated deposition, due to either reduced impurity incorporation or the intrinsic stability of ultrastable glasses.[215,216] This possibility should be examined more closely in further studies.

The mechanism for reduced SOP with increasing deposition temperatures is likely related to the fact that higher deposition temperatures tend to randomize molecular orientation, evidenced by reduced optical anisotropy.[21,226] SOP is thought to originate from preferred orientation of molecules with a permanent dipole moment (PDM),[201] leading to a net polarization of the film. It is sensible, then, that the more randomized molecular orientation at higher temperatures would reduce SOP. Supporting this view, the threshold substrate temperature for eliminating SOP of $\sim 0.9 T_g$ agrees well with the temperature at which common molecular glasses become optically isotropic.[21] We note that while optical anisotropy is not correlated with SOP (ref. [20], i.e. preferred orientation of transition dipole moments (TDMs) does not necessarily correspond to orientation of PDMs), randomization of molecular orientation eliminates both types of anisotropy.[21,226,227]

It is worth noting that similar results could be achieved by annealing devices near T_g after fabrication, as SOP has been shown to be eliminated in Alq_3 films heated at $\sim 150\,^{\circ}C$.[227] But because this approach would require a higher temperature applied for a longer time, it could cause other issues, such as: intermixing of layers, increased roughness, reduced density and charge carrier mobility, delamination, and even film fracture if thermal expansion coefficients differ sufficiently. For instance, in work discussed in Chapter 8, we observed fracture of Au and Alq_3 layers coated on TPBi films when heating above T_g.*

These findings could also be important for other light-emitting device (LED) technologies, such as quantum dot and metal halide perovskite LEDs (PeLEDs). Many record efficiency PeLEDs have used TPBi,[228] and it seems likely that the polarization of TPBi influences device performance, given that PeLED efficiency and ion migration within perovskites are sensitive

*Granted, this effect was probably due to the relatively large volume change when converting from the dense, vapor-deposited glass phase to the supercooled liquid phase. If annealing temperatures are kept below the lowest T_g in the stack, this should not be an issue.

to hole density and electric field.[229–231] Interestingly, a recent study showed that performance could be optimized by using a mixed ETL consisting of B3PyMPM and TPBi.[232] Yan et al. [232] argued that the mixture improved performance by tuning electron injection and mobility, but another contributing effect could be that the mixture balances opposing effects of SOP and outcoupling efficiency (B3PyMPM should have lower η_{OC} due to its larger index of refraction). Beyond just efficiency, these findings may also have implications for the stability of PeLEDs, as the presence of holes can destabilize metal halide perovskites.[229] As such, the increased hole density in a device containing a polar ETL could reduce device lifetime.

In summary, this work demonstrates that spontaneous orientation polarization of organic thin films strongly influences OLED performance. When a device includes a polar layer, mobile charge carriers accumulate in an adjacent layer to compensate for the bound polarization charge. These charge carriers, which are usually holes, quench excitons at biases below device turn-on and ultimately reduce peak efficiency by >15%. Notably, quenching losses of this sort can be mitigated by heating samples during deposition. We find that the reduction in exciton quenching is nearly identical to the efficiency enhancement, clarifying the mechanism for efficiency improvement in OLEDs containing ultrastable glasses. Our findings illustrate that properly measuring and accounting for SOP-induced exciton quenching is critical to fully quantifying and understanding efficiency roll-off in OLEDs. SOP should be considered during the design and selection of materials and the optimization of device fabrication processes.

6.8 Methods

6.8.1 Device fabrication

Devices with an active area of 25 mm^2 were fabricated on glass substrates pre-patterned with a 150-nm-thick anode layer of indium-tin-oxide (ITO, Xinyan). Substrates were cleaned with solvents followed by exposure to ambient UV-ozone. A hole-injection layer of AQ1250 (Sigma Aldrich) was spin-cast on the ITO anode in a N2 glovebox and annealed for 30 minutes at 150 °C. The remaining layers are deposited by vacuum thermal evaporation at a base pressure $<7 \times 10^{-7}$ Torr and a rate of 0.2 $nm\,s^{-1}$. LiF and Al layers were grown through a shadow mask to define the active area. Devices were encapsulated with epoxy and a cover glass in a N2 glovebox. Thermally evaporated organic materials were purchased from Lumtec (sublimed grade) and used as received: TCTA, CBP, $Ir(ppy)_3$, TPBi, and B3PyMPM.

For heated depositions, substrates were mounted on a solid copper sample holder with a pyrolytic graphite sheet (Panasonic) placed between the holder and the substrate to reduce thermal contact resistance. The holder was backside heated by a lamp and temperature was monitored by a freestanding reference thermocouple placed above the backside of the holder. The reference thermocouple was calibrated prior to deposition with a thermocouple mounted on a glass slide on the front surface of the sample holder. The substrate surface temperature during deposition was also confirmed with one-time use temperature indicators (McMaster-Carr) placed on a glass slide next to the substrate. The lamp was turned off immediately prior to deposition, resulting in a 1–3 °C decline in temperature over the course of the deposition; this decline is reflected in the quoted temperature error bars. The deposition tooling factor decreased at higher temperatures, possibly due to a reduction in the driving force for condensation, and was calibrated prior to fabrication of devices (Figure 6.14). To confirm tooling factor accuracy, the combined thickness of the emissive layer and electron transport layer of each device was measured with a Si substrate placed next to the device active area; all heated deposition devices reported here had a combined EML/ETL thickness of 70 ± 5 nm.

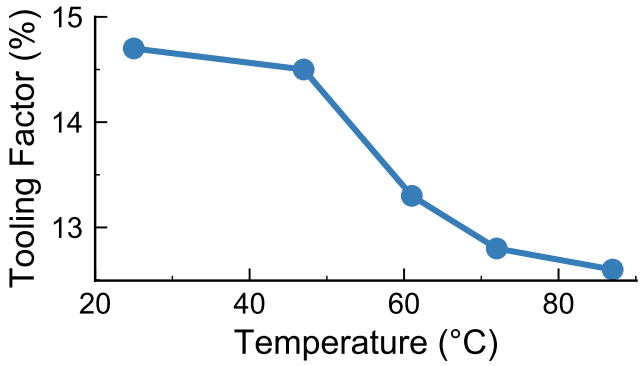

Fig. 6.14. Tooling factor of TPBi vs. deposition temperature.

Heated depositions were made sequentially with vacuum breaks between each deposition, starting at room temperature and increasing substrate temperature with each batch in order to reduce cooling time between depositions. Devices were fabricated on two days to reproduce trends: average deposition temperatures were 25, 47, 61, 72, and 87 °C on the first day and 25, 74, and 107 °C on the second day.

6.8.2 Device characterization

An Agilent 4155C parameter analyzer and a large area photodiode (Hamamatsu S3584–08) were used to measure device current and luminance as a function of bias, and Lambertian emission was assumed for luminance calculations. A Princeton Instruments FERGIE integrated spectrograph was used to collect electroluminescence (EL) spectra.

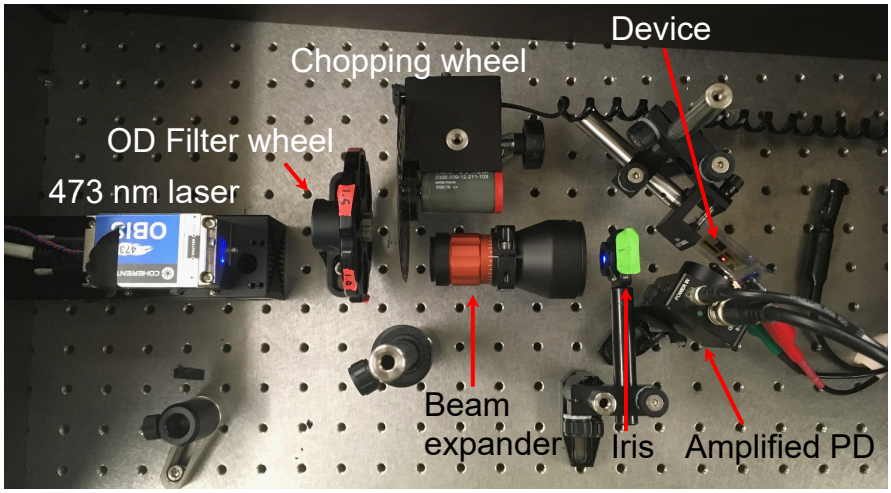

Fig. 6.15. Labeled picture of lock-in PL measurement set-up.

The bias-dependent photoluminescence measurements applied here are similar to previously reported methods.[206,207] A Keithley 2636B was used to source a constant device voltage and measure current. Sweeps were taken from -4 V to 8 V with a step size of 0.2 V, a settle time of 0.25 s, and an integration time of ~1 s per step. Sweep rate was not found to have a significant effect on the measured magnitude of PL quenching, though noise was higher for faster sweeps. Control software for these measurements is provided at github.com/jsbangsund/measurement-automation-tools. Devices were optically pumped with a 100 mW $\lambda = 405$ nm laser (Coherent OBIS 405LX), which was attenuated with a neutral density filter, chopped at 2 kHz, and expanded with a Thorlabs GBE05-A 5X achromatic Galilean beam expander to a $1/e^2$ diameter of ~4 mm. Beam expansion serves to improve signal without increasing the exciton density. Devices were masked and the beam was passed through an adjustable iris to prevent excitation outside the device area. The PL signal was passed through a 450 nm long pass filter to prevent detection of stray laser light, collected with a Thorlabs PDA36A Si adjustable gain photodetector, and measured with a Stanford Research Systems SR810 lock-in amplifier. The lock-in

amplifier serves to reject the baseline EL signal, ensuring only PL is measured. The PL signal was kept below an equivalent brightness of 50 cd m^{-2} (pump power density of ~5 mW cm^{-2}), ensuring that the probe has minimal impact on quenching. A schematic of the measurement set-up is shown in Figure 6.3 and a labeled photo of the set-up is shown in Figure 6.15.

As shown in Figure 6.16, pump fluence has no discernible effect on PL quenching at low biases, indicating that photogenerated charge density is much smaller than SOP-induced hole density. At high biases ($V > 4.5$ V), PL roll-off is slightly less severe for high pump fluences. This effect could be due to light-induced suppression of charge injection,[151,152,233,234] resulting in lower current density at a given voltage (lower current density during illumination was observed in similar devices shown in Figure 6.17).

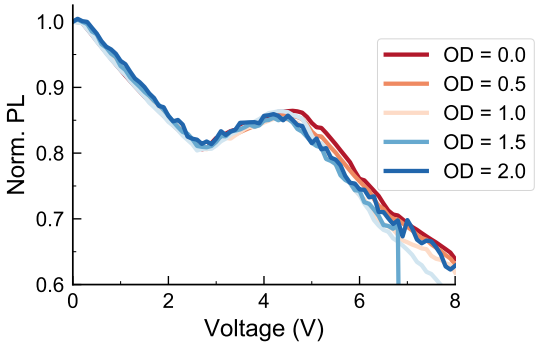

Fig. 6.16. Effect of pump fluence on the PL quenching measurement for CBP:Ir(ppy)$_3$/TPBi devices similar to those in Figure 6.4 ($d_{ETL} = 40$ nm). Fluence is indicated in the legend by the optical density (OD) of the attenuating filter, where fluence is proportional to 10^{-OD}. The pump laser wavelength is $\lambda = 405$ nm.

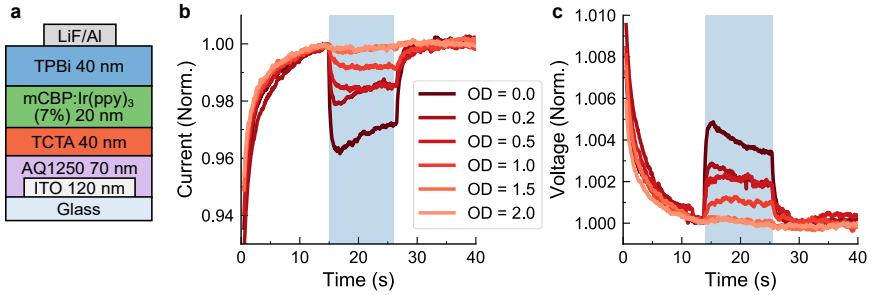

Fig. 6.17. Effect of pump fluence on current density and voltage. (**a**) Structure of mCBP:Ir(ppy)$_3$/TPBi devices. (**b**) Transient current at a constant bias of 7 V. (**c**) Transient voltage at a constant current density of 4 mA cm^{-2}. Shaded boxes indicate when the laser is on. Fluence is indicated in the legend by the optical density (OD) of the attenuating filter, where fluence is proportional to 10^{-OD}. The pump laser wavelength is $\lambda = 473$ nm.

In the devices studied in this chapter, measured PL quenching was relatively independent of chopping frequency—any frequency above ~300 Hz yielded similar results. However, the occasional device shows short-timescale photo-induced transient effects which lead to artifacts in the

PL quenching measurement. One such example is shown in Figure 6.18, for a mCP:TPBi co-host device with 4CzIPn—which exhibits TADF—as an emitter. At low chopping frequencies, PL increases dramatically at large biases, an artifact that is most likely due to photo-induced changes in charge injection. (It could also be a consequence of photoconductivity, but because the PL rises almost exponentially with bias, a reduced injection barrier seems likely). This effect is eliminated by increasing chopping frequency to ~3 kHz, indicating that the timescale of this transient effect is on the order of 100 µs. To ensure that nothing of this sort is occurring, a chopping frequency dependence should be measured on all new device architectures during initial characterization.

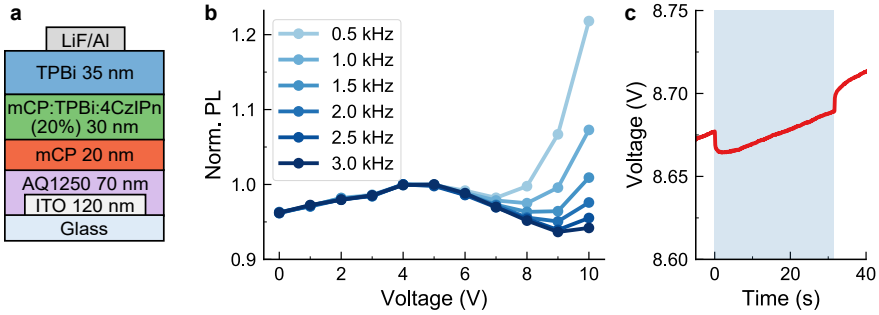

Fig. 6.18. Effect of chopping frequency on PL quenching measurement. (**a**) Structure of mCBP:Ir(ppy)$_3$/TPBi devices. (**b**) PL quenching vs. voltage for a range of chopping frequencies. (**c**) Transient voltage at a constant current density of 4 mA cm^{-2}, showing reduced driving voltage under illumination. The shaded box indicates when the laser is on.

Photoluminescence transients were detected with a Thorlabs APD430A avalanche photodiode and recorded with a Tektronix TDS5104B digital phosphor oscilloscope. Films were excited with an Optical Building Blocks pulsed nitrogen laser (λ =337 nm) with a pulse width of ~1 ns and a repetition rate of 6 Hz. Emission was focused on the photodiode with a series of lenses. Exciton lifetimes were extracted by fitting an exponential decay to the data from 2–5 µs after the laser pulse, to avoid any non-linearities due to triplet-triplet annihilation at short times.

Displacement current measurements were collected using a Pine Research WaveDriver 10 potentiostat. Displacement current was measured during triangle wave sweeps with a sweep rate of 1 V s^{-1}, a step size of 5 mV, a lower potential varying from −5 V to −3 V, and an upper potential of +3 V. Sweep cycles were repeated three times for each measurement. Raw data is smoothed using a moving average with a window of 0.1 V.

DCM data was analyzed with the methods outlined by Noguchi et al. [203]: The hole-injection voltage, V_{inj}, was extracted from DCM curves by finding the intersection between

lines fit to the lower reverse bias plateau and the accumulation region, where current begins to increase. The total hole density, σ_h, which is injected prior to the turn-on voltage, V_{th}, is calculated by integrating the DCM curve from V_{inj} to Vth:

$$\sigma_h = \int_{V_{inj}}^{V_{th}} C_{app} dV = \int_{V_{inj}}^{V_{th}} \frac{J_{DCM}}{dV/dt} dV \tag{6.5}$$

where C_{app} is the apparent capacitance of the device, J_{DCM} is the measured current density, and dV/dt is the voltage sweep rate. Measurements were taken in the quasistatic regime, which was verified by increasing sweep rate and observing no change in the sweep-rate-normalized current. As such, the conduction current below device turn-on is negligible and $J_{DCM} = C_{app} \times dV/dt$.[213]

Lifetime measurements with simultaneous EL and PL characterization was carried out using previously described methods (see Chapter 3).[91,157]

6.8.3 Optical outcoupling calculations

Light outcoupling efficiency was calculated using a classical dipole emission model.[74] Calculations were weighted evenly by five dipole emission planes spread across the emissive layer (i.e. a flat emission zone was assumed). Dipole orientation was assumed to be isotropic and input optical constants were measured using spectroscopic ellipsometry. Note that a lower outcoupling efficiency was calculated for B3PyMPM devices than TPBi devices due to the higher index of refraction of B3PyMPM ($n = 1.99$ for B3PyMPM and $n = 1.77$ for TPBi at 510 nm, the peak emission wavelength of $Ir(ppy)_3$).[235] When modeling exciton quenching, outcoupling was calculated with a finer grid and the emission zone was input based on the stated model assumptions. Changes to the radiative rate, exciton lifetime, and effective photoluminescence efficiency due to the Purcell effect were calculated using the following intrinsic emissive properties of dilute $Ir(ppy)_3$: the exciton lifetime, τ, was measured as 1.3 µs (Figure 6.9), and the photoluminescence efficiency, η_{PL}, was assumed to be 92%, both of which are consistent with reported values.[38,41,42,236] Code for these calculations is provided at github.com/jsbangsund/oledpy/. Results of the outcoupling code were validated with Setfos 5.0 (Fluxim AG) and found to differ by less than 5% (relative). Setfos simulations tended to give systematically higher outcoupling efficiencies, but the relative (normalized) outcoupling efficiencies were almost identical.

6.9 Acknowledgments and Contributions

The work presented in this chapter was originally published in:

J. S. Bangsund, J. Van Sambeek, N. M. Concannon, and R. J. Holmes. "Sub-Turn-on Exciton Quenching Due to Molecular Orientation and Polarization in Organic Light-Emitting Devices". *Science Advances* 6 (2020). DOI: 10.1126/sciadv.abb2659

Jack R. Van Sambeek and Nolan M. Concannon were co-authors. J.R.V. contributed significantly to the heated deposition experiments, and N.M.C. assisted with modeling efforts, helping to develop the exciton diffusion and quenching model, as well as performing drift-diffusion modeling and outcoupling modeling in Setfos (Fluxim AG). We acknowledge Dr. Peter Trefonas, Dr. Dominea C. K. Rathwell, Jeong-Hwan Jeon, and Hong-Yeop Na for useful discussions, as well as the lab of Prof. C. D. Frisbie for the use of their potentiostat.

Detailed contributions: J.S.B. conceived of the project, designed the experiments, built the experimental apparatuses, and carried out characterization. J.R.V. fabricated samples, performed the heated deposition experiments, and assisted with characterization and analysis. J.S.B. and N.M.C. carried out exciton quenching and optical modeling. J.S.B. and R.J.H. interpreted the results and wrote the manuscript. All authors discussed and reviewed the manuscript. R.J.H. supervised the work.

Funding and support for this work was provided by DuPont Electronics and Imaging. J.S.B. and N.M.C. were supported by the National Science Foundation Graduate Research Fellowship under grant no. 00074041. Parts of this work were carried out in the Characterization Facility, University of Minnesota, which receives partial support from the NSF through the MRSEC program.

6.10 Supplemental figures

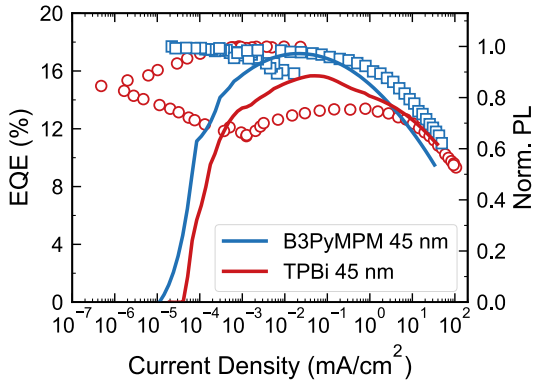

Fig. 6.19. External quantum efficiency and normalized PL for polar and non-polar ETLs. EQE shown in solid lines and PL shown in symbols.

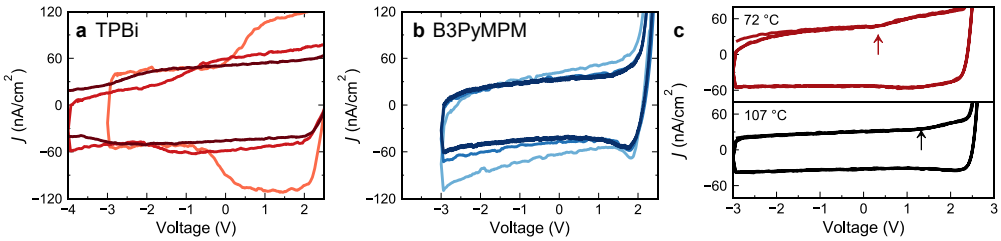

Fig. 6.20. Displacement current measurements. DCM curves for devices from Figure 6.6a with a (**a**) polar TPBi ETL and (**b**) non-polar B3PyMPM ETL as a function of ETL thickness. (**c**) DCM for devices from Figure 6.7c at deposition temperatures not included in the main text. Arrows represent the assigned hole-injection voltage, based on the change in slope of the current vs. Voltage curve. Each measurement was reproduced on at least three separate pixels. Sweep rate was 1 V s^{-1} for all curves.

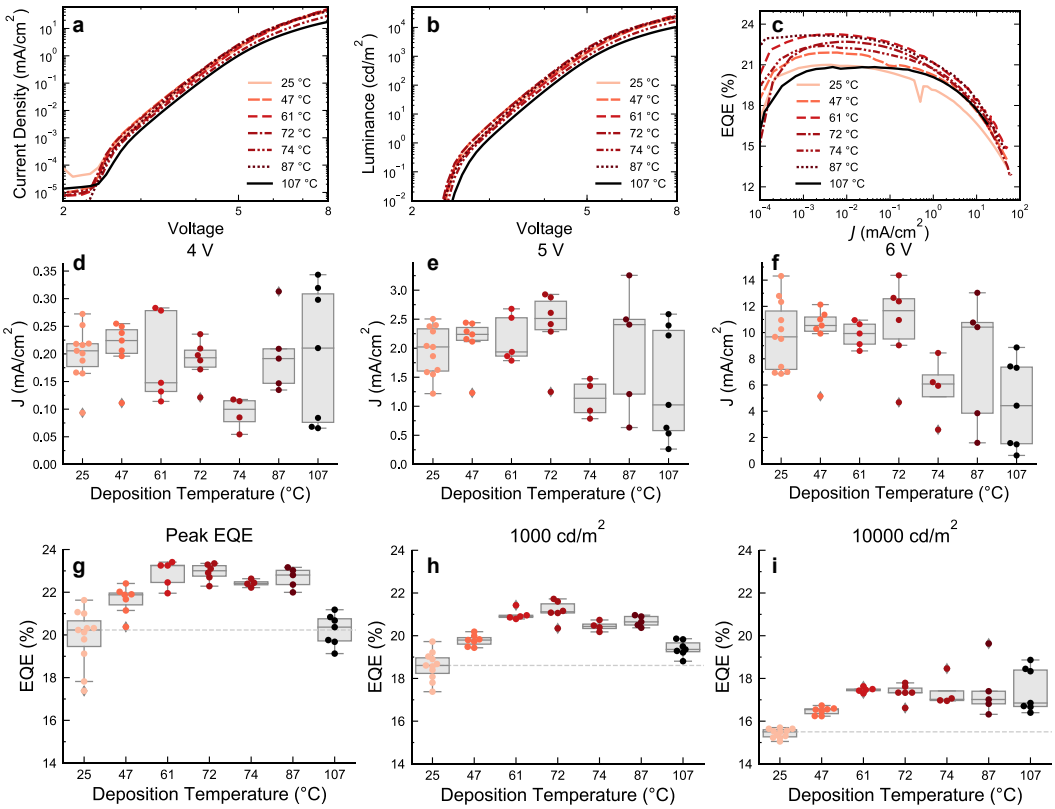

Fig. 6.21. Current density, luminance, and efficiency characteristics for heated devices. Representative (**a**) Current-density vs. voltage (J-V), (**b**) luminance vs. voltage, and (**c**) EQE vs. voltage characteristics of TPBi:Ir(ppy)$_3$ devices heated at various temperatures during deposition. Boxplots showing distributions of current density at (**d**) 4 V, (**e**) 5 V, and (**f**) 6V. Boxplots showing distributions of EQE at (**g**) peak efficiency, (**h**) 1000 cd m^{-2}, and (**i**) 10,000 cd m^{-2}. These distributions illustrate that J-V behavior is not significantly influenced by deposition temperature, while the EQE shows a clear increase and saturation at higher deposition temperatures. The slightly lower efficiency and current density for devices fabricated at 74 °C and 107 °C is due to the larger ETL thickness in these devices (see Table 6.1). Note: EQE values in this figure are not corrected for outcoupling variations due to these differences in ETL thickness, but in the main text EQE are corrected by the factors in Table 6.1.

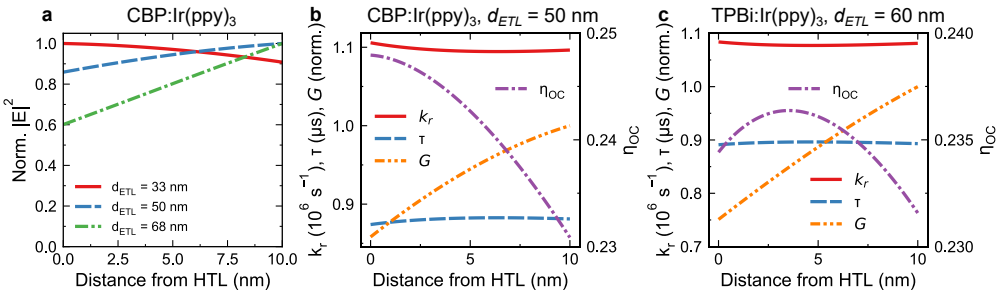

Fig. 6.22. Simulated spatial profiles for optical excitation and outcoupling. (**a**) Optical field profiles for the $\lambda = 405\,\text{nm}$ pump laser at 45° for the devices in Figure 6.4 for the studied ETL thicknesses. Spatial dependence of radiative rate (k_r), exciton lifetime (τ), exciton generation rate (G), and outcoupling efficiency (η_{OC}) for the devices in (**b**) Figure 6.4 and (**c**) Figure 6.7. These parameters are calculated using an optical transfer matrix formalism and a classical dipole emission model.

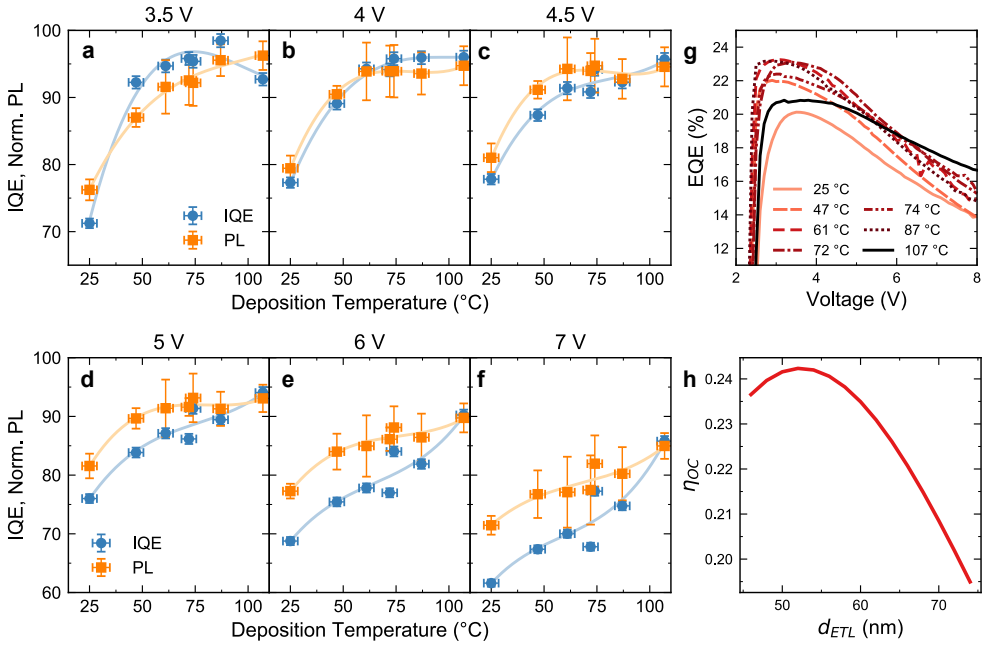

Fig. 6.23. Internal quantum efficiency (IQE) and photoluminescence quenching as a function of deposition temperature. The IQE and normalized PL are extracted at the following voltages: (**a**) 3.5 V, (**b**) 4 V, (**c**) 4.5 V, (**d**) 5 V, (**e**) 6 V, and (**f**) 7 V. Error bars are 95% confidence intervals of the mean weighted by Student's t factor based on measurements of three to six separate pixels. IQE and normalized PL agree well between 3.5 V and 5 V, indicating that in this region IQE loss is dominated by exciton quenching. Above 5 V, IQE and PL show increasing disagreement, particularly at low deposition temperatures, possibly indicating that charge balance losses begin to contribute to efficiency roll-off at high voltages. This disagreement could also result from a recombination zone which becomes narrower at high voltages, increasing error in the PL measurement. (**g**) EQE vs. voltage characteristics for various deposition temperatures. (**h**) Simulated out-coupling efficiency, η_{OC}, as a function of ETL thickness for TPBi:Ir(ppy)$_3$ devices.

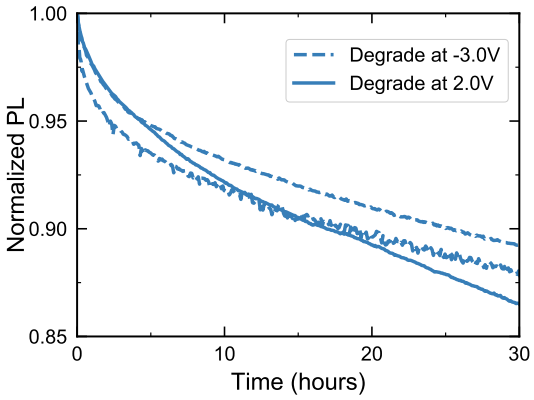

Fig. 6.24. Photostability under forward (hole-accumulated) and reverse (hole-depleted) bias conditions. Devices have the structure in Figure 6.4a with a 68-nm-thick TPBi ETL and are illuminated with a $\lambda = 405\,\text{nm}$ laser with a power density of $50\,\text{mW}\,\text{cm}^{-2}$. PL stability is modestly increased under reverse bias, suggesting that SOP-induced hole accumulation may slightly accelerate degradation but is not a major degradation pathway.

Table 6.1. Measured ETL thickness and simulated outcoupling efficiency for heated deposition devices. Batch-to-batch variations in ETL thickness lead to slight differences in outcoupling efficiency for each batch. The table shows the measured ETL thickness and simulated outcoupling efficiency for each device. The combined emissive layer and ETL thickness were measured with spectroscopic ellipsometry, and the ETL thickness was calculated based on the nominal deposited thickness of each layer. The outcoupling efficiency here was used to calculate the IQE values in Figure 6.23. The EQE values in Figure 6.7b and Figure 6.8a are multiplied by the correction factor, calculated as $\eta_{OC}(d_{ETL} = 60\,\text{nm})/\eta_{OC}(d_{ETL} = X\text{nm})$ to account for differences in ETL thickness.

Temperature °C	d_{ETL} nm	η_{OC} %	EQE Correction Factor
25	58.7±1.0	23.7	0.99
25 (batch 2)	53.7±1.0	24.2	0.97
47	61.6±1.0	23.2	1.01
61	60.2±1.0	23.5	1.00
72	56.9±1.0	23.9	0.98
74	65.1±1.0	22.3	1.05
87	63.0±1.0	22.8	1.03
107	70.3±1.0	20.8	1.13

7

Changes in Bimolecular Quenching with Degradation

Efficiency roll-off and intrinsic luminance degradation are two of the primary limitations of organic light-emitting devices (OLEDs). While both phenomena have been studied separately in detail, they are rarely considered together. Previous analyses of OLED degradation have largely neglected changes in efficiency roll-off and bimolecular quenching, and the magnitude of these changes and their impact on device lifetime remains unclear. We present experimental and modeling results to quantify the magnitude of these changes, which we find range from ~2% to above 10% in magnitude and increase in importance at high brightness or in devices with significant exciton-exciton annihilation.

7.1 Introduction

The performance of OLEDs in high brightness applications such as lighting[196,238] is still limited by the processes of reversible efficiency roll-off[75] and irreversible luminance loss due to intrinsic degradation.[46] Both of these phenomena are primarily caused by bimolecular reactions such as exciton-exciton annihilation and exciton-polaron quenching,[38,41,97,112] yet the interplay between roll-off and degradation has rarely been considered. In general, changes in bimolecular quenching (BQ) have been neglected in proposed OLED degradation models,[97,126] and no direct experimental work has been reported to justify this assumption. How large these changes may be, or even their sign, remains unclear. For instance, it has been argued that triplet exciton-polaron quenching increases over time due to accumulated trapped charges,[119] whereas we have previously argued that BQ should become less significant over time due to reduced exciton density and exciton lifetime (see Chapter 3).[91,157]

Understanding and quantifying degradation-induced changes in BQ could be valuable for

several reasons. For OLEDs operated at high brightness, the magnitude of BQ is often initially significant, and hence alleviation of these bimolecular reactions during degradation could serve to improve the device lifetime. Additionally, the slope extracted from accelerated aging at high brightness may be sensitive to the evolution of BQ during degradation. More fundamentally, measurements of changes in BQ could provide insight into the properties of quenching defects and help to validate degradation modeling.

We first provide a theoretical treatment of the degradation dependence of BQ, applying an exciton and polaron dynamics model to estimate how the severity of bimolecular quenching should change in degraded OLEDs. Bimolecular quenching is then probed during degradation using lock-in amplifier measurements of photoluminescence as a function of bias. We find that the magnitude of BQ is generally reduced with degradation due to the proportional losses in exciton density and exciton lifetime with decreasing luminance.

The total measured changes in BQ are typically <5% in magnitude over the course of a typical lifetime test, but they become increasingly important in devices operated at high brightness or devices with significant exciton-exciton annihilation. This study improves understanding of how bimolecular quenching changes in degraded devices and demonstrates that changes in BQ and efficiency roll-off should not be neglected in a complete analysis of OLED degradation.

7.2 Estimating degradation-induced changes in η_τ

To estimate changes in η_τ, we apply a spatially averaged exciton and polaron kinetics model, described previously.[41] While exciton and polaron densities will generally vary spatially, this simple treatment provides a reasonable approximation of how quenching scales with the magnitude of these populations. We treat the case of a phosphorescent emitter and we assume that the dominant excitonic decay processes are 1) natural decay (i.e. the radiative and non-radiative decay of the emitter in the device, defined by lifetime $\tau = 1/(k_r + k_{nr})$, 2) triplet-triplet annihilation (TTA), and 3) triplet-polaron quenching (TPQ). Considering these competing processes, η_τ can be expressed as:

$$\eta_\tau = \frac{n_T/\tau}{n_T/\tau + \frac{1}{2}k_{TT}n_T^2 + k_{TP}n_T n_P} = \frac{1/\tau}{1/\tau + \frac{1}{2}k_{TT}n_T + k_{TP}n_P} \tag{7.1}$$

where n_T is the triplet exciton density, n_P is the polaron density (averaging the behavior of electrons and holes), k_{TT} is the TTA rate constant, and k_{TP} is the TPQ rate constant. Both n_T and n_P will vary with current density (J), whereas τ, k_{TT}, and k_{TP} are assumed to be independent of J. To estimate the impact of degradation on η_τ, we assume that n_P, k_{TT}, and k_{TP} are constant with time. This estimate likely represents an upper bound to the change in η_τ, as charge density typically rises during degradation.[119] Assuming that the radiative rate and η_{OC} are constant, the triplet density will vary proportionally with the normalized electroluminescence intensity (EL):

$$n_T(t) = n_T(0) \times EL(t)/EL(0) \tag{7.2}$$

The exciton lifetime will vary with time proportionally to the normalized photoluminescence efficiency, (i.e. changes in η_{PL} reflect an increase in the non-radiative decay rate, k_{nr}, and hence decreased τ, as $\eta_{PL} = k_r\tau = k_r/(k_r + k_{nr})$:

$$\tau(t) = \tau(0) \times \eta_{PL}(t)/\eta_{PL}(0) \tag{7.3}$$

Combining Eqs. (7.1) to (7.3), η_τ can be estimated as a function of EL degradation. For this analysis, we consider changes in η_τ for the archetypical phosphorescent emitter Ir(ppy)$_3$ in a CBP host, taking the measured constants and model from ref. [41]: $k_{TT} = 7.1 \times 10^{-12}\,\mathrm{cm^3\,s^{-1}}$, $k_{TP} = 0.3 \times 10^{-13}\,\mathrm{cm^3\,s^{-1}}$, $k_F = 1.6 \times 10^{-11}\,\mathrm{cm^3\,s^{-1}}$, $\tau = 0.61\,\mu\mathrm{s}$, and a recombination zone width of $w = 10\,\mathrm{nm}$. The calculated current density dependence of η_τ, n_T, and n_P for an undegraded device are shown in Figure 7.1(a). For this device, TTA becomes the dominant exciton decay pathway at high current densities.

In Figure 7.1(b), the change in η_τ as a function of EL degradation is shown for hypothetical degradation pathways with different degrees of PL degradation (where reductions in η_{PL} result in increased non-radiative decay and a reduced exciton lifetime, see Eq. (7.3)). The rise in η_τ is largest when PL degradation is the dominant degradation pathway, almost twice as large as the case where the PL efficiency is constant ($PL/PL_0 = 1$). Physically, these scenarios respectively likely represent degradation dominated by the introduction of exciton quenchers which decrease η_{PL} and degradation *via* the formation of non-radiative charge carrier recombination centers which reduce η_{EF}.[97] When PL degradation is dominant, the exciton lifetime is significantly decreased, thus funneling the majority of excitons to natural decay and reducing the magnitude of TTA and TPQ. In practice, most devices show evidence of both degradation

pathways,[116] and hence the case where PL loss comprises roughly half of the total degradation ($PL/PL_0 = \sqrt{EL/EL_0}$) provides the best estimate in the absence of direct measurements of PL degradation.[91]

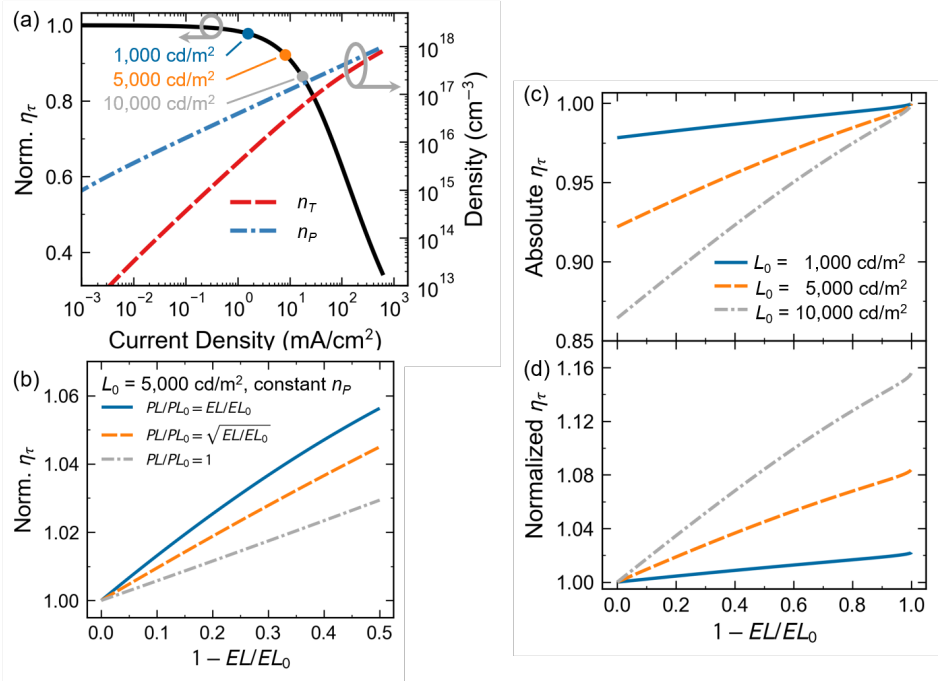

Fig. 7.1. (**a**) Calculated current density dependence of the natural decay efficiency (η_τ), the triplet exciton density (n_T), and the polaron density (n_P) for an undegraded CBP:Ir(ppy)$_3$ device. (**b**) Estimated change in η_τ as a function of the degree of EL degradation ($1 - EL/EL_0$). Comparison curves show how the severity of PL degradation impacts η_τ. The rise in η_τ is largest when PL degradation is the dominant degradation pathway ($PL/PL_0 = EL/EL_0$), as the natural lifetime is significantly shortened in this case. These calculations are carried out for a device operated at an initial luminance of $L_0 = 5000\,\mathrm{cd\,m^{-2}}$, and polaron density, n_P, is assumed to be constant with degradation. (**c**) Absolute and (**d**) normalized change in η_τ as a function of degradation for $L_0 = 1000\,\mathrm{cd\,m^{-2}}$, $5000\,\mathrm{cd\,m^{-2}}$, and $10{,}000\,\mathrm{cd\,m^{-2}}$. The rise in η_τ is larger at higher initial luminances, as the initial degree of roll-off is greater. For this calculation, PL degradation is assumed to contribute to half of the total EL degradation ($PL/PL_0 = \sqrt{EL/EL_0}$), and n_P is again constant.

In Figure 7.1(c)-(d), the degradation-dependent rise in η_τ is shown for several initial luminances, again assuming constant polaron density and that PL loss contributes to about half of the degradation ($PL/PL_0 = \sqrt{EL/EL_0}$). Due to the increasing severity of TTA and TPQ, the rise in η_τ increases in magnitude at higher initial luminance, reaching 10% by $EL/EL_0 = 50\%$ for $L_0 = 10{,}000\,\mathrm{cd\,m^{-2}}$. η_τ approaches unity in the limit of complete degradation and the relative rise in η_τ increases at higher luminances due to the lower initial value of η_τ (more severe initial roll-off).

7.3 Influence of dominant bimolecular annihilation mechanism

We next consider how the exciton quenching kinetics influence the degradation-dependent behavior of η_τ. In Figure 7.2, we compare two hypothetical devices which have efficiency roll-off dominated by TTA and TPQ, respectively. The TTA dominated device is modeled with the same kinetic parameters as in Figure 7.1, and the TPQ dominated device is modeled with $k_{TT} = 3.1 \times 10^{-13}\,\mathrm{cm^3\,s^{-1}}$ and $k_{TP} = 2.0 \times 10^{-12}\,\mathrm{cm^3\,s^{-1}}$ (all other constants are identical). The current-density-dependent roll-off in η_τ, shown in Figure 7.2(a), display the typical functional dependences for each mechanism. For the sake of comparison, we calculate η_τ as a function of degradation for the operating condition at which the roll-off is equivalent for the two devices ($J = 47\,\mathrm{mA\,cm^{-2}}$), shown in Figure 7.2(b). In the limit of complete degradation, the η_τ of both devices converges to unity ($\eta_\tau/\eta_{\tau,0} = 1.34$), but at moderate degradation ($1 - EL/EL_0 < 0.5$) the TTA dominated device shows over twice the rise in η_τ as the TPQ dominated device.

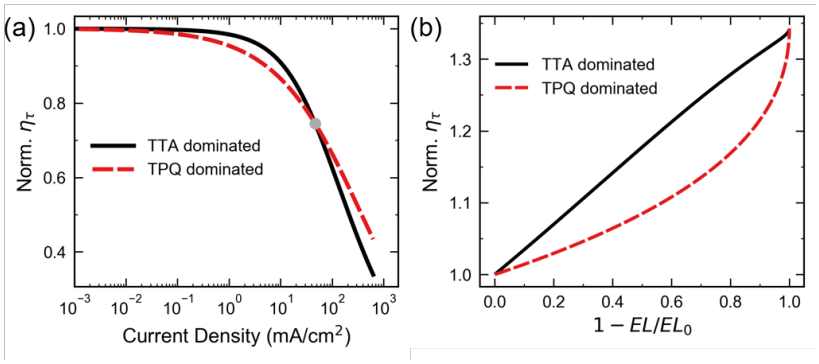

Fig. 7.2. Calculated influence of dominant bimolecular quenching mechanism on degradation-induced changes in η_τ. (**a**) Current density dependence of η_τ for a hypothetical TTA dominated device ($k_{TT} = 7.1 \times 10^{-12}\,\mathrm{cm^3\,s^{-1}}$ and $k_{TP} = 3.3 \times 10^{-13}\,\mathrm{cm^3\,s^{-1}}$) and a hypothetical TPQ dominated device ($k_{TT} = 3.1 \times 10^{-13}\,\mathrm{cm^3\,s^{-1}}$ and $k_{TP} = 2.0 \times 10^{-12}\,\mathrm{cm^3\,s^{-1}}$). The circle at $47\,\mathrm{mA\,cm^{-2}}$ denotes the operating condition at which total roll-off is equal for the two devices. (**b**) η_τ as a function of EL degradation for the TTA and TPQ dominated devices at the matched operating condition ($J = 47\,\mathrm{mA\,cm^{-2}}$). PL degradation is again assumed to contribute to half of the total EL degradation ($PL/PL_0 = \sqrt{EL/EL_0}$), and n_P is constant. For both calculations, the initial triplet exciton density is $n_T(0) = 1.3 \times 10^{17}\,\mathrm{cm^{-3}}$ and $n_P = 2.7 \times 10^{17}\,\mathrm{cm^{-3}}$.

These results indicate that changes in η_τ should effectively serve to improve device stability at high luminance. Further, the active bimolecular quenching mechanism may impact the operational lifetime via the degradation behavior of η_τ.

7.4 Measuring degradation-induced changes in η_τ

The OLEDs of interest are based on the archetypical phosphorescent emitter $Ir(ppy)_3$ doped in a CBP host. The device architecture, shown in Figure 7.3(b), includes a TCTA hole transport layer (HTL) and a TPBi electron transport layer (ETL). While these transport layers differ from those employed previously,[41] the EQE roll-off shown in Figure 7.3(c) is almost identical to the previous report. Above $J = 1\,\mathrm{mA\,cm^{-2}}$, the lock-in measurement of PL shows a similar degree of roll-off as the EQE, confirming that EQE roll-off is dominated by bimolecular quenching and hence reductions in η_τ. The slight discrepancy between lock-in PL and EQE roll-off likely reflects the current-density dependence of charge leakage and exciton formation efficiency. It is also possible the recombination zone (i.e. the spatial profile of electrically generated excitons) differs from the optically generated exciton profile, causing the measurement to slightly underestimate the total degree of exciton quenching. We minimize this spatial mismatch effect by employing thin emissive layers (10–20 nm).[157]

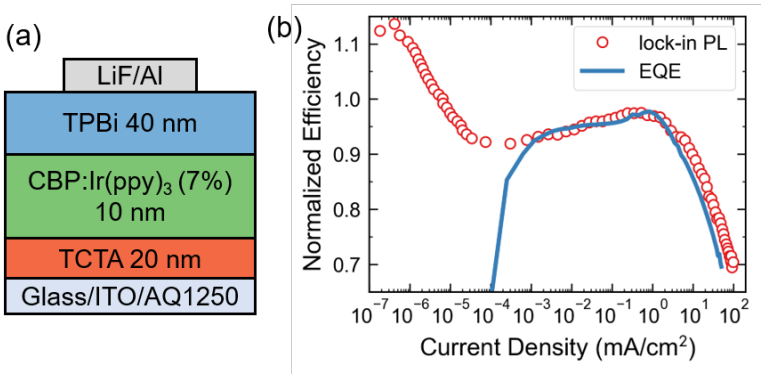

Fig. 7.3. (**a**) Device architecture for the archetypical CBP:$Ir(ppy)_3$ device studied here. (**b**) Comparison of lock-in PL measurement (symbol) as a function of applied current density with EQE (blue solid line). At current densities above $J = 1\,\mathrm{mA\,cm^{-2}}$, the roll-off in lock-in PL is almost identical to the roll-off in EQE, confirming that reductions in η_τ dominate the EQE roll-off. The ~20% drop in lock-in PL at low current densities is attributed to TPQ with injected holes prior to turn-on.

Below turn-on (<2.5 V, $J < 10^{-5}\,\mathrm{mA\,cm^{-2}}$), a drop in PL of ~20% is observed. This low current PL quenching is discussed in detail in Chapter 6. It is not a measurement artifact, as it is observed across a range of laser fluences, chopping frequencies, pump wavelengths. We have also observed this effect to varying extents in other device architectures and materials systems. This result is somewhat surprising, as conventionally quenching is thought to be significant only at current densities above $\sim 1\,\mathrm{mA\,cm^{-2}}$.[75] Yet, a previous report showed a ~5% decline in

PL lifetime below 1 mA cm^{-2},[197] and recent modeling work on a CBP:Ir(ppy)$_3$-based device suggested that TPQ was the dominant deactivation pathway at low biases.[209]

Based on these previous reports, and the evidence presented in Chapter 6, the low current drop in PL arises from TPQ with holes which accumulate prior to turn-on, while the subsequent rise in PL between 3 V and 4.5 V likely reflects the reduction of hole density above turn-on due to recombination with injected electrons.[209] This behavior cannot be described by the simplified polaron dynamics in the spatially averaged model considered in Section 7.2. The apparent polaron density needed to describe this behavior is shown in Figure 7.4, showing significant accumulation at much lower biases than predicted by the simplified model. This full dependence could be more rigorously treated with a drift-diffusion formalism, and the large n_P at low biases is due to spontaneous orientation polarization of TPBi (as discussed in Chapter 6).[119,203] However, describing the full bias-dependence is beyond the scope of this work. We are instead interested in understanding the degradation-dependent behavior of η_τ at a fixed current density—as is relevant to a typical lifetime test.

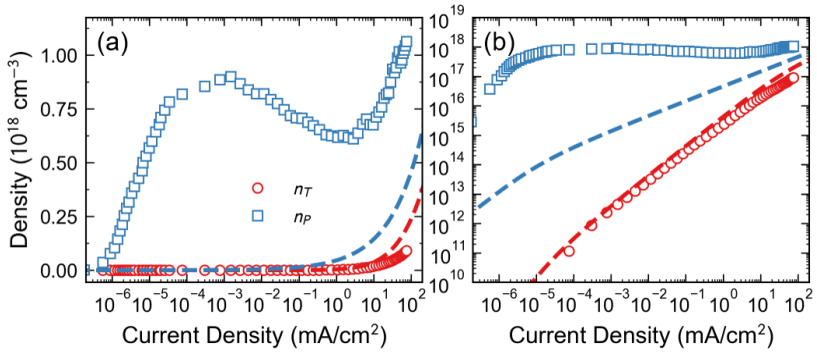

Fig. 7.4. Apparent densities of triplet excitons (n_T) and polarons (n_P) as a function of current density for the CBP:Ir(ppy)$_3$ device. Data in (**a**) and (**b**) are identical but plotted on linear-logarithmic and logarithmic-logarithmic scales for clarity. n_T is extracted from luminance measurements by assuming a recombination zone width of $w = 10$ nm, outcoupling efficiency of $\eta_{OC} = 0.21$, and exciton lifetime of $\tau = 0.69$ µs. n_P is extracted from the lock-in PL data from Figure 7.3 using Eq. (7.1) and fixed quenching parameters: $k_{TT} = 8.5 \times 10^{-12}$ cm^3 s^{-1}, and $k_{TP} = 4 \times 10^{-13}$ cm^3 s^{-1} (similar to those found in ref. [41]). Dashed lines are calculated using the spatially averaged dynamics model.[41] The slight deviation between extracted and calculated n_T likely reflects current-dependent charge leakage and/or SOP-induced TPQ. The large deviation between extracted and calculated n_P is due to simplicity of the polaron dynamics model, which does not account for injection barriers or field-dependent mobility.

Figure 7.5 shows the degradation dependence of PL and η_τ for devices operated at $L_0 =$ 5000 cd m^{-2} and 10,000 cd m^{-2}. PL measurements are taken intermittently during the lifetime test with and without an applied current. As shown in Figure 7.5(b), PL measured with an applied J decays more slowly than PL with $J = 0$. This slower decay corresponds to a reduction

in bimolecular quenching and a rise in η_τ, as shown in Figure 7.5(c). Similar to the trends predicted in Figure 7.1(c), the rise in η_τ increases at higher luminances, ranging from 7.3% at $EL/EL_0 = 50\%$ for $L_0 = 5000\,\mathrm{cd\,m^{-2}}$ to 11.2% by $EL/EL_0 = 50\%$ for $L_0 = 10{,}000\,\mathrm{cd\,m^{-2}}$. These increases in η_τ are significant and further indicate that changes in η_τ should not be neglected in a quantitative analysis of OLED degradation at high operating luminances.

Shown in Figure 7.5(c) as dashed lines are fits based on Eqs. (7.1) to (7.3), where polaron density is assumed to be constant with degradation, exciton density is calculated as described in the caption of Figure 7.4, the exciton lifetime is fixed at $\tau = 0.69\,\mu\mathrm{s}$, and k_{TP} is fixed at $4 \times 10^{-13}\,\mathrm{cm^3\,s^{-1}}$. k_{TT} is varied to simultaneously fit the two lifetime tests and n_P is allowed to vary between tests, resulting in the extracted parameters $k_{TT} = 8.5 \times 10^{-12}\,\mathrm{cm^3\,s^{-1}}$ and $n_P = 4.8 \times 10^{17}\,\mathrm{cm^{-3}}$ for $L_0 = 5000\,\mathrm{cd\,m^{-2}}$ and $n_P = 4.4 \times 10^{17}\,\mathrm{cm^{-3}}$ for $L_0 = 10{,}000\,\mathrm{cd\,m^{-2}}$. These parameters agree well with previous reports for similar devices,[38,41] and while the extracted polaron densities are larger than calculated by these previous models, they are in line with expectations from drift-diffusion calculations.[209] The divergence between the fit and the data at high degradation ($EL/EL_0 < 50\%$) could indicate that the constant polaron density approximation is no longer valid, as accumulated trapped charges may contribute to TPQ and offset the expected rises in η_τ.

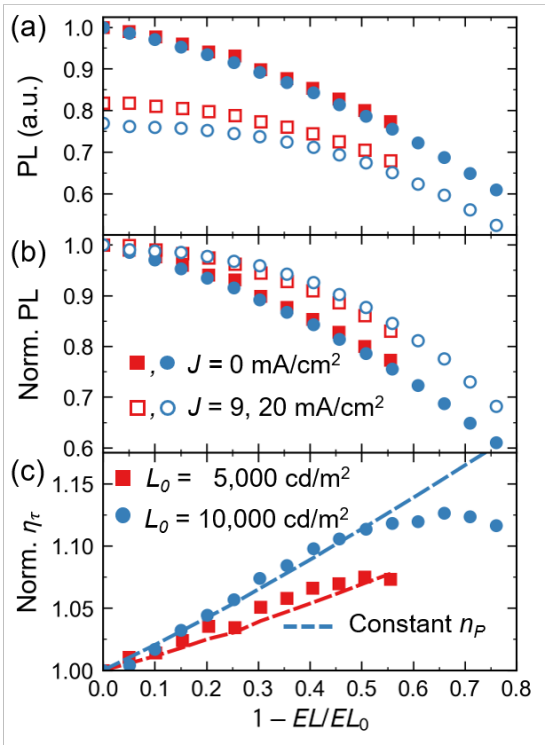

Fig. 7.5. (**a**) Absolute PL decays for a CBP:Ir(ppy)$_3$ device operated at $L_0 = 5000\,\mathrm{cd\,m^{-2}}$ and $10{,}000\,\mathrm{cd\,m^{-2}}$. Solid symbols are PL measured with the current off ($J = 0\,\mathrm{mA\,cm^{-2}}$) and open symbols are PL measured with the current on ($J = 9$ and $20\,\mathrm{mA\,cm^{-2}}$). The lower PL with the current on reflects bimolecular quenching. For undegraded devices, $\eta_\tau = 0.82$ at $5000\,\mathrm{cd\,m^{-2}}$ and $\eta_\tau = 0.77$ at $10{,}000\,\mathrm{cd\,m^{-2}}$. (**b**) Normalized PL decays from (a). PL with the current on decays more slowly than PL with the current off, indicating a reduction in bimolecular quenching (i.e. a rise in η_τ). (**c**) Normalized η_τ measured from lock-in PL ($\eta_\tau = PL(J_{op},t)/PL(J_{norm} = 0,t)$). Lines are fits based on Eqs. (7.1) to (7.3) and an assumption of constant polaron density.

This agreement suggests that the assumption of constant n_P provides a reasonable approximation to changes in η_τ. Alternative explanations invoking a non-constant polaron density cannot be entirely ruled out, however. The accuracy of predictions made with the constant n_P assumption is inherently limited by knowledge of the inputs of polaron density and kinetic parameters. If the input k_{TT} and k_{TP} are inaccurate, the degradation data could only be explained by non-negligible changes in polaron density.

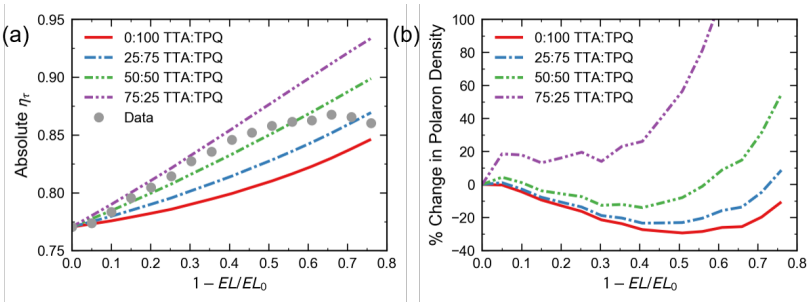

Fig. 7.6. (**a**) η_τ as a function of EL degradation measured from lock-in PL ($\eta_\tau = PL(J_{op}, t)/PL(J_{norm} = 0, t)$) for an initial luminance of 10,000 cd m^{-2}. Lines are estimates based on Eq. (7.1) and an assumption of constant polaron density. The relative contributions of TTA and TPQ to the overall quenching are varied from 0:100 TTA:TPQ (only TPQ) to 75:25 (predominantly TTA). The k_{TT} used in these calculations is 0 cm^3 s^{-1}, 3.25×10^{-12} cm^3 s^{-1}, 7.15×10^{-12} cm^3 s^{-1}, and 11.5×10^{-12} cm^3 s^{-1} for 0:100, 25:75, 50:50, and 75:25 TTA:TPQ, respectively. The product $k_{TP}n_P$ is varied in each case to match the initial value of $\eta_\tau = 0.77$. (**b**) Percent change in polaron density as a function of EL degradation which would be needed to describe the measured η_τ from (a) for different initial contributions of TTA and TPQ.

To illustrate this, we calculated the expected rise in η_τ for devices with quenching dominated by TTA, dominated by TPQ, or by some combination of the two (Figure 7.6(a)). The device with equal contributions of TTA and TPQ shows the best agreement with the data. The device dominated by TTA exceeds the data, indicating that polaron density would need to rise during degradation and TPQ would need to increase in magnitude to describe the data. However, the case of dominant TTA is unlikely, as the quenching below 3 V can only be explained by polaron quenching or field quenching. It is instead more likely that TTA and TPQ contribute comparably to overall quenching, or that TPQ is dominant.[197] For devices with more dominant TPQ, the constant n_P assumption underestimates the rise in η_τ, implying that polaron density would need to decline to match the measured rise. While defect quenching models predict that the free polaron density will decline during degradation,[97,126] the total charge density generally rises due to the accumulation of trapped charge.[116,119] Whether these trapped charges can quench excitons has not been directly demonstrated, but it seems unlikely that the reductions

in free polaron density would be sufficient to explain this discrepancy. The change in polaron density needed to match the data for each of these scenarios is shown in Figure 7.6(b). For the case of equal contributions of TTA and TPQ, polaron density stays roughly constant until $EL/EL_0 = 50\%$. At higher levels of degradation, polaron density then begins to rise. Regardless of the TTA:TPQ ratio, a rise in polaron density is always needed to describe the data at high degradation. This most likely occurs due to either a reduction in emissive layer mobility[119] or due to trapped charges.[116]

7.5 Full Bias and Degradation Dependence of EQE and PL

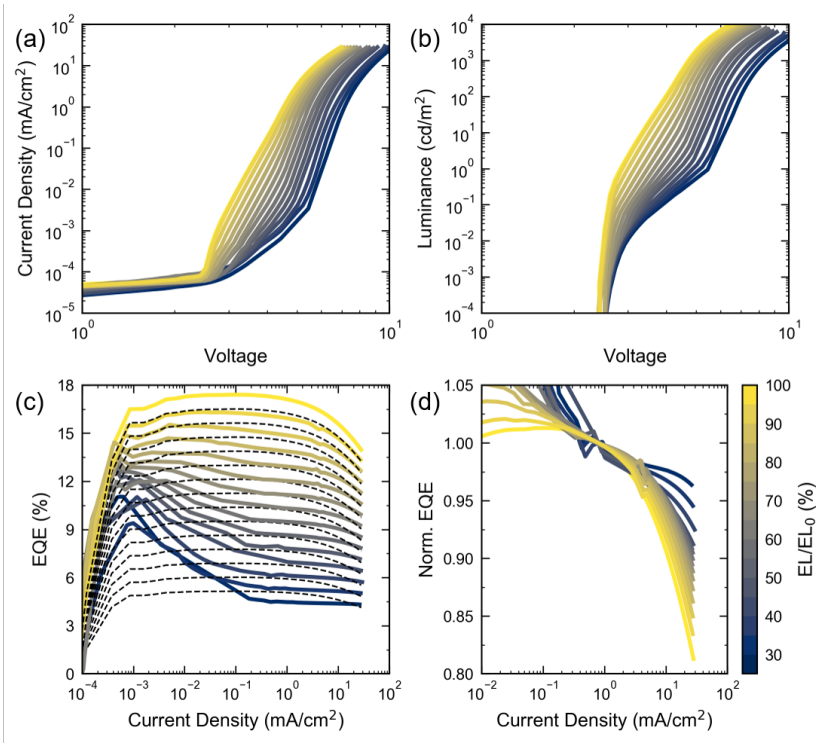

Fig. 7.7. Sweep characteristics at various levels of EL degradation for a CBP:Ir(ppy)$_3$ device operated at $L_0 = 10{,}000\,\mathrm{cd\,m^{-2}}$ ($J = 20\,\mathrm{mA\,cm^{-2}}$): (**a**) Current density vs. voltage, (**b**) Luminance vs. voltage, (**c**) EQE vs. current density, and (**d**) normalized EQE vs. current density. The dashed lines in (**c**) are the undegraded EQE curve multiplied by the degradation percent, representing the expected EQE if degradation occurred uniformly across current density. Deviation between the measured data and the dashed lines originates primarily from changes in $\eta_\tau(J)$ and $\eta_{EF}(J)$.

Next, we study how the full bias dependence of roll-off in EQE and lock-in PL evolve during degradation. The current-voltage-luminance characteristics and EQE taken intermittently

during a lifetime test are shown in Figure 7.7. In degraded devices, the current-voltage characteristics show a trap-filling regime, with the turn-on voltage shifting from ~2.5 V to >3 V.[125] Interestingly, the luminance-voltage shows a less pronounced increase in turn-on voltage, corresponding to a relative enhancement in the EQE below $\sim 10^{-1}$ mA cm^{-2} (Figure 7.7(c)). This effect and the peak which emerges at $\sim 10^{-3}$ mA cm^{-2} are likely due to the introduction of charge traps which modify charge balance in the device. Another contributing factor may be the bias-dependent RZ often exhibited by OLEDs,[157,209] which could lead to spatial variation in defect concentration. The device is degraded at high bias with the RZ peaked near the HTL side of the emissive layer (EML), and hence the defect population should be highest at the HTL/EML interface. At low biases, the RZ is peaked at the EML/ETL interface, where defect density is lower and hence efficiency is higher. However, given the thin EML of these devices, it seems unlikely that defect density variation alone can fully account for the dramatic low current peak seen in Figure 7.7(c).

In Figure 7.7(d), the EQE is normalized to $J = 2\,\mathrm{mA\,cm^{-2}}$ to illustrate how the roll-off at high current density is changing. As the device degrades, the roll-off is monotonically reduced, consistent with reduced bimolecular quenching and increased η_τ. Below, we discuss whether the magnitude of this change can be entirely attributed to η_τ.

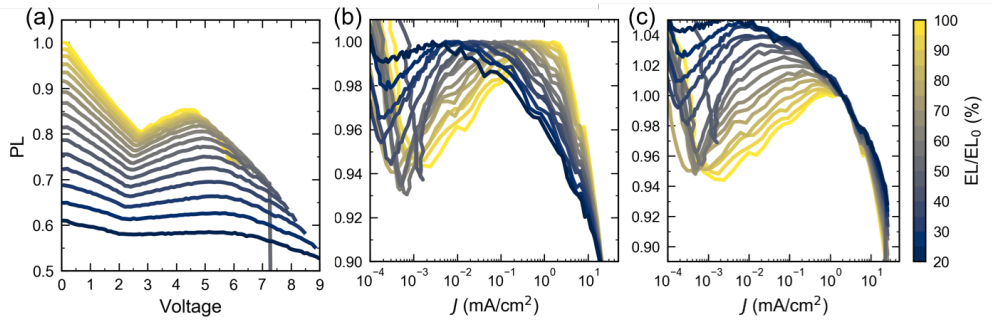

Fig. 7.8. Lock-in measured PL as a function of bias at various levels of EL degradation for a CBP:Ir(ppy)$_3$ device operated at $L_0 = 10{,}000\,\mathrm{cd\,m^{-2}}$ ($J = 20\,\mathrm{mA\,cm^{-2}}$). (**a**) Absolute PL vs. voltage. (**b**) PL normalized the maximum above $J = 10^{-3}\,\mathrm{mA\,cm^{-2}}$. (**c**) PL normalized to the value at $J = 2\,\mathrm{mA\,cm^{-2}}$.

Figure 7.8 shows the bias dependence of lock-in PL taken intermittently during degradation. The absolute PL intensity (Figure 7.8(a)) systematically decreases due to the introduction of exciton quenchers. Shown in the peak-normalized PL in Figure 7.8(b), the slope of PL vs. J systematically decreases with increasing degradation, reflecting reduced bimolecular quenching. Because the peak position shifts, likely due to the above described polaron dynamics not

captured by our model, a normalization condition nearest to the peak of the undegraded device is needed. With this normalization (Figure 7.8(c)), the normalized value of PL near the operating point ($J = 20\,\mathrm{mA\,cm^{-2}}$) increases with degradation, indicating an increase in η_τ.

In Figure 7.9, we compare the changes in roll-off observed in EQE and PL. Note that PL roll-off reflects η_τ, whereas EQE can reflect a combination of η_τ, η_{EF}, or η_{OC}. The decrease in roll-off measured from EQE is much larger than that measured from lock-in PL (when both normalized to the same current density of $J = 2\,\mathrm{mA\,cm^{-2}}$), indicating that changes in η_τ can likely not fully explain the changes in EQE roll-off. Instead, the current dependence of η_{EF} likely dominates the degradation-dependent EQE behavior observed here. This discrepancy underscores the fact that degradation-dependent EQE roll-off cannot be used reliably to extract changes in η_τ. Given that the efficiency roll-off analysis is often based solely on EQE measurements, this finding underscores the importance of using optical probes to assess quenching at very low current densities, in agreement with previous arguments.[197]

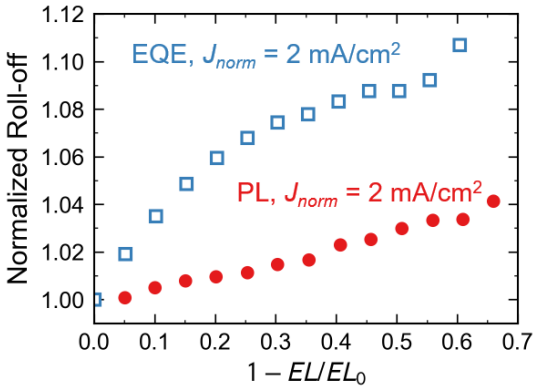

Fig. 7.9. Comparison of the change in roll-off measured from EQE and lock-in PL for a CBP:Ir(ppy)$_3$ device operated at $L_0 = 10{,}000\,\mathrm{cd\,m^{-2}}$ ($J = 20\,\mathrm{mA\,cm^{-2}}$). Here the normalized roll-off is defined as the roll-off at a given point in time ($PL(J_{op},t)/PL(J_{norm},t)$ or $EQE(J_{op},t)/EQE(J_{norm},t)$) divided by the initial (undegraded) roll-off ($PL(J_{op},t=0)/PL(J_{norm},t=0)$). Here, $J_{op} = 20\,\mathrm{mA\,cm^{-2}}$ is the operating condition for the lifetime test and $J_{norm} = 2\,\mathrm{mA\,cm^{-2}}$. The disparity indicates that changes in EQE roll-off are significantly driven by changes in η_{EF} rather than η_τ.

7.6 Conclusions

We have presented an analysis of the degradation-induced changes in bimolecular quenching and efficiency roll-off in an archetypical phosphorescent OLED. Using lock-in amplifier measurements of photoluminescence, bimolecular quenching can be directly characterized during degradation of OLEDs. We find that the natural decay efficiency (η_τ) typically rises by less than 5% (reflecting reduced bimolecular quenching) but becomes increasingly important at high

luminance, at times exceeding 10%. The magnitude of these changes quenching can be estimated by accounting for the reductions in exciton density and exciton lifetime during degradation and assuming polaron density remains constant. However, at high levels of degradation ($EL/EL_0 < 50\%$), reduced roll-off is partly offset by increased polaron density due to either trapped charges or reduced mobility. This study underscores that the degradation behavior of η_τ should not be neglected when degrading devices at high luminance ($L_0 \geq 5000\,\mathrm{cd\,m^{-2}}$) or in devices with significant exciton-exciton annihilation.

8

Pattern formation during thin film crystallization

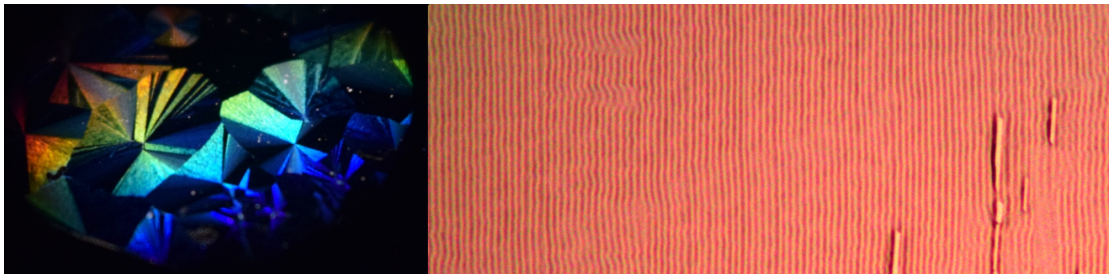

Material depletion and accumulation at the crystallization front of organic semiconductor films results in large-area patterns with a periodicity relevant to optoelectronic applications in the visible and near-infrared.

Self-organizing patterns with micrometer-scale feature sizes are promising for the large-area fabrication of photonic devices and scattering layers in optoelectronics. Pattern formation would ideally occur in the active semiconductor to avoid the need for further processing steps. Here, we report an approach to form periodic patterns in single layers of organic semiconductors by a simple annealing process. When heated, a crystallization front propagates across the film, producing a sinusoidal surface structure with wavelengths comparable to that of near-infrared light. These surface features form initially in the amorphous region within a micron of the crystal growth front, likely due to competition between crystal growth and surface mass transport. The pattern wavelength can be tuned from 800 nm to 2,400 nm by varying film thickness and annealing temperature, and millimeter-scale domain sizes are obtained. This phenomenon could be exploited for self-assembly of microstructured organic optoelectronic devices.

8.1 Introduction

Methods for spontaneously forming periodic surface structures at the nanometer or micrometer scale have received considerable attention for lithography-free patterning applications.[239–244] Spontaneous pattern formation is attractive as it can be easily scaled to large areas, potentially

enabling higher throughput and lower cost than serial processes.[239,245] These self-assembly techniques have primarily exploited phase separation of block copolymers or strain-induced wrinkling of polymeric thin films. Block copolymers are effective for patterning sub-100-nm features,[245–247] but are not amenable to create features on the length scale of visible light. Thin film wrinkling can form structures with periodicities ranging from ~400 nm—10 μm,[248] and is hence suitable for optoelectronic and photonic applications in the visible and near-infrared region.[249–253] While wrinkling approaches have afforded remarkable control and tunability over pattern formation, aligned patterns are more challenging to realize, and often require the application of anisotropic stress during film deposition or additional patterning.[240,248,254] Further, these approaches rely on the use of multiple layers and often lack thermal stability.[255,256]

Here, we report a crystallization-mediated mechanism in which aligned, periodic surface structures are formed along the amorphous-to-crystal transformation front during annealing of single-layer thin films of small molecule organic semiconductors. The observed topography originates in the form of material depletion and accumulation in the amorphous region within ~0.5 μm of the crystal front, likely due to mass-transport-limited crystal growth. These patterns appear related to structures which form during banded-spherulitic growth of various polymers and small molecules,[257–259] growth of hexagonal lamellar crystals of isotactic polystyrene,[260] polymorph transformations in the small molecule, ROY,[261] and explosive crystallization of amorphous Si.[262]

The current work is distinguished from these previous demonstrations by several promising features, including: large-area pattern coverage with millimeter-scale single crystal domains, direct integration into single layers of organic semiconductors, feature depths which span nearly the entire film thickness, and pattern wavelengths which are tunable over a range useful for optoelectronic applications. The periodicity of the observed wrinkling can be tuned from 800 nm to 2,400 nm by varying film thickness and annealing temperature. Further, the resulting structures exhibit excellent thermal stability since they occur with a transition to a crystalline phase.

Since many organic semiconducting molecules form glasses when deposited and crystallize readily when annealed,[263–265] the method reported here of crystallization-mediated periodic patterning could be generalizable to a wide range of materials. As a proof of concept, we report pattern formation in four archetypical organic semiconductors. This phenomenon could find application in a variety of optoelectronic settings including the improvement of light trapping

in solar cells,[252] enhancing light extraction from emissive devices,[253,266,267] and the fabrication of self-assembled organic lasers.[250,268]

8.2 Formation and tunability of aligned periodic patterns

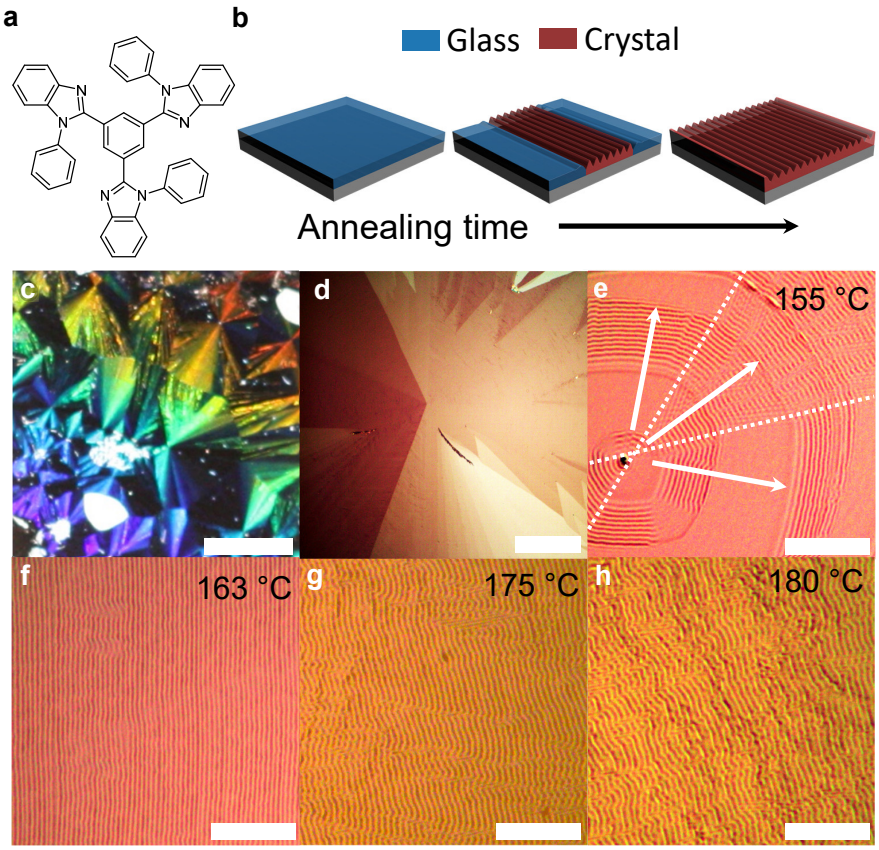

Fig. 8.1. Periodic pattern formation in TPBi films and dependence on temperature: (**a**) Molecular structure of TPBi. (**b**) Schematic depicting amorphous (blue) to crystalline (orange) transformation which propagates across the TPBi film when annealed for several minutes at a temperature above 150 °C, leading to large-area pattern formation. (**c**) Macroscopic photo of optical diffraction from a 30-nm-thick TPBi film on Si annealed at 170 °C. The sample is illuminated by unpolarized white light at an oblique angle. Note that dark regions are due to the orientation of the corrugation relative to the illumination source and are diffractive at different viewing angles. Scalebar is 0.5 cm. (**d**) Cross-polarized optical micrograph of 30-nm-thick TPBi annealed at 170 °C showing a millimeter-scale crystalline grain. Scalebar is 0.5 mm. (**e**)–(**h**), Unpolarized optical micrographs of 30-nm-thick TPBi films on Si substrates annealed at various temperatures. (**e**) 155 °C with periodicity $d = 1.20 \pm 0.05\,\mu$m. Arrows indicate the growth direction of three crystal facets from a single nucleation point. The slower-growing facets (top and bottom regions) show plateau regions without periodic topography. (**f**) 163 °C with $d = 1.25 \pm 0.06\,\mu$m, showing exquisite alignment of the periodic ridges. (**g**) 175 °C with $d = 1.48 \pm 0.05\,\mu$m, and (**h**) 180 °C with $d = 1.51 \pm 0.12\,\mu$m, showing a more disordered topography due to the higher growth rate at high temperatures. Scalebars for (**e**)–(**h**) are 20 µm.

Pattern formation is examined by annealing organic semiconductor thin films on Si substrates at temperatures of 20–80 °C above their bulk glass transition temperature (T_g). While several materials are observed to form periodic surface structure, we first provide a comprehensive analysis in 2,2′,2"-(1,3,5-benzinetriyl)-tris(1-phenyl-1-H-benzimidazole) (TPBi, Figure 8.1a), a common electron-transporting material in organic light-emitting devices (OLEDs). As-deposited films of TPBi appear smooth and featureless, typical of glassy vapor-deposited films. When annealed above $T_g \approx 124$ °C[177] in the range of 150–185 °C, TPBi films crystallize readily and spontaneously form periodic undulations perpendicular to the growth direction (Figure 8.1).

The pattern periodicity, d, increases monotonically with annealing temperature, ranging from 1.20 ± 0.05 µm at 155 °C to 1.48 ± 0.05 µm at 175 °C for a 30-nm-thick film (Figure 8.1e-h and Figure 8.2c). In the range of 160–175 °C, the crystal growth front is smooth and continuous, resulting in a highly aligned grating topography with millimeter-sized grains (Figure 8.1c-d). At higher temperatures (180 °C, Figure 8.1h), the film transformation occurs more rapidly along an uneven growth front producing more disordered structures. Below 160 °C, corrugation along certain growth directions is occasionally interrupted by plateaus (155 °C, Figure 8.1e). Films annealed below 150 °C instead show faceted growth rings with irregular spacings (Figure 8.25), similar to structures previously observed in rubrene.[263] This transition from periodic topography to growth rings at lower temperatures suggests that both surface features arise from the same physical mechanism.

Two crystalline phases of TPBi can form over the temperature range of interest. The phase which shows periodic corrugation forms relatively smooth, platelet-like grains (Figure 8.1d) and covers >90% of the film surface at annealing temperatures below 170 °C and above ~180 °C. A second phase which has a dendritic morphology and significant roughness becomes more dominant between 170 °C and 180 °C with surface coverages ranging from 20–80% (Figure 8.23).* Diffraction of visible light can also be observed in these images, illustrating that the periodic surface structures have nearly complete surface coverage in the platelet-like grains. It is worth noting that these crystals are not spherulites, in contrast to banded spherulites.[269] As shown in Figure 8.1d and below in Figure 8.3a, extinction in cross-polarized optical micrographs is

*The relative dominance of the dendritic and platelet-like phases here likely reflects a competition between kinetic and thermodynamic factors. However, we have also observed that nucleation can also influence the phase composition. Samples which are dirty (e.g. containing dust inclusions) or scratched tend to show greater nucleation density of the dendritic phase.

uniform within a crystalline grain, indicating that these platelet-like grains consist of a single crystal orientation.[257,263,265]

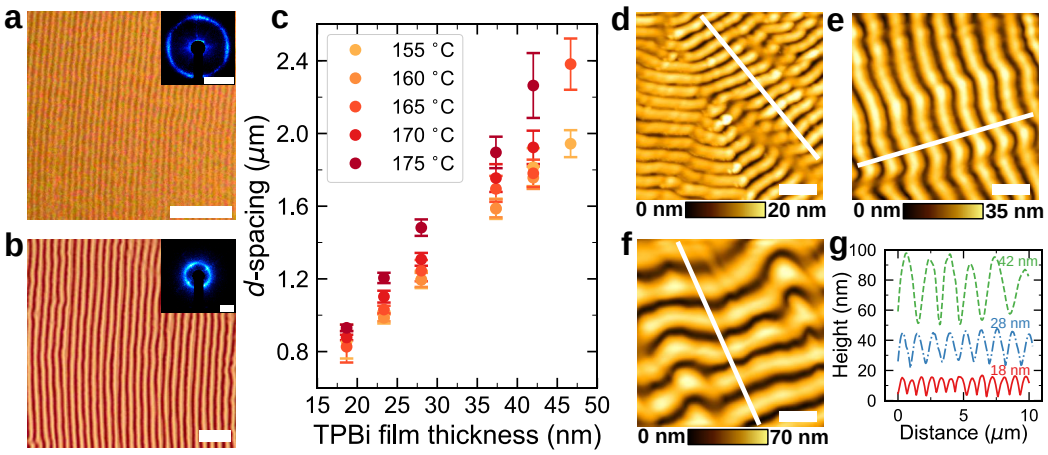

Fig. 8.2. Characterization of pattern tunability and surface topography: (**a**) 25-nm-thick film of TPBi on Si annealed at 165 °C with periodicity $d = 1.03 \pm 0.03$ µm. Scalebar is 10 µm. Inset is a diffraction pattern produced by illuminating the sample with a $\lambda = 473$ nm laser, with a scalebar of 1 µm^{-1}. (**b**) 47-nm-thick TPBi film on Si annealed at 165 °C showing $d = 2.38 \pm 0.14$ µm. Scalebar is 10 µm. Inset is a diffraction pattern with a scalebar of 0.47 µm^{-1}. The inset images in (**a**) and (**b**) are both 11.9 cm wide (see Methods). (**c**) Dependence of pattern d-spacing on film thickness and temperature, as extracted from fast Fourier transforms of optical microscopy images. Error bars are 95% confidence intervals using the Student's t-distribution for small sample sizes and averaged over at least ten images. (**d**)–(**f**), AFM height images TPBi films on Si annealed at 165 °C with thicknesses of (**d**), 18 nm, (**e**), 28 nm, and (**f**), 42 nm. Scale bars are 2 µm in (**d**)-(**f**). (**g**) Height profiles for 18-, 28-, and 42-nm-thick TPBi films. Profiles are vertically offset for clarity. The pattern periodicity extracted from these profiles (0.77 µm, 1.2 µm, and 1.8 µm, respectively) is consistent with measurements from optical microscopy. The average peak-to-valley amplitude extracted from these profiles is 13 nm, 22 nm, and 42 nm, respectively.

The pattern periodicity observed in TPBi shows a roughly linear dependence on film thickness, ranging from $d = 0.83 \pm 0.09$ µm for an 18-nm-thick film to $d = 2.38 \pm 0.14$ µm for a 47-nm-thick film at a constant temperature of 165 °C (Figure 8.2c). The periodicity is determined from fast Fourier transforms (FFTs) of optical micrographs and checked for consistency with measurements from atomic force microscopy (AFM) images (Figure 8.2d-g) and diffraction (Figure 8.2a,b and Figure 8.15).Statistical analysis of pattern quality (i.e. the degree of alignment and order) is discussed in the Section 8.9.2.

Under ex situ examination with AFM (Figure 8.2d-g), the films show well-defined periodicity which is nearly sinusoidal, with wavelengths of 0.77 ± 0.01 µm, 1.2 ± 0.1 µm, and 1.8 ± 0.1 µm for 18-, 28-, and 42-nm-thick films of TPBi annealed at 165 °C, in good agreement with the values extracted from optical micrographs. The peak-to-valley amplitude increases with film thickness from 13 ± 1 nm for an 18-nm-thick film, 22 ± 2 nm for a 28-nm-thick film,

and to 42 ± 7 nm for a 42-nm-thick film. The total feature depth is nearly as large as the entire film thickness for a 42-nm-thick film, and over 70% of the film thickness for 18- and 28-nm-thick films.

8.3 Pattern formation mechanism

To study the formation of these structures, films were imaged in situ during annealing. The time evolution of the growth front for a 30-nm-thick film annealed at 165 °C is shown in Figure 8.3. The periodic pattern is formed as the crystal growth front progresses (at ~0.6 μm s^{-1}), with the ridges appearing at the left side of the image window of Figure 8.3b and then extending along the length of the growth front. Cross-polarized micrographs on the same film show birefringence contrast progressing simultaneously with the onset of the periodic features, indicating that height variations form concurrently with crystallization (Figure 8.3a). Finer time steps are shown in Figure 8.3c, showing individual ridges progressing laterally across the growth front at a rate of ~3 μm s^{-1}. These time series are taken along the slower-growing crystal facet, suggesting that growth of the crystal along this direction partly occurs via molecular attachment on the faster growing crystal plane.[263] Crystallinity of the transformed material was confirmed with X-ray diffraction (Figure 8.28). Once formed, these patterns show a fixed spacing and are thermally stable, with no significant change in periodicity or morphology after post-annealing for several hours at 150 °C. Thermal stability appears to be limited by sublimation loss.[263]

Crystal growth rate increases exponentially with temperature and modestly with film thickness, with 40-nm-thick films showing ~30% higher growth rates than 20-nm-thick films. The thickness trend likely arises due to the film-substrate interaction.[270,271] Correspondingly, the topography becomes more disordered with increases in either temperature (Figure 8.1) or film thickness (Figure 8.27). Higher disorder is also observed along the faster-growing facets of TPBi crystals (Figure 8.24), suggesting that pattern quality depends on the transformation front velocity. Growth rate evidently also plays a role in the formation of the smooth regions seen at temperatures below 160 °C (Figure 8.1e), as only the slower-growing facets form these plateaus. Absolute growth rates are likely less important than the velocity relative to other kinetic factors, such as the mobility of the supercooled liquid, as fast-growth facets show higher disorder across a range of annealing temperatures with growth rates of ~0.5–3 μm s^{-1}.

To probe how the surface topography forms at the growth front, partially crystallized films

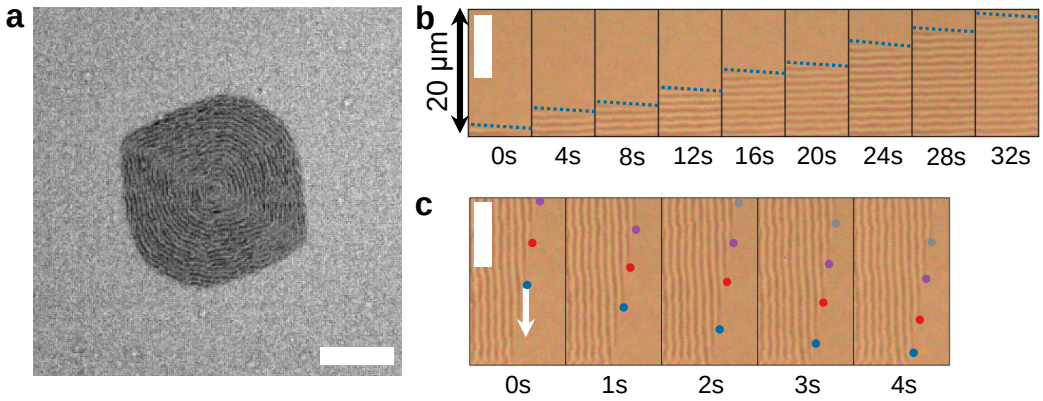

Fig. 8.3. In situ optical microscopy of periodic pattern formation during annealing: (**a**) Cross-polarized optical micrograph of a single crystalline grain in a 30-nm-thick TPBi film during annealing at 165 °C. The grating pattern is aligned parallel to the growth front and is only observed within the crystallized region. The surrounding material with lower extinction is amorphous, showing no birefringence, unlike the crystalline grain. Scalebar is 20 µm. (**b**) Time series of unpolarized optical micrographs during annealing of a 30-nm-thick TPBi film at 165 °C, showing pattern formation along the boundary of the amorphous-to-crystalline transformation front which propagates at a rate of ~0.6 µm s^{-1}. Time between frames is 4 seconds, scalebar is 10 µm. Dashed lines indicate the edge of the crystalline growth front. (**c**) Finer timesteps (1 second between frames) of the same region in (**b**), showing individual ridges extending along the length of the growth front at a rate of ~3 µm s^{-1}. To guide the eye, colored circles are placed at endpoints of each individual ridge. Scalebar is 10 µm. The source video for (**b**) and (**c**) is provided in the Supplementary Material.

were examined ex situ with peak force quantitative nanomechanical (PF-QNM) AFM, which allows amorphous and crystalline regions to be distinguished by their mechanical properties. Stark contrast in adhesion is seen between these regions (Figure 8.4b,d), where the amorphous material exhibits greater adhesion, reflecting the increased degrees of freedom for molecular rearrangement and interaction with the tip. Strikingly, the onset of surface height variations does not coincide with the grain boundary, but extends into the surrounding amorphous material by ~0.5 µm (Figure 8.4e,f) with both significant accumulation and depletion in this region. This indicates that the periodic topography originates here rather than solely in the crystal.

This behavior appears distinct from conventional diffusion-limited crystal growth which is characterized by a depletion zone surrounding the growth front,[270,272,273] where only the crystal rises above the height of the neat amorphous material due to upwards growth by surface diffusion.[274] However, these height profiles resemble the damped-oscillation solutions yielded by the Mullins model for surface diffusion and a similar model for viscous surface flow at steady-state (see Figure 8.8),[272,275,276] and share features with the depletion and halo regions recently reported during crystallization of isotactic polystyrene.[260] These similarities suggest that this periodic surface topography arises due to a competition between long-range mass transport and

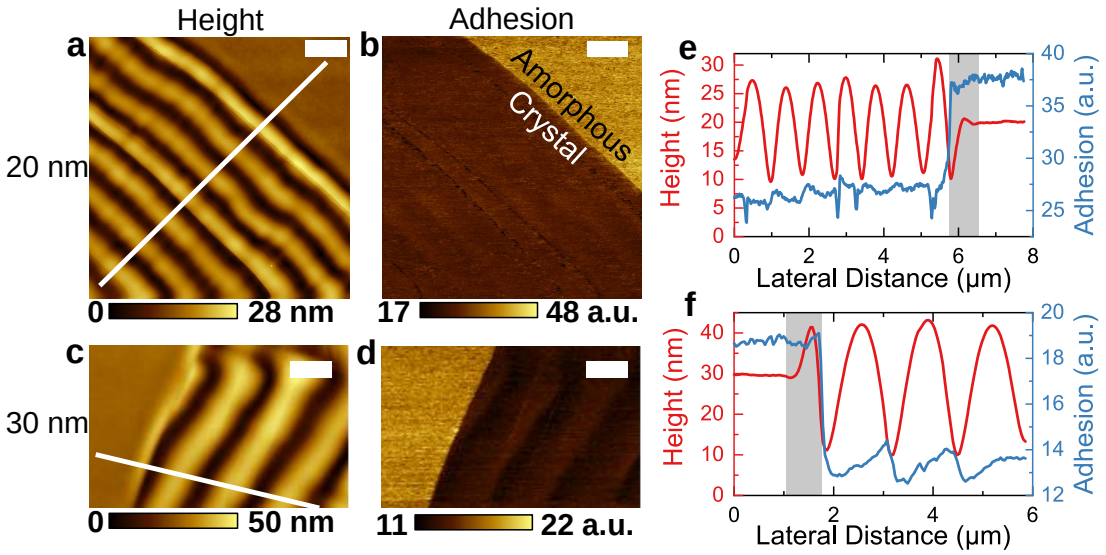

Fig. 8.4. Topography and mechanical properties near the crystal growth front: (**a**) Height and (**b**) adhesion images for 20-nm-thick TPBi on Si annealed at 163 °C. Scalebars are 1 μm. (**c**) Height and (**d**) adhesion images for 30-nm-thick TPBi on Si annealed at 165 °C. Scalebars are 1 μm. All images are acquired with peak force AFM. Height and adhesion profiles across the crystal growth front are shown for 20- and 30-nm-thick TPBi in (**e**) and (**f**), respectively. The white lines in (**a**) and (**c**) correspond to the center lines for the height and adhesion profiles plotted in (**e**) and (**f**), with profiles averaged laterally over 10 pixels in the perpendicular direction. The adhesion image provides contrast between crystalline and untransformed amorphous regions, due the difference in mechanical properties of the two phases. The shaded regions in (**e**) and (**f**) highlight the portion of the amorphous region near the crystal growth front which shows both accumulation and depletion of material.

crystal growth.[277] The observed height variations could then be explained by a cyclical process which starts with the region near the growth front depleting as growth outpaces long-range mass transport. Growth then slows at high depletion, due to reduced availability of material and increased substrate interactions,[260,271] allowing mass transport to replenish the depleted region and increase the height of the accumulation region. As the region leading the crystal front thickens, growth will again accelerate and restart the cycle. Mass transport here is likely dominated by viscous flow and not surface diffusion, as annealing is performed 20–60 °C above T_g, well above the reported transition between these regimes for common molecular glasses.[278] This proposed mechanism is illustrated schematically in Figure 8.5

We confirmed the role of surface transport in pattern formation by capping the top interface of TPBi films. Only smooth crystals without periodic topography formed in TPBi capped with 10-nm-thick films of Au or a high-T_g organic (Alq_3, see Figure 8.6). Further, capped films show suppressed crystal growth rate, confirming that crystal growth is primarily fed by surface transport.

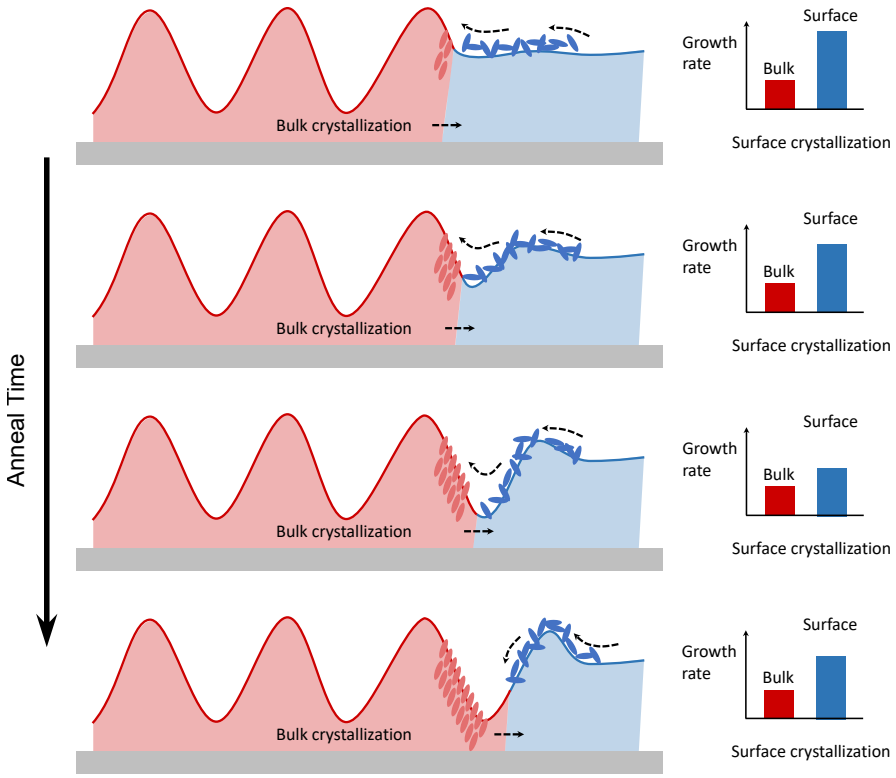

Fig. 8.5. Schematic of proposed pattern formation mechanism, described in the main text, where the surface growth rate depends on the degree of depletion near the crystal growth front. When the amorphous region is only slightly depleted, the surface growth rate is much faster than "bulk" growth (meaning crystallization that occurs due to rearrangement away from the free surface), leading to depletion (the height of the amorphous region near the boundary decreases). As depletion increases, the surface and bulk growth rates become comparable, pushing the crystal front into the thicker portions of the amorphous film. This cycle repeats as the crystal propagates, giving rise to the periodic pattern.

For these confined films, substrate interactions become important,[279] and hence bulk crystallization and surface crystallization may both be active.[272,280] Surface crystallization is likely responsible for the formation of depletion and accumulation features, whereas bulk crystallization may continue to drive growth when the depletion depth becomes large and limits the supply of material for surface growth. In capped TPBi films, the crystal growth rate is reduced by 50—90% compared to uncapped films but is not entirely deactivated (Figure 8.6e-f). This confirms that transport at the free surface is the primary mechanism for feeding crystal growth, but that crystallization in the bulk of the film contributes non-negligibly. Several other effects may contribute to the observed patterns. The volume change upon crystallization may induce stresses in

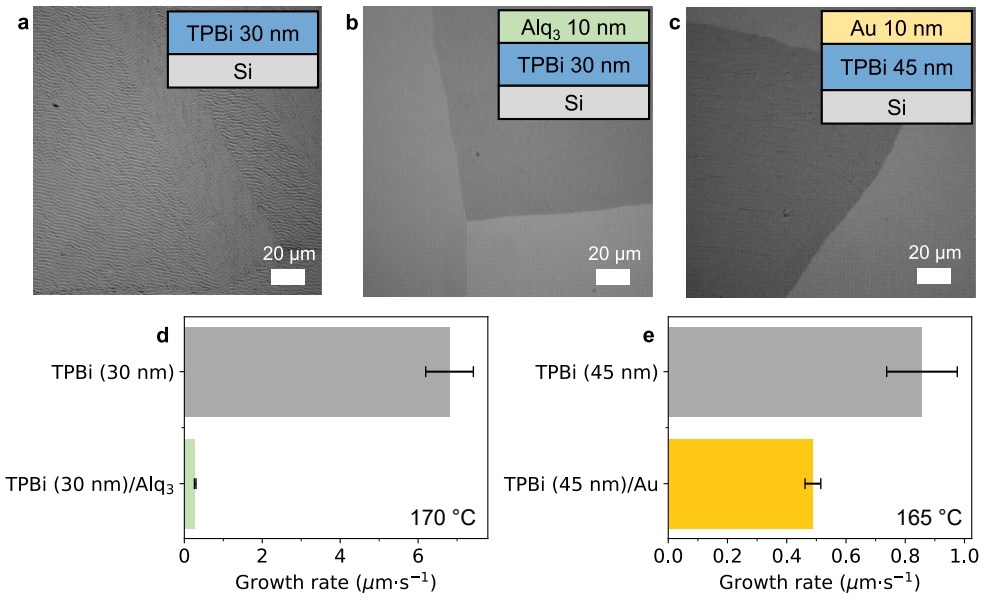

Fig. 8.6. Impact of surface transport on pattern formation and crystal growth. Polarized optical micrographs of (**a**) 30-nm-thick TPBi on Si, (**b**) 30-nm-thick TPBi on Si with a 10-nm-thick capping layer of Alq_3, a high-T_g small molecule, and **c** 45-nm-thick TPBi on Si with a 10-nm-thick capping layer of Au. All samples in these images were annealed at 170 °C, but the absence of pattern formation was confirmed over a larger range of temperatures from 160–190 °C. No pattern formation or diffraction is observed in capped samples, supporting the hypothesis that pattern formation results from surface-fed crystal growth which depletes the amorphous region surrounding the crystal front. **d**–(**e**) Average crystal growth rate in uncapped and capped films of TPBi. The suppressed growth rate in capped films indicates that surface transport is the dominant contributor to crystal growth in these films. Error bars represent standard deviations over at least five growth rate measurement.

the surrounding amorphous region, providing a driving force surface feature formation. Additionally, mobility near the growth front may be periodically enhanced by the release of heat of fusion or from tension arising from crystallization.[262,281]

With this view of the pattern formation mechanism, the increase in pattern wavelength at higher annealing temperatures may stem from mobility of the supercooled liquid having a steeper function of temperature than the crystal growth rate, allowing flow to occur over a larger distance. This interpretation should lead to some flattening of the pattern features, in qualitative agreement with AFM measurements showing a decreased amplitude at annealing temperatures >175 °C (Figure 8.7). The dependence of pattern wavelength on thickness could partially be a consequence of the variation in T_g and growth rate with film thickness,[279,282] and also the total supply of material (i.e. thicker films take longer to deplete, allowing more time for the depletion zone width to increase).[260] The flat regions at low temperatures (Figure 8.1e and Figure 8.25) likely form due to mass transport rates matching or exceeding crystal growth, preventing the

formation of depletion regions.

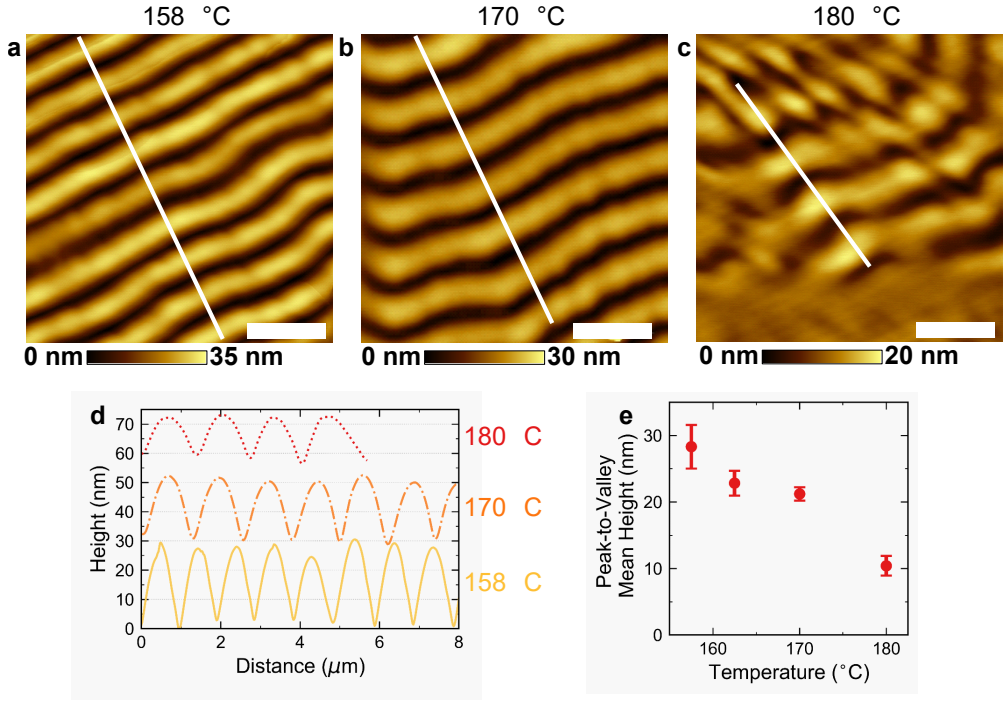

Fig. 8.7. Temperature dependence of pattern wavelength and depth. AFM images of 30-nm-thick TPBi films on Si annealed at (**a**) 158 °C, (**b**) 170 °C, and (**c**) 180 °C. Scalebars are 20 μm for all images, and white lines indicate positions of the height profiles plotted in (**d**). Profiles are vertically offset for clarity. Average peak-to-valley height taken across 3-4 images at each temperature are shown in (**e**). Error bars are 95% confidence intervals using the Student's t-distribution for small sample sizes. The pattern wavelength is found to systematically increase with temperature and the peak-to-valley height decreases. These trends likely result from the mobility of the supercooled liquid increasing more steeply with temperature than the crystal growth rate, allowing flow to occur over a larger distance and leading to flattening of the pattern features.

To see whether these results qualitatively agree with surface transport, we applied a steady-state surface diffusion model for material depletion near a crystal growth front.[272] Figure 8.8 shows steady-state solutions to Mullins's surface diffusion model fit to the AFM profiles from Figure 8.4 (equations included in Section 8.9.3) . The width of the depletion zone is well-described by this model, but the overall amplitude of accumulation in the amorphous region is not. This discrepancy could partly be due to complicating factors which are not included in the model, such as the competition between bulk and surface crystallization[274] and a gradient in film mobility due to tension from the contracting crystal.[281] It is also likely that these profiles are not truly at steady-state and time varying effects (such as a periodic variation in growth rate[260]) contribute to this discrepancy. Further, interactions with the substrate can strongly

influence glass transition temperature[279,282] and crystal growth rate[283] in films less than 100 nm thick; it seems probable that these substrate effects play a role in pattern formation. Indeed, as discussed below in Section 8.4, crystal growth is slowed and pattern formation can be turned off completely on a MoO_3-coated substrate. Still, these simplified modeling results support that the height features seen near the growth front are consistent with a surface transport-driven mechanism.

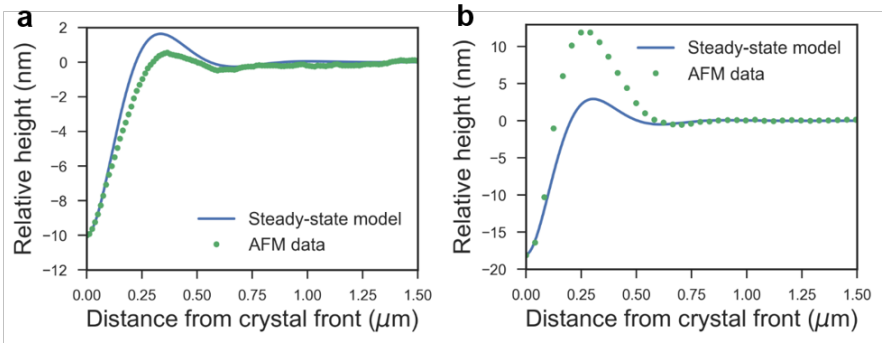

Fig. 8.8. Comparison between AFM profile and steady-state surface diffusion predictions: (**a**) 20-nm-thick TPBi and (**b**) 30-nm-thick TPBi. Steady-state surface diffusion is modeled following Hasebe, Musumeci, and Yu [272], adjusting the parameters for surface diffusion coefficient, crystal growth rate, and crystal thickness. While no measured diffusion coefficients for TPBi are available, the diffusion coefficient which leads to the best fit of the AFM data (~10^6 μm^2 s^{-1}) is of the same order as the reported coefficients of other organic glasses extrapolated to this temperature.[278]

8.4 Alternative molecules and surfaces for pattern formation

To enable device integration, it is important to realize patterns in other organic semiconductors and on common electrode surfaces. As many vapor-deposited organic semiconductors form glassy films and crystallize above T_g, a variety of materials may be amenable to crystallization-mediated patterning. We tested a wide range of materials for crystallization and pattern formation, summarized in Table 8.1. Of these, we observed periodic pattern formation in the hole-transport material α-NPD, the ambipolar host material BCBP, and the archetypical organic semiconductor rubrene. α-NPD (bulk T_g = 95 °C)[284] forms a pattern with $d = 0.98 \pm 0.05$ μm for a 30-nm-thick film annealed at 170 °C (Figure 8.9a). BCBP (bulk $T_g = 120$ °C)[285] forms a pattern with $d = 1.6 \pm 0.1$ μm for a 35-nm-thick film annealed at 170 °C (Figure 8.9b). Rubrene crystallizes above ~115 °C,[263,265] and forms a pattern with $d = 1.75 \pm 0.10$ μm for a 30-nm-thick film annealed at 185 °C (Figure 8.9c). While the quality and surface coverage of

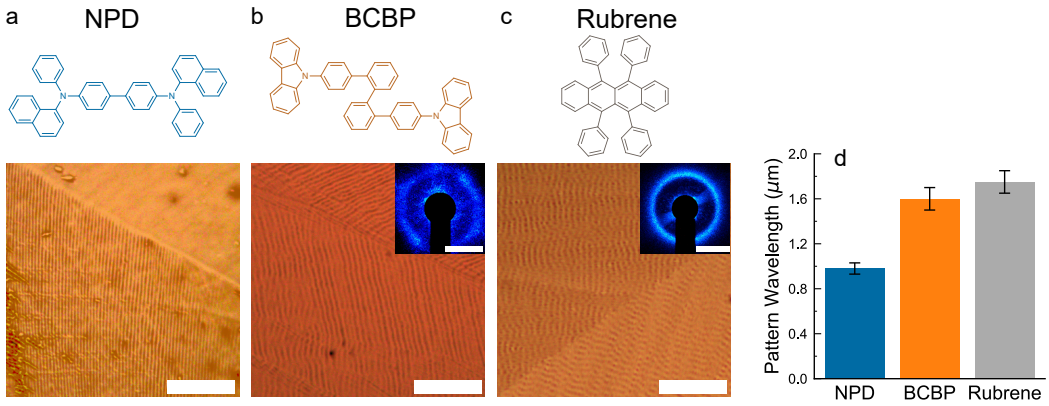

Fig. 8.9. Pattern formation in other organic semiconductors: Molecular structures and unpolarized optical microscope images of pattern formation in (**a**) a 30-nm-thick film of α-NPD annealed at 170 °C with periodicity $d = 0.98 \pm 0.05$ µm, (**b**) a 35-nm-thick film of BCBP annealed at 170 °C with periodicity $d = 1.6 \pm 0.1$ µm, and (**c**) a 30-nm-thick film of rubrene annealed at 185 °C with periodicity $d = 1.75 \pm 0.10$ µm. Insets of (**b**) and (**c**) are diffraction images of the same films with scalebars of 0.64 µm^{-1} and 0.57 µm^{-1}, respectively, and the same physical width of 6.8 cm. Diffraction was not observable for α-NPD due to incomplete surface coverage of the pattern, with the majority of the film forming flat crystalline regions as shown in the upper right corner of the image in (**a**). Scalebars are 20 µm for all images.

periodic patterns in these materials has not been fully optimized, differences in molecular structure and T_g suggest that the method is generalizable, and that the pattern periodicity could be further tuned by varying materials properties. The formation of these patterns in both electron- and hole-transporting materials also improves the flexibility of this method for device integration.

Several other materials showed trace signs of pattern formation. TCTA, the widely used HTL material, showed platelet-like crystals when annealed from 190–220 °C. Tom Fielitz observed some height variations in these crystals, but we were later unable to reproduce this. The TADF emitter, 4CzIPN, large smooth platelet-like grains with growth rings, suggesting that this material could also be optimized to form periodic patterns (Figure 8.22).

As a base criterion for pattern formation, a candidate material must form a glassy film that transforms to large-area, platelet-like crystals when annealed. However, due to the observed impact of crystal growth rate on pattern quality, it is likely that a balance of kinetic and thermodynamic factors such as T_g, steric bulk, and the supercooled liquid viscosity will determine whether surface structure will form upon crystallization. Crystal structure does not appear to impact whether periodic topography forms during crystallization. The phase of rubrene here has an orthorhombic crystal structure,[263] whereas α-NPD is most likely triclinic.[286] The thin-film

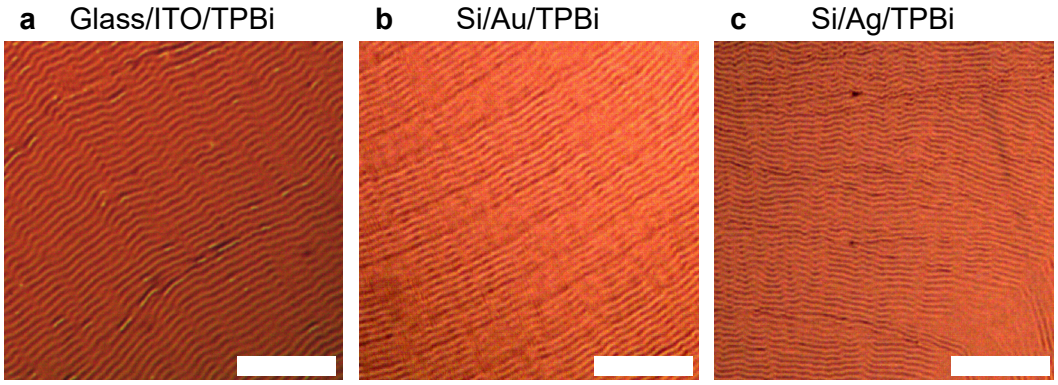

Fig. 8.10. Pattern formation on common electrode surfaces: Unpolarized optical microscope images of pattern formation in 30-nm-thick TPBi film deposited on common electrode surfaces: (**a**) Glass/ITO, (**b**) Si/Au, and (**c**) Si/Ag. All films are annealed at 163 °C. Scalebars are 20 µm for all images.

crystal structures of BCBP and TPBi have not been reported, to our knowledge.

To inform device integration and assess the potential for direct pattern formation on electrode surfaces, TPBi films were deposited and annealed on a variety of surfaces. We observe pattern formation on common electrode materials such as ITO, Au, and Ag (Figure 8.9d-f), as well as other substrates, such as Al_2O_3, quartz, glass, and WO_3-coated Si. The substrate was observed to impact crystal growth rate, in agreement with previous work on rubrene where more hydrophobic substrates decreased the crystal growth rate.[270] The pattern wavelength decreases modestly in substrates with slower crystal growth, possibly reflecting substrate interactions which inhibit molecular motion in the supercooled liquid and thus lower the depletion zone width. For example, growth rate in 34-nm-thick TPBi films is reduced from $0.4\,\mu m\,s^{-1}$ on Si/SiO_2 substrates to $0.15\,\mu m\,s^{-1}$ on Si/Au substrates, and the pattern wavelength decreases from $1.46 \pm 0.05\,\mu m$ to $1.32 \pm 0.05\,\mu m$.

8.5 Strategies to improve control of pattern formation

To tailor patterns for arbitrary applications, further control is needed over long-range pattern alignment, pattern quality, and feature depth. Since these patterns form along crystal grain edges, alignment across a sample is limited by grain size. Millimeter-scale domains are

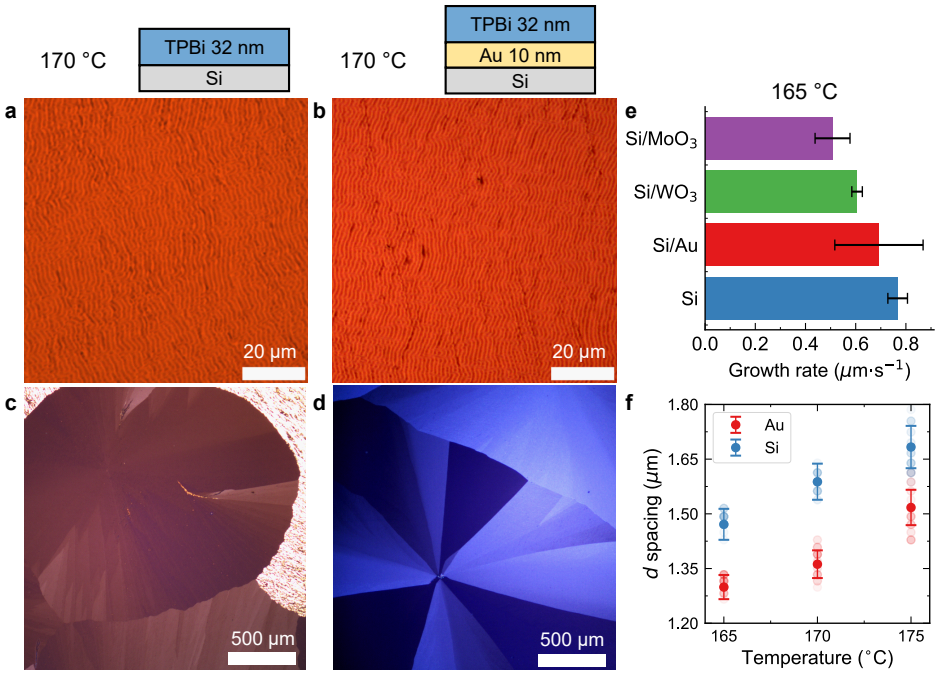

Fig. 8.11. Influence of substrate on pattern quality, crystal morphology, and growth rate: Unpolarized optical micrograph of surface patterns in (**a**) 32-nm-thick TPBi on a Si substrate, and (**b**) 32-nm-thick TPBi deposited on a Si substrate coated with 10 nm Au. Both samples are annealed at 170 °C, and the sample on Au shows higher pattern quality. Polarized optical micrographs of the same samples are shown in (**c**) and (**d**), respectively, illustrating that the Au surface results in reduced crystal branching and smoother growth fronts. The dendritic morphology is also almost completely non-existent in the sample grown on an Au surface, suggesting that the surface properties can also impact crystal phase composition and nucleation. (**e**) Crystal growth rate at 165 °C for TPBi on Si, Si/Au, Si/WO_3, and Si/MoO_3 substrates. (**f**) Average pattern d-spacing for TPBi films on Si and Si/Au substrates.

achieved here (Figure 8.1c,d), and could be further expanded by selecting optimal underlayers.[265] However, long-range alignment is not needed for many applications where randomly-oriented periodic structures can be tolerated or even desired. For example, outcoupling enhancement layers for OLEDs often consist of random structures to minimize viewing angle dependences.[287]

Feature depths of at least 70 nm are typically desired for optoelectronic applications,[267,268] and hence future work should focus on increasing pattern depth. One strategy to achieve larger amplitudes is to improve the quality of pattern formation in thicker films using the above methods. As feature depth can exceed 90% of the film thickness, sufficient depths should be obtained in ~70-nm-thick films. This comes with the obvious trade-off of increased pattern d-spacing, so likely other strategies will be needed in parallel to lower the d-spacing in thick films.

Pattern quality could be engineered by tuning substrate surface properties to control growth

rate.[270] As a demonstration of this strategy, we compared pattern quality and crystal morphology in TPBi films on Si/SiO_2 and Si/Au substrates (Figure 8.11). The reduced crystal growth rate on Si/Au substrates leads to smoother growth fronts and improved pattern quality across all tested annealing temperatures (Figure 8.12). As noted above, the reduced growth rate is accompanied by a reduction in pattern wavelength, indicating that substrate properties could also be used to tune the d-spacing. Another route is to use low-T_g underlayer materials,[265] which have been shown in rubrene to increase grain size, reduce branching, and reduce nucleation of other phases. Additives or mixtures could also be employed to alter crystal growth rate and shape by suppressing molecular attachment to certain crystal facets.[264]

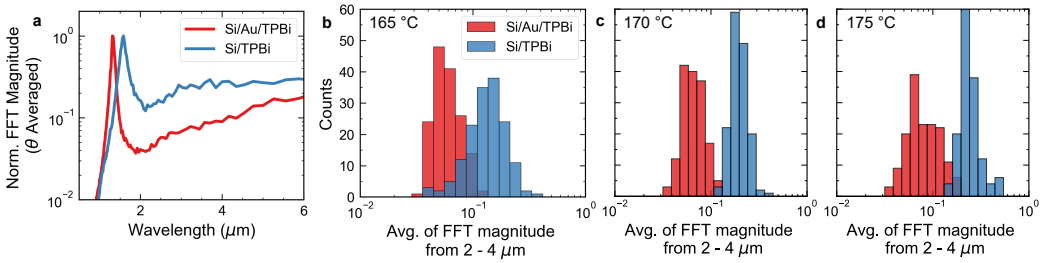

Fig. 8.12. Influence of substrate on pattern quality—FFT Analysis: (**a**) Azimuthally-averaged FFT power spectra for 32-nm-thick TPBi samples on Si and Si/Au (10 nm) substrates, annealed at 170 °C. The pattern wavelength is slightly reduced on an Au surface, and the pattern quality is significantly improved. (**b**)–(**d**) Histograms of the average FFT magnitude from 2–4 μm for >150 images for each test condition, with images taken at random locations across each sample. The area of each image is 0.005 mm^2, and hence each histogram is sampled over ~0.7 mm^2 of the pattern. The pattern quality is systematically improved on the Au substrate, due to the reduced crystal growth rate and improved crystal morphology. This result illustrates that surface chemistry could be used to engineer pattern quality and wavelength.

Interestingly, below a certain threshold growth rate, pattern formation seems to be turned off entirely. We see this at low annealing temperatures (e.g. Figures 8.1 and 8.25), where the pattern transitions into irregularly spaced growth rings. The same thing happens in substrates coated with MoO_3, where the growth rate is lowered and activation energy for crystal growth is increased (Figure 8.13). At low to moderate temperatures (<165 °C), pattern formation is suppressed or completely eliminated, despite platelet-like crystals still being formed.

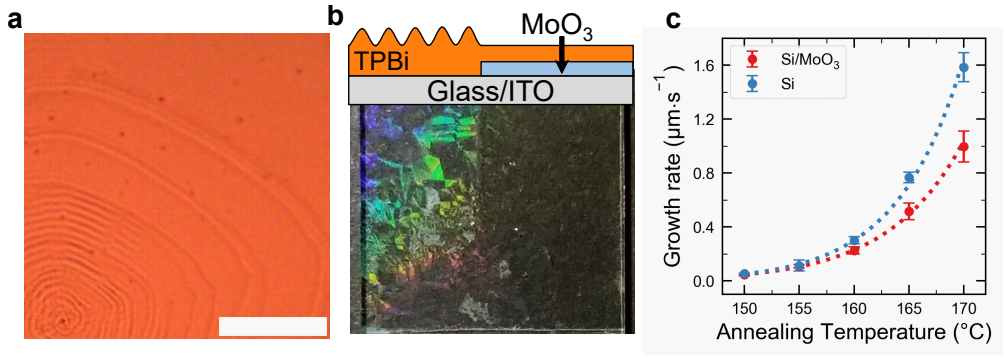

Fig. 8.13. Suppression of growth rate and pattern formation on MoO_3 surfaces: (**a**) Optical micrograph of TPBi crystal on MoO_3, showing growth rings but little pattern formation. (**b**) Macroscopic photo of crystallized TPBi sample where half the substrate was coated with MoO_3, showing no optical diffraction in this region. Films in (a) and (b) were annealed at 155 °C. (**c**) Crystal growth rate as a function of annealing temperature with Arrhenius fits to extract activation energy, which increases from 2.5 eV for Si substrates to 2.8 eV for Si/MoO_3 substrates.

8.5.1 Prospects for outcoupling enhancement

The wavelength of these patterns is particularly amenable to improving outcoupling in red and NIR OLEDs. Other work has incorporated photolithographically defined gratings with wavelengths of 700 nm[267] and 1000 nm[288] into red OLEDs, and these studies have found an enhancement of ~15 - 25% in outcoupling efficiency can be achieved for structures with a depth of ~75 nm. The grating reported here has a similar wavelength with a reduced depth of ~22 nm (see Figure 8.7f), so the expected outcoupling enhancement using our patterns can be roughly estimated at ~5-10%, assuming that the enhancement varies linearly with feature depth.

As a preliminary effort we have attempted to incorporate these structures into NIR OLEDs to induce an enhancement in outcoupling. The corrugated devices achieve an external quantum efficiency of ~5%, but we are unable to directly compare device external quantum efficiencies to assess outcoupling changes in this case, as we lack a suitable control. The crystallization of TPBi significantly impacts the electrical properties of the film, so changes in device efficiency are dominated by the electrical properties of the transport layers and not the optical properties of the periodic pattern. Instead, we probed outcoupling efficiency in these structures via optical pumping and found that PL emission was increased by ~8% in corrugated structures (Figure 8.14). This can be ascribed to an outcoupling enhancement, as transfer matrix modeling considering varying thickness of the corrugated layer shows that absorption within the emissive layer is negligibly changed compared to the neat, unannealed device. The main limitation for further improvements is clearly feature depth, and further work will need to focus on increasing

this depth to ~50-80 nm before convincing progress can be made on practical applications.

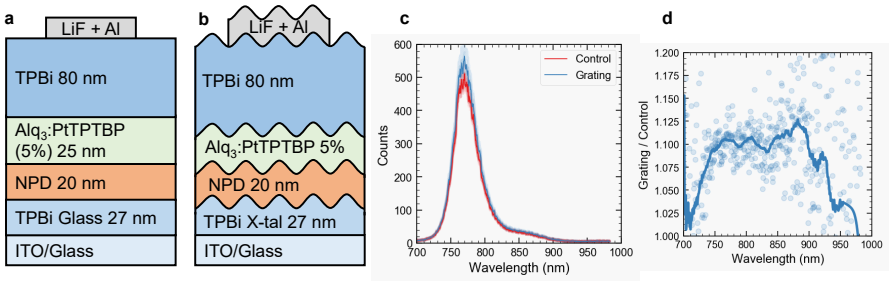

Fig. 8.14. Control and corrugated device architectures used in assessing impact on outcoupling efficiency of near-infrared OLEDs using PtTPTBP as an emitter. Corrugated devices were fabricated by growing a TPBi film on ITO substrates, annealing at 165 °C, and then depositing the remaining layers over top. (**c**) PL intensity for control devices (uncrystallized TPBi) and devices corrugated with crystalline TPBi, pumped by a $\lambda = 405$ nm laser at an incident angle of 45°. Semitransparent lines represent individual scans and solid lines are averages over 10 devices. (**d**) Relative enhancement in PL emission as a function of wavelength. Solid line is a moving average that serves as a guide to the eye. This modest enhancement of 8-10% is consistent with expectations based on literature results for similar architectures.

8.6 Conclusions

In summary, we report a crystallization-mediated mechanism for the spontaneous formation of highly-aligned periodic structures in organic semiconductor thin films. These features develop during annealing along the periphery of the crystal growth front, likely due to competition between crystal growth and surface mass transport, and are quickly incorporated into the crystal grain, producing a sinusoidal surface topography. The wavelength of these structures can be widely tuned from 800 nm to 2,400 nm by changing film thickness. We show that these patterns are thermally stable and can form on a variety of electrode materials, enabling direct integration into optoelectronic devices. Multiple glassy organic semiconductors are found to form these periodic patterns, suggesting that this method could be generally applied to any readily crystallized materials. We find that crystal growth rate is an important factor in determining whether periodic patterns will form and the overall pattern quality.

Going forward, to make this method commercially viable, further research is needed to understand how surface properties, materials properties, and additives influence crystallization and pattern formation. Specifically, aspects such as surface energy, the interaction strength between the substrate and the film, and the steric bulk and diffusivity of the molecule could all influence pattern depth and d-spacing. Developing a transport model which can accurately

describe and predict pattern features will be a key step to understanding and controlling each of these factors. If these challenges can be overcome, this phenomenon could be exploited for low-cost lithography-free patterning and could provide a novel assembly method for nanostructured organic optoelectronics.

8.7 Methods

TPBi, α-NPD, BCBP, and rubrene were purchased from Luminescence Technology Corp. and used as received (sublimed grade). All films were deposited using high-vacuum ($< 7 \cdot 10^{-7}$ Torr) thermal evaporation at a deposition rate of 0.1 nm s^{-1}. Silicon substrates have a 2-nm-thick native oxide layer and were exposed to a UV-ozone ambient for 10 minutes prior to deposition and remained at ambient (25 °C) temperature during deposition. For the surface variation experiments, 10-nm-thick films of Ag (Aldrich Chemistry, 99.999% trace metals basis), Au (Alfa Aesar, 99.9995% trace metals basis), and Tungsten (VI) oxide (WO_3, Puratronic, 99.998% trace metals basis) were thermally evaporated on cleaned Si substrates prior to deposition of TPBi films. Film thicknesses were measured with variable angle spectroscopic ellipsometry.

Annealing was initiated by placing a substrate onto a homebuilt temperature-controlled microscope stage purged with nitrogen and pre-heated at the annealing temperature. Episcopic (reflection) optical micrographs were taken with polarized light using a Lumenera Infinity 1.0 camera. Where noted, images were captured with a cross-polarizer to identify grains by birefringence contrast. All other optical micrographs were captured without a cross-polarizer. To improve visibility of the periodic pattern, histogram equalization was applied to the images in Figure 8.1g, Figure 8.2a,b, and Figure 8.9a and linear contrast stretching was applied to all other images using the scikit-image package in Python.

Atomic force microscopy was conducted using a Bruker Nanoscope V with a Multimode 8. Images in Figure 8.2 and Figure 8.7 were acquired in tapping mode, attractive regime, and AFM cantilevers were aluminum-coated highly doped monolithic silicon with a nominal spring constant of 42 N m^{-1}. Images in Figure 8.4 were acquired in PF-QNM mode, and AFM cantilevers were aluminum-coated n-type silicon with a nominal force constant of 0.6 N m^{-1}. Full AFM scan parameters are tabulated in Tables 8.2 and 8.3.

Periodicity in optical microscopy and AFM images was measured using a Fast Fourier

Transform (FFT) using the Python package SciPy[289] and Gwyddion.[290] The code used to analyze pattern periodicity and pattern quality is available at github.com/jsbangsund/pattern-image-analysis. Optical diffraction measurements were performed at normal incidence using a laser with a wavelength of $\lambda = 473$ nm having a spot diameter of 0.8 mm, and images were captured on a 16 cm $\times$ 16 cm screen with a camera length of 9 cm (schematic of measurement geometry is shown in Figure 8.15). X-ray diffraction patterns were taken in the theta-theta geometry with a Co Kα source ($\lambda = 0.179$ nm).

Crystal growth rates were extracted from in situ optical microscopy time series. To automate grain boundary detection, images were histogram equalized, thresholded and despeckled. The code and interactive graphical user interface used to extract crystal growth rates is provided at github.com/jsbangsund/crystal-growth-rate-analysis.

8.8 Acknowledgments and Contributions

The work presented in this chapter was originally published in:

J. S. Bangsund, T. R. Fielitz, T. J. Steiner, K. Shi, J. R. V. Sambeek, C. P. Clark, and R. J. Holmes. “Formation of Aligned Periodic Patterns during the Crystallization of Organic Semiconductor Thin Films”. En. *Nature Materials* (2019), p. 1. DOI: 10.1038/s41563-019-0379-3

This work was the most collaborative effort of my graduate studies, and it would not have been possible without the contributions of my colleagues. Dr. Thomas R. Fielitz initiated the project, and handed off "just a few last details" to me, completely unsuspecting of the coordinated effort this would become. Jack R. Van Sambeek and Trevor J. Steiner together prepared most of the samples and performed the majority of the annealing and microscopy presented here. Kaicheng Shi performed AFM. Catherine P. Clark performed XRD and also frequently discussed the project with me over its two-year duration.

Detailed contributions: J.S.B. designed the experiments and analysed the data. T.R.F. made the initial observation and characterization of the pattern formation phenomenon. J.S.B., T.R.F., T.J.S. and J.R.V.S. prepared, annealed and imaged samples. K.S. performed tapping mode AFM measurements. J.R.V.S. fabricated devices for the outcoupling experiments. J.S.B. performed peak force AFM measurements. C.P.C. performed XRD measurements. J.S.B., T.R.F. and R.J.H. interpreted the results and wrote the manuscript. All authors discussed and reviewed the

manuscript. R.J.H. supervised the work.

Funding for this work was provided by the NSF Program in Solid-State and Materials Chemistry under grant numbers DMR-1307066 and DMR-1708177. I was supported by the NSF Graduate Research Fellowship under grant no. 00039202. We acknowledge helpful discussions with C. Teresi, as well as the groups of P. Dauenhauer, C. D. Frisbie and R. L. Penn for the use of their high-speed camera, atomic force microscope and X-ray diffractometer, respectively. Parts of this work were carried out in the Characterization Facility, University of Minnesota, which receives partial support from the NSF through the MRSEC program.

8.9 Supplemental details

8.9.1 Measuring pattern wavelength

Optical diffraction

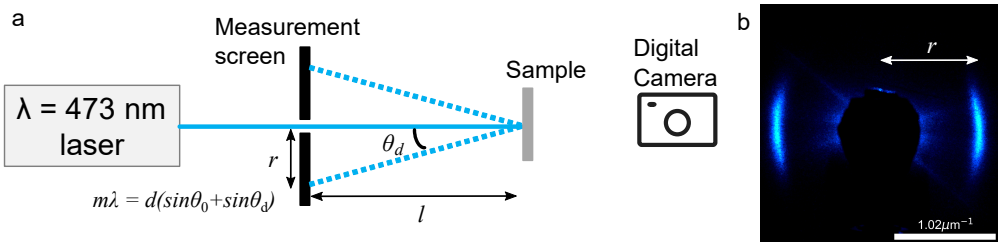

Fig. 8.15. (**a**) Schematic of optical diffraction measurement. The illuminated measurement screen is captured with a DSLR camera, and distances in the image are calibrated with a ruler. The laser spot size is approximately 1 mm in diameter. (**b**) Example diffraction image.

The diffraction equation for gratings is:[249]

$$m\lambda = d(\sin\theta_i + \sin\theta_d) \tag{8.1}$$

Where θ_i is the incident angle from normal, θ_d is the diffracted angle, m is the diffraction order, d is the spacing, and λ is the wavelength of incident light.

For our geometry, we measure a "camera length", or the distance from the sample to the measurement screen (l), and the distance from the specularly reflected beam and the diffraction

ring, r. In terms of these measured parameters:

$$\sin\theta_d = \frac{r}{\sqrt{r^2 + l^2}} \tag{8.2}$$

Scalebars in units of inverse d-spacing are often given for TEM diffraction images. This can be done because TEM's have large camera lengths ($l > 200$ mm) for relatively small camera sizes ($r < 10$ mm), so the small angle approximation is valid:

$$\sin\theta \approx \tan\theta \approx \theta \approx r/l$$

Scalebars are not accurate for diffraction images if not at small angles (less than a few degrees) as shown in Figure 8.16. For this reason, scalebars on diffraction images earlier in this chapter are given at the inverse length of the d-spacing.

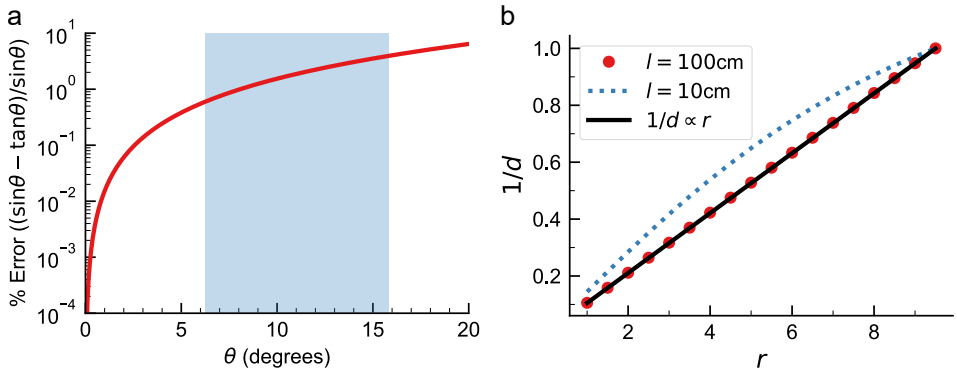

Fig. 8.16. Error from small-angle approximation in diffraction images with a small camera length: (**a**) Percent error of the small-angle approximation as a function of diffraction angle. The shaded region is approximately the region of interest for the diffraction images taken here. (**b**) Inverse d-spacing as a function of radius from the center of the diffraction image for different camera lengths. For a large camera length, the dependence is linear, meaning the small-angle approximation is valid and a scalebar can accurately be used. For small camera lengths, such as those used here, the dependence is no longer linear.

Below, code for extracting d-spacing from optical diffractions is included. The function rescaleAxes is derived by using Pythagorean's theorem on each calibration point, and solving

for scaling factors a and b (cm/pixel conversion) for the x and y axes, respectively:

$$\begin{aligned} r_1^2 &= (ax_1)^2 + (by_1)^2 \\ r_2^2 &= (ax_2)^2 + (by_2)^2 \\ a^2 &= \frac{r_1^2 - b^2 y_1^2}{x_1^2} \\ b^2 &= \frac{r_2^2 - r_1^2/x_1^2}{y_2^2 - y_1^2 x_2^2/x_2^2} \end{aligned} \tag{8.3}$$

```
import imageio, glob, os
import numpy as np
# Helper functions
def getScalingFactors(img,origin,p1,p2,r1,r2):
    '''Function to rescale axes, given calibration points
    origin = tuple of Y,X indices of origin
    p1,p2 = tuples of Y,X of two calibration points
    r1,r2 = distance from origin of calibration points
    returns a and b, conversion factors for x and y axes
        from pixels to length unit of r1 and r2
    '''
    # First, specify origin
    # Get length of each dimension
    ylen, xlen = img.shape
    # Make x and y arrays
    X = np.arange(0,xlen,1)
    Y = np.arange(0,ylen,1)
    X = X-X[origin[0]]
    Y = Y-Y[origin[1]]
    x1,x2,y1,y2 = X[p1[0]],X[p2[0]],Y[p1[1]],Y[p2[1]]
    b = np.sqrt( (r2**2 - r1**2/x1**2)
                / (y2**2 - y1**2 * x2**2 / x1**2) )
    a = np.sqrt( (r1**2 - b**2 * y1**2)/x1**2 )
    return a,b
def getScaledAxes(img,origin,a,b):
    # Get length of each dimension
    ylen, xlen = img.shape
```

```
28      # Make x and y arrays
29      X = np.arange(0,xlen,1)#np.linspace(-5,5,num=xlen)
30      Y = np.arange(0,ylen,1)#np.linspace(-5,5,num=ylen)
31      # Align origin and rescale to match distance
32      X = X-X[origin[0]]
33      Y = Y-Y[origin[1]]
34      X = X*a
35      Y = Y*b
36      return(X,Y)
37  def radial_profile(img,origin,a,b,factor=300):
38      '''
39      a is length/pixel conversion for x
40      b is length/pixel conversion for y
41      origin is (x,y) tuple of the origin
42      factor defines how many bins are integrated over
43      because the integration method uses integer bins
44      '''
45      y, x = np.indices((img.shape))
46      r = np.sqrt(((x-origin[0])*a)**2 + ((y-origin[1])*b)**2)*factor
47      r = r.ravel().astype(np.int)
48      tbin = np.bincount(r, img.ravel())
49      nr = np.bincount(r)
50      radialprofile = tbin / nr
51      r=np.indices((radialprofile.shape))[0]/factor
52      return r,radialprofile
53  def d_spacing(r,l=9,m=1,wavelength=474.5,theta_i=0):
54      '''
55      r is measured radius on screen in cm
56      l is distance from sample to screen in cm
57      m is diffraction order
58      theta_i is incident angle from normal
59      wavelength is the laser wavelength
60      default parameters are for the geometry of the
61      diffraction measurement used in this work
62      '''
63      return m*wavelength / (np.sin(theta_i) + r/np.sqrt(r**2+l**2))
64  # Calibration is performed on an image with a scalebar
65  # Manually calibrate these points
66  # Plot the image using %matplotlib notebook (interactive)
```

```
# Then find indices for origin and calibration points
origin = (2101,1405) # x,y in pixel #
p1 = (2992,1430) # x,y, calibration point
r1 = 5 #cm, distance from origin to p1
p2 = (2104,534) # x,y, second calibration point
r2 = 5 #cm
a,b = getScalingFactors(calibration_image,origin,p1,p2,r1,r2)
# Select images to analyze
diffractionDir = 'path\to\folder'
image_files = glob.glob(os.path.join(diffractionDir,'*.jpg')
images = []
for idx,f in enumerate(image_files):
    images.append(imageio.imread(f,mode='L'))
# Loop through images and extract d-spacing
r_peak=[]
r_avg=[]
r_std=[]
d_avg=[]
d_std=[]
for idx,image in enumerate(images):
    r,radial = radial_profile(image,origin,a,b,factor=100)
    # Crop pixels below r=0.5 cm or intensity<10 (approximate noise floor)
    crop_idx = np.argwhere( (r>2.2) & (radial>10) )
    r = r[crop_idx]
    radial=radial[crop_idx]
    # Find peak, avg, and standard deviations
    r_peak.append(r[radial==np.nanmax(radial)][0])
    r_avg.append(np.average(r,weights=np.nan_to_num(radial)))
    r_std.append(np.sqrt(np.average((r-r_avg[idx])**2,
                         weights=np.nan_to_num(radial))))
    d_avg.append(d_spacing(r_peak[idx]))
    d_std.append((-d_spacing(r_avg[idx]+r_std[idx])+
                  d_spacing(r_avg[idx]-r_std[idx]))/2)
```

Fourier Transforms of optical micrographs

Fast Fourier Transforms (FFTs) can be used to convert a real-space image into frequency-space and vice-versa. Conceptually, the methods presented below are quite similar to the optical diffraction approach. The reason for this is that diffraction provides a measurement of reciprocal space—in essence, taking an FFT of a real-space image provides the same information as a diffraction image.

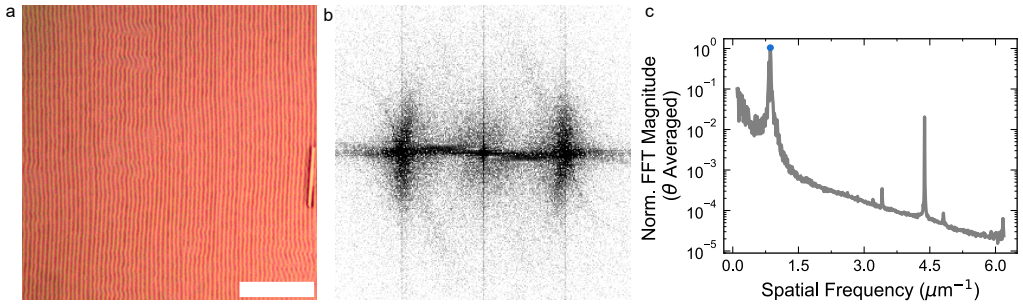

Fig. 8.17. Example FFT analysis to extract the pattern d-spacing from an optical micrograph: (**a**) Optical micrograph of 30-nm-thick TPBi film annealed at 162.5 °C, (**b**) FFT image of the optical micrograph, (**c**) θ-averaged (i.e. azimuthally-integrated) FFT power density spectrum. The primary peak, marked by the blue circle, corresponds to the pattern d-spacing.

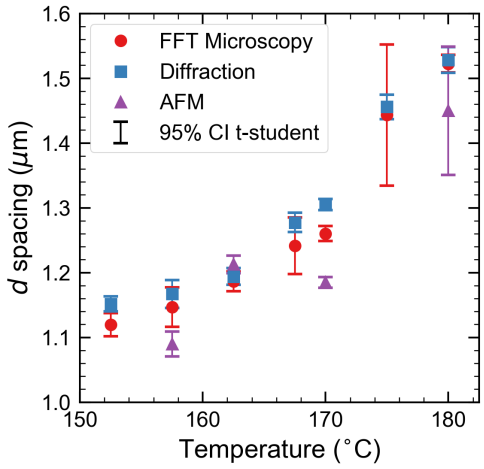

Fig. 8.18. Pattern periodicity extracted from various measurement methods for a 30-nm-thick TPBi film on Si. d-spacings extracted from AFM show slightly more variation than the other techniques due to the small sampling area of AFM images (100 μm^2). Error bars are 95% confidence intervals using the Student's t-distribution for small sample sizes and averaged over at least ten images for measurements from optical microscopy and diffraction, and at least three images for measurements from AFM.

The core functions used to calculate pattern periodicity are included below (see source code in image_helper.py at: github.com/jsbangsund/pattern-image-analysis):

```
##### Imports
from skimage.color import rgb2gray
from scipy.signal import argrelextrema
from scipy import fftpack
import numpy as np
##### FFT analysis
def radial_profile_fft(fft_img,scale,factor=300):
    '''
    This function azimuthally integrates a 2D fft of an image
    to generate a one dimensional frequency distribution function
    i.e. power density (radial_profile) vs. 1/length (k)

    Inputs:
    fft_img = numpy array of an fft image, created by e.g.:
            img = imageio.imread(image_file)
            gray_image = rgb2gray(img)
            # Rescale to 0-255 (instead of 0-1)
            gray_image = ((gray_image - np.min(gray_image))/
                          (np.max(gray_image) - np.min(gray_image)))
            # Take FFT and shift so 0 frequency is at center
            fft_img=fftpack.fft2(gray_image)
    scale = length/pixel conversion for x
    factor = integer, how many bins are integrated over

    Outputs:
    k = wavevector, or 1/length spatial frequency
    radial_profile = azimuthally averaged radial profile of 2D fft
    '''
    # Get frequency wavenumbers based on image size
    # Then shift so that center of image is 0 frequency
    ky = np.fft.fftshift(np.fft.fftfreq(fft_img.shape[0],
                                        scale))
    kx = np.fft.fftshift(np.fft.fftfreq(fft_img.shape[1],
                                            scale))
    kx=kx*np.ones(fft_img.shape)
    #[:,None] changes shape from (N,) to (N,1)
```

```
    #identical to ky.reshape((ky.shape[0],1))
    ky=ky[:,None]*np.ones(fft_img.shape)
    k = np.sqrt(kx**2 + ky**2)*factor
    k=k.ravel().astype(np.int)
    # Average azimuthally
    # See: https://stackoverflow.com/a/21242776
    tbin = np.bincount(k, fft_img.ravel())
    nr = np.bincount(k)
    radialprofile = tbin / nr
    k=np.indices((radialprofile.shape))[0]/factor
    # return arrays without region near origin
    # as this region is often saturated
    s_idx = 10#np.where(1/k < 10)[0][0]
    return k[s_idx:],radialprofile[s_idx:]
# Calibration values for Nikon microscope
micron_per_pixel = {'4x':1000/696, '10x':1000/1750,
                    '20x':500/1740, '50x':230/2016}
def d_from_fft(image,scale=micron_per_pixel['50x'],
               order=20,factor=100,
               d_lower=0.7,d_upper=1.8):
    '''
    This function identifies the primary periodic lengthscale, d
    of an image by taking an FFT, azimuthally integrating, and
    finding relative extrema in this power density distribution.

    Inputs:
    image = numpy array of an image, created by e.g.
                imageio.imread(image_file)
    scale = length/pixel conversion for x
    order = How many points on each side to use for the comparison,
            passed to argrelextrema, see docs:
    factor = integer, how many bins are integrated over
             passed to radial_profile_fft
    d_lower = lower d-spacing bound in peak search. Same units as scale
    d_upper = lower d-spacing bound in peak search. Same units as scale

    Outputs:
    dictionary containing keys:
        d_peak = primary peak_idx
```

```
        k = wavevector, or 1/length spatial frequency
        radial = azimuthally averaged radial profile of a 2D fft image
        peak_idx = list of peak indices identified by argrelextrema
    '''
    gray_image = rgb2gray(image)
    # Rescale to 0-255 (instead of 0-1)
    gray_image = ((gray_image - np.min(gray_image))/
                  (np.max(gray_image) - np.min(gray_image)))
    # Take FFT and shift so 0 frequency is at center
    fft_image=fftpack.fft2(gray_image)
    fft_image=fftpack.fftshift(fft_image)
    # Take power spectral density
    # Not sure if squared is correct or not
    power2D = np.abs(fft_image)**2
    # Get azimuthally averaged radial profile of k=1/d
    k,radial=radial_profile_fft(power2D,scale,factor=factor)
    # Find local maxima
    # order could possibly be reduced to 10
    # background subtract might be useful
    peak_idx = argrelextrema(radial,np.greater,order=order)[0]
    # Take d only within reasonable range
    # This could be more robust
    d_peaks = 1/k[peak_idx]
    d_peak = d_peaks[(d_peaks>d_lower) & (d_peaks<d_upper)]
    if len(d_peak>=1):
        return {'d_peak':d_peak[0],'k':k,
               'radial':radial,'peak_idx':peak_idx}
    else:
        return {'d_peak':-1,'k':k,'radial':radial,'peak_idx':peak_idx}
```

8.9.2 Quantifying pattern quality

One possible measure of the periodic pattern quality (i.e. the degree of alignment and consistency of the feature wavelength) is the magnitude of long wavelength portion of the power density spectra from FFTs of images of the corrugated surface. As shown in Figure 8.19, the FFT magnitude for wavelengths greater than two microns is larger at higher temperatures, due

to the increasing disorder seen at high temperatures. However, for the multiple images at each temperature plotted here, variations in the FFT spectra are relatively minor, which indicates that the quality of the grating is reproducible across multiple images.

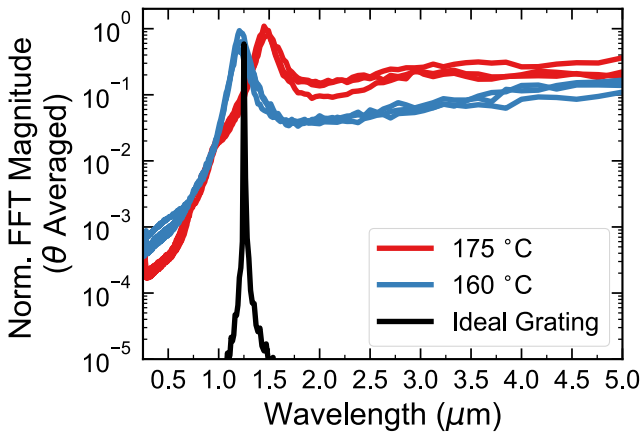

Fig. 8.19. Azimuthally-averaged FFT power spectra for 30-nm-thick TPBi on Si annealed at 160 and 175 °C, compared to an ideal sinusoidal grating. As is noted in the text, increasing temperature increases the d-spacing, but there is not a large difference in the breadth of the FFT peak. However, there is a considerable increase in the amplitude of the long-wavelength portion of the spectrum at high temperatures, and this portion is attributed to the increased disorder seen at temperatures above 170 °C (as shown in Figure 8.2g-h). Image areas are 0.04 mm^2 (234 μmx176 μm).

As another demonstration of the correspondence between grating disorder and long wavelength FFT magnitude, images for a single sample along ordered and disordered growth directions are compared in Figure 8.20. As noted in the manuscript text, and shown in Figure 8.24, the grating becomes more disordered along certain fast-growing directions. This leads to a large long-wavelength magnitude in the FFT spectrum, particularly from 2–4 μm. This region can then be used to compare a large number of images to quantify how representative a given image is of the average grating quality. A histogram of the average FFT magnitude from 2–4 μm of a large number of images for samples with similar preparation as that in Figure 8.1f is included in Figure 8.21. The histogram demonstrates that the grating quality of the image selected in Figure 8.1f is reasonably representative, while certain areas are more disordered. Note that images containing multiple orientations of the pattern (e.g. between grains) will also show an elevated FFT magnitude in this range. Hence, to use this as a useful proxy for pattern quality, all selected images are cropped to contain a single pattern orientation.

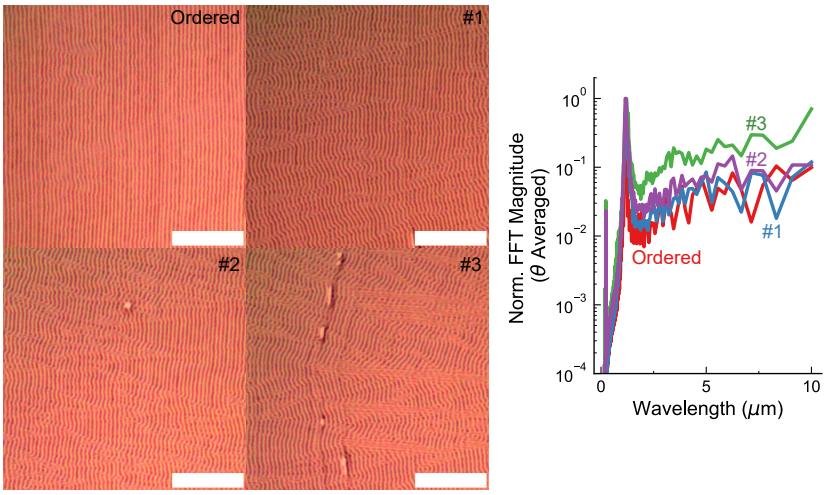

Fig. 8.20. Images along ordered ("Ordered") and disordered (Images 1-3) growth directions. As can be seen in the normalized FFT magnitude plotted at the right, the region of the FFT spectrum from 2–4 µm corresponds well with the qualitative degree of order of the grating. Scalebars are all 20 µm.

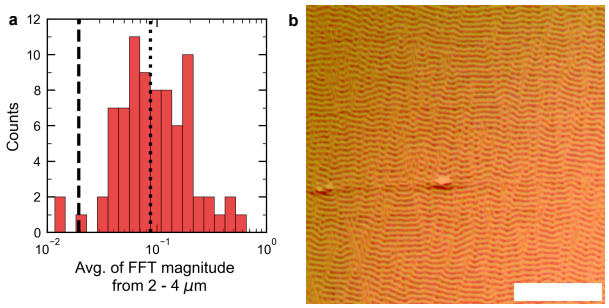

Fig. 8.21. (**a**) Histogram of the average FFT magnitude from 2–4 µm for 80 images of 30 nm TPBi annealed at 163 °C taken across samples from two separate deposition runs. The area of each image is 0.005 mm^2. The dashed black line corresponds to the average FFT magnitude from 2–4 µm for the image in Figure 8.1f. The dotted black line corresponds to the median pattern quality. (**b**) The image most representative of the median pattern quality. Scalebar is 20 µm.

Example code for calculating the average disorder is included below (see more examples in the "Pattern Quality Analysis.ipynb" notebook at: github.com/jsbangsund/pattern-image-analysis):

```
import os, glob
import numpy as np
from skimage import exposure
from imageio import imread
# Example analysis of pattern quality
# Select images to analyze
thicknessDir = 'Path\to\image_folder'
image_files = glob.glob(os.path.join(thicknessDir,'*.tif'))
# Loop through and calculate FFTs
```

```
fft_no_crop=[]
for i,image_file in enumerate(image_files):
    # Load file
    rot_img = imread(image_file)
    # Improve contrast
    rot_img = exposure.equalize_hist(rot_img)
    # d_from_fft function can be found in image_helper.py
    fft_no_crop.append(d_from_fft(rot_img,order=15,d_upper=2))
# average the portion of the fft spectrum between 2 and 4 microns
# and normalize to the primary peak
average_fft_2_to_4_um=[]
for i,d in enumerate(fft_no_crop):
    wavelength=1/d['k']
    # This normalization range is selected in the typical
    # d-spacing window, to avoid normalizing to noise at
    # long wavelengths (low frequencies)
    norm_range_idx = np.logical_and(wavelength<2.5,wavelength>.8)
    norm_fft = d['radial']/np.amax(d['radial'][norm_range_idx])
    avg_range_idx = np.logical_and(wavelength<4,wavelength>2)
    average_fft_2_to_4_um.append(np.mean(norm_fft[avg_range_idx]))
# Plot histogram
import matplotlib.pyplot as plt
plt.hist(average_fft_2_to_4_um,bins=25,edgecolor='k')
plt.xlabel('Avg. of FFT magnitude \n from 2 - 4 $\mu$m')
plt.ylabel('Counts')
```

8.9.3 Diffusion model

The Mullins's surface diffusion equation at steady-state with a moving reference frame, $\varepsilon = x - ut$, which accounts for the propagating crystal growth front, can be written as:[275,292]

$$By'''' - uy' + \frac{\partial y}{\partial t} = 0 \tag{8.4}$$

where u is the crystal growth rate, y is the surface height, and $B = D_s\gamma\Omega^2\nu/kT$ is a collection of constants (surface diffusivity, surface tension, molecular volume, number of molecules per unit area, respectively).

Hasebe, Musumeci, and Yu [272] applied the following boundary conditions:

$$\begin{aligned} y(\infty) &= 0 \\ y'(0) &= 0 \\ y'''(0) &= j = \frac{F_c \Omega}{b} \end{aligned} \tag{8.5}$$

where j is the crystallization flux and F_c is the number flux of molecules attaching to the crystal.

Applying these B.C.'s results in the following solution:

$$y = \frac{2j}{\alpha^3\sqrt{3}} \exp\left(-\frac{\alpha\varepsilon}{2}\right) \cos\left(\frac{\sqrt{3}}{2}\alpha\varepsilon - \frac{\pi}{6}\right) \tag{8.6}$$

Parameters similar to those in refs. [272, 278] were used to model the AFM profiles from Figure 8.4, only allowing surface diffusivity, film thickness, and crystal growth rate to vary.

8.9.4 Supplemental figures and tables

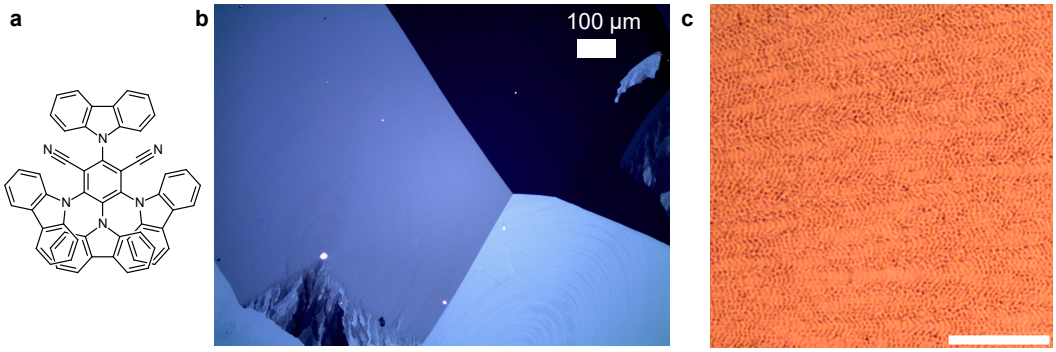

Fig. 8.22. (**a**) molecular structure of 4CzIPN, a green TADF emitter. (**b**) Platelet-like crystals in 4CzIPN (30 nm film on Si annealed at 185 °C). Growth rings were observed in most grains, suggesting that patterns may form in the material under the right conditions. (**c**) Disordered pattern formation with an average spacing of $d \approx 0.96\,\mu$m for a 30-nm-thick film of 4CzIPn on Si annealed at 195 °C. Scalebar is 20 µm

Table 8.1. Materials investigated for crystallization and pattern formation. Rows shaded in green formed periodic patterns. Rows shaded in yellow showed some platelet-like grains and some traces of pattern formation, suggesting that they could be optimized. Where available, thin film T_g values are provided in parentheses.

Material	**Bulk** T_g °C	d nm	**Morphology**	**Notes**
TPD	58[293] (74)[265]	—	—	No crystallization in range of 60–120 °C
CBP	62[294]	—	Dendritic	No grating. Rapid crystallization from 110–140 °C
m-MTDATA	75[284] (92)[265]	—	—	Rapid dewetting
BCP	83[295]	—	Dendritic	No grating. Rapid crystallization from 110–165 °C
BAlq	92[296]	—	—	Minimal crystallization observed
α-NPD	95[284]	980	Platelet	30 nm film at 165 °C, poor coverage
4p-NPD	—	—	—	Dewetting, no observed crystallization
26DCzPPy	102[297]	—	—	Rapid dewetting
3TPYMB	106[298]	—	—	No crystallization in range of 160–225 °C
mCBP	107[299]	—	—	Extensive dewetting above 165 °C
CDBP	—	—	—	Dewetting, no crystallization 165–200 °C
BCBP	120[285]	1600	Platelet	35 nm film at 165 °C, good coverage, slow growth, somewhat poor quality
TPBi	124[177,300]	1250	Platelet or dendritic	30 nm film at 165 °C, full coverage
DMFL-CBP	131[301]	—	—	Does not crystallize in range of 110–220 °C
Rubrene	~150[263]	1750	Platelet or dendritic	Pattern formation above 180 °C
TCTA	151[302]	—	Platelet or dendritic	T. Fielitz saw traces of pattern formation but T. Steiner could not reproduce this from 170–230 °C
Alq3	175[303]	—	Needle-like	Small, slow-growing needle crystallites)
4CzIPN	—	—	Platelet	Large area platelet-like grains. Signs of growth rings and some disordered pattern formation from 180–195 °C

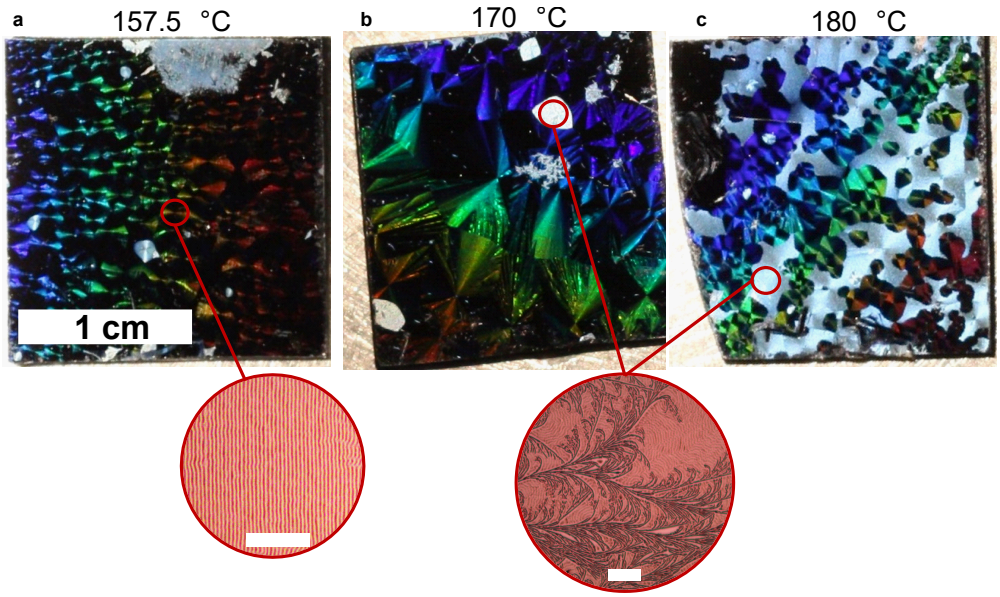

Fig. 8.23. Macroscopic photos for 30-nm-thick TPBi on Si annealed at (**a**) 157.5 °C, (**b**) 170 °C, and (**c**) 180 °C. The 1 cm scale bar applies to all three images. Insets show unpolarized optical microscopy images of representative morphologies for the two crystalline phases which are observed. Scale bars are 20 µm in both insets. For samples annealed between 155 and 170 °C, surface coverage of the corrugated, platelet-like crystal phase is >90%. At temperatures between 170–180 °C, a dendritic phase becomes increasingly dominant, comprising 20-80% of the surface area. At temperatures below 155 °C, the platelet like phase remains dominant, but growth rate slows sufficiently to reduce the surface coverage of the corrugated regions (see Figure 8.2e and Figure 8.25). The color in the platelet-like grains is due to diffraction of the oblique illumination light source by the periodic patterns. These images illustrate that the periodic features have complete surface coverage in the platelet-like grains. Dark regions where diffraction is not visible are simply due to the orientation of the illumination light, and diffraction in these regions is evident upon rotating the samples.

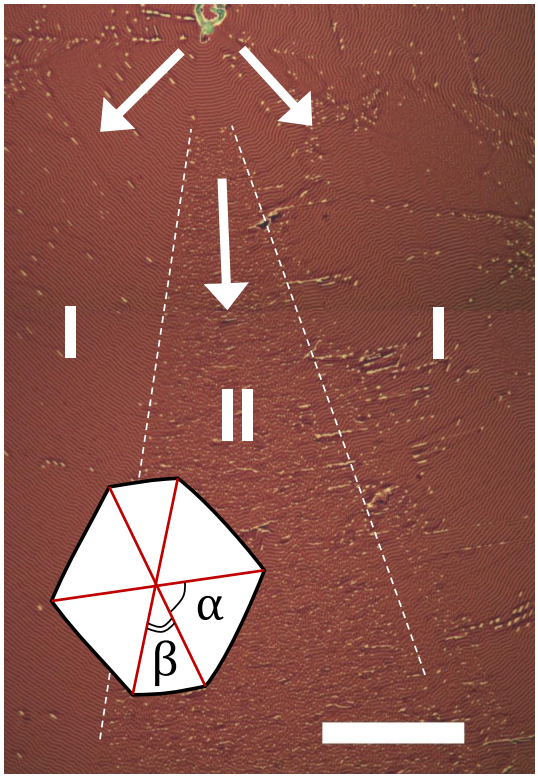

Fig. 8.24. Unpolarized optical micrograph of a TPBi film annealed at 180 °C, showing growth from the nucleation site (arrows) and areas of periodic (I) and disordered (II) domains. The inset schematic shows a TPBi grain growing, with $\alpha = 75°$ and $\beta = 30°$ for the above film. Regions with a high degree of disorder tends to occur along crystal directions which are oriented to give a more rapid growth rate of individual domains, as in Region II. The dissimilarity in angles α and β results in Region II growing approximately 20% faster. Film is 30-nm-thick with a 60-nm-thick epitaxial TPBi layer deposited after annealing to improve visibility. Scale bar is 50 µm. Figure from Dr. Thomas Fielitz.

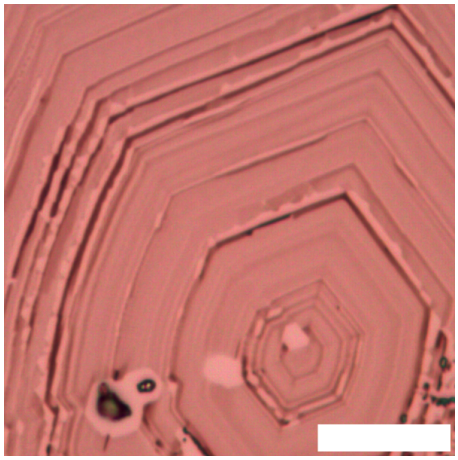

Fig. 8.25. Unpolarized optical micrograph of a 30-nm-thick TPBi film annealed at 145 °C, showing formation of growth rings spaced at random intervals by flat crystalline regions. Scalebar is 20 µm.

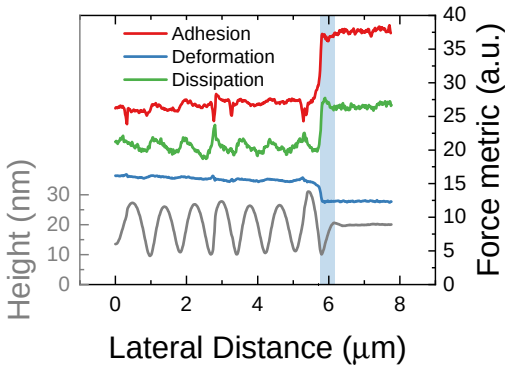

Fig. 8.26. Mechanical contrast between amorphous and crystalline phases. Contrast is seen in all mechanical property metrics: adhesion, deformation, and dissipation.

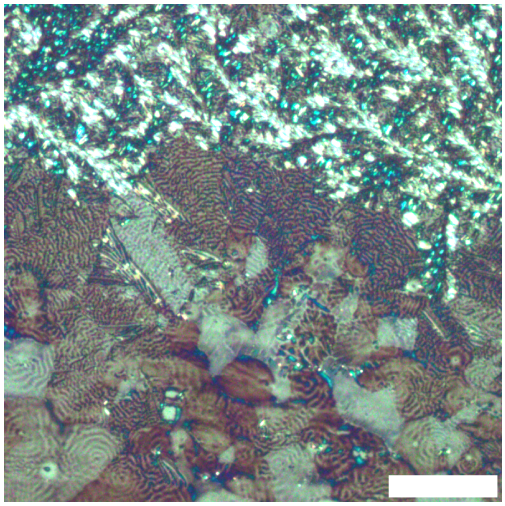

Fig. 8.27. Disordered morphology of a 60-nm-thick film of TPBi on a Si substrate annealed at 160 °C. At high thicknesses (>50 nm), pattern quality, surface coverage, and long-range alignment is disrupted by increases in the nucleation density, leading to smaller grains, and increased prominence of the dendritic crystalline phase. Scale bar is 50 µm.

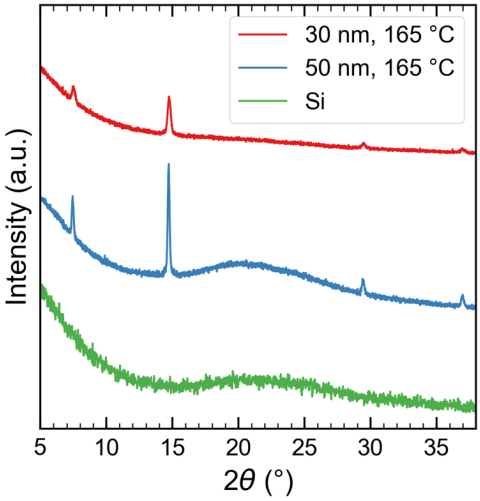

Fig. 8.28. X-ray diffraction patterns taken in the theta-theta geometry for 30- and 50-nm-thick TPBi films annealed at 165 °C on Si substrates, and a background scan on an uncoated Si substrate. Both films show the same peaks and are confirmed to be crystalline. Unannealed, glassy films do not show any diffraction peaks.

Table 8.2. Tapping Mode (attractive regime) AFM scan parameters for Figure 8.7d-f

Parameter	**Figure 8.7d**	**Figure 8.7e**	**Figure 8.7f**
Scan Size		10 µm	
Aspect Ratio		1	
Pixel Dimensions		512 × 512	
Scan Rate		1 Hz	
Scan Angle		0°	
Feedback Integral Gain	1.000	1.225	1.000
Feedback Proportional Gain	5.000	5.000	5.000
Amplitude Setpoint	362.3 mV	334.2 mV	379.9 mV
Drive Frequency	268.3 Hz	260.0 Hz	268.3 Hz
Drive Amplitude	10.4 mV	15.6 mV	9.2 mV
Cantilever Type		NanoWorld ArrowTM NCR	
Cantilever Resonance Frequency (nominal)		285 Hz	
Cantilever Spring Constant (nominal)		42 N/m	
Cantilever Length		160 µm	
Cantilever Mean Width		45 µm	
Cantilever Thickness		4.6 µm	

Table 8.3. Peak Force Quantitative Nanomechanical AFM scan parameters for Figure 8.4

Parameter	Figure 8.4a,b	Figure 8.4c-d
Scan Size	6.45 µm	16.6 µm
Aspect Ratio	1	1
Pixel Dimensions	512 × 512	400 × 400
Scan Rate	0.8 Hz	0.4 Hz
Peak Force Setpoint	4 nN	4 nN
Feedback Gain	22	15
Peak Force Amplitude	150 nm	150 nm
Peak Force Frequency	2000 Hz	2000 Hz
Z-Limit	1 µm	1 µm
Cantilever Type	HQ:NSC36/AL BS	
Cantilever Spring Constant (nominal)	0.6 N/m	
Tip Radius	8 nm	
Tip Half Angle	20°	
Cantilever Length	130 µm	
Cantilever Mean Width	32.5 µm	
Cantilever Thickness	1.0 µm	

9

Conclusions and Future Directions

Throughout this dissertation, we have uncovered deeper insight into the mechanisms of efficiency roll-off and degradation in OLEDs using combined electrical and optical analysis techniques. In terms of degradation, we have shown that multiple kinetic pathways determine the degradation rate, where the radiative efficiency of the emitter (η_{PL}) is deteriorated by exciton-induced reactions in the emissive layer, while charge leakage and non-radiative recombination losses (η_{EF}) are aggravated by reactions outside the emissive layer involving polarons or at interfaces where exciton-polaron quenching interactions are significant. These findings led to the development of a design method in commercially relevant materials systems, where a wide-energy-gap, insulating host is added to an ambipolar emissive layer to tune charge transport and reduce interfacial degradation.

We have further unraveled how host triplet states can accelerate degradation, demonstrating how minor molecular structural differences can lead to drastic changes in device stability. In this particular case study, the addition of two methyl groups to CBP, an archetypical carbazole host, induced steric twisting which in turn pushed the excited state from the central biphenyl group to the carbazole end groups. Here, the excited state could more easily couple with neighboring molecules, forming an intermolecular excimer state which accelerated degradation. This finding—which could be applied as a materials screening method—relied on combined electrical and optical degradation schemes and comparisons between singlet (fluorescent) and triplet (phosphorescent) emitter stability to decouple the role of different spin states.

By modifying these optical measurements to be superimposed over an electrically-biased device, we have also gained further insight into quenching and efficiency roll-off in OLEDs. Notably, we have shown that exciton quenching near peak EQE, and even prior to device turn-on, can be non-negligible—in some cases exceeding 20-35%. Accounting for this effect is critical to accurate quantification of the components of EQE. Here, this analysis revealed that many standard devices have near-unity charge balance, contradicting conventional estimates

which have placed charge balance at 80-90%. We further demonstrated that this sub-turn-on quenching effect was a consequence of preferred molecular orientation, which leads to net polarization, of the electron transport layer. By heating films during deposition or selecting non-polar molecules, this effect can be avoided entirely.

Together, the findings in this work highlight the advantages, but also the limitations, of using combined electrical and optical analysis. Photoluminescence-based measurements are fundamentally limited by the different mechanisms and spatial distribution of electrical and optical excitation. With careful device design, error from this spatial mismatch can be minimized. The analysis approaches presented here can also be used to estimate this error and the range of physical situations which can describe a given measurement. Wider application of these approaches may help researchers more quickly develop new materials and design strategies for efficient and durable OLEDs.

Going forward, there are several key areas where this work could be expanded on to further advance the phyics of OLEDs and emerging LED materials systems.

9.1 Understanding SOP and low-bias quenching

The work in Chapter 6 focused only on two ETLs: TPBi and B3PyMPM. This technique should be applied to a wider range of ETL materials to determine whether these findings are general. The magnitude of SOP varies widely between electron transport materials,[20] depending both on the permanent dipole moment of the molecule and the tendency for the film to show preferred orientation. How this magnitude of SOP influences quenching should be examined closely. It seems likely that low-bias quenching scales linearly with SOP magnitude (i.e. GSP slope), as this reflects the interfacial charge density. But it is also possible that there is a threshold of sorts, below which the SOP-induced charge can be effectively compensated by injected electrons. This study should ideally include partnering with industry to examine commercially-relevant materials. In preliminary work on proprietary devices from DuPont, included in Appendix D, we find that low-bias quenching is minimal in most commercial devices and that SOP may have been mostly optimized out of commercial materials. Still, these materials do not appear to be entirely non-polar, confirming our current view that a certain magnitude of SOP can be tolerated without sacrificing performance.

Another related area which should be examined is how the energy levels and relative mobilities of the transport layers influence low-bias quenching. Several recent studies have shown that the mobility of the emissive layer and the transport layers can significantly impact polaron accumulation in the EML, in turn influencing efficiency roll-off and lifetime.[164,200] It seems plausible that, in addition to SOP effects, mobility and injection imbalances could also increase quenching near device turn-on and peak EQE. In preliminary work not included here, we have seen appreciable differences in low-bias quenching by simply varying the hole-injection layer and hole transport layer. These early results suggest that these considerations could be critical to determining the magnitude of low-bias quenching and the peak EQE. They further indicate that the conventional wisdom that changing injection and transport layers will alter charge balance is not necessarily the entire story: instead, changes in bimolecular quenching may be the more dominant effect.

9.1.1 SOP in TADF and oriented emitters

Further study should also be directed at the trade-offs between emitter orientation and spontaneous orientation polarization. Many emitters with horizontal TDM orientation, such as $Ir(ppy)_2(acac)$,[20] show a corresponding PDM orientation. Many TADF emitters (e.g. 4CzIPN, 2CzPN, 4CzPN)[20] also show significant SOP, which has been demonstrated to directly cause field-induced exciton quenching.[57] Having horizontally oriented TDMs is desirable for improving outcoupling efficiency,[22] but as we have shown, SOP can also deteriorate performance (Chapter 6).[237] The method to eliminate SOP by heating during deposition would also necessarily eliminate TDM orientation. To fully optimize device performance, these competing effects should be balanced and their relative magnitudes compared. Perhaps the EML can be deposited at room temperature, preserving horizontal TDM orientation, while the polar ETL can be heated to remove SOP. Alternatively, it may be possible to design emitters with oriented TDMs but either small magnitude PDMs or PDMs oriented in-plane (which would avoid surface polarization). These design considerations will also have to be weighed against their potential impacts on charge carrier mobility, exciton lifetime, and other relevant material properties.

It would also be worthwhile to more generally apply our lock-in PL measurement technique to study quenching in TADF-based devices. In preliminary work, shown in Figure 9.1, we found that devices based on the archetypical, green TADF emitter 4CzIPN showed similar magnitudes of sub–turn-on quenching as the $Ir(ppy)_3$ based devices in Chapter 6. Interestingly,

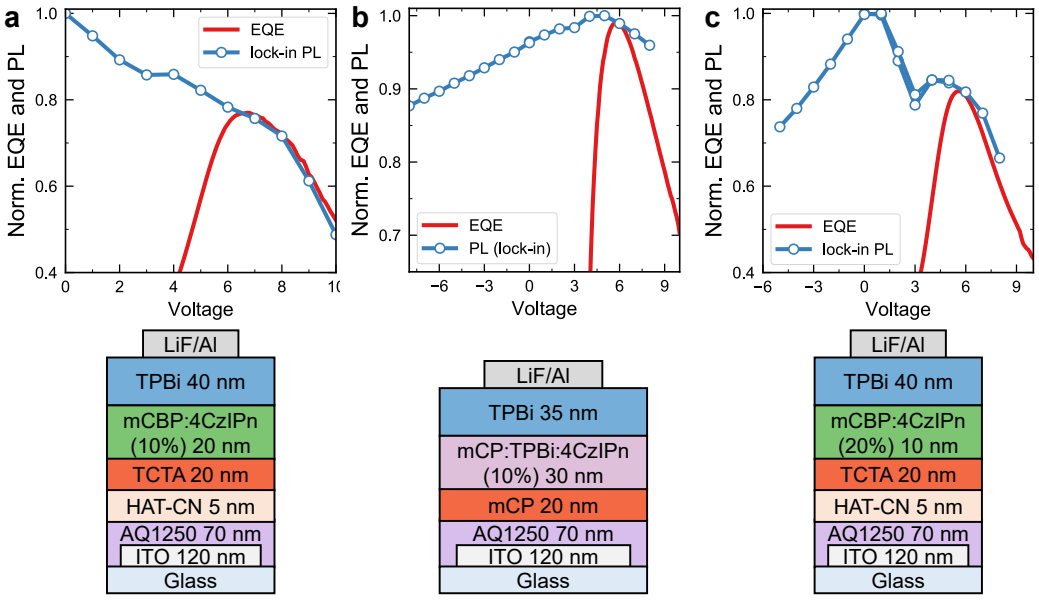

Fig. 9.1. Low-bias quenching in devices with the TADF emitter 4CzIPn: Comparison of PL quenching and EQE (top) and device architecture (bottom) for devices with emissive layers consisting of: (**a**) mCBP:4CzIPn (10%, 20 nm), (**b**) mCP:TPBi:4CzIPn (10%, 30 nm), and (**c**) mCBP:4CzIPn (20%, 10 nm).

these devices also showed significant reverse bias quenching, suggesting that these TADF emitters are more sensitive to electric field induced exciton dissociation (which is consistent with previous reports[57]). We also noted significant differences in the quenching behavior depending on the host: in devices with a mCBP host, PL quenching showed excellent agreement with EQE roll-off, indicating a broad recombination zone and roll-off dominated by exciton quenching; in devices with a mixed mCP:TPBi host, EQE roll-off far exceeded the measured PL quenching, suggesting either a narrow recombination zone or an η_{EF}-dominated roll-off (or both). These emitter and host dependent quenching properties should be studied in more detail to better understand what limits the high brightness performance of TADF-based devices.

9.1.2 Probing spatial distribution of charge carriers

The holes which accumulate in an OLED due to SOP are generally assumed to be tightly confined within several nanometers of the interface of the polar layer.[213] Knowing the extent of this distribution is important for understanding and modeling SOP-induced exciton quenching (as discussed in Section 6.6).

One potential approach to measuring this distribution is to exploit spatial variation of the

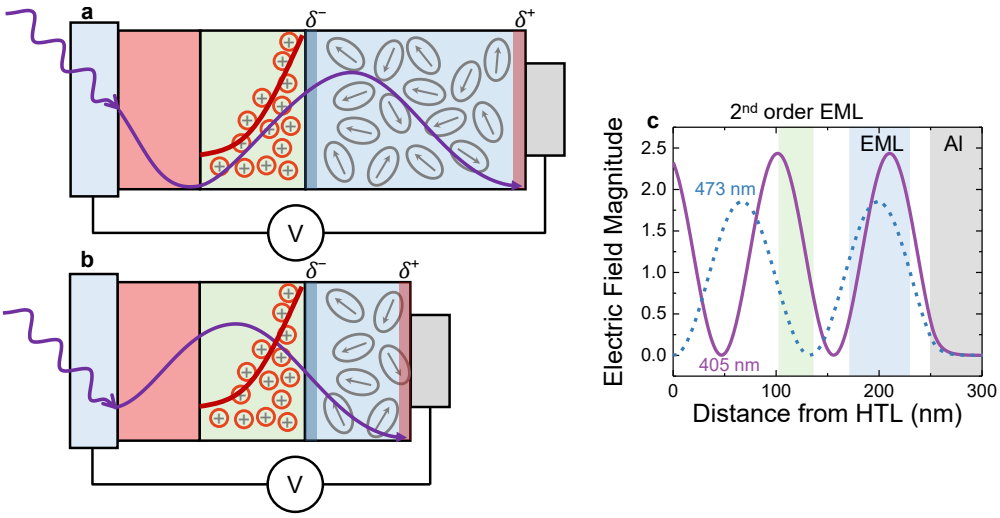

Fig. 9.2. Measuring spatial distribution of SOP-induced hole density: (**a**)-(**b**) Schematic of spatial distribution of holes (red line and circles) and the optical field of the laser (purple line) for two different ETL thicknesses. (**c**) Spatial distribution of optical field for a $\lambda = 405\,\text{nm}$ laser and a $\lambda = 473\,\text{nm}$ laser, illustrating how pump wavelength could be used to probe different areas of the emissive layer.

optical field of the pump laser (shown schematically in Figure 9.2). By changing the wavelength of the pump or the thickness of the ETL, the location of the EML which is probed can be controlled. By probing different areas of the EML, we should be able to determine where the charge density is peaked (presumably near the ETL) and also how broad the distribution is.

To model this measurement, we need the relevant rate equation describing the different pathways which consume excitons:

$$\frac{d\Delta n_{ex}}{dt} = G_{ex} - \frac{\Delta n_{ex}}{\tau} - \frac{1}{2}k_{TT}\Delta n_{ex}^2 - k_{TP}\Delta n_{ex} n_{pol} \tag{9.1}$$

where G_{ex} is the optical exciton generation rate, which can be calculated using the transfer matrix method,[154] Δn_{ex} is the optically-generated exciton density (note that this measurement will operate below device turn-on, so electrically-generated excitons can be neglected), n_{pol} is polaron density (electrons and holes), k_{TP} is the triplet-polaron quenching rate constant, k_{TT} is the triplet-triplet quenching rate constant, and $\tau = 1/(k_r + k_{nr})$ is the natural lifetime.* Note that G_{ex}, k_r, and τ all vary spatially due to cavity effects; k_r and τ can be calculated by

*To simplify this example analysis, I am neglecting diffusion (which would require an additional $D\frac{\partial^2 n_{ex}}{\partial x^2}$ term). Ultimately, diffusion will need to be accounted for to ensure the measurement is accurate, and should be accompanied by supporting exciton diffusion length measurements.[191]

multiplying the intrinsic emitter properties outside a cavity by the Purcell factor.[74] Of the above parameters, only k_{TP} is assumed to be spatially uniform. Because we are using as small a pump power as is practical to achieve good signal, we can neglect TTA. Further, we are measuring at steady-state ($\frac{d\Delta n_{ex}}{dt} = 0$), so we can solve for Δn_{ex} as:

$$\Delta n_{ex,+2V} = \frac{G_{ex}(x)}{\frac{1}{\tau(x)} + k_{TP} n_{pol}(x)} \tag{9.2}$$

These simulated spatial profiles are shown in Figure 9.3.

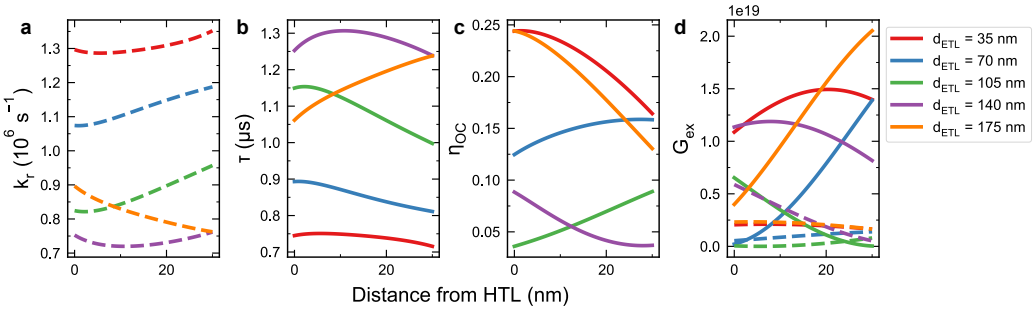

Fig. 9.3. Simulated spatial profiles for (**a**) radiative rate, (**b**) exciton lifetime, (**c**) outcoupling, and (**d**) exciton generation.

At sufficient reverse bias, charges are swept out of the emissive layer and quenching is eliminated. In this case, Δn_{ex} is solved as:

$$\Delta n_{ex,-4V} = G_{ex}(x)\tau(x) \tag{9.3}$$

Now, how can we relate these exciton densities to a physical measurement? Here, we will excite the device with a laser, apply a bias, and measure photoluminescence with a photodetector. When we measure a PL signal as a photodetector current (I_{PD} in A or C s^{-1}), this is directly proportional to the number of outcoupled photons per second. The number of outcoupled photons per second can be related to the exciton density (n_{ex}) within the emissive layer by multipling n_{ex} by the radiative rate (k_r) (accounting for how many excitons relax radiatively per second), weighting by the outcoupling efficiency, and integrating across x (the out-of-plane direction for a device stack). A is the device area, and emission is assumed to be uniform in

this y-z plane (in-plane of the thin film stack).

$$I_{PD} \propto A \int_{EML} k_r(x) n_{ex}(x) \eta_{OC}(x) dx \tag{9.4}$$

By taking a ratio of the PL under forward and reverse biases, we are measuring the fraction of excitons which are quenched. This yields:

$$\frac{I_{PL,+2V}}{I_{PL,-4V}} = \frac{A \int_{EML} k_r(x) \Delta n_{ex,+2V}(x) \eta_{OC}(x) dx}{A \int_{EML} k_r(x) \Delta n_{ex,-4V}(x) \eta_{OC}(x) dx} \tag{9.5}$$

$$\frac{I_{PL,+2V}}{I_{PL,-4V}} = \frac{\int_{EML} \frac{k_r(x) \eta_{OC}(x) G_{ex}(x)}{1/\tau(x) + k_{TP} n_{pol}(x)} dx}{\int_{EML} k_r(x) \eta_{OC}(x) G_{ex}(x) \tau(x) dx} \tag{9.6}$$

For simplicity, we will assume here that $n_{pol}(x)$ decays exponentially from the EML/ETL interface with characteristic length L:

$$n_{pol}(x) = Ae^{-(d_{EML}-x)/L} \tag{9.7}$$

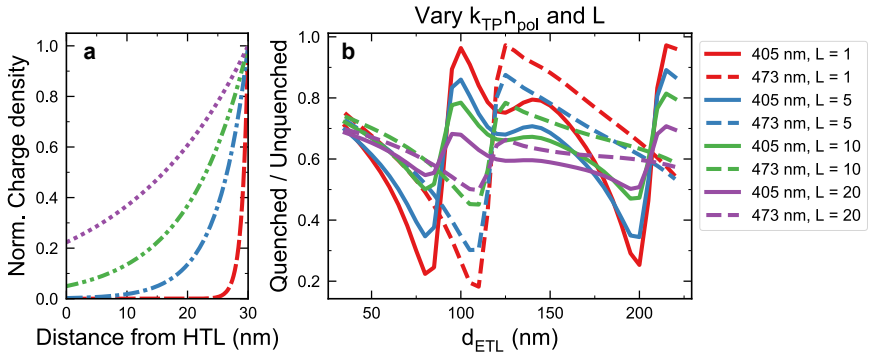

Fig. 9.4. (**a**) Hypothetical hole distributions, decaying exponentially with $L = 1$, 5, 10, and 20 nm. (**b**) Simulated PL quenching as a function of ETL thickness for various hole distribution widths. Solid lines are for a $\lambda = 405$ nm laser and dashed lines for a $\lambda = 473$ nm laser.

As shown in Figure 9.4, the functional dependence of quenching on d_{ETL} and pump wavelengths for this range of hole distribution widths. Quenching for d_{ETL} between 75 and 125 nm is expected to vary by as much as 20-40%, which should be easily resolvable.

Another potential approach is to use a doped-strip method, in analogy to the recombination zone measurements presented in Section 3.3. Here, most of the emissive layer will be left

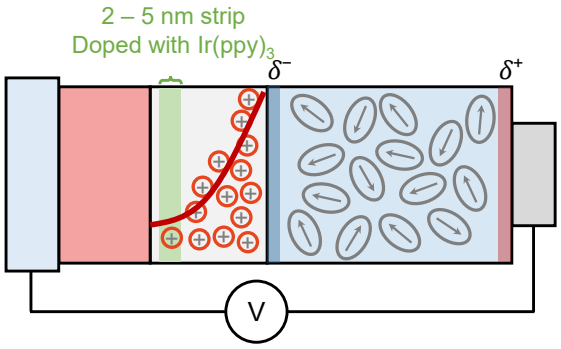

Fig. 9.5. Schematic of localized doping approach to measuring hole distribution, where the emitter ($Ir(ppy)_3$) is placed in thin strips at different positions within the emissive layer.

un-doped (only the host is present), and the emitter will be placed in thin (3-6 nm) strips at different locations within the emissive layer. The magnitude of quenching can then be compared for each location to evaluate the hole concentration within a Förster radius of the doped strip. This approach has the advantage of being relatively direct and understandable, but the spatial resolution is limited by the width of the strip (which must be finite to achieve sufficient signal) and the exciton-hole Förster radius. Another limitation is that this approach assumes that the presence of the emitter has no influence on the hole distribution, which may not be true if the emitter serves as a hole trap. Quenching in this case may not be representative of a real device which as $Ir(ppy)_3$ doped across the entire emissive layer.

9.1.3 Effect of ultrastable glass formation in non-polar systems

We found in Chapter 6 that heating during deposition improves efficiency in device with polar (i.e. exhibiting SOP) layers by reducing SOP and exciton-polaron quenching. Heated deposition of non-polar layers therefore should only have a marginal effect, if any, on efficiency. Still, it is possible that in some systems η_{PL} or η_{EF} could vary significantly with film density and molecular orientation; for example, the high electron mobility of BPy-OXD has been attributed to its preferred horizontal orientation,[23] so changes in its orientation should tune mobility, recombination zone position, and charge balance. Consequently, there may be systems that show stronger dependences on deposition temperature, even if the heated layers do not exhibit SOP.

We also found that ultrastable glass formation seemed to improve optical stability but not electrical stability, contradicting results from ref. [214]. We speculated that this discrepancy was possibly due to differences in processing steps, the specifics of the deposition tool, or impurities incorporated during deposition. These factors should be studied systematically, and

the effect of ultrastable glass formation on device lifetime should be investigated in a wide range of materials. Testing these effects in non-polar materials could be most instructive, as it would eliminate potential ambiguities surrounding reduced charge density when SOP is eliminated at high temperature.

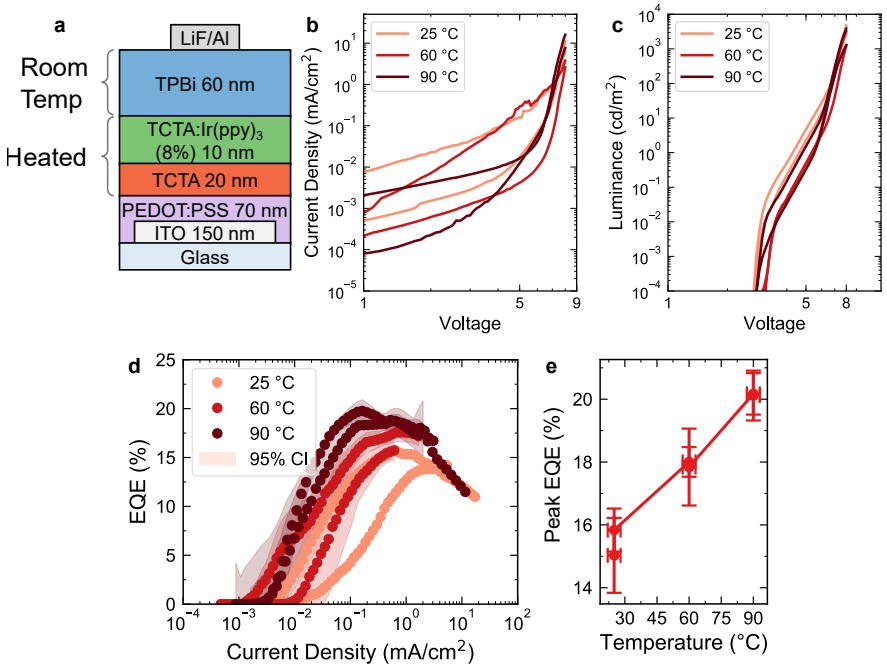

Fig. 9.6. Effect of heated deposition on non-polar layers in TCTA:Ir(ppy)$_3$ device: (**a**) Device structure, where the HTL and EML (TCTA:Ir(ppy)$_3$) are deposited at elevated temperature and the ETL (TPBi) and cathode are deposited near room temperature after letting the substrate holder cool. (**b**) Current-voltage, (**c**) luminance-voltage, and (**d**) EQE-current density characteristics for devices deposited at 25 °C, ~60 °C, and ~90 °C. (**e**) Peak EQE as a function of deposition temperature.

As a preliminary test of how heated deposition of non-polar layers influences performance, we fabricated devices with a TCTA:Ir(ppy)$_3$ EML and a TPBi ETL (Figure 9.6) and we varied the deposition temperature of the HTL and EML while keeping the ETL deposition at room temperature. In the heated devices, we see a 10–20% enhancement in peak EQE. These results appear promising for the potential of heated deposition in other systems, but they are complicated by the fact that the leakage current varies substantially between devices and the initial device is rather unoptimized and resistive. It is also possible that substrates weren't fully cooled to room temperature prior to TPBi deposition. Further studies should focus on eliminating these issues and ambiguities, while showing a robust effect from multiple materials systems.

9.2 Degradation in blue OLEDs

In this thesis, we have primarily discussed green OLEDs despite blue emitters generally having much lower stability. One reason for this is simply that green emitters such as $Ir(ppy)_3$ are archetypical and widely characterized, allowing us to borrow from existing literature. Another is that there are simply very few blue phosphorescent emitters available which are stable enough to be analyzed by our techniques. For example, FIrpic, one of the first sky blue phosphorescent emitters, degrades in mere seconds or minutes. Still, going forward the techniques presented here should be applied more systematically to blue emitters.

An immediate question is whether the balance of η_{PL} and η_{EF} degradation is similar for blue OLEDs. In preliminary work, we found that some blue emitters tend to be almost exclusively dominated by η_{PL} degradation at short times, suggesting that direct emitter dissociation limits these devices. Another area of interest is whether blue emitters predominantly degrade *via* exciton-exciton interactions or exciton-polaron interactions, which could be studied using a combination of optical, single-carrier device, and electrical degradation. Knowledge of this degradation mechanism, which will likely vary based on the emitter, host, and transport layer properties, could help guide design efforts by indicating which species should be minimized within the emissive layer. For more discussion of our preliminary results on blue OLEDs and future study directions in blue OLED degradation, see Appendix E.

Another path is to apply the methods in Chapter 7 to evaluate how quenching and η_τ change over time in triplet-fusion-enhanced fluorescent OLEDs, which are used in most commercial blue pixels. Since these devices rely on triplet-triplet annihilation to achieve high efficiency, it seems almost certain that a reduction in η_τ will be a prominent source of luminance loss. To quantitatively analyze the changes in triplet fusion during degradation, we could apply the coupled singlet-triplet exciton kinetic model developed by Zhang and Forrest [40] to model lock-in PL, EQE roll-off, and potentially EL transients over time.

9.3 Perovskite LEDs

Metal halide perovskites (MHPs) have emerged in the last decade as a disruptive solar cell technology,[304] and in the last five years they have gained attention as a new material for LEDs[228,305–307] and lasers.[308,309] Efficiency roll-off and stability of these materials are now

the primary challenges to their commercialization.[207,229,310,311] The techniques applied in this thesis could also be important to improving understanding of loss pathways in these materials and ultimately developing stable perovskite LEDs (PeLEDs).

One area of immediate interest is what effect spontaneous orientation polarization of the ETL has on PeLEDs. As discussed in Chapter 6, many record efficiency PeLEDs have used TPBi,[228] and it seems likely that the polarization of TPBi influences device performance, given that PeLED efficiency and ion migration within perovskites are sensitive to hole density and electric field.[229–231] Interestingly, a recent study showed that performance could be optimized by using a mixed ETL consisting of B3PyMPM and TPBi.[232] Yan et al. [232] argued that the mixture improved performance by tuning electron injection and mobility, but another contributing effect could be that the mixture balances opposing effects of SOP and outcoupling efficiency (B3PyMPM should have lower η_{OC} due to its larger index of refraction). Beyond just efficiency, these findings may also have implications for the stability of PeLEDs, as the presence of holes can destabilize metal halide perovskites (excess holes can neutralize and liberate halide ions, allowing them to diffuse and promote decomposition).[229] As such, the increased hole density in a device containing a polar ETL could reduce device lifetime.

Another area of interest is to identify whether optical stability in MHP materials is a useful proxy for electrical stability. Using the optical degradation techniques developed in this thesis (see Chapter 5), we could attempt to quickly screen MHPs for intrinsic stability in the absence of confounding interactions with electrodes and neighboring layers (electrochemical interactions with electrodes and ion diffusion into external layers are notorious issues in MHPs[310]). This approach should be useful—at least for screening out highly unstable materials—since photostability is often a reasonable proxy for electrical stability in other systems, such as quantum dot and organic LEDs.[312,313] But because different mechanisms will be active under optical and electrical pumping, photodegradation might not capture the stability-limiting mechanisms. For instance, field-driven ion migration or electrochemical reactions will not be present in photodegradation, and photogenerated charge carrier densities may differ from those electrically injected in a working device. Highlighting the difficulty of extrapolating electrical stability from optical stability, a recent study of 2D MHPs (Ruddlesden-Popper) found that PL showed no degradation over 30 h of illumination, while EL degraded to <15% of the peak within 16 h.[314] Still, some MHP formulations do show significant degradation under optical pumping alone, and screening out these poor performing materials could be useful in accelerating discovery.

Whether or not photodegradation turns out not to be a useful screening metric, achieving stable PeLEDs will require high-quality diffusion barrier layers which still efficiently inject charge.[315,316] To develop barrier layers for stable PeLEDs, progress in MHP solar cells could be used as a starting point.[317] However, because operating conditions differ dramatically for solar cells and LEDs, optimal interlayers are unlikely to be identical for the two. Ideal barrier layers will satisfy several criteria: 1) negligible reactivity with MHPs,[318] 2) low diffusivity of halide ions, metals, and moisture,[317] and 3) energy level alignment suitable for charge injection.

Successful cathode-side barrier layers have included ZnO,[316] SnO_2,[317] and MgZnO.[315] Other transition-metal oxides could be selected based on energy level alignment for charge injection.[319] To screen candidates on the first two criteria, X-ray photoelectron spectroscopy (XPS) measurements could be performed on MHP films coated with the barrier layer (thickness of >10 nm to exceed the XPS sampling depth).[318,320] Samples could be annealed or illuminated with white light to activate diffusion and/or MHP-barrier reactions. Because XPS is surface sensitive, observation of halide peaks would indicate diffusion into the barrier layer, and the kinetics of their emergence could be used to estimate halide diffusivity. Barrier reactivity with MHPs could be evaluated based on changes in the oxidation state of the barrier layer peaks.[318]

Charge injection properties of the most promising barrier layers could then be determined with current-voltage measurements of PeLEDs with and without the barrier layers. Some optimization may be required to balance electron- and hole-injection PeLEDs; thin work-function-modifying layers such as MoO_3 and LiF could be used to fine-tune injection. A series of PeLEDs consisting of the most photostable MHP formulations could then be fabricated. Electrical lifetimes of devices with and without without barrier layers could be used to examine the effect of barrier layer on efficiency and lifetime, and the most promising MHP and barrier layer candidates could then be optimized by iterating the whole process.

9.4 Outlook

Many problems in OLEDs have been solved commercially by brute-force optimization. Applying the combined optical and electrical techniques in this thesis has allowed for improved fundamental understanding of efficiency loss in these devices. Further development and systematic application of these methods may help accelerate discovery and development of efficient and stable OLED materials. To be most effective, these techniques should be part of

a larger toolkit of screening and analysis methods, which should include both computational screening[186,321,322] (e.g. density functional theory calculations of bond energy or excimer formation,[112,193] or kinetic Monte Carlo and molecular dynamics simulations of film formation and spontaneous orientation polarization[323]) and early-stage experimental screening (e.g. solution-based measurements of PL efficiency, PL stability under optical pumping,[324] and stability under electrochemical cycling[325]). The device-based methods shown here can be used at a later stage in development to uncover and quantify efficiency loss pathways, guiding device optimization.

References

[1] Vladsinger. *English: Various Representations of Benzene*. 2009. URL: https://commons.wikimedia.org/wiki/File:Benzene_Representations.svg (visited on 05/18/2020).

[2] P. W. Atkins, J. D. Paula, and J. Keeler. *Atkins' Physical Chemistry*. en. Eighth. Oxford University Press, 2006.

[3] H. A. M. van Mullekom, J. A. J. M. Vekemans, E. E. Havinga, and E. W. Meijer. "Developments in the Chemistry and Band Gap Engineering of Donor–Acceptor Substituted Conjugated Polymers". en. *Materials Science and Engineering: R: Reports* 32.1 (2001), pp. 1–40. DOI: 10.1016/S0927-796X(00)00029-2.

[4] S. A. Bagnich et al. "Excimer Formation by Steric Twisting in Carbazole and Triphenylamine-Based Host Materials". *The Journal of Physical Chemistry C* 119.5 (2015), pp. 2380–2387. DOI: 10.1021/jp512772j.

[5] A. Köhler and H. Bässler. *Electronic Processes in Organic Semiconductors: An Introduction*. Weinheim, GERMANY: John Wiley & Sons, Incorporated, 2015.

[6] Q. Wang and H. Aziz. "Degradation of Organic/Organic Interfaces in Organic Light-Emitting Devices Due to Polaron–Exciton Interactions". *ACS Applied Materials & Interfaces* 5.17 (2013), pp. 8733–8739. DOI: 10.1021/am402537j.

[7] R. Kabe and C. Adachi. "Organic Long Persistent Luminescence". en. *Nature* 550.7676 (2017), pp. 384–387. DOI: 10.1038/nature24010.

[8] M. Knupfer. "Exciton Binding Energies in Organic Semiconductors". en. *Applied Physics A* 77.5 (2003), pp. 623–626. DOI: 10.1007/s00339-003-2182-9.

[9] J.-H. Lee, S. Lee, S.-J. Yoo, K.-H. Kim, and J.-J. Kim. "Langevin and Trap-Assisted Recombination in Phosphorescent Organic Light Emitting Diodes". en. *Advanced Functional Materials* 24.29 (2014), pp. 4681–4688. DOI: 10.1002/adfm.201303453.

[10] X. Ai et al. "Efficient Radical-Based Light-Emitting Diodes with Doublet Emission". en. *Nature* 563.7732 (2018), pp. 536–540. DOI: 10.1038/s41586-018-0695-9.

[11] Q. Peng, A. Obolda, M. Zhang, and F. Li. "Organic Light-Emitting Diodes Using a Neutral π Radical as Emitter: The Emission from a Doublet". en. *Angewandte Chemie International Edition* 54.24 (2015), pp. 7091–7095. DOI: 10.1002/anie.201500242.

[12] M. A. Baldo et al. "Highly Efficient Phosphorescent Emission from Organic Electroluminescent Devices". en. *Nature* 395.6698 (1998), pp. 151–154. DOI: 10.1038/25954.

[13] M. A. Baldo, D. F. O'Brien, M. E. Thompson, and S. R. Forrest. "Excitonic Singlet-Triplet Ratio in a Semiconducting Organic Thin Film". *Physical Review B* 60.20 (1999), pp. 14422–14428. DOI: 10.1103/PhysRevB.60.14422.

[14] N. K. Hien et al. "Exceptional Case of Kasha's Rule: Emission from Higher-Lying Singlet Electron Excited States into Ground States in Coumarin-Based Biothiol Sensing". en. *Dyes and Pigments* 152 (2018), pp. 118–126. DOI: 10.1016/j.dyepig.2018.01.046.

[15] H. H. Jaffe and A. L. Miller. "The Fates of Electronic Excitation Energy". *Journal of Chemical Education* 43.9 (1966), p. 469. DOI: 10.1021/ed043p469.

[16] M. Kasha. "Characterization of Electronic Transitions in Complex Molecules". en. *Discussions of the Faraday Society* 9.0 (1950), pp. 14–19. DOI: 10.1039/DF9500900014.

[17] Y. Zhang and H. Aziz. "The Influence of the Guest on the Aggregation of the Host by Exciton-Polaron Interactions and Its Effects on the Stability of Phosphorescent Organic Light-Emitting Devices". *ACS Applied Materials & Interfaces* 8.22 (2016), pp. 14088–14095. DOI: 10.1021/acsami.6b02946.

[18] K.-H. Kim et al. "Crystal Organic Light-Emitting Diodes with Perfectly Oriented Non-Doped Pt-Based Emitting Layer". en. *Advanced Materials* 28.13 (2016), pp. 2526–2532. DOI: 10.1002/adma.201504451.

[19] X. Yang, X. Feng, J. Xin, H. Wang, and D. Yan. "High-Performance Crystalline Organic Light-Emitting Diodes Based on Multi-Layer High-Quality Crystals". *Organic Electronics* 64 (2019), pp. 236–240. DOI: 10.1016/j.orgel.2018.10.023.

[20] K. Osada et al. "Observation of Spontaneous Orientation Polarization in Evaporated Films of Organic Light-Emitting Diode Materials". *Organic Electronics* 58 (2018), pp. 313–317. DOI: 10.1016/j.orgel.2018.04.026.

[21] S. S. Dalal, D. M. Walters, I. Lyubimov, J. J. de Pablo, and M. D. Ediger. "Tunable Molecular Orientation and Elevated Thermal Stability of Vapor-Deposited Organic Semiconductors". en. *Proceedings of the National Academy of Sciences* 112.14 (2015), pp. 4227–4232. DOI: 10.1073/pnas.1421042112.

[22] T. D. Schmidt et al. "Emitter Orientation as a Key Parameter in Organic Light-Emitting Diodes". *Physical Review Applied* 8.3 (2017), p. 037001. DOI: 10.1103/PhysRevApplied.8.037001.

[23] D. Yokoyama, A. Sakaguchi, M. Suzuki, and C. Adachi. "Enhancement of Electron Transport by Horizontal Molecular Orientation of Oxadiazole Planar Molecules in Organic Amorphous Films". *Applied Physics Letters* 95.24 (2009), p. 243303. DOI: 10.1063/1.3274135.

[24] Y. Cang et al. "Extreme Elasticity Anisotropy in Molecular Glasses". en. *Advanced Functional Materials* 30.23 (2020), p. 2001481. DOI: 10.1002/adfm.202001481.

[25] Y. Shen and N. C. Giebink. "Monte Carlo Simulations of Nanoscale Electrical Inhomogeneity in Organic Light-Emitting Diodes and Its Impact on Their Efficiency and Lifetime". *Physical Review Applied* 4.5 (2015), p. 054017. DOI: 10.1103/PhysRevApplied.4.054017.

[26] S. Reineke, G. Schwartz, K. Walzer, M. Falke, and K. Leo. "Highly Phosphorescent Organic Mixed Films: The Effect of Aggregation on Triplet-Triplet Annihilation". *Applied Physics Letters* 94.16 (2009), p. 163305. DOI: 10.1063/1.3123815.

[27] S. Sanderson, B. Philippa, G. Vamvounis, P. L. Burn, and R. D. White. "Understanding Charge Transport in Ir(Ppy)3:CBP OLED Films". *The Journal of Chemical Physics* 150.9 (2019), p. 094110. DOI: 10.1063/1.5083639.

[28] H. van Eersel, P. A. Bobbert, R. A. J. Janssen, and R. Coehoorn. "Monte Carlo Study of Efficiency Roll-off of Phosphorescent Organic Light-Emitting Diodes: Evidence for Dominant Role of Triplet-Polaron Quenching". *Applied Physics Letters* 105.14 (2014), p. 143303. DOI: 10.1063/1.4897534.

[29] R. Coehoorn, H. van Eersel, P. Bobbert, and R. Janssen. "Kinetic Monte Carlo Study of the Sensitivity of OLED Efficiency and Lifetime to Materials Parameters". en. *Advanced Functional Materials* 25.13 (2015), pp. 2024–2037. DOI: 10.1002/adfm.201402532.

[30] M. L. Tietze et al. "Elementary Steps in Electrical Doping of Organic Semiconductors". en. *Nature Communications* 9.1 (2018), p. 1182. DOI: 10.1038/s41467-018-03302-z.

[31] J.-L. Brédas, D. Beljonne, V. Coropceanu, and J. Cornil. "Charge-Transfer and Energy-Transfer Processes in π-Conjugated Oligomers and Polymers: A Molecular Picture". *Chemical Reviews* 104.11 (2004), pp. 4971–5004. DOI: 10.1021/cr040084k.

[32] S. M. Menke and R. J. Holmes. "Exciton Diffusion in Organic Photovoltaic Cells". en. *Energy & Environmental Science* 7.2 (2014), pp. 499–512. DOI: 10.1039/C3EE42444H.

[33] G. D. Scholes. "Long-Range Resonance Energy Transfer in Molecular Systems". *Annual Review of Physical Chemistry* 54.1 (2003), pp. 57–87. DOI: 10.1146/annurev.physchem.54.011002.103746.

[34] T. Fielitz. "Understanding and Engineering Molecular Order in Organic Semiconductors". en (2017). URL: http://conservancy.umn.edu/handle/11299/201048 (visited on 06/05/2020).

[35] N. J. Turro. *Modern Molecular Photochemistry*. en. University Science Books, 1991.

[36] C. Adachi, M. A. Baldo, S. R. Forrest, and M. E. Thompson. "High-Efficiency Organic Electrophosphorescent Devices with Tris(2-Phenylpyridine)Iridium Doped into Electron-Transporting Materials". *Applied Physics Letters* 77.6 (2000), pp. 904–906. DOI: 10.1063/1.1306639.

[37] T. Tsuboi. "Electronic States of Phosphorescent Molecules Ir(Ppy)3 and PtOEP Used in Organic Light Emitting Diodes". en. *Journal of Luminescence*. Dynamical Processes in Excited States of Solids 119-120 (2006), pp. 288–292. DOI: 10.1016/j.jlumin.2006.01.015.

[38] S. Reineke, K. Walzer, and K. Leo. "Triplet-Exciton Quenching in Organic Phosphorescent Light-Emitting Diodes with Ir-Based Emitters". *Physical Review B* 75.12 (2007), p. 125328. DOI: 10.1103/PhysRevB.75.125328.

[39] M. Inoue et al. "Effect of Reverse Intersystem Crossing Rate to Suppress Efficiency Roll-off in Organic Light-Emitting Diodes with Thermally Activated Delayed Fluorescence Emitters". *Chemical Physics Letters* 644 (2016), pp. 62–67. DOI: 10.1016/j.cplett.2015.11.042.

[40] Y. Zhang and S. R. Forrest. "Triplets Contribute to Both an Increase and Loss in Fluorescent Yield in Organic Light Emitting Diodes". *Physical Review Letters* 108.26 (2012), p. 267404. DOI: 10.1103/PhysRevLett.108.267404.

[41] K. W. Hershey and R. J. Holmes. "Unified Analysis of Transient and Steady-State Electrophosphorescence Using Exciton and Polaron Dynamics Modeling". *Journal of Applied Physics* 120.19 (2016), p. 195501. DOI: 10.1063/1.4966615.

[42] Y. Kawamura, J. Brooks, J. J. Brown, H. Sasabe, and C. Adachi. "Intermolecular Interaction and a Concentration-Quenching Mechanism of Phosphorescent Ir(III) Complexes in a Solid Film". *Physical Review Letters* 96.1 (2006), p. 017404. DOI: 10.1103/PhysRevLett.96.017404.

[43] D. Y. Kondakov, T. D. Pawlik, T. K. Hatwar, and J. P. Spindler. "Triplet Annihilation Exceeding Spin Statistical Limit in Highly Efficient Fluorescent Organic Light-Emitting Diodes". *Journal of Applied Physics* 106.12 (2009), p. 124510. DOI: 10.1063/1.3273407.

[44] Y.-J. Luo, Z.-Y. Lu, and Y. Huang. "Triplet Fusion Delayed Fluorescence Materials for OLEDs". *Chinese Chemical Letters* 27.8 (2016), pp. 1223–1230. DOI: 10.1016/j.cclet.2016.06.002.

[45] D. Y. Kondakov. "Triplet–Triplet Annihilation in Highly Efficient Fluorescent Organic Light-Emitting Diodes: Current State and Future Outlook". en. *Phil. Trans. R. Soc. A* 373.2044 (2015), p. 20140321. DOI: 10.1098/rsta.2014.0321.

[46] S. Scholz, D. Kondakov, B. Lüssem, and K. Leo. "Degradation Mechanisms and Reactions in Organic Light-Emitting Devices". *Chemical Reviews* 115.16 (2015), pp. 8449–8503. DOI: 10.1021/cr400704v.

[47] M. Pope, N. E. Geacintov, and F. Vogel. "Singlet Exciton Fission and Tri Plet-Tri Plet Exciton Fusion in Crystalline Tet Racene". *Molecular Crystals* 6.1 (1969), pp. 83–104. DOI: 10.1080/15421406908082953.

[48] P. M. Zimmerman, Z. Zhang, and C. B. Musgrave. "Singlet Fission in Pentacene through Multi-Exciton Quantum States". en. *Nature Chemistry* 2.8 (2010), pp. 648–652. DOI: 10.1038/nchem.694.

[49] N. C. Giebink, B. W. D'Andrade, M. S. Weaver, J. J. Brown, and S. R. Forrest. "Direct Evidence for Degradation of Polaron Excited States in Organic Light Emitting Diodes". *Journal of Applied Physics* 105.12 (2009), p. 124514. DOI: 10.1063/1.3151689.

[50] R. Coehoorn, P. A. Bobbert, and H. van Eersel. "Forster-Type Triplet-Polaron Quenching in Disordered Organic Semiconductors". *Physical Review B* 96.18 (2017), p. 184203. DOI: 10.1103/PhysRevB.96.184203.

[51] T. Matsushima et al. "Interfacial Charge Transfer and Charge Generation in Organic Electronic Devices". en. *Organic Electronics* 12.3 (2011), pp. 520–528. DOI: 10.1016/j.orgel.2011.01.001.

[52] T. Rabe et al. "Highly Sensitive Determination of the Polaron-Induced Optical Absorption of Organic Charge-Transport Materials". *Physical Review Letters* 102.13 (2009), p. 137401. DOI: 10.1103/PhysRevLett.102.137401.

[53] T. Glaser et al. "Infrared Study of the MoO3 Doping Efficiency in 4,4′-Bis(N-Carbazolyl)-1,1′-Biphenyl (CBP)". en. *Organic Electronics* 14.2 (2013), pp. 575–583. DOI: 10.1016/j.orgel.2012.11.031.

[54] A. S. D. Sandanayaka, K. Yoshida, T. Matsushima, and C. Adachi. "Exciton Quenching Behavior of Thermally Activated Delayed Fluorescence Molecules by Charge Carriers". *The Journal of Physical Chemistry C* 119.14 (2015), pp. 7631–7636. DOI: 10.1021/acs.jpcc.5b01314.

[55] B. Nell, K. Ortstein, O. V. Boltalina, and K. Vandewal. "Influence of Dopant–Host Energy Level Offset on Thermoelectric Properties of Doped Organic Semiconductors". *The Journal of Physical Chemistry C* 122.22 (2018), pp. 11730–11735. DOI: 10.1021/acs.jpcc.8b03804.

[56] K. Kanemoto, S. Hatanaka, K. Kimura, Y. Ueda, and H. Matsuoka. "Field-Induced Dissociation of Electron-Hole Pairs in Organic Light Emitting Diodes Monitored Directly from Bias-Dependent Magnetic Resonance Techniques". *Physical Review Materials* 1.2 (2017), p. 022601. DOI: 10.1103/PhysRevMaterials.1.022601.

[57] T. Yamanaka, H. Nakanotani, and C. Adachi. "Slow Recombination of Spontaneously Dissociated Organic Fluorophore Excitons". *Nature Communications* 10.1 (2019), p. 5748. DOI: 10.1038/s41467-019-13736-8.

[58] F. Bencheikh, A. S. D. Sandanayaka, T. Fukunaga, T. Matsushima, and C. Adachi. "Origin of External Quantum Efficiency Roll-off in 4,4′-Bis[(N-Carbazole)Styryl]Biphenyl (BSBCz)-Based Inverted Organic Light Emitting Diode under High Pulsed Electrical Excitation". *Journal of Applied Physics* 126.18 (2019), p. 185501. DOI: 10.1063/1.5121485.

[59] A. Bernanose. “Electroluminescence of Organic Compounds”. en. *British Journal of Applied Physics* 6.S4 (1955), S54–S55. DOI: 10.1088/0508-3443/6/S4/319.

[60] M. Pope, H. P. Kallmann, and P. Magnante. “Electroluminescence in Organic Crystals”. *The Journal of Chemical Physics* 38.8 (1963), pp. 2042–2043. DOI: 10.1063/1.1733929.

[61] M. Pope and C. E. Swenberg. *Electronic Processes in Organic Crystals and Polymers*. Oxford University Press on Demand, 1999.

[62] C. W. Tang and S. A. VanSlyke. “Organic Electroluminescent Diodes”. *Applied Physics Letters* 51.12 (1987), pp. 913–915. DOI: 10.1063/1.98799.

[63] M. A. Baldo, M. E. Thompson, and S. R. Forrest. “High-Efficiency Fluorescent Organic Light-Emitting Devices Using a Phosphorescent Sensitizer”. en. *Nature* 403.6771 (2000), pp. 750–753. DOI: 10.1038/35001541.

[64] M. A. Baldo, S. Lamansky, P. E. Burrows, M. E. Thompson, and S. R. Forrest. “Very High-Efficiency Green Organic Light-Emitting Devices Based on Electrophosphorescence”. *Applied Physics Letters* 75.1 (1999), pp. 4–6. DOI: 10.1063/1.124258.

[65] C. Adachi, M. A. Baldo, M. E. Thompson, and S. R. Forrest. “Nearly 100% Internal Phosphorescence Efficiency in an Organic Light-Emitting Device”. *Journal of Applied Physics* 90.10 (2001), pp. 5048–5051. DOI: 10.1063/1.1409582.

[66] A. Buckley. *Organic Light-Emitting Diodes (OLEDs): Materials, Devices and Applications*. en. Elsevier, 2013.

[67] *Kodak LS633 First with OLED Display*. URL: https://www.dpreview.com/articles/0923133050/kodakls633 (visited on 07/01/2020).

[68] *Nokia | OLED-Info*. URL: https://www.oled-info.com/nokia-oled (visited on 05/12/2020).

[69] “List of Nokia Products”. en. *Wikipedia* (2020). URL: https://en.wikipedia.org/wiki/List_of_Nokia_products (visited on 05/12/2020).

[70] “Motorola Timeport”. en. *Wikipedia* (2020). URL: https://en.wikipedia.org/wiki/Motorola_Timeport (visited on 05/12/2020).

[71] F. Templier. *OLED Microdisplays: Technology and Applications*. en. John Wiley & Sons, 2014.

[72] *BenQ-Siemens S88 | OLED-Info*. URL: https://www.oled-info.com/mobile_phones/benq_siemens_s88 (visited on 05/12/2020).

[73] “BenQ Mobile”. en. *Wikipedia* (2020). URL: https://en.wikipedia.org/wiki/BenQ_Mobile (visited on 05/12/2020).

[74] M. Furno, R. Meerheim, S. Hofmann, B. Lüssem, and K. Leo. “Efficiency and Rate of Spontaneous Emission in Organic Electroluminescent Devices”. *Physical Review B* 85.11 (2012), p. 115205. DOI: 10.1103/PhysRevB.85.115205.

[75] C. Murawski, K. Leo, and M. C. Gather. “Efficiency Roll-Off in Organic Light-Emitting Diodes”. en. *Advanced Materials* 25.47 (2013), pp. 6801–6827. DOI: 10.1002/adma.201301603.

[76] Y. Luo and H. Aziz. “Correlation Between Triplet–Triplet Annihilation and Electroluminescence Efficiency in Doped Fluorescent Organic Light-Emitting Devices”. en. *Advanced Functional Materials* 20.8 (2010), pp. 1285–1293. DOI: 10.1002/adfm.200902329.

[77] H. Uoyama, K. Goushi, K. Shizu, H. Nomura, and C. Adachi. "Highly Efficient Organic Light-Emitting Diodes from Delayed Fluorescence". en. *Nature* 492.7428 (2012), pp. 234–238. DOI: 10.1038/nature11687.

[78] J. Frischeisen, D. Yokoyama, C. Adachi, and W. Brütting. "Determination of Molecular Dipole Orientation in Doped Fluorescent Organic Thin Films by Photoluminescence Measurements". *Applied Physics Letters* 96.7 (2010), p. 073302. DOI: 10.1063/1.3309705.

[79] D. Yokoyama. "Molecular Orientation in Small-Molecule Organic Light-Emitting Diodes". en. *Journal of Materials Chemistry* 21.48 (2011), pp. 19187–19202. DOI: 10.1039/C1JM13417E.

[80] *UniversalPHOLED® Materials*. URL: https://oled.com/solutions/universalpholed-materials/ (visited on 06/08/2020).

[81] A. S. D. Sandanayaka et al. "Indication of Current-Injection Lasing from an Organic Semiconductor". en. *Applied Physics Express* 12.6 (2019), p. 061010. DOI: 10.7567/1882-0786/ab1b90.

[82] L. S. Hung, C. W. Tang, and M. G. Mason. "Enhanced Electron Injection in Organic Electroluminescence Devices Using an Al/LiF Electrode". *Applied Physics Letters* 70.2 (1997), pp. 152–154. DOI: 10.1063/1.118344.

[83] S. E. Shaheen et al. "Bright Blue Organic Light-Emitting Diode with Improved Color Purity Using a LiF/Al Cathode". *Journal of Applied Physics* 84.4 (1998), pp. 2324–2327. DOI: 10.1063/1.368299.

[84] H. Ishii, K. Sugiyama, E. Ito, and K. Seki. "Energy Level Alignment and Interfacial Electronic Structures at Organic/Metal and Organic/Organic Interfaces". en. *Advanced Materials* 11.8 (1999), pp. 605–625. DOI: 10.1002/(SICI)1521-4095(199906)11:8<605::AID-ADMA605>3.0.CO;2-Q.

[85] G. He et al. "High-Efficiency and Low-Voltage P-i-n Electrophosphorescent Organic Light-Emitting Diodes with Double-Emission Layers". *Applied Physics Letters* 85.17 (2004), pp. 3911–3913. DOI: 10.1063/1.1812378.

[86] G. He et al. "Very High-Efficiency and Low Voltage Phosphorescent Organic Light-Emitting Diodes Based on a p-i-n Junction". *Journal of Applied Physics* 95.10 (2004), pp. 5773–5777. DOI: 10.1063/1.1702143.

[87] G. He et al. "Ultra-High-Efficiency Electrophosphorescent p-i-n OLEDs with Double Emission Layers". Vol. 5519. 2004, pp. 42–47. DOI: 10.1117/12.563310.

[88] A. Chaskar, H.-F. Chen, and K.-T. Wong. "Bipolar Host Materials: A Chemical Approach for Highly Efficient Electrophosphorescent Devices". en. *Advanced Materials* 23.34 (2011), pp. 3876–3895. DOI: 10.1002/adma.201101848.

[89] S. Forrest, D. Bradley, and M. Thompson. "Measuring the Efficiency of Organic Light-Emitting Devices". en. *Advanced Materials* 15.13 (2003), pp. 1043–1048. DOI: 10.1002/adma.200302151.

[90] M. Anaya et al. "Best Practices for Measuring Emerging Light-Emitting Diode Technologies". en. *Nature Photonics* 13.12 (2019), pp. 818–821. DOI: 10.1038/s41566-019-0543-y.

[91] K. W. Hershey, J. Suddard-Bangsund, G. Qian, and R. J. Holmes. "Decoupling Degradation in Exciton Formation and Recombination during Lifetime Testing of Organic Light-Emitting Devices". *Applied Physics Letters* 111.11 (2017), p. 113301. DOI: 10.1063/1.4993618.

[92] M. Segal, M. A. Baldo, R. J. Holmes, S. R. Forrest, and Z. G. Soos. "Excitonic Singlet-Triplet Ratios in Molecular and Polymeric Organic Materials". *Physical Review B* 68.7 (2003), p. 075211. DOI: 10.1103/PhysRevB.68.075211.

[93] J.-S. Kim, P. K. H. Ho, N. C. Greenham, and R. H. Friend. "Electroluminescence Emission Pattern of Organic Light-Emitting Diodes: Implications for Device Efficiency Calculations". *Journal of Applied Physics* 88.2 (2000), pp. 1073–1081. DOI: 10.1063/1.373779.

[94] M. C. Gather and S. Reineke. "Recent Advances in Light Outcoupling from White Organic Light-Emitting Diodes". *Journal of Photonics for Energy* 5.1 (2015), pp. 057607–057607. DOI: 10.1117/1.JPE.5.057607.

[95] J. Song et al. "Lensfree OLEDs with over 50% External Quantum Efficiency via External Scattering and Horizontally Oriented Emitters". en. *Nature Communications* 9.1 (2018), p. 3207. DOI: 10.1038/s41467-018-05671-x.

[96] C. Coburn and S. R. Forrest. "Effects of Charge Balance and Exciton Confinement on the Operational Lifetime of Blue Phosphorescent Organic Light-Emitting Diodes". *Physical Review Applied* 7.4 (2017), p. 041002. DOI: 10.1103/PhysRevApplied.7.041002.

[97] N. C. Giebink et al. "Intrinsic Luminance Loss in Phosphorescent Small-Molecule Organic Light Emitting Devices Due to Bimolecular Annihilation Reactions". *Journal of Applied Physics* 103.4 (2008), p. 044509. DOI: 10.1063/1.2884530.

[98] D. Y. Kondakov, J. R. Sandifer, C. W. Tang, and R. H. Young. "Nonradiative Recombination Centers and Electrical Aging of Organic Light-Emitting Diodes: Direct Connection between Accumulation of Trapped Charge and Luminance Loss". *Journal of Applied Physics* 93.2 (2003), pp. 1108–1119. DOI: 10.1063/1.1531231.

[99] N. C. Giebink and S. R. Forrest. "Quantum Efficiency Roll-off at High Brightness in Fluorescent and Phosphorescent Organic Light Emitting Diodes". *Physical Review B* 77.23 (2008), p. 235215. DOI: 10.1103/PhysRevB.77.235215.

[100] J. Lee et al. "Hot Excited State Management for Long-Lived Blue Phosphorescent Organic Light-Emitting Diodes". *Nature Communications* 8 (2017), p. 15566. DOI: 10.1038/ncomms15566.

[101] H. Aziz et al. "Humidity-Induced Crystallization of Tris (8-Hydroxyquinoline) Aluminum Layers in Organic Light-Emitting Devices". *Applied Physics Letters* 72.7 (1998), pp. 756–758. DOI: 10.1063/1.120867.

[102] W. Wang, S. F. Lim, and S. J. Chua. "Bubble Formation and Growth in Organic Light-Emitting Diodes Composed of a Polymeric Emitter and a Calcium Cathode". *Journal of Applied Physics* 91.9 (2002), pp. 5712–5715. DOI: 10.1063/1.1467395.

[103] F. Nehm et al. "Importance of Interface Diffusion and Climate in Defect Dominated Moisture Ultrabarrier Applications". *ACS Applied Materials & Interfaces* 8.30 (2016), pp. 19807–19812. DOI: 10.1021/acsami.6b04561.

[104] R. Meerheim, K. Walzer, M. Pfeiffer, and K. Leo. "Ultrastable and Efficient Red Organic Light Emitting Diodes with Doped Transport Layers". *Applied Physics Letters* 89.6 (2006), p. 061111. DOI: 10.1063/1.2268354.

[105] R. Meerheim et al. "Influence of Charge Balance and Exciton Distribution on Efficiency and Lifetime of Phosphorescent Organic Light-Emitting Devices". *Journal of Applied Physics* 104.1 (2008), p. 014510. DOI: 10.1063/1.2951960.

[106] T. Yoshioka et al. “45.1: An Improved Method for Lifetime Prediction Based on Decoupling of the Joule Self-Heating Effect from Coulombic Degradation in Accelerated Aging Tests of OLEDs”. en. *SID Symposium Digest of Technical Papers* 45.1 (2014), pp. 642–645. DOI: 10.1002/j.2168-0159.2014.tb00168.x.

[107] H. Aziz and Z. D. Popovic. “Degradation Phenomena in Small-Molecule Organic Light-Emitting Devices”. *Chemistry of Materials* 16.23 (2004), pp. 4522–4532. DOI: 10.1021/cm040081o.

[108] H. Aziz et al. “Degradation Processes at the Cathode/Organic Interface in Organic Light Emitting Devices with Mg:Ag Cathodes”. *Applied Physics Letters* 72.21 (1998), pp. 2642–2644. DOI: 10.1063/1.121442.

[109] A. R. G. Smith et al. “Investigating Morphology and Stability of Fac-Tris (2-Phenylpyridyl)Iridium(III) Films for OLEDs”. en. *Advanced Functional Materials* 21.12 (2011), pp. 2225–2231. DOI: 10.1002/adfm.201002365.

[110] W. Sotoyama et al. “Development of Efficiency and Stability of Phosphorescent Organic Electroluminescent Devices”. *Fujifilm Research and Development* 055 (2010), pp. 24–28. URL: http://www.fujifilm.com/about/research/report/055/pdf/index/ff_rd055_all_en.pdf\#page=28 (visited on 12/30/2016).

[111] Y. Masumoto and T. Mori. “Application of Organic Bathocuproine-Based Alloy Film to Organic Light-Emitting Diodes”. *Thin Solid Films* 516.10 (2008), pp. 3350–3356. DOI: 10.1016/j.tsf.2007.11.082.

[112] S. Schmidbauer, A. Hohenleutner, and B. König. “Chemical Degradation in Organic Light-Emitting Devices: Mechanisms and Implications for the Design of New Materials”. en. *Advanced Materials* 25.15 (2013), pp. 2114–2129. DOI: 10.1002/adma.201205022.

[113] S. Scholz, K. Walzer, and K. Leo. “Analysis of Complete Organic Semiconductor Devices by Laser Desorption/Ionization Time-of-Flight Mass Spectrometry”. en. *Advanced Functional Materials* 18.17 (2008), pp. 2541–2547. DOI: 10.1002/adfm.200700816.

[114] C. Jeong et al. “Understanding Molecular Fragmentation in Blue Phosphorescent Organic Light-Emitting Devices”. *Organic Electronics* 64 (2019), pp. 15–21. DOI: 10.1016/j.orgel.2018.10.001.

[115] F. So and D. Kondakov. “Degradation Mechanisms in Small-Molecule and Polymer Organic Light-Emitting Diodes”. en. *Advanced Materials* 22.34 (2010), pp. 3762–3777. DOI: 10.1002/adma.200902624.

[116] D. Y. Kondakov. “The Role of Homolytic Reactions in the Instrinsic Degradation of OLEDs.” *Organic Electronics*. Ed. by F. So. Boca Raton, FL: CRC Press, 2010, pp. 211–242.

[117] S. Scholz, R. Meerheim, B. Lüssem, and K. Leo. “46.1: Invited Paper: Exciton Induced Chemical Reactions in Organic Light Emitting Devices”. en. *SID Symposium Digest of Technical Papers* 40.1 (2009), pp. 681–684. DOI: 10.1889/1.3256875.

[118] D. Kondakov. “Role of Chemical Reactions of Arylamine Hole Transport Materials in Operational Degradation of Organic Light-Emitting Diodes”. *Journal of Applied Physics* 104.8 (2008), p. 084520. DOI: 10.1063/1.3006890.

[119] T. D. Schmidt, L. Jäger, Y. Noguchi, H. Ishii, and W. Brütting. “Analyzing Degradation Effects of Organic Light-Emitting Diodes via Transient Optical and Electrical Measurements”. *Journal of Applied Physics* 117.21 (2015), p. 215502. DOI: 10.1063/1.4921829.

[120] S. Nowy, W. Ren, J. Wagner, J. A. Weber, and W. Brütting. "Impedance Spectroscopy of Organic Hetero-Layer OLEDs as a Probe for Charge Carrier Injection and Device Degradation". Vol. 7415. 2009, 74150G–74150G–12. DOI: 10.1117/12.824856.

[121] Q. Wang, B. Sun, and H. Aziz. "Exciton–Polaron-Induced Aggregation of Wide-Bandgap Materials and Its Implication on the Electroluminescence Stability of Phosphorescent Organic Light-Emitting Devices". en. *Advanced Functional Materials* 24.20 (2014), pp. 2975–2985. DOI: 10.1002/adfm.201303840.

[122] H. Aziz, Z. D. Popovic, N.-X. Hu, A.-M. Hor, and G. Xu. "Degradation Mechanism of Small Molecule-Based Organic Light-Emitting Devices". en. *Science* 283.5409 (1999), pp. 1900–1902. DOI: 10.1126/science.283.5409.1900.

[123] Z. D. Popovic and H. Aziz. "Reliability and Degradation of Small Molecule-Based Organic Light-Emitting Devices (OLEDs)". *IEEE Journal of Selected Topics in Quantum Electronics* 8.2 (2002), pp. 362–371. DOI: 10.1109/2944.999191.

[124] Y. J. Cho, Y. Zhang, H. Yu, and H. Aziz. "The Root Causes of the Limited Stability of Solution-Coated Small-Molecule Organic Light-Emitting Devices: Faster Host Aggregation by Exciton–Polaron Interactions". en. *Advanced Functional Materials* (2016), n/a–n/a. DOI: 10.1002/adfm.201603542.

[125] Y. Zhang and H. Aziz. "Degradation Mechanisms in Blue Phosphorescent Organic Light-Emitting Devices by Exciton–Polaron Interactions: Loss in Quantum Yield versus Loss in Charge Balance". *ACS Applied Materials & Interfaces* 9.1 (2017), pp. 636–643. DOI: 10.1021/acsami.6b13823.

[126] Y. Zhang, J. Lee, and S. R. Forrest. "Tenfold Increase in the Lifetime of Blue Phosphorescent Organic Light-Emitting Diodes". en. *Nature Communications* 5 (2014), p. 5008. DOI: 10.1038/ncomms6008.

[127] Z. D. Popovic, H. Aziz, N.-X. Hu, A. Ioannidis, and P. N. M. dos Anjos. "Simultaneous Electroluminescence and Photoluminescence Aging Studies of Tris(8-Hydroxyquinoline) Aluminum-Based Organic Light-Emitting Devices". *Journal of Applied Physics* 89.8 (2001), pp. 4673–4675. DOI: 10.1063/1.1354631.

[128] S. Winter, S. Reineke, K. Walzer, and K. Leo. "Photoluminescence Degradation of Blue OLED Emitters". *Proc. SPIE*. Vol. 6999. 2008, 69992N. DOI: 10.1117/12.782784.

[129] Z. Wu et al. "Achieving Extreme Utilization of Excitons by an Efficient Sandwich-Type Emissive Layer Architecture for Reduced Efficiency Roll-Off and Improved Operational Stability in Organic Light-Emitting Diodes". *ACS Applied Materials & Interfaces* 8.5 (2016), pp. 3150–3159. DOI: 10.1021/acsami.5b10532.

[130] B. D. Chin et al. "Carrier Trapping and Efficient Recombination of Electrophosphorescent Device with Stepwise Doping Profile". *Applied Physics Letters* 86.13 (2005), p. 133505. DOI: 10.1063/1.1894596.

[131] J. Y. Lee. "17.3: Study of Light Emission Mechanism and Long Lifetime in Phosphorescent Organic Light Emitting Diodes Using Graded Doping Structure". en. *SID Symposium Digest of Technical Papers* 37.1 (2006), pp. 1103–1105. DOI: 10.1889/1.2433167.

[132] A. B. Chwang, R. C. Kwong, and J. J. Brown. "Graded Mixed-Layer Organic Light-Emitting Devices". *Applied Physics Letters* 80.5 (2002), pp. 725–727. DOI: 10.1063/1.1446992.

[133] N. C. Erickson and R. J. Holmes. “Investigating the Role of Emissive Layer Architecture on the Exciton Recombination Zone in Organic Light-Emitting Devices”. en. *Advanced Functional Materials* 23.41 (2013), pp. 5190–5198. DOI: 10.1002/adfm.201300101.

[134] T.-H. Han, Y.-H. Kim, M. H. Kim, W. Song, and T.-W. Lee. “Synergetic Influences of Mixed-Host Emitting Layer Structures and Hole Injection Layers on Efficiency and Lifetime of Simplified Phosphorescent Organic Light-Emitting Diodes”. *ACS Applied Materials & Interfaces* 8.9 (2016), pp. 6152–6163. DOI: 10.1021/acsami.5b11791.

[135] Y.-C. Tsai and J.-H. Jou. “Long-Lifetime, High-Efficiency White Organic Light-Emitting Diodes with Mixed Host Composing Double Emission Layers”. *Applied Physics Letters* 89.24 (2006), p. 243521. DOI: 10.1063/1.2408663.

[136] J.-H. Lee, C.-I. Wu, S.-W. Liu, C.-A. Huang, and Y. Chang. “Mixed Host Organic Light-Emitting Devices with Low Driving Voltage and Long Lifetime”. *Applied Physics Letters* 86.10 (2005), p. 103506. DOI: 10.1063/1.1879093.

[137] C. T. Brown and D. Kondakov. “A New Generation of High-Efficiency Red-Emitting Electroluminescent Devices with Exceptional Stability”. en. *Journal of the Society for Information Display* 12.3 (2004), pp. 323–327. DOI: 10.1889/1.1821305.

[138] V.-E. Choong et al. “Efficient and Durable Organic Alloys for Electroluminescent Displays”. en. *Journal of Physics D: Applied Physics* 33.7 (2000), p. 760. DOI: 10.1088/0022-3727/33/7/302.

[139] S. W. Liu et al. “Blue Mixed Host Organic Light Emitting Devices”. *Thin Solid Films*. Proceedings of Symposium H on Photonic Processing of Surfaces, Thin Films and Devices, of the E-MRS 2003 Spring Conference 453–454 (2004), pp. 312–315. DOI: 10.1016/j.tsf.2003.11.092.

[140] P. Wellmann et al. “High-Efficiency p-i-n Organic Light-Emitting Diodes with Long Lifetime”. en. *Journal of the Society for Information Display* 13.5 (2005), pp. 393–397. DOI: 10.1889/1.1927730.

[141] W. S. Jeon et al. “Low Roll-off Efficiency Green Phosphorescent Organic Light-Emitting Devices with Simple Double Emissive Layer Structure”. *Applied Physics Letters* 93.6 (2008), p. 063303. DOI: 10.1063/1.2969040.

[142] B. D. Chin. “Enhancement of Efficiency and Stability of Phosphorescent OLEDs Based on Heterostructured Light-Emitting Layers”. en. *Journal of Physics D: Applied Physics* 44.11 (2011), p. 115103. DOI: 10.1088/0022-3727/44/11/115103.

[143] K. S. Yook, S. O. Jeon, C. W. Joo, and J. Y. Lee. “Correlation of Lifetime and Recombination Zone in Green Phosphorescent Organic Light-Emitting Diodes”. *Applied Physics Letters* 94.9 (2009), p. 093501. DOI: 10.1063/1.3083547.

[144] A. S. D. Sandanayaka, T. Matsushima, and C. Adachi. “Degradation Mechanisms of Organic Light-Emitting Diodes Based on Thermally Activated Delayed Fluorescence Molecules”. *The Journal of Physical Chemistry C* 119.42 (2015), pp. 23845–23851. DOI: 10.1021/acs.jpcc.5b07084.

[145] K. S. Yook and J. Y. Lee. “Recombination Zone Study of Phosphorescent Organic Light-Emitting Diodes with Triplet Mixed Host Emitting Structure”. *Journal of Industrial and Engineering Chemistry* 16.2 (2010), pp. 181–184. DOI: 10.1016/j.jiec.2009.08.007.

[146] N. C. Erickson and R. J. Holmes. “Engineering Efficiency Roll-Off in Organic Light-Emitting Devices”. en. *Advanced Functional Materials* 24.38 (2014), pp. 6074–6080. DOI: 10.1002/adfm.201401009.

[147] M. D. Perez, C. Borek, S. R. Forrest, and M. E. Thompson. “Molecular and Morphological Influences on the Open Circuit Voltages of Organic Photovoltaic Devices”. *Journal of the American Chemical Society* 131.26 (2009), pp. 9281–9286. DOI: 10.1021/ja9007722.

[148] M. Furno et al. “Outcoupling Efficiency in Small-Molecule OLEDs: From Theory to Experiment”. *Proc. SPIE*. Vol. 7617. 2010, p. 761716. DOI: 10.1117/12.840043.

[149] L. A. A. Pettersson, L. S. Roman, and O. Inganäs. “Modeling Photocurrent Action Spectra of Photovoltaic Devices Based on Organic Thin Films”. *Journal of Applied Physics* 86.1 (1999), pp. 487–496. DOI: 10.1063/1.370757.

[150] Q. Wang and H. Aziz. “Role of the Cathode Interfacial Layers in Improving the Stability of Organic Optoelectronic Devices”. Vol. 8476. 2012, pp. 84760D–84760D–5. DOI: 10.1117/12.929111.

[151] Q. Wang, Y. Luo, and H. Aziz. “Photodegradation of the Organic/Metal Cathode Interface in Organic Light-Emitting Devices”. *Applied Physics Letters* 97.6 (2010), p. 063309. DOI: 10.1063/1.3480412.

[152] Q. Wang, G. Williams, and H. Aziz. “Photo-Degradation of the Indium Tin Oxide (ITO)/Organic Interface in Organic Optoelectronic Devices and a New Outlook on the Role of ITO Surface Treatments and Interfacial Layers in Improving Device Stability”. *Organic Electronics* 13.10 (2012), pp. 2075–2082. DOI: 10.1016/j.orgel.2012.06.017.

[153] W. Song and J. Y. Lee. “Degradation Mechanism and Lifetime Improvement Strategy for Blue Phosphorescent Organic Light-Emitting Diodes”. en. *Advanced Optical Materials* 5.9 (2017), p. 1600901. DOI: 10.1002/adom.201600901.

[154] S. J. Byrnes. “Multilayer Optical Calculations”. *arXiv:1603.02720 [physics]* (2016). arXiv: 1603.02720 [physics]. URL: http://arxiv.org/abs/1603.02720 (visited on 02/21/2018).

[155] C. Coburn, J. Lee, and S. R. Forrest. “Charge Balance and Exciton Confinement in Phosphorescent Organic Light Emitting Diodes”. en. *Advanced Optical Materials* 4.6 (2016), pp. 889–895. DOI: 10.1002/adom.201600067.

[156] S. K. Jeon and J. Y. Lee. “Direct Monitoring of Recombination Zone Shift during Lifetime Measurement of Phosphorescent Organic Light-Emitting Diodes”. *Journal of Industrial and Engineering Chemistry* 32 (2015), pp. 332–335. DOI: 10.1016/j.jiec.2015.09.011.

[157] J. S. Bangsund, K. W. Hershey, and R. J. Holmes. “Isolating Degradation Mechanisms in Mixed Emissive Layer Organic Light-Emitting Devices”. *ACS Applied Materials & Interfaces* 10.6 (2018), pp. 5693–5699. DOI: 10.1021/acsami.7b16643.

[158] M. Tanaka, H. Noda, H. Nakanotani, and C. Adachi. “Effect of Carrier Balance on Device Degradation of Organic Light-Emitting Diodes Based on Thermally Activated Delayed Fluorescence Emitters”. en. *Advanced Electronic Materials* 0.0 (2019), p. 1800708. DOI: 10.1002/aelm.201800708.

[159] N. C. Erickson and R. J. Holmes. “Relating Charge Transport and Performance in Single-Layer Graded-Composition Organic Light-Emitting Devices”. *Journal of Applied Physics* 110.8 (2011), p. 084515. DOI: 10.1063/1.3653285.

[160] S. Lee et al. “The Role of Charge Balance and Excited State Levels on Device Performance of Exciplex-Based Phosphorescent Organic Light Emitting Diodes”. en. *Scientific Reports* 7.1 (2017), p. 11995. DOI: 10.1038/s41598-017-12059-2.

[161] C.-H. Hsiao, Y.-H. Chen, T.-C. Lin, C.-C. Hsiao, and J.-H. Lee. “Recombination Zone in Mixed-Host Organic Light-Emitting Devices”. *Applied Physics Letters* 89.16 (2006), p. 163511. DOI: 10.1063/1.2361266.

[162] W. Song et al. “Electroplex as a New Concept of Universal Host for Improved Efficiency and Lifetime in Red, Yellow, Green, and Blue Phosphorescent Organic Light-Emitting Diodes”. en. *Advanced Science* 5.2 (2018), p. 1700608. DOI: 10.1002/advs.201700608.

[163] S. K. Jeon and J. Y. Lee. “Four Times Lifetime Improvement of Blue Phosphorescent Organic Light-Emitting Diodes by Managing Recombination Zone”. *Organic Electronics* 27 (2015), pp. 202–206. DOI: 10.1016/j.orgel.2015.09.016.

[164] J.-M. Kim, C.-H. Lee, and J.-J. Kim. “Mobility Balance in the Light-Emitting Layer Governs the Polaron Accumulation and Operational Stability of Organic Light-Emitting Diodes”. *Applied Physics Letters* 111.20 (2017), p. 203301. DOI: 10.1063/1.5004623.

[165] H. Shin et al. “Blue Phosphorescent Organic Light-Emitting Diodes Using an Exciplex Forming Co-Host with the External Quantum Efficiency of Theoretical Limit”. en. *Advanced Materials* 26.27 (2014), pp. 4730–4734. DOI: 10.1002/adma.201400955.

[166] Y. Yamada et al. “52-4: Achievement of Blue Phosphorescent Organic Light-Emitting Diode with High Efficiency, Low Driving Voltage, and Long Lifetime by Exciplex—Triplet Energy Transfer Technology”. en. *SID Symposium Digest of Technical Papers* 47.1 (2016), pp. 711–714. DOI: 10.1002/sdtp.10782.

[167] B. W. D’Andrade et al. “Relationship between the Ionization and Oxidation Potentials of Molecular Organic Semiconductors”. *Organic Electronics* 6.1 (2005), pp. 11–20. DOI: 10.1016/j.orgel.2005.01.002.

[168] B. W. D’Andrade, R. J. Holmes, and S. R. Forrest. “Efficient Organic Electrophosphorescent White-Light-Emitting Device with a Triple Doped Emissive Layer”. *Advanced Materials* 16.7 (2004), pp. 624–628. DOI: 10.1002/adma.200306670.

[169] H. Yoshida and K. Yoshizaki. “Electron Affinities of Organic Materials Used for Organic Light-Emitting Diodes: A Low-Energy Inverse Photoemission Study”. *Organic Electronics* 20 (2015), pp. 24–30. DOI: 10.1016/j.orgel.2015.01.037.

[170] P. I. Djurovich, E. I. Mayo, S. R. Forrest, and M. E. Thompson. “Measurement of the Lowest Unoccupied Molecular Orbital Energies of Molecular Organic Semiconductors”. *Organic Electronics* 10.3 (2009), pp. 515–520. DOI: 10.1016/j.orgel.2008.12.011.

[171] K. Goushi, R. Kwong, J. J. Brown, H. Sasabe, and C. Adachi. “Triplet Exciton Confinement and Unconfinement by Adjacent Hole-Transport Layers”. *Journal of Applied Physics* 95.12 (2004), pp. 7798–7802. DOI: 10.1063/1.1751232.

[172] K. Goushi, Y. Kawamura, H. Sasabe, and C. Adachi. “Unusual Phosphorescence Characteristics of Ir(Ppy)3 in a Solid Matrix at Low Temperatures”. en. *Japanese Journal of Applied Physics* 43.7A (2004), p. L937. DOI: 10.1143/JJAP.43.L937.

[173] A. Völcker, H. J. Adick, R. Schmidt, and H. D. Brauer. “Near-Infrared Phosphorescence Emission of Compounds with Low-Lying Triplet States”. en. *Chemical Physics Letters* 159.1 (1989), pp. 103–108. DOI: 10.1016/S0009-2614(89)87462-7.

[174] B. Sim, C.-K. Moon, K.-H. Kim, and J.-J. Kim. "Quantitative Analysis of the Efficiency of OLEDs". *ACS Applied Materials & Interfaces* 8.48 (2016), pp. 33010–33018. DOI: 10.1021/acsami.6b10297.

[175] J. S. Bangsund et al. "Improved Stability in Organic Light-Emitting Devices by Mixing Ambipolar and Wide Energy Gap Hosts". en. *Journal of the Society for Information Display* 27.7 (2019), pp. 434–441. DOI: 10.1002/jsid.761.

[176] H. Sasabe and J. Kido. "Development of High Performance OLEDs for General Lighting". en. *Journal of Materials Chemistry C* 1.9 (2013), p. 1699. DOI: 10.1039/c2tc00584k.

[177] Y. Tao, C. Yang, and J. Qin. "Organic Host Materials for Phosphorescent Organic Light-Emitting Diodes". en. *Chemical Society Reviews* 40.5 (2011), pp. 2943–2970. DOI: 10.1039/C0CS00160K.

[178] S. Tokito et al. "Confinement of Triplet Energy on Phosphorescent Molecules for Highly-Efficient Organic Blue-Light-Emitting Devices". *Applied Physics Letters* 83.3 (2003), pp. 569–571. DOI: 10.1063/1.1594834.

[179] R. J. Holmes et al. "Blue Organic Electrophosphorescence Using Exothermic Host–Guest Energy Transfer". *Applied Physics Letters* 82.15 (2003), pp. 2422–2424. DOI: 10.1063/1.1568146.

[180] S. T. Hoffmann et al. "Triplet Excimer Emission in a Series of 4,4′-Bis(N-Carbazolyl)-2,2′-Biphenyl Derivatives". *The Journal of Physical Chemistry B* 115.3 (2011), pp. 414–421. DOI: 10.1021/jp107408e.

[181] A. Y. Freidzon et al. "Predicting the Operational Stability of Phosphorescent OLED Host Molecules from First Principles: A Case Study". *The Journal of Physical Chemistry C* 121.40 (2017), pp. 22422–22433. DOI: 10.1021/acs.jpcc.7b05761.

[182] H. Yu and H. Aziz. "Exciton-Induced Degradation of Hole Transport Layers and Its Effect on the Efficiency and Stability of Phosphorescent Organic Light-Emitting Devices". en. *Advanced Optical Materials* 7.5 (2018), p. 1800923. DOI: 10.1002/adom.201800923.

[183] T. Setzer et al. "Meltdown! Local Heating by Decaying Excited Host Positive Polarons Triggers Aggregation Quenching in Blue PhOLEDs". en. *ChemPhysChem* 19.21 (2018), pp. 2961–2966. DOI: 10.1002/cphc.201800250.

[184] D. F. O'Brien, M. A. Baldo, M. E. Thompson, and S. R. Forrest. "Improved Energy Transfer in Electrophosphorescent Devices". *Applied Physics Letters* 74.3 (1999), pp. 442–444. DOI: 10.1063/1.123055.

[185] S. A. Bagnich, A. Rudnick, P. Schroegel, P. Strohriegl, and A. Köhler. "Triplet Energies and Excimer Formation in Meta- and Para-Linked Carbazolebiphenyl Matrix Materials". *Philosophical Transactions of the Royal Society A: Mathematical, Physical and Engineering Sciences* 373.2044 (2015), p. 20140446. DOI: 10.1098/rsta.2014.0446.

[186] D. Jacquemin and D. Escudero. "The Short Device Lifetimes of Blue PhOLEDs: Insights into the Photostability of Blue Ir(III) Complexes". en. *Chemical Science* 8.11 (2017), pp. 7844–7850. DOI: 10.1039/C7SC03905K.

[187] D. Y. Kondakov. "Characterization of Triplet-Triplet Annihilation in Organic Light-Emitting Diodes Based on Anthracene Derivatives". *Journal of Applied Physics* 102.11 (2007), p. 114504. DOI: 10.1063/1.2818362.

[188] N. Lin, J. Qiao, L. Duan, L. Wang, and Y. Qiu. "Molecular Understanding of the Chemical Stability of Organic Materials for OLEDs: A Comparative Study on Sulfonyl, Phosphine-Oxide, and Carbonyl-Containing Host Materials". *The Journal of Physical Chemistry C* 118.14 (2014), pp. 7569–7578. DOI: 10.1021/jp412614k.

[189] I. R. de Moraes, S. Scholz, B. Lüssem, and K. Leo. "Analysis of Chemical Degradation Mechanism within Sky Blue Phosphorescent Organic Light Emitting Diodes by Laser-Desorption/Ionization Time-of-Flight Mass Spectrometry". *Organic Electronics* 12.2 (2011), pp. 341–347. DOI: 10.1016/j.orgel.2010.11.004.

[190] S. Reineke, G. Schwartz, K. Walzer, and K. Leo. "Direct Observation of Host–Guest Triplet–Triplet Annihilation in Phosphorescent Solid Mixed Films". en. *physica status solidi (RRL) – Rapid Research Letters* 3.2-3 (2009), pp. 67–69. DOI: 10.1002/pssr.200802266.

[191] D. Rai and R. J. Holmes. "Measurement of the Triplet Exciton Diffusion Length in Organic Semiconductors". en. *Journal of Materials Chemistry C* 7.19 (2019), pp. 5695–5701. DOI: 10.1039/C9TC00686A.

[192] R. Seifert et al. "Chemical Degradation Mechanisms of Highly Efficient Blue Phosphorescent Emitters Used for Organic Light Emitting Diodes". *Organic Electronics* 14.1 (2013), pp. 115–123. DOI: 10.1016/j.orgel.2012.10.003.

[193] R. Newcomb et al. "Role of Host Excimer Formation in the Degradation of Organic Light-Emitting Devices". *Applied Physics Letters* 116.6 (2020), p. 063302. DOI: 10.1063/1.5124802.

[194] R. Meerheim, M. Furno, S. Hofmann, B. Lüssem, and K. Leo. "Quantification of Energy Loss Mechanisms in Organic Light-Emitting Diodes". *Applied Physics Letters* 97.25 (2010), p. 253305. DOI: 10.1063/1.3527936.

[195] Y. Noguchi, N. Sato, Y. Tanaka, Y. Nakayama, and H. Ishii. "Threshold Voltage Shift and Formation of Charge Traps Induced by Light Irradiation during the Fabrication of Organic Light-Emitting Diodes". *Applied Physics Letters* 92.20 (2008), p. 203306. DOI: 10.1063/1.2936084.

[196] S. Reineke, M. Thomschke, B. Lüssem, and K. Leo. "White Organic Light-Emitting Diodes: Status and Perspective". *Reviews of Modern Physics* 85.3 (2013), pp. 1245–1293. DOI: 10.1103/RevModPhys.85.1245.

[197] S. Wehrmeister et al. "Combined Electrical and Optical Analysis of the Efficiency Roll-Off in Phosphorescent Organic Light-Emitting Diodes". *Physical Review Applied* 3.2 (2015), p. 024008. DOI: 10.1103/PhysRevApplied.3.024008.

[198] D. Zhao and H.-P. Loebl. "The Accumulation of Diffusive Charges in Organic Light-Emitting Diodes". *Organic Electronics* 24 (2015), pp. 147–152. DOI: 10.1016/j.orgel.2015.05.020.

[199] D. Song, S. Zhao, Y. Luo, and H. Aziz. "Causes of Efficiency Roll-off in Phosphorescent Organic Light Emitting Devices: Triplet-Triplet Annihilation versus Triplet-Polaron Quenching". en. *Applied Physics Letters* 97.24 (2010), p. 243304. DOI: 10.1063/1.3527085.

[200] J.-M. Kim and J.-J. Kim. "Charge Transport Layers Manage Mobility and Carrier Density Balance in Light-Emitting Layers Influencing the Operational Stability of Organic Light Emitting Diodes". en. *Organic Electronics* 67 (2019), pp. 43–49. DOI: 10.1016/j.orgel.2018.12.026.

[201] Y. Noguchi, W. Brütting, and H. Ishii. “Spontaneous Orientation Polarization in Organic Light-Emitting Diodes”. en. *Japanese Journal of Applied Physics* 58.SF (2019), SF0801. DOI: 10.7567/1347-4065/ab0de8.

[202] E. Ito et al. “Spontaneous Buildup of Giant Surface Potential by Vacuum Deposition of Alq3 and Its Removal by Visible Light Irradiation”. *Journal of Applied Physics* 92.12 (2002), pp. 7306–7310. DOI: 10.1063/1.1518759.

[203] Y. Noguchi et al. “Charge Accumulation at Organic Semiconductor Interfaces Due to a Permanent Dipole Moment and Its Orientational Order in Bilayer Devices”. *Journal of Applied Physics* 111.11 (2012), p. 114508. DOI: 10.1063/1.4724349.

[204] K. Masui, H. Nakanotani, and C. Adachi. “Analysis of Exciton Annihilation in High-Efficiency Sky-Blue Organic Light-Emitting Diodes with Thermally Activated Delayed Fluorescence”. *Organic Electronics* 14.11 (2013), pp. 2721–2726. DOI: 10.1016/j.orgel.2013.07.010.

[205] T. Furukawa, H. Nakanotani, M. Inoue, and C. Adachi. “Dual Enhancement of Electroluminescence Efficiency and Operational Stability by Rapid Upconversion of Triplet Excitons in OLEDs”. *Scientific Reports* 5 (2015), p. 8429. DOI: 10.1038/srep08429.

[206] Y. Shirasaki, G. J. Supran, W. A. Tisdale, and V. Bulović. “Origin of Efficiency Roll-Off in Colloidal Quantum-Dot Light-Emitting Diodes”. *Physical Review Letters* 110.21 (2013), p. 217403. DOI: 10.1103/PhysRevLett.110.217403.

[207] W. Zou et al. “Minimising Efficiency Roll-off in High-Brightness Perovskite Light-Emitting Diodes”. En. *Nature Communications* 9.1 (2018), p. 608. DOI: 10.1038/s41467-018-03049-7.

[208] M. Kröger et al. “Temperature-Independent Field-Induced Charge Separation at Doped Organic/Organic Interfaces: Experimental Modeling of Electrical Properties”. *Physical Review B* 75.23 (2007), p. 235321. DOI: 10.1103/PhysRevB.75.235321.

[209] M. Regnat, K. P. Pernstich, and B. Ruhstaller. “Influence of the Bias-Dependent Emission Zone on Exciton Quenching and OLED Efficiency”. *Organic Electronics* 70 (2019), pp. 219–226. DOI: 10.1016/j.orgel.2019.04.027.

[210] S. Egusa, A. Miura, N. Gemma, and M. Azuma. “Carrier Injection Characteristics of Organic Electroluminescent Devices”. en. *Japanese Journal of Applied Physics* 33.5R (1994), p. 2741. DOI: 10.1143/JJAP.33.2741.

[211] T. Morgenstern et al. “Correlating Optical and Electrical Dipole Moments To Pinpoint Phosphorescent Dye Alignment in Organic Light-Emitting Diodes”. *ACS Applied Materials & Interfaces* 10.37 (2018), pp. 31541–31551. DOI: 10.1021/acsami.8b08963.

[212] H.-F. Xiang, Z.-X. Xu, V. a. L. Roy, C.-M. Che, and P. T. Lai. “Method for Measurement of the Density of Thin Films of Small Organic Molecules”. *Review of Scientific Instruments* 78.3 (2007), p. 034104. DOI: 10.1063/1.2712932.

[213] Y. Noguchi, H. Ishii, T. Tamura, and H. J. Kim. “Device Properties of Alq3-Based Organic Light-Emitting Diodes Studied by Displacement Current Measurement”. *Journal of Photonics for Energy* 2.1 (2012), p. 021214. DOI: 10.1117/1.JPE.2.021214.

[214] J. Ràfols-Ribé et al. “High-Performance Organic Light-Emitting Diodes Comprising Ultrastable Glass Layers”. en. *Science Advances* 4.5 (2018), eaar8332. DOI: 10.1126/sciadv.aar8332.

[215] Y. Esaki, T. Matsushima, and C. Adachi. “Dependence of the Amorphous Structures and Photoluminescence Properties of Tris(8-Hydroxyquinolinato)Aluminum Films on Vacuum Deposition Conditions”. *Organic Electronics* 67 (2019), pp. 237–241. DOI: 10.1016/j.orgel.2019.01.032.

[216] Y. Qiu, L. W. Antony, J. J. de Pablo, and M. D. Ediger. “Photostability Can Be Significantly Modulated by Molecular Packing in Glasses”. *Journal of the American Chemical Society* 138.35 (2016), pp. 11282–11289. DOI: 10.1021/jacs.6b06372.

[217] D.-G. Ha et al. “Dominance of Exciton Lifetime in the Stability of Phosphorescent Dyes”. en. *Advanced Optical Materials* 7.21 (2019), p. 1901048. DOI: 10.1002/adom.201901048.

[218] Y. Qiu, L. W. Antony, J. M. Torkelson, J. J. de Pablo, and M. D. Ediger. “Tenfold Increase in the Photostability of an Azobenzene Guest in Vapor-Deposited Glass Mixtures”. *The Journal of Chemical Physics* 149.20 (2018), p. 204503. DOI: 10.1063/1.5052003.

[219] H. Fujimoto et al. “Influence of Vacuum Chamber Impurities on the Lifetime of Organic Light-Emitting Diodes”. *Scientific Reports* 6 (2016). DOI: 10.1038/srep38482.

[220] H. Fujimoto et al. “Vacuum Chamber Considerations for Improved Organic Light-Emitting Diode Lifetime”. *AIP Advances* 8.8 (2018), p. 085025. DOI: 10.1063/1.5047542.

[221] A. P. Marchetti, T. L. Haskins, R. H. Young, and L. J. Rothberg. “Permanent Polarization and Charge Distribution in Organic Light-Emitting Diodes (OLEDs): Insights from near-Infrared Charge-Modulation Spectroscopy of an Operating OLED”. *Journal of Applied Physics* 115.11 (2014), p. 114506. DOI: 10.1063/1.4867779.

[222] Y. Divayana and X. W. Sun. “Existence of Optimum Intermolecular Spacing for Maximum Exciton Diffusion Length in Tris(2-Phenylpyridine) Iridium(III)”. en. *Organic Electronics* 11.1 (2010), pp. 67–73. DOI: 10.1016/j.orgel.2009.09.029.

[223] X. de Vries, P. Friederich, W. Wenzel, R. Coehoorn, and P. A. Bobbert. “Triplet Exciton Diffusion in Metalorganic Phosphorescent Host-Guest Systems from First Principles”. *Physical Review B* 99.20 (2019), p. 205201. DOI: 10.1103/PhysRevB.99.205201.

[224] A. P. Proudian, M. B. Jaskot, D. R. Diercks, B. P. Gorman, and J. D. Zimmerman. “Atom Probe Tomography of Molecular Organic Materials: Sub-Dalton Nanometer-Scale Quantification”. *Chemistry of Materials* 31.7 (2019), pp. 2241–2247. DOI: 10.1021/acs.chemmater.8b04476.

[225] M. Regnat, K. P. Pernstich, S. Züfle, and B. Ruhstaller. “Analysis of the Bias-Dependent Split Emission Zone in Phosphorescent OLEDs”. *ACS Applied Materials & Interfaces* 10.37 (2018), pp. 31552–31559. DOI: 10.1021/acsami.8b09595.

[226] M. Oh-e, H. Ogata, and F. Araoka. “Randomization and Constraint of Molecular Alignment and Orientation: Temperature-Dependent Anisotropy and Phase Transition in Vapor-Deposited Thin Films of an Organic Cross-Shaped Molecule”. *ACS Omega* 4.1 (2019), pp. 39–47. DOI: 10.1021/acsomega.8b02560.

[227] N. Kajimoto, T. Manaka, and M. Iwamoto. “Decay Process of a Large Surface Potential of Alq3 Films by Heating”. *Journal of Applied Physics* 100.5 (2006), p. 053707. DOI: 10.1063/1.2338137.

[228] X. Zhao, J. D. A. Ng, R. H. Friend, and Z.-K. Tan. “Opportunities and Challenges in Perovskite Light-Emitting Devices”. *ACS Photonics* 5.10 (2018), pp. 3866–3875. DOI: 10.1021/acsphotonics.8b00745.

[229] H. Kim et al. “Hybrid Perovskite Light Emitting Diodes under Intense Electrical Excitation”. en. *Nature Communications* 9.1 (2018), pp. 1–9. DOI: 10.1038/s41467-018-07383-8.

[230] A. Walsh and S. D. Stranks. “Taking Control of Ion Transport in Halide Perovskite Solar Cells”. *ACS Energy Letters* 3.8 (2018), pp. 1983–1990. DOI: 10.1021/acsenergylett.8b00764.

[231] G. Y. Kim et al. “Large Tunable Photoeffect on Ion Conduction in Halide Perovskites and Implications for Photodecomposition”. en. *Nature Materials* 17.5 (2018), pp. 445–449. DOI: 10.1038/s41563-018-0038-0.

[232] F. Yan et al. “Highly Efficient Visible Colloidal Lead-Halide Perovskite Nanocrystal Light-Emitting Diodes”. *Nano Letters* 18.5 (2018), pp. 3157–3164. DOI: 10.1021/acs.nanolett.8b00789.

[233] Q. Wang and H. Aziz. “Correlation between Exciton-Induced Degradation of Organic/Metal Interfaces and Energy Barrier for Electron Injection at Organic/Metal Interfaces in Organic Optoelectronic Devices”. Vol. 8829. 2013, pp. 882920–882920–9. DOI: 10.1117/12.2023639.

[234] Q. Wang, G. Williams, T. Tsui, and H. Aziz. “Photochemical Deterioration of the Organic/Metal Contacts in Organic Optoelectronic Devices”. *Journal of Applied Physics* 112.6 (2012), p. 064502. DOI: 10.1063/1.4752252.

[235] A. Salehi et al. “Highly Efficient Organic Light-Emitting Diode Using A Low Refractive Index Electron Transport Layer”. en. *Advanced Optical Materials* 5.11 (2017), p. 1700197. DOI: 10.1002/adom.201700197.

[236] A. Endo et al. “Measurement of Photoluminescence Efficiency of Ir(III) Phenylpyridine Derivatives in Solution and Solid-State Films”. en. *Chemical Physics Letters* 460.1 (2008), pp. 155–157. DOI: 10.1016/j.cplett.2008.05.064.

[237] J. S. Bangsund, J. Van Sambeek, N. M. Concannon, and R. J. Holmes. “Sub-Turn-on Exciton Quenching Due to Molecular Orientation and Polarization in Organic Light-Emitting Devices”. *Science Advances* 6 (2020). DOI: 10.1126/sciadv.abb2659.

[238] M. C. Gather, A. Köhnen, and K. Meerholz. “White Organic Light-Emitting Diodes”. en. *Advanced Materials* 23.2 (2011), pp. 233–248. DOI: 10.1002/adma.201002636.

[239] A. Schweikart, A. Horn, A. Böker, and A. Fery. “Controlled Wrinkling as a Novel Method for the Fabrication of Patterned Surfaces”. en. *Complex Macromolecular Systems I*. Advances in Polymer Science. Springer, Berlin, Heidelberg, 2009, pp. 75–99. DOI: 10.1007/12_2009_22.

[240] J. Y. Chung, A. J. Nolte, and C. M. Stafford. “Surface Wrinkling: A Versatile Platform for Measuring Thin-Film Properties”. en. *Advanced Materials* 23.3 (2011), pp. 349–368. DOI: 10.1002/adma.201001759.

[241] B. Li, Y.-P. Cao, X.-Q. Feng, and H. Gao. “Mechanics of Morphological Instabilities and Surface Wrinkling in Soft Materials: A Review”. en. *Soft Matter* 8.21 (2012), pp. 5728–5745. DOI: 10.1039/C2SM00011C.

[242] A. del Campo and E. Arzt. “Fabrication Approaches for Generating Complex Micro- and Nanopatterns on Polymeric Surfaces”. *Chemical Reviews* 108.3 (2008), pp. 911–945. DOI: 10.1021/cr050018y.

[243] Y. Mei, S. Kiravittaya, S. Harazim, and O. G. Schmidt. “Principles and Applications of Micro and Nanoscale Wrinkles”. *Materials Science and Engineering: R: Reports*.

3rd IEEE International NanoElectronics Conference (INEC) 70.3 (2010), pp. 209–224. DOI: 10.1016/j.mser.2010.06.009.

[244] S. P. Lacour, S. Wagner, Z. Huang, and Z. Suo. "Stretchable Gold Conductors on Elastomeric Substrates". *Applied Physics Letters* 82.15 (2003), pp. 2404–2406. DOI: 10.1063/1.1565683.

[245] M. Park, C. Harrison, P. M. Chaikin, R. A. Register, and D. H. Adamson. "Block Copolymer Lithography: Periodic Arrays of ~10$\hat{1}$1 Holes in 1 Square Centimeter". en. *Science* 276.5317 (1997), pp. 1401–1404. DOI: 10.1126/science.276.5317.1401.

[246] C. M. Bates, M. J. Maher, D. W. Janes, C. J. Ellison, and C. G. Willson. "Block Copolymer Lithography". *Macromolecules* 47.1 (2014), pp. 2–12. DOI: 10.1021/ma401762n.

[247] R. A. Segalman. "Patterning with Block Copolymer Thin Films". *Materials Science and Engineering: R: Reports* 48.6 (2005), pp. 191–226. DOI: 10.1016/j.mser.2004.12.003.

[248] N. Bowden, W. T. S. Huck, K. E. Paul, and G. M. Whitesides. "The Controlled Formation of Ordered, Sinusoidal Structures by Plasma Oxidation of an Elastomeric Polymer". *Applied Physics Letters* 75.17 (1999), pp. 2557–2559. DOI: 10.1063/1.125076.

[249] C. Palmer and E. G. Loewen. *Diffraction Grating Handbook*. en. New York: Newport Corporatin, 2005.

[250] I. D. W. Samuel and G. A. Turnbull. "Organic Semiconductor Lasers". *Chemical Reviews* 107.4 (2007), pp. 1272–1295. DOI: 10.1021/cr050152i.

[251] C. Lu, H. Möhwald, and A. Fery. "A Lithography-Free Method for Directed Colloidal Crystal Assembly Based on Wrinkling". en. *Soft Matter* 3.12 (2007), pp. 1530–1536. DOI: 10.1039/B712706E.

[252] J. B. Kim et al. "Wrinkles and Deep Folds as Photonic Structures in Photovoltaics". en. *Nature Photonics* 6.5 (2012), pp. 327–332. DOI: 10.1038/nphoton.2012.70.

[253] W. H. Koo et al. "Light Extraction from Organic Light-Emitting Diodes Enhanced by Spontaneously Formed Buckles". en. *Nature Photonics* 4.4 (2010), pp. 222–226. DOI: 10.1038/nphoton.2010.7.

[254] C. F. Guo et al. "Path-Guided Wrinkling of Nanoscale Metal Films". *Advanced Materials* 24.22 (2012), pp. 3010–3014. DOI: 10.1002/adma.201200540.

[255] J. Kim and H. H. Lee. "Wave Formation by Heating in Thin Metal Film on an Elastomer". en. *Journal of Polymer Science Part B: Polymer Physics* 39.11 (2001), pp. 1122–1128. DOI: 10.1002/polb.1088.

[256] E. P. Chan et al. "Viscoelastic Properties of Confined Polymer Films Measured via Thermal Wrinkling". en. *Soft Matter* 5.23 (2009), pp. 4638–4641. DOI: 10.1039/B916207K.

[257] A. G. Shtukenberg, Y. O. Punin, E. Gunn, and B. Kahr. "Spherulites". *Chemical Reviews* 112.3 (2012), pp. 1805–1838. DOI: 10.1021/cr200297f.

[258] E. M. Woo and G. Lugito. "Origins of Periodic Bands in Polymer Spherulites". *European Polymer Journal* 71 (2015), pp. 27–60. DOI: 10.1016/j.eurpolymj.2015.07.045.

[259] B. Crist and J. M. Schultz. "Polymer Spherulites: A Critical Review". *Progress in Polymer Science* 56 (2016), pp. 1–63. DOI: 10.1016/j.progpolymsci.2015.11.006.

[260] P. Poudel, S. Majumder, S. Chandran, H. Zhang, and G. Reiter. "Formation of Periodically Modulated Polymer Crystals". *Macromolecules* 51.15 (2018), pp. 6119–6126. DOI: 10.1021/acs.macromol.8b01366.

[261] Y. Sun, H. Xi, S. Chen, M. D. Ediger, and L. Yu. "Crystallization near Glass Transition: Transition from Diffusion-Controlled to Diffusionless Crystal Growth Studied with Seven Polymorphs". *The Journal of Physical Chemistry B* 112.18 (2008), pp. 5594–5601. DOI: 10.1021/jp7120577.

[262] K. Ohdaira, T. Fujiwara, Y. Endo, S. Nishizaki, and H. Matsumura. "Explosive Crystallization of Amorphous Silicon Films by Flash Lamp Annealing". *Journal of Applied Physics* 106.4 (2009), p. 044907. DOI: 10.1063/1.3195089.

[263] T. R. Fielitz and R. J. Holmes. "Crystal Morphology and Growth in Annealed Rubrene Thin Films". *Crystal Growth & Design* 16.8 (2016), pp. 4720–4726. DOI: 10.1021/acs.cgd.6b00783.

[264] T. R. Fielitz, C. M. Phenicie, and R. J. Holmes. "Effects of Additives on Crystallization in Thin Organic Films". *Crystal Growth & Design* 17.9 (2017), pp. 4522–4526. DOI: 10.1021/acs.cgd.7b00880.

[265] M. A. Fusella et al. "Use of an Underlayer for Large Area Crystallization of Rubrene Thin Films". *Chemistry of Materials* 29.16 (2017), pp. 6666–6673. DOI: 10.1021/acs.chemmater.7b01143.

[266] K. Meerholz and D. C. Müller. "Outsmarting Waveguide Losses in Thin-Film Light-Emitting Diodes". *Advanced Functional Materials* 11.4 (2001), pp. 251–253. DOI: 10.1002/1616-3028(200108)11:4<251::AID-ADFM251>3.0.CO;2-Y.

[267] C. Fuchs et al. "Quantitative Allocation of Bragg Scattering Effects in Highly Efficient OLEDs Fabricated on Periodically Corrugated Substrates". EN. *Optics Express* 21.14 (2013), pp. 16319–16330. DOI: 10.1364/OE.21.016319.

[268] A. J. C. Kuehne and M. C. Gather. "Organic Lasers: Recent Developments on Materials, Device Geometries, and Fabrication Techniques". *Chemical Reviews* 116.21 (2016), pp. 12823–12864. DOI: 10.1021/acs.chemrev.6b00172.

[269] J. Xu et al. "Direct AFM Observation of Crystal Twisting and Organization in Banded Spherulites of Chiral Poly(3-Hydroxybutyrate-Co-3-Hydroxyhexanoate)". *Macromolecules* 37.11 (2004), pp. 4118–4123. DOI: 10.1021/ma0499122.

[270] S.-W. Park et al. "Amorphous-to-Crystalline Phase Transformation of Thin Film Rubrene". *The Journal of Physical Chemistry B* 114.17 (2010), pp. 5661–5665. DOI: 10.1021/jp910459p.

[271] Y.-X. Liu and E.-Q. Chen. "Polymer Crystallization of Ultrathin Films on Solid Substrates". *Coordination Chemistry Reviews*. Novel and Smart Materials: Design, Synthesis, Structure, Properties and Applications. In Celebration of the Centennial Anniversary of Chemical Research and Education at Peking University 254.9 (2010), pp. 1011–1037. DOI: 10.1016/j.ccr.2010.02.017.

[272] M. Hasebe, D. Musumeci, and L. Yu. "Fast Surface Crystallization of Molecular Glasses: Creation of Depletion Zones by Surface Diffusion and Crystallization Flux". *The Journal of Physical Chemistry B* 119.7 (2015), pp. 3304–3311. DOI: 10.1021/jp512400c.

[273] J. Tao, G. Mao, and L. Daehne. “Asymmetrical Molecular Aggregation in Spherulitic Dye Films”. *Journal of the American Chemical Society* 121.14 (1999), pp. 3475–3485. DOI: 10.1021/ja983842v.

[274] Y. Sun, L. Zhu, K. L. Kearns, M. D. Ediger, and L. Yu. “Glasses Crystallize Rapidly at Free Surfaces by Growing Crystals Upward”. en. *Proceedings of the National Academy of Sciences* 108.15 (2011), pp. 5990–5995. DOI: 10.1073/pnas.1017995108.

[275] W. W. Mullins. “Flattening of a Nearly Plane Solid Surface Due to Capillarity”. *Journal of Applied Physics* 30.1 (1959), pp. 77–83. DOI: 10.1063/1.1734979.

[276] Y. Chai et al. “A Direct Quantitative Measure of Surface Mobility in a Glassy Polymer”. en. *Science* 343.6174 (2014), pp. 994–999. DOI: 10.1126/science.1244845.

[277] Y. Li, Z. Yao, L. Wu, and Z. Wang. “Nonbirefringent Bands in Thin Films of a Copolymer Melt: Rapid Rhythmic Crystal Growth with an Unusual Crystal–Melt Interface”. en. *CrystEngComm* 20.16 (2018), pp. 2221–2226. DOI: 10.1039/C8CE00134K.

[278] L. Zhu et al. “Surface Self-Diffusion of an Organic Glass”. *Physical Review Letters* 106.25 (2011), p. 256103. DOI: 10.1103/PhysRevLett.106.256103.

[279] Y. Zhang et al. “Effect of Substrate Interactions on the Glass Transition and Length-Scale of Correlated Dynamics in Ultra-Thin Molecular Glass Films”. *The Journal of Chemical Physics* 149.18 (2018), p. 184902. DOI: 10.1063/1.5038174.

[280] W. Zhang, C. W. Brian, and L. Yu. “Fast Surface Diffusion of Amorphous O-Terphenyl and Its Competition with Viscous Flow in Surface Evolution”. *The Journal of Physical Chemistry B* 119.15 (2015), pp. 5071–5078. DOI: 10.1021/jp5127464.

[281] K. Paeng, C. T. Powell, L. Yu, and M. D. Ediger. “Fast Crystal Growth Induces Mobility and Tension in Supercooled O-Terphenyl”. *The Journal of Physical Chemistry Letters* 3.18 (2012), pp. 2562–2567. DOI: 10.1021/jz301111x.

[282] W. Zhang, J. F. Douglas, and F. W. Starr. “Why We Need to Look beyond the Glass Transition Temperature to Characterize the Dynamics of Thin Supported Polymer Films”. en. *Proceedings of the National Academy of Sciences* 115.22 (2018), pp. 5641–5646. DOI: 10.1073/pnas.1722024115.

[283] S. S. Lee et al. “Guiding Crystallization around Bends and Sharp Corners”. *Advanced Materials* 24.20 (2012), pp. 2692–2698. DOI: 10.1002/adma.201104619.

[284] S. Yin, Z. Shuai, and Y. Wang. “A Quantitative Structure-Property Relationship Study of the Glass Transition Temperature of OLED Materials”. *Journal of Chemical Information and Computer Sciences* 43.3 (2003), pp. 970–977. DOI: 10.1021/ci034011y.

[285] Y. Agata, H. Shimizu, and J. Kido. “Syntheses and Properties of Novel Quarterphenylene-Based Materials for Blue Organic Light-Emitting Devices”. *Chemistry Letters* 36.2 (2007), pp. 316–317. DOI: 10.1246/cl.2007.316.

[286] J.-A. Cheng and P.-J. Cheng. “Crystal Study of N,N′-Diphenyl-N,N′-Bis(1-Naphthyl)-1,1′-Biphenyl-4,4′-Diamine”. en. *Journal of Chemical Crystallography* 40.6 (2010), pp. 557–560. DOI: 10.1007/s10870-010-9748-0.

[287] J.-W. Shin et al. “Random Nano-Structures as Light Extraction Functionals for Organic Light-Emitting Diode Applications”. *Organic Electronics* 15.1 (2014), pp. 196–202. DOI: 10.1016/j.orgel.2013.11.007.

[288] T. Schwab et al. “Coherent Mode Coupling in Highly Efficient Top-Emitting OLEDs on Periodically Corrugated Substrates”. EN. *Optics Express* 22.7 (2014), pp. 7524–7537. DOI: 10.1364/OE.22.007524.

[289] P. Virtanen et al. “SciPy 1.0: Fundamental Algorithms for Scientific Computing in Python”. en. *Nature Methods* 17.3 (2020), pp. 261–272. DOI: 10.1038/s41592-019-0686-2.

[290] D. Nečas and P. Klapetek. “Gwyddion: An Open-Source Software for SPM Data Analysis”. en. *Open Physics* 10.1 (2012), pp. 181–188. DOI: 10.2478/s11534-011-0096-2.

[291] J. S. Bangsund et al. “Formation of Aligned Periodic Patterns during the Crystallization of Organic Semiconductor Thin Films”. En. *Nature Materials* (2019), p. 1. DOI: 10.1038/s41563-019-0379-3.

[292] W. W Mullins. “The Effect of Thermal Grooving on Grain Boundary Motion”. *Acta Metallurgica* 6.6 (1958), pp. 414–427. DOI: 10.1016/0001-6160(58)90020-8.

[293] M. Aonuma, T. Oyamada, H. Sasabe, T. Miki, and C. Adachi. “Material Design of Hole Transport Materials Capable of Thick-Film Formation in Organic Light Emitting Diodes”. *Applied Physics Letters* 90.18 (2007), p. 183503. DOI: 10.1063/1.2733627.

[294] M.-H. Tsai et al. “3-(9-Carbazolyl)Carbazoles and 3,6-Di(9-Carbazolyl)Carbazoles as Effective Host Materials for Efficient Blue Organic Electrophosphorescence”. *Advanced Materials* 19.6 (2007), pp. 862–866. DOI: 10.1002/adma.200600822.

[295] J.-H. Lee, M.-H. Wu, C.-C. Chao, H.-L. Chen, and M.-K. Leung. “High Efficiency and Long Lifetime OLED Based on a Metal-Doped Electron Transport Layer”. en. *Chemical Physics Letters* 416.4 (2005), pp. 234–237. DOI: 10.1016/j.cplett.2005.09.104.

[296] B. W. D’Andrade, S. R. Forrest, and A. B. Chwang. “Operational Stability of Electrophosphorescent Devices Containing p and n Doped Transport Layers”. en. *Applied Physics Letters* 83.19 (2003), p. 3858. DOI: 10.1063/1.1624473.

[297] S.-J. Su, C. Cai, and J. Kido. “Three-Carbazole-Armed Host Materials with Various Cores for RGB Phosphorescent Organic Light-Emitting Diodes”. en. *Journal of Materials Chemistry* 22.8 (2012), pp. 3447–3456. DOI: 10.1039/C2JM14151E.

[298] D. Tanaka, T. Takeda, T. Chiba, S. Watanabe, and J. Kido. “Novel Electron-Transport Material Containing Boron Atom with a High Triplet Excited Energy Level”. *Chemistry Letters* 36.2 (2007), pp. 262–263. DOI: 10.1246/cl.2007.262.

[299] P. Schrögel et al. “Meta-Linked CBP-Derivatives as Host Materials for a Blue Iridium Carbene Complex”. en. *Organic Electronics* 12.12 (2011), pp. 2047–2055. DOI: 10.1016/j.orgel.2011.08.012.

[300] C. Mayr and W. Brütting. “Control of Molecular Dye Orientation in Organic Luminescent Films by the Glass Transition Temperature of the Host Material”. *Chemistry of Materials* 27.8 (2015), pp. 2759–2762. DOI: 10.1021/acs.chemmater.5b00062.

[301] N. Negishi et al. “Method for Manufacturing Top Emission Organic Electroluminescence Element”. Pat. US20150236304A1. 2015. URL: https://patents.google.com/patent/US20150236304A1/en (visited on 05/27/2020).

[302] Y. Kuwabara, H. Ogawa, H. Inada, N. Noma, and Y. Shirota. “Thermally Stable Multilared Organic Electroluminescent Devices Using Novel Starburst Molecules, 4,4′,4″-Tri(N-Carbazolyl)Triphenylamine (TCTA) and 4,4′,4″-Tris(3-Methylphenylphenylamino)Triphenylamine (m-MTDATA), as Hole-Transport Materials”. *Advanced Materials* 6.9 (1994), pp. 677–679. DOI: 10.1002/adma.19940060913.

[303] M. Cölle, J. Gmeiner, W. Milius, H. Hillebrecht, and W. Brütting. “Preparation and Characterization of Blue-Luminescent Tris(8-Hydroxyquinoline)-Aluminum (Alq3)”. en. *Advanced Functional Materials* 13.2 (2003), pp. 108–112. DOI: 10.1002/adfm.200390015.

[304] M. A. Green, A. Ho-Baillie, and H. J. Snaith. “The Emergence of Perovskite Solar Cells”. en. *Nature Photonics* 8.7 (2014), pp. 506–514. DOI: 10.1038/nphoton.2014.134.

[305] K. Lin et al. “Perovskite Light-Emitting Diodes with External Quantum Efficiency Exceeding 20 per Cent”. en. *Nature* 562.7726 (2018), pp. 245–248. DOI: 10.1038/s41586-018-0575-3.

[306] Y. Zou, Z. Yuan, S. Bai, F. Gao, and B. Sun. “Recent Progress Toward Perovskite Light-Emitting Diodes with Enhanced Spectral and Operational Stability”. *Materials Today Nano* (2019), p. 100028. DOI: 10.1016/j.mtnano.2019.100028.

[307] L. N. Quan et al. “Perovskites for Next-Generation Optical Sources”. *Chemical Reviews* 119.12 (2019), pp. 7444–7477. DOI: 10.1021/acs.chemrev.9b00107.

[308] Y. Jia, R. A. Kerner, A. J. Grede, B. P. Rand, and N. C. Giebink. “Continuous-Wave Lasing in an Organic–Inorganic Lead Halide Perovskite Semiconductor”. en. *Nature Photonics* 11.12 (2017), pp. 784–788. DOI: 10.1038/s41566-017-0047-6.

[309] Y. Jia et al. “Diode-Pumped Organo-Lead Halide Perovskite Lasing in a Metal-Clad Distributed Feedback Resonator”. *Nano Letters* 16.7 (2016), pp. 4624–4629. DOI: 10.1021/acs.nanolett.6b01946.

[310] Q. Dong, L. Lei, J. Mendes, and F. So. “Operational Stability of Perovskite Light Emitting Diodes”. en. *Journal of Physics: Materials* (2019). DOI: 10.1088/2515-7639/ab60c4.

[311] W. B. Gunnarsson and B. P. Rand. “Electrically Driven Lasing in Metal Halide Perovskites: Challenges and Outlook”. *APL Materials* LEPM2020.1 (2020), p. 030902. DOI: 10.1063/1.5143265@apm.2020.LEPM2020.issue-1.

[312] R. Seifert, S. Scholz, B. Lussem, and K. Leo. “Comparison of Ultraviolet- and Charge-Induced Degradation Phenomena in Blue Fluorescent Organic Light Emitting Diodes”. *Applied Physics Letters* 97.1 (2010), p. 013308. DOI: 10.1063/1.3460285.

[313] T. Davidson-Hall and H. Aziz. “The Role of Excitons within the Hole Transporting Layer in Quantum Dot Light Emitting Device Degradation”. en. *Nanoscale* 11.17 (2019), pp. 8310–8318. DOI: 10.1039/C8NR09560D.

[314] H. Tsai et al. “Stable Light-Emitting Diodes Using Phase-Pure Ruddlesden–Popper Layered Perovskites”. en. *Advanced Materials* 30.6 (2018), p. 1704217. DOI: 10.1002/adma.201704217.

[315] Z. Shi et al. “High-Efficiency and Air-Stable Perovskite Quantum Dots Light-Emitting Diodes with an All-Inorganic Heterostructure”. *Nano Letters* 17.1 (2017), pp. 313–321. DOI: 10.1021/acs.nanolett.6b04116.

[316] Z. Shi et al. “Strategy of Solution-Processed All-Inorganic Heterostructure for Humidity/Temperature-Stable Perovskite Quantum Dot Light-Emitting Diodes”. *ACS Nano* 12.2 (2018), pp. 1462–1472. DOI: 10.1021/acsnano.7b07856.

[317] C. C. Boyd et al. “Barrier Design to Prevent Metal-Induced Degradation and Improve Thermal Stability in Perovskite Solar Cells”. *ACS Energy Letters* 3.7 (2018), pp. 1772–1778. DOI: 10.1021/acsenergylett.8b00926.

[318] R. A. Kerner and B. P. Rand. “Electrochemical and Thermal Etching of Indium Tin Oxide by Solid-State Hybrid Organic–Inorganic Perovskites”. *ACS Applied Energy Materials* 2.8 (2019), pp. 6097–6101. DOI: 10.1021/acsaem.9b01356.

[319] M. T. Greiner et al. “Universal Energy-Level Alignment of Molecules on Metal Oxides”. en. *Nature Materials* 11.1 (2012), pp. 76–81. DOI: 10.1038/nmat3159.

[320] R. A. Kerner et al. “Reactions at Noble Metal Contacts with Methylammonium Lead Triiodide Perovskites: Role of Underpotential Deposition and Electrochemistry”. *APL Materials* 7.4 (2019), p. 041103. DOI: 10.1063/1.5083812.

[321] S.-Y. Lu, S. Mukhopadhyay, R. Froese, and P. M. Zimmerman. “Virtual Screening of Hole Transport, Electron Transport, and Host Layers for Effective OLED Design”. *Journal of Chemical Information and Modeling* (2018). DOI: 10.1021/acs.jcim.8b00044.

[322] R. Gómez-Bombarelli et al. “Design of Efficient Molecular Organic Light-Emitting Diodes by a High-Throughput Virtual Screening and Experimental Approach”. en. *Nature Materials* 15.10 (2016), pp. 1120–1127. DOI: 10.1038/nmat4717.

[323] P. Friederich, V. Rodin, F. von Wrochem, and W. Wenzel. “Built-In Potentials Induced by Molecular Order in Amorphous Organic Thin Films”. *ACS Applied Materials & Interfaces* 10.2 (2018), pp. 1881–1887. DOI: 10.1021/acsami.7b11762.

[324] S. Schmidbauer, A. Hohenleutner, and B. König. “Studies on the Photodegradation of Red, Green and Blue Phosphorescent OLED Emitters”. en. *Beilstein Journal of Organic Chemistry* 9.1 (2013), pp. 2088–2096. DOI: 10.3762/bjoc.9.245.

[325] S. Seo et al. “P-132: Long-Lived Deeply Red Phosphorescent OLEDs Based on Electrochemically Stable Ir Complexes”. en. *SID Symposium Digest of Technical Papers* 36.1 (2005), pp. 806–809. DOI: 10.1889/1.2036568.

[326] K. Hershey. “Multi-Scale Dynamics of Organic Light-Emitting Devices”. en (2018). URL: http://conservancy.umn.edu/handle/11299/206264 (visited on 07/06/2020).

[327] C. Peng et al. “Probing the Emission Zone Length in Organic Light Emitting Diodes via Photoluminescence and Electroluminescence Degradation Analysis”. *ACS Applied Materials & Interfaces* 9.47 (2017), pp. 41421–41427. DOI: 10.1021/acsami.7b13537.

[328] T. D. Schmidt et al. “Degradation Induced Decrease of the Radiative Quantum Efficiency in Organic Light-Emitting Diodes”. *Applied Physics Letters* 101.10 (2012), p. 103301. DOI: 10.1063/1.4749815.

[329] Q. Wang and H. Aziz. “Exciton-Induced Degradation of Organic/Electrode Interfaces in Ultraviolet Organic Photodetectors”. *Organic Electronics* 14.11 (2013), pp. 3030–3036. DOI: 10.1016/j.orgel.2013.09.013.

[330] Q. Wang and H. Aziz. “Poor Photo-Stability of the Organic/LiF/Al Contact in Organic Optoelectronic Devices”. *Organic Electronics* 12.9 (2011), pp. 1571–1575. DOI: 10.1016/j.orgel.2011.06.003.

[331] K. Bagchi et al. “Origin of Anisotropic Molecular Packing in Vapor-Deposited Alq3 Glasses”. *The Journal of Physical Chemistry Letters* 10.2 (2019), pp. 164–170. DOI: 10.1021/acs.jpclett.8b03582.

[332] J. Sohn et al. “Degradation Mechanism of Blue Thermally Activated Delayed Fluorescent Organic Light-Emitting Diodes under Electrical Stress”. *Organic Electronics* (2019). DOI: 10.1016/j.orgel.2019.04.033.

[333] H. Lee, H. Ahn, and C. Lee. “Device Characteristics of Blue Phosphorescent Organic Light-Emitting Diodes Depending on the Electron Transport Materials”. *Journal of Information Display* 12.4 (2011), pp. 219–222. DOI: 10.1080/15980316.2011.621323.

[334] M. Kim, S. K. Jeon, S.-H. Hwang, and J. Y. Lee. “Stable Blue Thermally Activated Delayed Fluorescent Organic Light-Emitting Diodes with Three Times Longer Lifetime than Phosphorescent Organic Light-Emitting Diodes”. en. *Advanced Materials* 27.15 (2015), pp. 2515–2520. DOI: 10.1002/adma.201500267.

[335] K. Klimes, Z.-Q. Zhu, and J. Li. “Efficient Blue Phosphorescent OLEDs with Improved Stability and Color Purity through Judicious Triplet Exciton Management”. en. *Advanced Functional Materials* 29.31 (2019), p. 1903068. DOI: 10.1002/adfm.201903068.

[336] G. Li, K. Klimes, T. Fleetham, Z.-Q. Zhu, and J. Li. “Stable and Efficient Sky-Blue Organic Light Emitting Diodes Employing a Tetradentate Platinum Complex”. *Applied Physics Letters* 110.11 (2017), p. 113301. DOI: 10.1063/1.4978674.

[337] Z.-Q. Zhu, C.-D. Park, K. Klimes, and J. Li. “Highly Efficient Blue OLEDs Based on Metal-Assisted Delayed Fluorescence Pd(II) Complexes”. en. *Advanced Optical Materials* 7.6 (2019), p. 1801518. DOI: 10.1002/adom.201801518.

[338] C. P. Clark, B. Voigt, E. S. Aydil, and R. J. Holmes. “Carrier-Gas Assisted Vapor Deposition for Highly Tunable Morphology of Halide Perovskite Thin Films”. en. *Sustainable Energy & Fuels* 3.9 (2019), pp. 2447–2455. DOI: 10.1039/C9SE00200F.

A

List of publications and presentations

A.1 Publications

12 CP Clark, J Mann, **JS Bangsund**, *et al*. Formation and Stability of All-Perovskite Heterojunctions. *In review*.

11 **JS Bangsund**, *et al*. Sub-turn-on Exciton Quenching Due to Molecular Orientation and Polarization in Organic Light-Emitting Devices. *Science Advances*, (2020). DOI: 10.1126/sciadv.abb2659

10 D Rai, **JS Bangsund**, *et al*. Impact of Molecular Structure on Singlet and Triplet Exciton Diffusion in Phenanthroline Derivatives. *Journal of Materials Chemistry C* (2020). DOI: 10.1039/D0TC00716A

9 R Newcomb*, **JS Bangsund***, *et al*. Role of Excimer Formation in Degradation of Organic Light-Emitting Devices. *Applied Physics Letters* (2020). DOI: 10.1063/1.5124802. **Editor's Pick**. *Equal contributors

8 **JS Bangsund** and Russell J. Holmes. Impacts of Degradation on Annihilation and Efficiency Roll-Off in Organic Light-Emitting Devices. *Proc. of SPIE*. (2019). DOI: 10.1117/12.2528780

7 **JS Bangsund**, *et al*. Spontaneous Formation of Aligned, Periodic Patterns During Crystallization of Organic Semiconductor Thin Films. *Nature Materials* (2019). DOI: 10.1038/s41563-019-0379-3

6 **JS Bangsund***, KW Hershey*, *et al*. Improved Stability in Organic Light-Emitting Devices by Mixing Ambipolar and Wide Energy Gap Hosts. *Journal of the Society for Information Display* (2019). DOI: 10.1002/jsid.761. *Equal contributors

5 **JS Bangsund**, *et al*. Isolating Degradation Mechanisms in Mixed Emissive Layer Organic Light-Emitting Devices. *ACS Applied Materials and Interfaces* (2018). DOI: 10.1021/acsami.7b16643

4 KW Hershey, **JS Bangsund**, *et al*. Decoupling Degradation in Exciton Formation and Recombination During Lifetime Testing of Organic Light-Emitting Devices. *Applied Physics Letters* (2017). DOI: 10.1063/1.4993618

3 CJ Traverse, M Young, **JS Bangsund**, *et al*. Anions for Near-Infrared Selective Organic Salt Photovoltaics. *Scientific Reports* (2017). DOI: 10.1038/s41598-017-16539-3

2 M Young, **JS Bangsund**, *et al*. Organic Heptamethine Salts for Photovoltaics and Detectors with Near-Infrared Photoresponse up to 1600 nm. *Advanced Optical Materials* (2016). DOI: 10.1002/adom.201600102

1 **JS Bangsund**, *et al*. Organic Salts as a Route to Energy Level Control in Low Bandgap, High Open-Circuit Voltage Organic and Transparent Solar Cells. *Advanced Energy Materials* (2016). DOI: 10.1002/aenm.201501659

A.2 Oral presentations

8 Impacts of Degradation on Annihilation and Efficiency Roll-off in Organic Light-Emitting Devices.
Oral Presentation. *SPIE Organic Electronics + Photonics*, San Diego, CA. 08/2019.

7 Controlling crystallization-mediated pattern formation in organic semiconductor thin films. *IPrime Annual Meeting*, Minneapolis, MN. 05/2019.

6 Fundamentals and Applications of Spectroscopic Ellipsometry. *IPrime Mid-Year Workshops*, Minneapolis, MN. 01/2019.

5 Role of the Recombination Zone in the Stability of Organic Light-Emitting Devices. *IPrime Annual Meeting*, Minneapolis, MN. 05/2018.

4 Quantifying Multiple Active Degradation Mechanisms in Mixed Host Organic Light-Emitting Devices.
Oral Presentation. *Materials Research Society Spring Meeting*, Phoenix, AZ. 4/2018.

3 Understanding Improved Lifetime in Mixed Emissive Layer Organic Light-Emitting Devices.
Oral Presentation. *Optical Society of America Solid-State Lighting Meeting*, Boulder, CO. 11/2017.

2 Origin of Lifetime Enhancement in Mixed Emissive Layer Organic Light-Emitting Device. *IPrime Annual Meeting*, Minneapolis, MN. 05/2017.

1 Energy Level Control in Organic Salts for Efficient, Deep Near-Infrared Organic and Transparent Photovoltaics.
Oral Presentation. *Materials Research Society Spring Meeting*, Phoenix, AZ. 3/2016.

A.3 Poster presentations

4 Assessing the interplay between efficiency roll-off and stability of organic light-emitting devices. *IPrime Annual Meeting*, Minneapolis, MN. 05/2019.

3 Spontaneous Formation of Aligned, Periodic Patterns During Crystallization of Organic Semiconductor Thin Films.
Poster Presentation. *Materials Research Society Fall Meeting*, Boston, MA. 11/2018.

2 Controlling Spontaneously Formed Periodic Patterns in Organic Semiconductor Thin Films. *IPrime Annual Meeting*, Minneapolis, MN. 05/2018.

1 Origin of Lifetime Enhancement in Mixed Emissive Layer Organic Light-Emitting Devices. *IPrime Annual Meeting*, Minneapolis, MN. 05/2017.

B

Outcoupling Modeling

Code for the dipole emission model, which is used to calculate OLED outcoupling efficiency and modifications to the radiative rate, is maintained on GitHub in the "dipole_emission.py" file at: github.com/jsbangsund/oledpy.

C

Development of combined EL and PL measurement

Measurements of both EL and PL during degradation of an OLED were key to many of the findings in this thesis (see Chapters 3 to 5 and refs. [91, 157, 175, 193]). Measurements of PL are simple in concept and have been applied to study OLED degradation since at least 2001,[127] but their practical implementation—achieving accurate, artifact-free, and reproducible measurements—is not necessarily straightforward. Some of the key issues and design ideas for this measurement are summarized below. For more detail, see the thesis by Hershey [326].

C.1 Measurement design considerations and checks

- The excitation light source in a device PL measurement should selectively pump the emitter molecule and no other materials in the device stack
- Light from the excitation source should be completely rejected in the measurement of PL intensity
- The exciton profiles under optical and electrical excitation should overlap significantly. Generally, the emissive layer should be kept thin (<20 nm) to minimize this error. The optical field should be simulated with a transfer matrix formalism and the RZ should be measured to estimate this error.
- Check whether PL loss reflects an increase in non-radiative decay or a reduction in absorption
- Avoid photodegradation from the excitation light source
- Confirm that PL degradation results from electrical operation and not confounding effects (e.g. intrinsic degradation over time, photodegradation from the pump, decreases in laser intensity which are not measured, movement of the sample or detector)
- Minimize laser warm-up effects by, e.g. allowing laser to warm-up for >30 s behind a mechanical shutter prior to measurement. Also, measure laser and PL intensity nearly simultaneously.

C.1.1 Selective pumping

The excitation light source* in a device PL measurement should selectively pump the emitter molecule and no other materials in the device stack. To confirm this, absorption of each material should be measured with UV-vis spectroscopy or spectroscopic ellipsometry. Further confirmation should be made by measuring the PL spectrum and comparing it to the EL spectrum of the device and the PL spectrum of the emitter in solution or a single-layer thin film. If any extraneous features are observed, the pump wavelength should be changed to avoid excitation of these features. Alternatively, an appropriate optical filter could be selected to reject the unwanted features, or the emission could be measured with a spectrometer and integrated over the range where only the emissive dopant is active.[327]

C.1.2 Rejecting pump light

If measuring the full PL spectrum with, e.g., a fiber-coupled spectrometer, rejection of the pump light intensity can be achieved by simply integrating the emission over a wavelength range which excludes the pump.[327] Normally, however, PL is measured as the photocurrent of a filtered photodiode. To check for successful rejection in this situation, one should measure the emission spectrum through the filter optics and confirm no pump peak is present. Ideally, dichroic longpass filters should be used—preventing potential luminescence from a colored glass filter—and the filter band edge should be separated by at least 20 nm from the pump emission edge to ensure sufficient rejection.

It should be noted that—because the pump light intensity is often more than an order of magnitude more intense than the device PL—the weak emission tail of a excitation light source that extends beyond a filter band edge can sometimes dominate a measured photocurrent signal. This can be checked by placing a non-emissive scattering object, such as a Teflon substrate, in the sample position to determine the upper-limit background photocurrent from scattered pump light. Rejection of scattered pump light can be especially important for samples which show increasing scattering over time. For example, in some perovskite films, we have observed a change in film morphology during photodegradation, leading to increased scattering and a higher background photocurrent which overwhelmed the PL signal.

*usually a laser, but could also be an LED coupled with a bandpass filter or a filtered/monochromated lamp

C.1.3 Spatial overlap between optical and electrical excitation

As discussed in detail in Sections 3.5 and 6.6, excitons are not generally generated in identical spatial regions by optical and electrical excitation, which can cause the PL measurement to diverge from the device-relevant η_{PL}. This potential error should be carefully quantified by measuring the electrical recombination zone and comparing with the simulated optical generation profile, as discussed in Section 3.5. This error can also be mitigated by designing devices with narrow emissive layers or by tuning the ETL thickness to ensure that the optical generation profile overlaps with the peak of the recombination zone.

C.1.4 PL loss: non-radiative decay or reduced absorption

In principle, PL intensity can be reduced by either an increase in the non-radiative decay rate (decreasing the exciton lifetime and η_{PL}) or by a decrease in absorption, which could occur if the absorption spectrum of emitter molecule fragments—which form during degradation—differs from the pristine molecule. To check which effect is dominant, steady-state PL measurements should be accompanied by transient PL measurements to look for changes in the exciton lifetime. In ref. [91], we showed that the transient and steady-state PL measurements agreed within error for CBP:Ir(ppy)$_3$ devices.

It is also worth noting that we have assumed throughout this thesis that only the non-radiative rate varies with time and the radiative rate is constant. This assumption is widely applied within the OLED literature, but there are some indications that the radiative rate can also decrease.[328] Schmidt et al. [328] speculate that changes in the local dielectric environment may be responsible.

C.1.5 Avoid photodegradation from the excitation light source

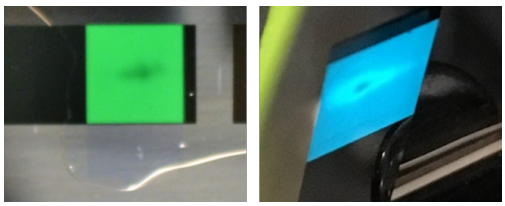

Fig. C.1. Examples of laser-induced dark (left) and bright (right) spots that form when the pump light source either negatively or positively influences emission.

The pump light source can lead to photodegradation effects, either by directly degrading emitter molecules or by degrading light-sensitive interfaces. To avoid this, and ensure the measurement solely reflects degradation from electrical excitation, the power density of the light source should be set as low as possible while still achieving sufficient signal-to-noise in the PL measurement. One way power density can be lowered without sacrificing signal is by expanding the pump beam, spreading the light out over a larger portion of the device. However, care must be taken to ensure only the device active area is excited in this case. Alternatively, PL measurements can be taken with a chopped laser and a lock-in amplifier to improve sensitivity (see Chapter 6).

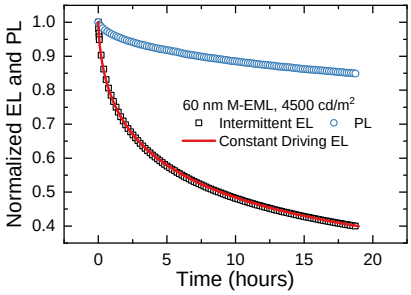

Fig. C.2. Example demonstrating that laser does not influence device lifetime

The absence of photodegradation effects should be checked in two ways. First, devices can be visually inspected after a test for the formation of dark spots in the pump-illuminated area (see Figure C.1). This is usually a sign that electrical injection has been suppressed by photodegradation of an interface.[151,152,234,329,330] Second, the electrical lifetime of a device should be measured with and without the PL measurement (see Figure C.2).

C.1.6 Confirming that PL degradation results from electrical operation

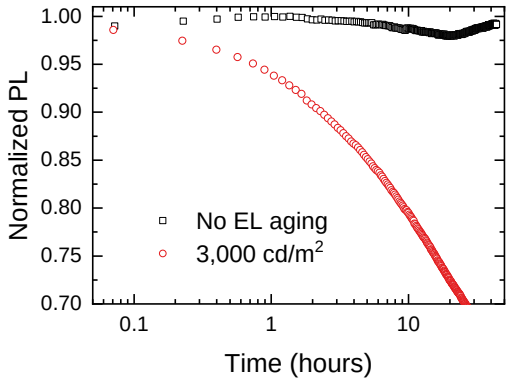

Fig. C.3. Example demonstrating that changes in PL are caused by electrical degradation. Intermittently measured PL of devices with (circles) and without (squares) applied current show that PL remains within error in the absence of electrical degradation.

When validating a new measurement set-up or testing a new device structure with unknown

degradation behavior, one should demonstrate that changes in PL stem from electrical degradation and not other confounding effects such as photodegradation, intrinsic degradation, changes in laser power, or movement of the sample/detector. This can be quickly demonstrated by measuring PL intermittently on a device with and without applying a current, as shown in Figure C.3. If the device without an applied current is showing substantial PL loss, one should first check for signs of photodegradation by examining whether a dark spot has formed where the laser is illuminating the device. If no photodegradation is evident, check to see whether the sample and detector mounts are properly tightened and measure the laser power to see whether it is fluctuating significantly.

C.1.7 Laser warm-up

Lasers often show a warm-up period during which their output power oscillates about the setpoint power. This warm-up period can vary even between lasers of the same make, let alone different models and manufacturers. For the Coherent Obis LX lasers used in this study, we saw 1–5% variations in power in the first 30 s after the laser is turned on (Figure C.4). The $\lambda = 473\,\text{nm}$ in particular showed more pronounced warm-up behavior which in turn could introduce additional measurement error. For example, if PL measurements are taken within the first 30 s after the laser is turned on, slight timing differences from measurement to measurement can lead to variations in the pump power, which in turn add noise to the measured PL.

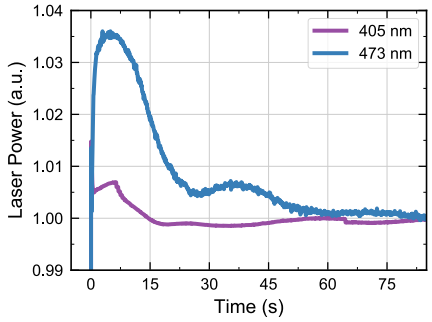

Fig. C.4. Transient warm-up behavior for the $\lambda = 405\,\text{nm}$ and $\lambda = 473\,\text{nm}$ lasers. Both lasers are Obis LX models from Coherent.

To avoid measurement error from this effect, the warm-up period should be characterized by measuring photodiode current over time after the laser turns on. The repeatability of the warm-up period should also be characterized, as shown in Figure C.5, by measuring the laser warm-up transient repeatedly in conditions similar to an actual lifetime test. Once the maximum stabilization time is identified, use a mechanical shutter to block the laser from the device during the warm-up period, preventing unnecessary photodegradation during the warm-up. Laser output power should also be tracked along with PL, in order to identify any long-timescale drift

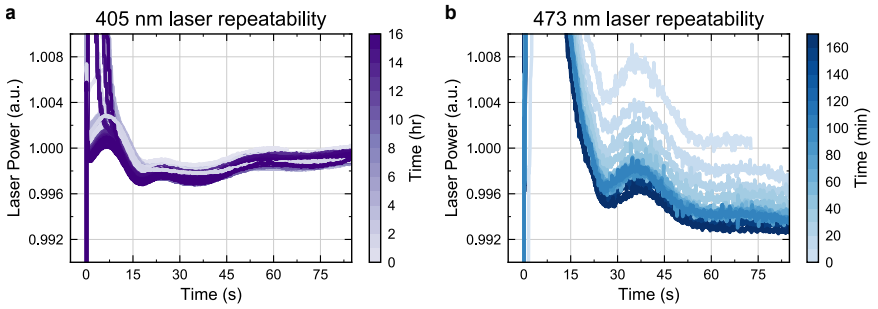

Fig. C.5. Repeatability of the transient warm-up behavior for the $\lambda = 405\,\text{nm}$ laser (left) and the $\lambda = 473\,\text{nm}$ laser (right).

in the power. Taking the laser and PL measurements as near to simultaneously on two separate source-measure unit channels helps further reduce error (as opposed to measuring them in sequence with a single SMU and a relay channel switcher). We have observed that when PL is normalized to the laser output power, separating these two measurements by even a few seconds can dramatically increase noise.

D

Analysis of DuPont hosts for red OLEDs

DuPont has supplied red devices with three different hosts (H1, H2 and H3). H1 has a high peak efficiency but shows steep efficiency roll-off and the lowest stability. H2 shows the best performance, with both high efficiency and stability. H3 shows low peak efficiency but mild roll-off and moderate stability. In this project, we sought to determine whether measurements of electroluminescence (EL) and photoluminescence (PL) could provide insights into the differing degradation behavior of these hosts. After making improvements to the resolution of the EL-PL measurement, we find that the degradation behavior in H1 and H3 devices is more dominated by PL losses than in H2 devices. H2 also shows a slightly higher voltage rise, consistent with increased formation of charge traps. One possible explanation for this trend is that increased bimolecular quenching in H1 and H3 devices funnels excess energy to emitter molecules, leading to more rapid emitter degradation and PL loss.

The molecular structures of these hosts and all other layers in these devices are proprietary, but some properties were disclosed. Only the emitter and H2 absorbs light above ~450 nm, so a 473 nm laser was selected for PL analysis to selectively pump the emissive layer. (The fact that H2 absorbs the pump laser but H1 and H3 do not could complicate analysis due to uncertain transfer efficiency from H2 to the dopant, but PL in H2 devices still comes purely from the dopant). Based on hole-only and electron-only devices with emitter-doped and undoped host layers, H1 appears to significantly trap holes but has a low electron injection barrier. Aside from these experimental differences in transport, the calculated HOMO, LUMO and triplet energy levels are similar for all three hosts. The layer structure and thicknesses were also not disclosed to us, except that the emissive layer thickness is 40 nm. This relatively thick emissive layer increases the risk of spatial mismatch errors (see Section 3.5), but in at least some of the devices studied here this type of error appears to be negligible.

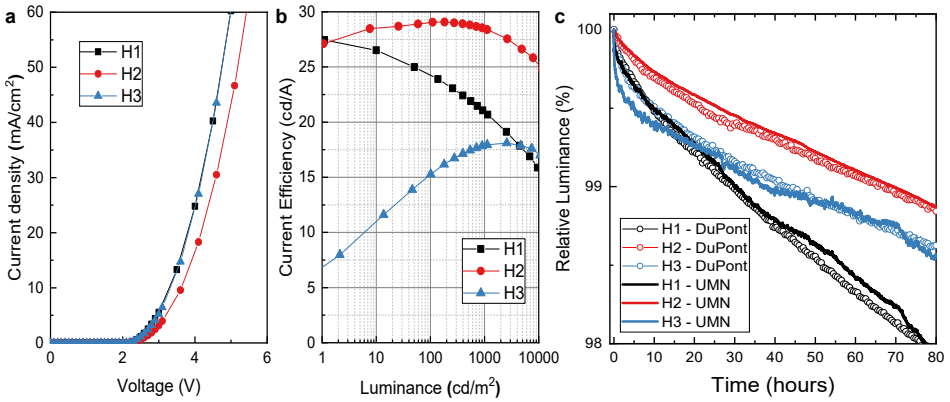

Fig. D.1. **(a)** Current density–voltage characteristics, **(b)** current efficiency–luminance characteristics, and **(c)** EL lifetime characteristics at $L_0 = 5000\,\mathrm{cd\,m^{-2}}$ for DuPont Hosts 1, 2, and 3 (H1, H2, H3).

D.1 Background and motivation for measuring EL and PL

Measuring PL during operation of OLEDs can provide additional mechanistic insight into degradation. Decreases in OLED brightness, i.e. EL, are primarily caused by the formation of charge traps and exciton quenchers. Charge traps are defects which can trap electrons and/or holes and can facilitate non-radiative charge carrier recombination. Charge traps thus reduce the efficiency of exciton formation (EF), as they provide a pathway for charge carriers to recombine before forming an exciton on an emitter molecule. Exciton quenchers are low energy defects which reduce the emitter quantum yield (i.e. the PL efficiency) by siphoning excitons from emitter molecules. (n.b. Exciton quenchers can serve as charge traps and vice versa).

Because these two pathways constitute the majority of OLED degradation, EL loss can be decoupled into losses in PL efficiency and EF efficiency by additionally measuring PL during degradation (n.b. it is important to consider spatial variations in exciton density when performing this measurement, and these considerations are discussed in detail in our previous work, see Section 3.5).[157]

In isolation, PL measurements reveal the relative contributions of the formation of charge traps and exciton quenchers to luminance loss. More speculatively, these contributions could suggest that the overall device stability is limited by either the emitter (in the case of PL dominated degradation) or the host and/or transport layer (EF dominated degradation).

However, combined EL-PL measurements can provide more insight when paired with other experimental measurements. For instance, in our early work we used spatial measurements of

the recombination zone (RZ) and experiments varying the emissive layer thickness to uncover several new insights into OLED degradation. We found that EF degradation is aggravated when the emission zone is located near an interface.[91] We also found that PL losses are governed by the density of excitons in the emissive layer, while EF losses appear to depend on current, and hence charge carrier density. These differences suggest that PL and EF losses are at least partly determined by separate mechanisms (see Chapter 3).[157]

In work studying other hosts provided by DuPont, PL measurements helped explain unexpected stability trends when mixing these proprietary host materials (see Chapter 4).[175] Adding an insulative host material (Host A), which had poor stability on its own, to a conductive host (Host B) improved stability. Using sensitizer-based measurements of RZ, we determined that the insulator moved the emission zone away from the interface between the hole transport layer and the emissive layer. By comparing lifetime data with these measurements of RZ, we found that PL stability was highest in devices with the widest RZ (conductive Host B-rich devices), but that overall EL stability was optimized in devices with a narrower RZ (50:50 Host A:Host B). The implication is that adding the insulator sacrifices some PL stability to reduce interfacial degradation and hence increase EF stability. This finding defied the standard intuition that a wider RZ is always preferable, as exciton density is minimized when RZ is maximized. With this more detailed understanding, this approach represents an unconventional design method to improving OLED stability.

The common aspect of all these studies is that measurements of PL degradation provide useful supporting data to other techniques, which, when combined, can enable deeper insights into degradation mechanisms. Other experiments, such as RZ measurements, single-carrier devices, and optical degradation, should be performed in tandem with PL measurements. These complementary approaches can serve to validate and estimate error in PL measurements, but also can provide corroborating evidence to the nature and causes of OLED degradation.

D.2 Challenges and improving PL measurement resolution

Most of the devices in our previous studies degrade to lower than 90% of the initial luminance within 10 hours of operation. In these red devices, however, the luminance remains within 98% of the initial value at 10 hours, even when operating at high brightness (15,000 nits). As such, the requirements on PL sensitivity are significantly increased. When we initially started

this project, the typical PL error of our system was on the order of $\pm 1\%$. In other words, the error exceeded the total PL degradation of these highly stable red devices. Ultimately, we were able to decrease this error to less than $\pm 0.25\%$, thus making minor differences between hosts resolvable.

To achieve this improvement in resolution, we took several steps (outlined in Appendix C). First, we monitored the stability of the pump laser used to measure PL and found that the laser fluctuates significantly within the first minute after turn-on. To mitigate this issue, we added an optical shutter to enable a long warm-up period before exposing a device to the laser. We also re-wrote our software to enable simultaneous measurements of PL intensity and the reference laser signal. Previously, for the sake of simplicity, these measurements were taken sequentially, within ~1 s of each other. Additionally, these measurements were integrated over longer time periods to average out random noise fluctuations in the laser power and photodiode currents.

We also reduced the number of parallel measurement channels from four to one. While this reduces measurement throughput, having a single channel reduces complexity and minimizes differences between tests. For instance, laser intensity varies slightly between each channel due to differences in reflected and transmitted intensity at each beam splitting optic. Due to practical limitations, measurements between channel are also not perfectly parallelized, and hence each device is exposed to the laser for a different amount of time prior to the PL measurement. We mention these limitations not to suggest that high resolution cannot be realized in a parallelized measurement set-up, simply that more careful engineering is needed to ensure identical test conditions across channels.

D.3 Results and conclusions

With the new capability to achieve high PL resolution, we compared the EL and PL degradation behavior for H1, H2, and H3 at 15,000 nits. At this high luminance, H2 and H3 show similar EL stability and EL slope, while H1 shows a much lower lifetime and a steeper slope (Figure D.2). However, H1 and H3 show a greater contribution of PL degradation than H2 (Figure D.3a). EF and PL loss contribute approximately equally to degradation in H2 (Figure D.3b). H2 also shows a slightly higher voltage rise, consistent with increased formation of charge traps (Figure D.4). One possible explanation for this trend is that increased bimolecular quenching in H1 and H3 devices funnels excess energy to emitter molecules, leading to more rapid emitter

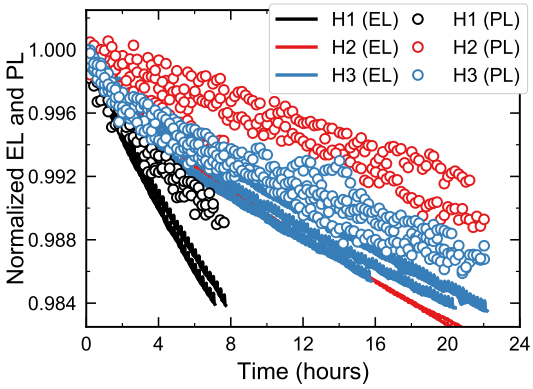

Fig. D.2. Comparison of EL and PL loss as a function of time for H1, H2, and H3. Data are normalized to the third PL point (at 15 min), to reduce the impact of fluctuations in laser power at the start of each test. H1 shows the worst stability. H2 shows a relatively higher PL stability.

degradation and PL loss.

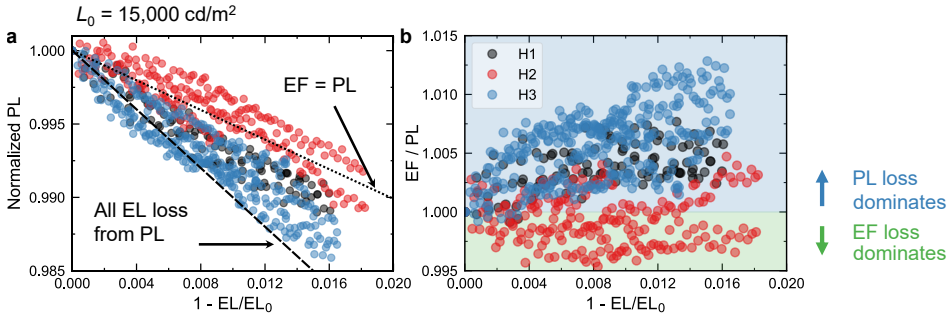

Fig. D.3. **(a)** Comparison of PL loss as a function of EL degradation $(1 - EL/EL_0)$ for H1, H2, and H3. The PL degradation of H3 is clearly distinguished from H2, comprising a greater fraction of the EL degradation. **(b)** Comparison of EF/PL as a function of EL degradation $(1 - EL/EL_0)$ for H1, H2, and H3. EF/PL provides a simple comparison whether EF or PL loss is the most significant loss pathway, where $EF/PL > 1$ signifies that PL loss is dominant and $EF/PL < 1$ signifies that EF loss is dominant.

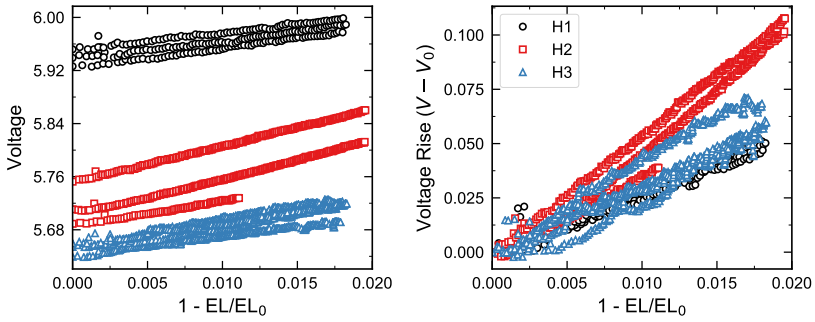

Fig. D.4. **(a)** Voltage over time and **(b)** voltage rise over time for H1, H2, and H3 degraded at $L_0 = 15{,}000\,\mathrm{cd\,m^{-2}}$. H1 and H3 show a slightly lower voltage rise than H2. This difference possibly corresponds to the lower exciton formation stability in H2, which should correlate with a larger density of charge traps.

Stronger conclusions and deeper insights could be achieved by combining these techniques with some of the experimental approaches described earlier. For instance, an alternative interpretation of the data is that the RZ for the H2 devices is slightly narrower, leading to an underestimate of PL loss. Measuring RZ directly in these devices could settle this ambiguity, while possibly also providing added clarity on the efficiency and stability differences between these hosts. For instance, H1 may simply have severe efficiency roll-off and poor stability due to a narrow RZ which is pinned against an interface. If this were the case, the underlying imbalance in charge could be rectified by adding a secondary host with complementary transport characteristics.

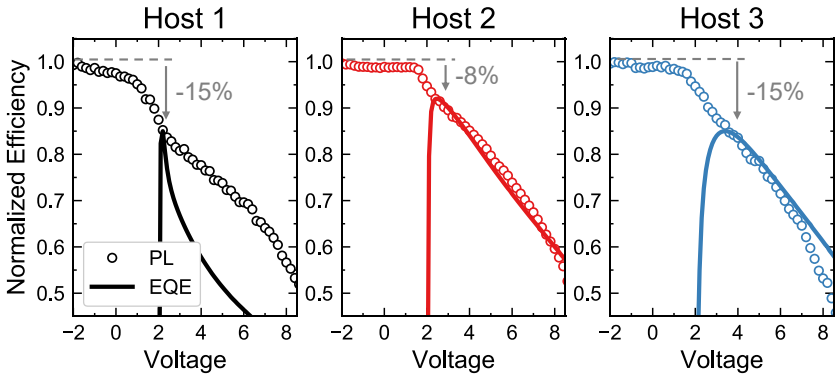

Fig. D.5. Comparison of EQE (solid lines) and PL quenching (symbols) in DuPont red OLEDs.

We also characterized hole accumulation and PL quenching in these devices (Figures D.5 and D.6), using the methods described in Chapter 6. We do not observe as pronounced of sub–turn-on quenching as seen in devices with a TPBi ETL. This could partially be a consequence of the thick emissive layer in these devices, reducing sensitivity to quenching at the EML/ETL interface. However, it seems more probable that spontaneous orientation polarization (SOP) has been mostly optimized out of these commercial materials (likely unknowingly).

Still, some quenching is observed prior to peak EQE in all devices. This quenching could arise from SOP of the host or the ETL, but it could also reflect an imbalance in electron and hole transport.[200] Host 2 shows the lowest PL roll-off prior to peak EQE (~8%), compared to ~15% quenching in Hosts 1 and 3. These differences in quenching can at least partly explain the trend in peak efficiency between these hosts. The lower degree of quenching is accompanied by an increase in hole injection voltage and decreased hole accumulation prior to turn-on (Figure D.6). This suggests that that triplet-polaron quenching may limit roll-off and lifetime in these devices,

and it is possible that this reduction in hole density in H2 devices is at least partly responsible for their lower lifetime. However, to conclusively confirm this, single-carrier device studies would need to be carried out to identify how sensitive the PL degradation rate is to hole current.

In Host 2 and Host 3, all roll-off is from bimolecular quenching but Host 2 shows a lower severity of quenching and EQE roll-off than Host 3. The agreement in PL and EQE in these devices indicates that the recombination zone must be relatively broad for both hosts (as a narrow recombination zone would lead to an underestimate of quenching in the PL measurement). In Host 1, on the other hand, the EQE roll-off is much steeper than the measured PL roll-off. This could indicate that charge balance (i.e. exciton formation) decreases at high current densities, or that the RZ is narrow, causing spatial mismatch measurement error.

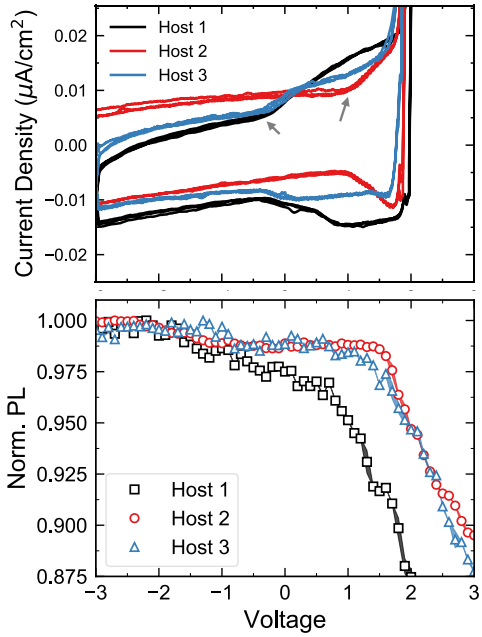

Fig. D.6. Comparison of EQE and PL quenching in DuPont red OLEDs.

Another interesting aspect of this data is that the hole injection voltage varies for the different hosts (H1 and H3 have $V_{inj} \approx -0.25\,\mathrm{V}$ while H2 has $V_{inj} \approx 1.25\,\mathrm{V}$). The larger hole injection voltage in Host 2 devices may result in more balanced electron and hole injection, leading to a broader recombination zone, lower charge accumulation, reduced EQE roll-off, and improved lifetime. Because all materials aside from the host in these devices is identical, this suggests that the SOP magnitude of the host materials varies and that the host SOP influences both hole injection voltage and the onset of PL quenching. This finding is important, because previously we had only explicitly demonstrated the effect of ETL SOP. Also, it indicates that differences in SOP in commercial hosts may (at least partly) explain differences in device performance that were previously not understood. In fact, one of the reasons DuPont wanted us to study these hosts is that they were unsure of what properties of the hosts were leading to these differences in performance. These findings provide some of the first evidence that SOP of materials should be explicitly considered during materials selection and device design, and

SOP magnitude (either experimental or simulated)[323,331] should be used as a screening metric.

D.4 Methods

Devices as received by DuPont are tested for EQE. The efficiency of each device is stored in a local database and used to calculate the current density required to achieve the desired test luminance. Prior to lifetime testing, the device area is masked with black masking tape to ensure the laser does not excite areas outside the active device. Devices are loaded on the decoupled electroluminescence (EL)/ photoluminescence (PL) setup, and the laser is aligned on the device by maximizing PL signal.

EL is measured in blocks of 10 min at 15,000 nits. PL is measured by pumping the device with an 473 nm laser (Coherent Obis LX) in between each EL block. EL and PL are measured with the same photodiode through a 500 nm long pass filter, while a separate photodiode measures the laser intensity directly. The laser is attenuated with an OD 2.0 filter. The PL signal of the device is normalized by the laser intensity to correct for laser fluctuations. Both EL and PL signals are normalized either to their initial values or to their values after ~20 min of operation. This latter normalization is used because the first several PL data points tend to be noisy due to a gradual laser warm-up. This noise is rather small (~0.5%) relative to normal EL-PL tests, but becomes noticeable for these stable red devices.

Exciton Formation (EF) losses are calculated by dividing the normalized EL signal by the normalized PL signal. This calculation assumes that outcoupling efficiency and the natural decay efficiency are constant with degradation (see Chapter 3).

E

EL-PL decoupling of blue OLEDs

OLEDs with blue emission tend to have significantly lower lifetime than green- and red-emitting pixels. To study this problem, we began preliminary work on degradation in blue OLEDs, applying our decoupled EL and PL degradation measurement. To date, very limited characterization of PL degradation in blue OLEDs has been reported.[97,128,332]

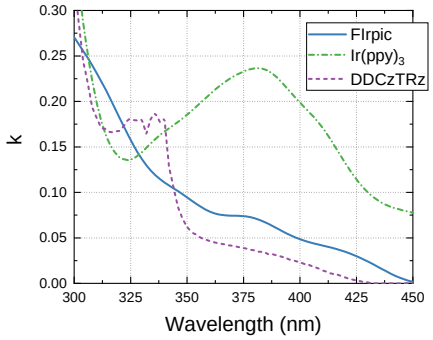

Fig. E.1. Extinction coefficient of FIrpic, DDCzTRz, and $Ir(ppy)_3$. FIrpic and DDCzTRz have lower absorption than $Ir(ppy)_3$ at 405 nm, the wavelength of the pump laser. As a result, a higher pump power or larger emitter concentration generally need to be used to achieve sufficient signal for these blue emitters.

One consideration for measuring PL of blue emitters is pump absorption. The absorption edge of blue emitters is generally blue-shifted relative to green emitters, concomitant with the shift in emission color. As such, lower pump wavelengths may be needed and the absorption at a given wavelength is generally lower in blue emitters (Figure E.1). In some cases, especially for deep-blue emission, emitter absorption may be difficult to isolate from transport layers and hosts within the device. To accurately study PL degradation, devices should be designed with all wide-gap materials to avoid convoluted PL emission. Though, in some cases these compromises in device design may make the results irrelevant to the degradation behavior of state-of-the-art structures. In our studies, we selected the sky-blue phosphorescent emitter FIrpic and the sky-blue TADF emitter DDCzTRz. Both of these have sufficient absorption at 405 nm to measure PL degradation.

Shown in Figure E.2, we constructed two architectures with FIrpic as an emitter: a single-host structure with a mCP:FIrpic emissive layer,[333] and a mixed-host exciplex structure with a mCP:B3PyMPM:FIrpic emissive layer.[165] These structures show comparable efficiencies of

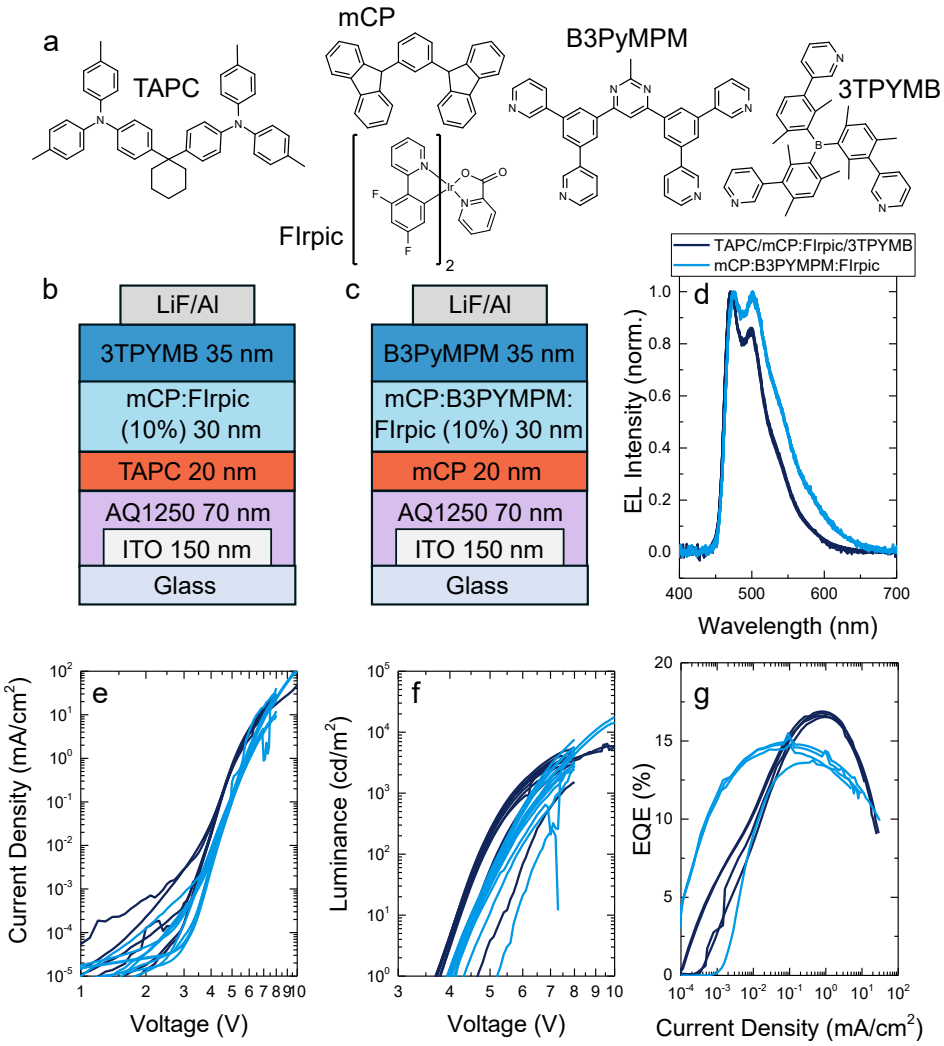

Fig. E.2. **(a)** Molecular structures of materials used in these blue OLEDs. **(b)-(c)** Device structures of single-host emissive layer (mCP:FIrpic) and mixed-host EML (mCP:B3PyMPM:FIrpic) blue OLEDs used in this study. **(d)** EL spectra, **(e)** Current density–voltage characteristics, **(f)** Luminance–voltage characteristics, and **(g)** EQE–current density characteristics of the mCP:FIrpic and mCP:B3PyMPM:FIrpic devices.

~15%–17%. The efficiency of the mCP:FIrpic device is almost identical to a previous report,[333] while the reported efficiency of the mCP:B3PyMPM:FIrpic is far below the previous report of 29% EQE.[165] This discrepancy may be due to an unoptimized emitter concentration or the thicker ITO and HIL in our device, leading to more light being trapped in waveguide modes.

The lifetime of these devices is shown in Figure E.3. EL degrades extraordinarily quickly in mCP:FIrpic devices, falling to 10% of the initial luminance ($100\,\mathrm{cd\,m^{-2}}$) within an hour.

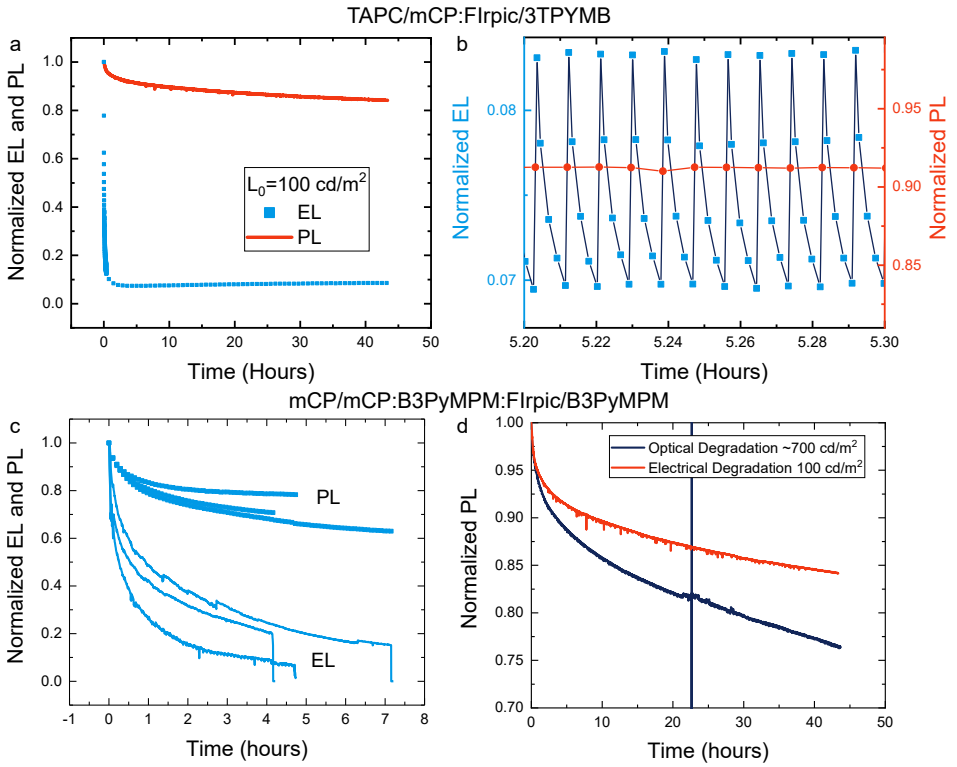

Fig. E.3. Electrical and optical degradation of FIrpic-based blue OLEDs. **(a)** EL and PL degradation of mCP:FIrpic devices at $L_0 = 100\,\mathrm{cd\,m^{-2}}$. **(b))** Zoomed view of EL recovery after laser exposure. **(c)** EL and PL degradation of mCP:B3PyMPM:FIrpic devices at $L_0 = 100\,\mathrm{cd\,m^{-2}}$. **(d)** Comparison of PL degradation under electrical (at $L_0 = 100\,\mathrm{cd\,m^{-2}}$) and optical pumping (at ~$L_0 = 700\,\mathrm{cd\,m^{-2}}$). Exciton densities in the two cases were not perfectly matched, complicating comparisons

Interestingly, EL saturates at this 10% level—even rising slightly—for over 40 hours. That the emission doesn't approach zero over time suggests that a primary degradation mechanism occurs rapidly at short times and then halts, perhaps indicating a depletion of reactants. For instance, if degradation is significantly interfacial, all of the FIrpic molecules might degrade near this interface by the time EL/EL_0 reaches 10%. The remaining FIrpic molecules away from this interface will be exposed to a much lower charge and exciton density, resulting in a significantly slower degradation rate.

EL was also observed to recover slightly after every PL measurement (Figure E.3b). This recovery may be partly due to relaxation during the device off time, if any of the degradation is reversible or if accumulated charges de-trap when voltage is not applied. However, a bright spot was observed in the area exposed to the laser, suggesting that laser exposure itself improves EL efficiency. This could possibly occur by photo-induced modifications to charge injection at the

interfaces[151] or by light absorption causing de-trapping of charges and reducing quenching or non-radiative recombination.

PL in these devices degrades much more slowly than EL, but it does degrade continuously with a stretched exponential form. The discrepancy between EL and PL suggests that the recombination zone in these devices may be narrow and the initial degradation may be predominantly interfacial, where the PL measurement is not very sensitive. This interpretation is supported by work from Prof. Hany Aziz's group comparing PL degradation in mCP:FIrpic devices with an either 20-nm-thick or 5-nm-thick emissive layer.[125] Zhang and Aziz [125] observed that the magnitude of PL loss much more closely matched that of EL loss in the thin emissive layer device.

Nonetheless, it is also possible (though perhaps less likely) that the primary defects formed during degradation are more likely to act as charge traps and non-radiative recombination centers than exciton quenchers. In this scenario, the EML-dependent behavior observed by Zhang and Aziz [125] might be interpreted as accelerating PL degradation by narrowing the recombination zone width (as we argued happens in TCTA:TPBi:Ir(ppy)$_3$ devices[157]). In any case, further studies should directly characterize the recombination zone in these devices to settle this ambiguity.

The mixed-host mCP:B3PyMPM:FIrpic devices are slightly more stable, with a half life of $t_{50} \approx 1\,\mathrm{h}$ at $L_0 = 100\,\mathrm{cd\,m^{-2}}$ (Figure E.3c). The discrepancy between PL and EL degradation in these device is less extreme, which is consistent with the wider recombination zone expected for mixed-host EMLs. Still, PL degradation represents less than half of the overall degradation, indicating that either the RZ is still relatively narrow for these devices or that η_{EF} degradation is a major loss pathway in these devices. For these high-triplet-energy blue devices, η_{EF} degradation could be partly interpreted as increasing exciton leakage from the EML over time, since we don't directly characterize exciton confinement here.[96,155*]

We also performed a preliminary comparison of the optical and electrical stability of PL in these devices, shown in Figure E.3d. We estimate the effective luminance under optical pumping at ~$700\,\mathrm{cd\,m^{-2}}$, based on comparisons of emission brightness under optical and electrical pumping. More rigorous comparisons in the future should take into account the power density

*It should be noted that exciton leakage would, in principle, be reflected in the measured PL intensity as it simply represents additional non-radiative decay rate. However, if the triplet exciton diffusivity is low and the RZ is narrower than the optical generation profile, the PL measurement will not be as sensitive to exciton leakage as the device EL.

of the laser, the simulated optical generation, the exciton lifetime of the emitter, the spatially-dependent outcoupling of the structure, and the photon flux emitted from the device at a given luminance. Applying a simple lifetime acceleration analysis (see Section 2.5.1 and eq. (2.7)), the difference in the PL degradation rate in these two cases can be explained by an acceleration factor of $n \approx 0.7$:

$$\begin{aligned} \frac{t_{85,el}}{t_{85,opt}} &= \left(\frac{L_{0,opt}}{L_{0,el}}\right)^n \\ \Rightarrow n &= \ln\left(\frac{t_{85,el}}{t_{85,opt}}\right) / \ln\left(\frac{L_{0,opt}}{L_{0,el}}\right) \\ n &\approx \ln\left(\frac{40\,\mathrm{h}}{10\,\mathrm{h}}\right) / \ln\left(\frac{700\,\mathrm{cd\,m^{-2}}}{100\,\mathrm{cd\,m^{-2}}}\right) \\ n &\approx 0.7 \end{aligned} \tag{E.1}$$

This value is much smaller than typical lifetime acceleration factors of $n \approx 1 - -2$, indicating that the observed PL degradation under electrical pumping cannot be explained solely by the exciton density. This supports the conclusion of other researchers that charge carriers (polarons) are involved in FIrpic degradation.[125] Further single-carrier degradation studies are needed to confirm this finding.

Going forward, it is clear that comprehensive recombination zone characterization, combined with single-carrier and optical degradation, of these blue devices is needed to carefully interpret the PL data. It may also be instructive to characterize exciton quenching with the lock-in PL methods presented in Chapters 6 and 7, as agreement between EQE roll-off and PL quenching here could shed light on the RZ extent. However, given the low intrinsic stability of FIrpic, we decided it was not worthwhile to further pursue characterization of these devices.

We next investigated the sky-blue TADF emitter DDCzTRz, which recently showed promising operational stability of $t_{80} \approx 50\,\mathrm{h}$ at $L_0 = 500\,\mathrm{cd\,m^{-2}}$.[334] The layer structure, energy levels, and performance of these devices is shown in Figure E.4. We measure an EQE of ~1.6%, relatively low for a TADF emitter and lower even than conventional fluorescent blue OLEDs (~5%). While this material showed a respectable EQE of 18% in a DPEPO host, the mCBP-host device

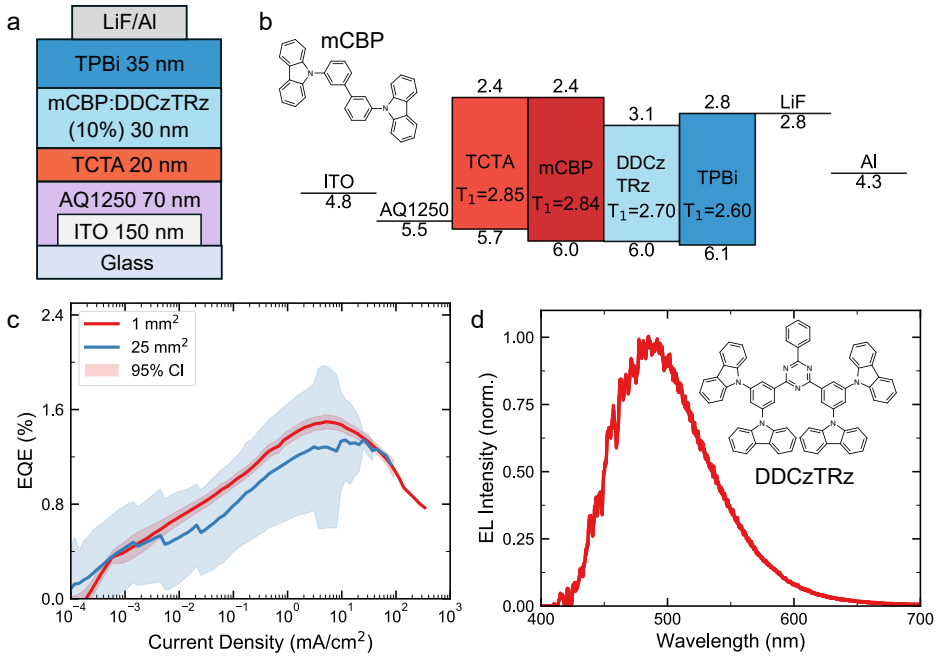

Fig. E.4. Structure and performance of DDCzTRz-based blue OLEDs. **(a)** Device structure, **(b)** energy levels and molecular structure of mCBP, **(c)** EQE–current density characteristics, and **(d)** EL spectrum of mCBP:DDCzTRz OLEDs.

that Kim et al. [334] employed for lifetime measurements only showed an EQE of ~2%.* Because of this poor efficiency, which is probably due to a combination of the low triplet energy of TPBi relative to DDCzTRz and the PL efficiency of DDCzTRz in mCBP, we decided to only perform a preliminary stability analysis of this material.

The lifetime data for these DDCzTRz devices is shown in Figure E.5. Interestingly, EL initially rises in the first hour and then declines, while PL monotonically decreases during the test. In addition, PL loss exceeds EL loss over the course of the entire test, indicating that degradation in this emitter is primarily driven by PL loss and not η_{EF}. This result is consistent with a result for the same emitter that was later published in 2019.[332] This finding should be extended to other blue TADF emitters to see whether they are similarly limited by PL stability. If so, optical degradation of emitters in solution or thin film may be a suitable screening method for quickly assessing the stability of TADF emitters.

Before further lifetime studies of blue emitters are undertaken, emitters with state-of-the-art

*Because this information was hidden away in the paper's supporting information and not mentioned in the main text, we unfortunately did not notice this before beginning the study.

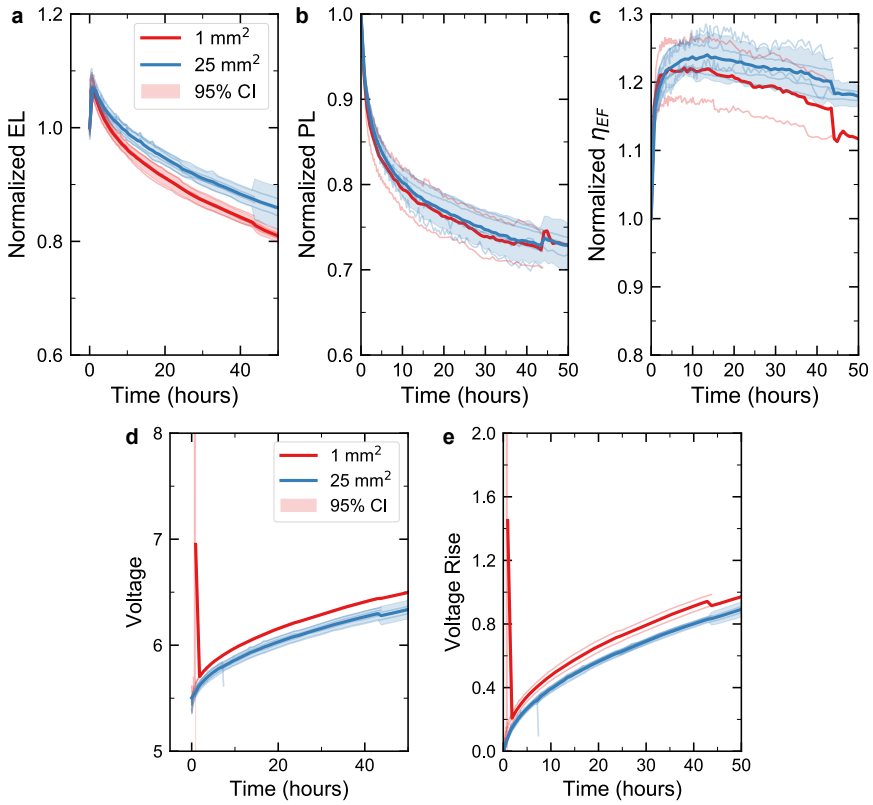

Fig. E.5. Electrical degradation of DDCzTRz-based blue OLEDs. Time dependence of **(a)** EL, **(b)** PL, **(c)** η_{EF}, **(d)** driving voltage, and **(e)** voltage rise ($V - V(t = 0)$) for mCBP:DDCzTRz devices operated at $L_0 = 100\,\mathrm{cd\,m^{-2}}$.

stability should be acquired, such as $Ir(dmp)_3$ from Universal Display Corporation,[97] $Ir(dbi)_3$ from Prof. Jun Yeob Li's group,[163] or the Pt and Pd complexes from Prof. Jian Li's group.[335–337] Once materials with reasonable stability are acquired, studies should focus on identifying kinetic mechanisms of degradation and what species limits degradation (i.e. exciton density or polaron density). Once these are understood, architecture design can begin to limit these degradation pathways (e.g. mixed emissive layers or dopant gradients for a broad recombination zone,[126,157] top-emitting cavity design to reduce exciton lifetime *via* the Purcell effect,[217] balancing charge mobility to lower polaron density[200]). It is entirely possible that the limitations facing blue OLEDs are mostly chemical in nature, and that advances in chemistry and high-throughput screening will be needed to achieve commercially viable lifetimes. But fundamental studies of degradation may provide hints to the weakest links in blue OLED stability, helping to focus molecular and device architecture design efforts in the most efficient directions.

F

Effect of photodegradation on exciton formation efficiency

The techniques described in this these have often focused on the kinetics of PL degradation, but the kinetics governing charge balance (η_{EF}) remain relatively unexplored. The influence of excitons, polarons, and their interactions on η_{EF} have been inferred from voltage rise and capacitance changes, and it is generally found that exciton-polaron interactions play a dominant role.[49,125] However, little direct measurement has yet been reported. It has often been argued that η_{EF} and PL can be degraded by identical processes, as the same defects which trap charges tend to have energetics which can quench excitons.[46,97,112,116] Our own work in Chapters 3 and 4 suggests that η_{EF} may be be mostly driven by polarons, interfacial degradation, and/or transport layer degradation.

Fig. F.1. Experimental layout for EL photodegradation measurement.

To test these ideas, we sought to reverse our typical EL and PL degradation measurement,

and instead study the influence of optical degradation on EL intensity. In this scheme, a functioning EL device is optically degraded with continuous measurements of the PL intensity. Measurements of EL intensity and voltage rise are taken intermittently at a low, fixed current that should not induce substantial degradation of its own (i.e. ~0.5 mA cm^{-2}). To ensure uniform degradation of the entire device area, the 405 nm laser beam was expanded with a achromatic Galilean beam expander (Figure F.1). The beam was passed through a neutral density (ND) filter, and the reflection from the filter was detected by a Si photodetector (filtered by a 450 nm short pass) to measure instabilities in the laser power output. A mask was placed on the substrate to prevent detection of PL emission outside the device area. Both EL and PL were measured by a Si photodetector filtered by a 450 nm long pass (to prevent detection of the beam). To aid comparisons with EL degradation, exciton density was approximately matched by matching the intensity of PL with EL intensity at 1000 cd m^{-2}.

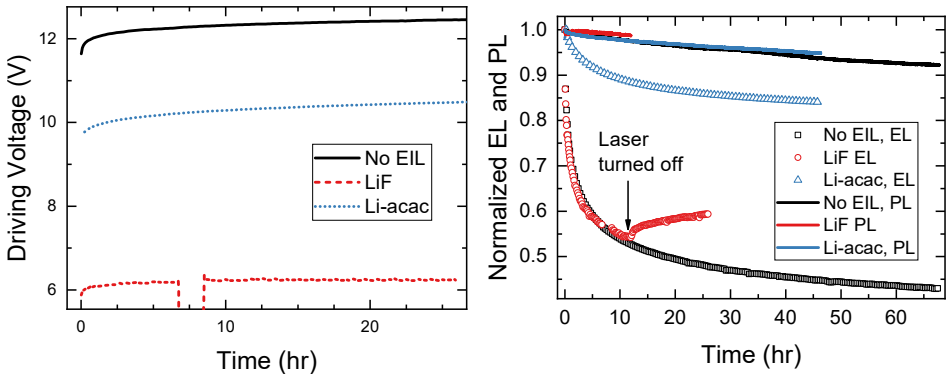

Fig. F.2. Comparison of EL photodegradation for devices with no EIL, a LiF EIL, and a Li-acac EIL.

We quickly ran into a snag in this project: our intermittently measured EL intensity degraded far faster than it would under an equivalent electrically-pumped exciton density (Figure F.2). This is most likely due to photodegradation of the organic/cathode interface, which has been shown to be surprisingly sensitive to violet/blue light.[150,233,234,329,330] What is most unintuitive about this degradation mechanism is that it apparently occurs even when the excitation energy is below the bandgap of the transport layers. It is possible that the light excites interfacial states present at the organic/cathode interface, or that charged molecules in an OLED have a red-shifted absorption which overlaps with the light source.

We initially tried to circumvent this issue by using a more stable electron injection material, Li-acac.[150,330] While EL degradation is significantly slowed with this EIL, as compared to LiF

and bare Al, the required driving voltage was much higher,* potentially making any results from this study less relevant to practical devices. In addition, there remains ambiguity about whether interfacial photodegradation had been completely eliminated or simply reduced in Li-acac device, making it unclear how to assign how much of the reduction in EL is due to exciton-induced η_{EF} degradation and how much is from interface degradation. One way this could potentially be assessed is by delaminating and re-depositing the cathode to see if the efficiency recovers, as shown in ref. [151], though this is a labor-intensive and error-prone approach.

When measuring the LiF device, we turned the laser off after ~10 h but continued turning the current on and off every 10 min. Interestingly, EL started to partially recover after the laser was turned off, indicating that this photodegradation effect is partially reversible. The origin of this reversibility is currently unclear.

Going forward, these studies might be best carried out on red-emitting OLEDs which can be pumped with green light which has limited influence on other layers in the OLED. To confirm that no optical degradation occurs outside of the emissive layer, comparison devices with an EML consisting of only an undoped host should be characterized.

Given that illumination can have such a large impact on EL intensity, we decided to shift focus and identify whether the device's own EL can lead to photodegradation. To do this, we passed a broadband light source through bandpass filters to mimic the emission of a green or sky-blue emitter (Figure F.3). We measured the power density using a photodetector and a 100 µm pinhole and used this to estimate the effective brightness of the illumination light source. This comparison is approximate, as only 15–25% of the emitted EL is outcoupled, and the remainder which is waveguided or coupled to surface-plasmon modes might contribute to photodegradation.

We then intermittently measured EL intensity, comparing the luminance loss for devices which were operated at constant current in the dark, with green illumination, or with blue illumination. During the EL measurement, the light source was blocked by a servo-controlled shutter and the background light intensity was subtracted before turning on the current. As shown in Figure F.4, the lifetime is within error for all conditions, suggesting that sky-blue and green light do not contribute significantly to photodegradation in this particular structure. Further studies should investigate whether this holds true for all ETL and HTL materials systems, and also should investigate the energy onset for photodegradation.

*We never optimized the Li-acac thickness, so it's possible this difference could be reduced with further work.

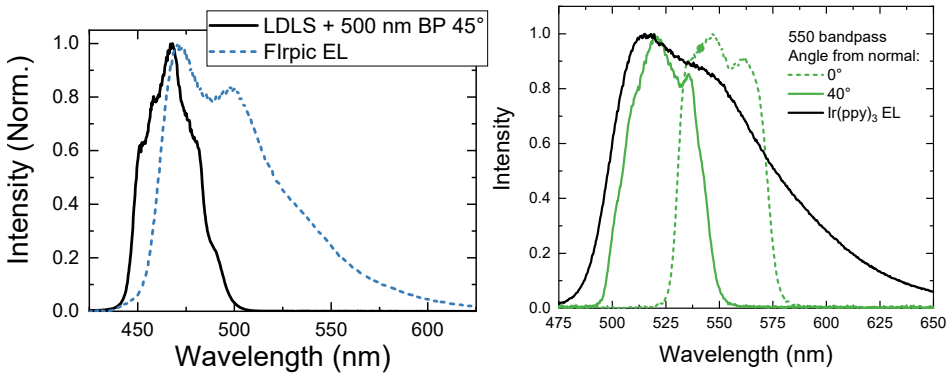

Fig. F.3. Illumination spectra for photodegradation with blue (left) and green (right) light achieved by passing the broadband laser-driven light source (LDLS, Energetiq) through a bandpass filter. Spectra were tuned to approximately match the EL spectra of FIrpic and $Ir(ppy)_3$ by varying the incident angle of the bandpass filter.

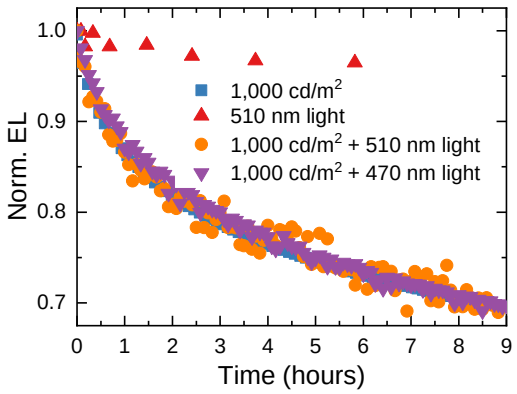

Fig. F.4. Photodegradation of EL with blue and green light compared to EL degradation . Device is a 10 nm TCTA:TPBi:$Ir(ppy)_3$ M-EML structure with a TCTA HTL, TPBi ETL, and AQ1200 HIL (see Figure 3.1).

G

Data Acquisition

One key to success in many of the chapters in this thesis has been automation of experiments using Python.* I have made available some of the Python acquisition software I developed at github.com/jsbangsund/measurement-automation-tools. A few of the more broadly applicable, and relatively concise, examples are included below.

G.1 Analog voltage controller

Catherine Clark's carrier-gas assisted deposition system uses mass flow controllers to set the gas flow rate through each source.[338] Our goal is to output a voltage signal that ranges from 0 - 2 V with ~2 mV resolution in order to set the flow rate on a mass flow controller. The mass flow controller can be controlled remotely by supplying a voltage signal of 0 - 5 V, where 5 V corresponds to the maximum flow rate, 200 standard cubic centimeters per minute (SCCM). Being able to control this remotely with a microcontroller (i.e. an Arduino) allows for this to be controlled with software, rather than a tedious manual potentiometer. For Catherine's deposition system, the useful range is only 0 - 50 SCCM with a required resolution of ~0.1 SCCM. This means that the required voltage resolution is 0.1 SCCM / 200 SCCM * 5 V = 2.5 mV. The actual voltage reference we will be using is 4.096 V, giving a resolution requirement of 2.05 mV. For a 12-bit DAC, the maximum resolution is 3.3 V / $2^{12} = 3.3/4096 = 0.8$ mV. In reality, the resolution is probably lowered slightly by inaccuracies in V_{out}, but the stability of the output is quite high.

It is worth noting that this sort of analog voltage controller can also be useful for setting LED power, as many LEDs have a transistor-transistor logic (TTL) input used to linearly adjust output power.

*To beginners in this area, I would recommend SweepMe!, which is an easy to use tool that can accomplish the vast majority of experiments you could imagine. I have not used this in any significant way (it was available too late to be worth transitioning), but I found it intuitive and easy to get started with.

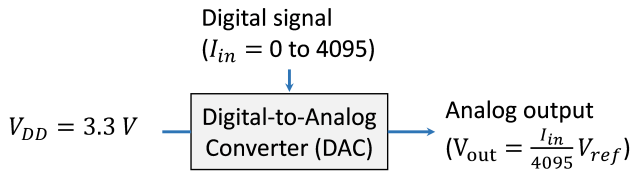

Fig. G.1. Flow diagram for inputs and outputs of digital-to-analog converter (DAC)

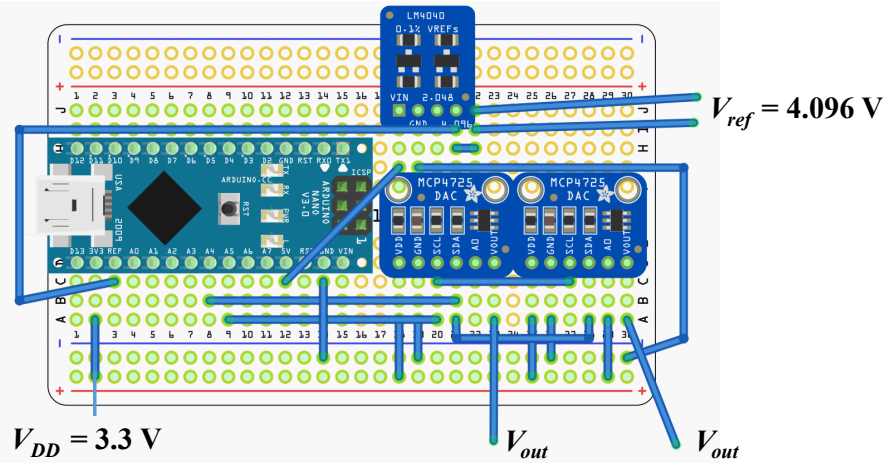

Fig. G.2. Circuit diagram for analog voltage controller

Using an arduino nano, two MCP4725 breakout boards, and an LM4040 breakout board, all soldered on to a half-sized permaproto board from adafruit. See the fritzing drawing for more detail.

The LM4040 serves as a stable voltage reference for the Arduino. The internal reference voltage in the Arduino is not stable and would be susceptible to drift over time, limiting both the precision and accuracy of the voltage output. This board takes an input voltage (V_{in}) of +5V (which we can conveniently supply from the +5V pin of the Arduino) and an input ground, which is tied to the GND pin of the Arduino. The LM4040 then outputs two reference voltages: 2.048 V and 4.096 V, each with an accuracy of ±0.1%. We will use the 4.096 reference voltage, connecting it to the REF pin on the Arduino. Alternatively, the LM4040 can be avoided altogether and we can use the +5V remote reference voltage pin from the mass flow controller to connect to the REF pin.

The MCP4725 breakout boards are 12-bit Digital-to-Analog Converters (DAC), which means they can convert a digital signal (integers from 0 to $2^{12} - 1 = 4095$) to an analog voltage (ranging from ~0 V to the reference voltage). The reference voltage we will use for the

MCP4725 boards is the +3.3V pin from the Arduino (which is stabilized by the LM4040, as it is referencing the REF pin). The actual voltage in our circuit is ~3.244 V. This voltage goes to the V_{DD} pin on the MCP4725 board. Then, we hook up the A4 pin and A5 pins of the Arduino to the SDA and SCL pins of the MCP4725, respectively. For one of the MCP4725 boards, the A0 pin is pulled up to V_{DD}, which gives this board a different I2C address (Hex 0x63 instead of 0x62).

This code is maintained in the dual_channel.ino file at github.com/jsbangsund/measurement-automation-tools

```
/*****************************************************************/
/*!
    Control two MCP4725 DACs to output constant voltage outputs
    Uses the Adafruit MCP4725 breakout board
    http://www.adafruit.com/products/935
    If having trouble with this uploading on an arduino nano, use:
    Processor: "ATmega328P (Old Bootloader)"
    Download the Adafruit_MCP4725 library here:
    https://github.com/adafruit/Adafruit_MCP4725
    Then copy that library directory to:
    C:\Program Files (x86)\Arduino\libraries\
*/
/*****************************************************************/
#include <Wire.h>
#include <Adafruit_MCP4725.h>
String inString = "";    // string to hold input
char active_dac = 'A'; // currently active dac
Adafruit_MCP4725 daca;
Adafruit_MCP4725 dacb;
void setup(void) {
  Serial.begin(9600);
  // For Adafruit MCP4725A1 the address is 0x62 (default)
  //     or 0x63 (ADDR pin tied to VCC)
  // For MCP4725A0 the address is 0x60 or 0x61
  // For MCP4725A2 the address is 0x64 or 0x65
  daca.begin(0x62);
  dacb.begin(0x63);
  //Serial.println("Input integer");
}
```

```
void loop(void) {
    int counter;
    // Run through the full 12-bit scale for a triangle wave
    // Read serial input:
    while (Serial.available() > 0) {
      // incoming string should have form: A#### or B####
      // where A or B is the channel, and #### is 0 to 4095
      char inChar = Serial.read();
      if (isAlpha(inChar)) {
          // turn laser on
          if(inChar=='A'){
            active_dac='A';
          }
            // turn current on
          if(inChar=='B'){
            active_dac='B';
          }
          if(inChar=='Q'){
            Serial.print(active_dac);
          }
      }
      if (isDigit(inChar)) {
        // convert the incoming byte to a char and add it to the string:
        inString += (char)inChar;
      }
      // if a newline is sent, set the voltage value
      if (inChar == '\n') {
        if(inString!=""){
          counter = inString.toInt();
          // clear the string for new input:
          inString = "";
          if(active_dac=='A'){
                daca.setVoltage(counter, false);
              }
          if(active_dac=='B'){
                dacb.setVoltage(counter, false);
              }
        }
      }
```

```
68          }
69      }
```

Python code to calibrate the voltage controller and adjust the voltage setpoint is maintained in the analogVoltageController.py file at github.com/jsbangsund/measurement-automation-tools. This software generated the calibration curve in Figure G.3.

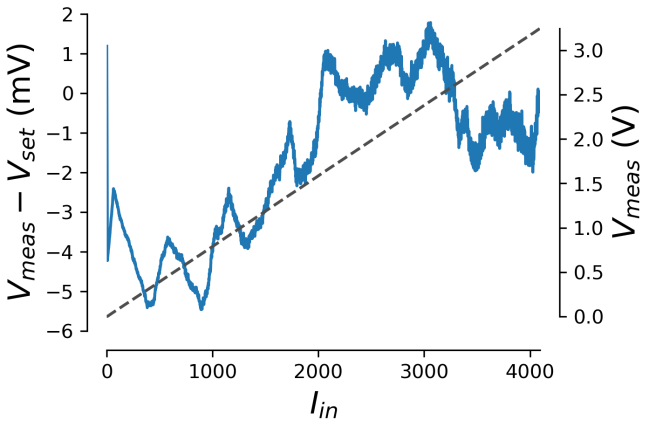

Fig. G.3. Calibration of analog voltage controller output. Deviation of the measured voltage from the voltage setpoint is shown in the left axis (blue line). The measured voltage output is shown in the right axis (dashed gray line). From 0–3.3 V, the error is generally less than 6 mV. This error is consistent and stable, related to the specific characteristics of the circuit and chips used here. As such, this curve can be used as a calibration curve to yield precision better than 1 mV. Correcting for such small deviations is necessary when operating at small voltages, which is often the relevant use case for the carrier-gas deposition system.

G.1.1 Specifics for the mass flow controller

The mass flow controller (MFC) used here is an Omega FMA5510A which can support a flow rate of 0–200 mL min^{-1}. To use remote control mode of this MFC, one of the jumper pins in the back of the MFC needs to be changed (NJ1 jumped between 11-12). See the manual for diagrams (Figure 2-2 and 2-3). This MFC supplies a regulated +5V reference, which could be used for the "REF" pin of the arduino instead of the LM4040. Originally, I thought a +5V reference needed to be supplied here (because Omega manuals are trash), but this caused all sorts of issues.

Pin connections:

- **Pin 11** - +5V reference provided by the MFC. Connect this to "REF" pin on arduino if not using LM4040.
- **Pin 10** - Connect to GND pin on arduino
- **Pin 8** - V_{out} from MCP4725
- **Pin 5/7** - Ground/+12V from DC power supply (wall-plug power supply comes with MFC)

G.2 Optical shutter and filter switcher

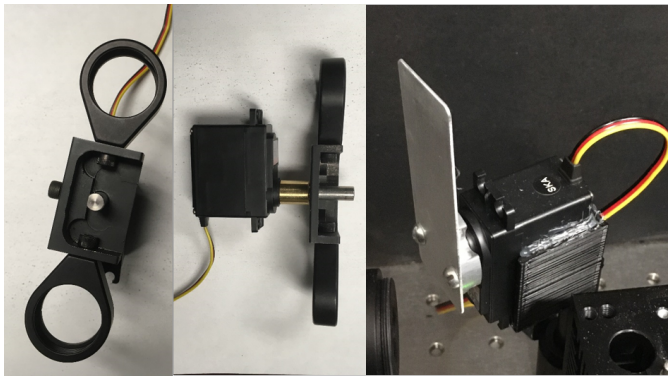

Fig. G.4. Optical shutters mounted on a servo: (Left) Front-view and (Middle) side-view of servo-controlled filter switcher. (Right) Simple optical shutter using a piece of sheet metal attached to a hub horn.

Optical shutters are useful for controlling when light sources are illuminating your sample or for moving filters in and out of the beam line to alter the illumination spectrum of a broadband light source. We used a low-cost servo (Hitec HS-422) in a 3D printed mount to connect with conventional optics posts (designed by Jack Van Sambeek). For a simple optical shutter, we used a standard hub horn (24 tooth, 6/32 screws) and a simple sheet metal piece with holes drilled to match the hub horn. For servo controlled filter switcher which could mount 1" optics, I custom-machined lens mount which was connected to the servo with a C1 Spline Servo to 1/4" Shaft Coupler and (1/4") x 1.00" Stainless Steel D-Shafting. These shutters are shown in Figure G.4.

```
#include <Servo.h>
char msg = ' ';
bool printed = 0;
```

```
4  Servo myservo;  // create servo object to control a servo
5  // To adjust the position of the servo in open and closed positions,
6  // vary the integers in myservo.write(#) in range 0 to 180
7  void setup() {
8    Serial.begin(9600);
9    myservo.attach(10);  // attaches the servo on pin 10 to the servo object
10 }
11 void loop() {
12   while (Serial.available()>0){
13     msg=Serial.read();
14     printed = 0;
15   }
16   // If 'W' command received, give unique identifier
17   if(msg=='W' && !printed)
18   {
19     Serial.print('B');
20     printed = 1;
21   }
22   if(msg=='O'){  // Set servo to open position
23     myservo.write(145);  // sets the servo position according to the scaled
       ↪ value
24     delay(15);   // waits for the servo to get there
25   }
26   if(msg=='C'){  // set servo to closed position
27     myservo.write(0); // sets the servo position according to the scaled
       ↪ value
28     delay(15);        // waits for the servo to get there
29   }
30   if(msg=='F'){   // set servo to filter position
31     myservo.write(165); // sets the servo position according to the scaled
       ↪ value
32     delay(15);          // waits for the servo to get there
33   }
34 }
```

G.3 Channel switcher

A substantial cost of lifetime measurements is source measure units (SMUs). The easiest way to implement a photodiode current measurement, for EL or PL measurements, is to use a single SMU channel per photodiode. However, because lifetime measurements only need to be taken intermittently (ranging from every ~15 s to ~10 min, depending on the rate of degradation), the same measurement could be achieved by cycling through each photodiode sequentially using a single SMU channel and a relay-based channel switcher to switch between photodiodes. Below the arduino code used to control a seven-way channel switcher, used to measure six device channels and a laser channel, is included. The basic concept is that when an integer corresponding to a channel is sent to the arduino, the arduino will turn the relay for that channel on (by setting one of the digital pins to HIGH) while turning the relays for all other channels off (setting digital pin to LOW).

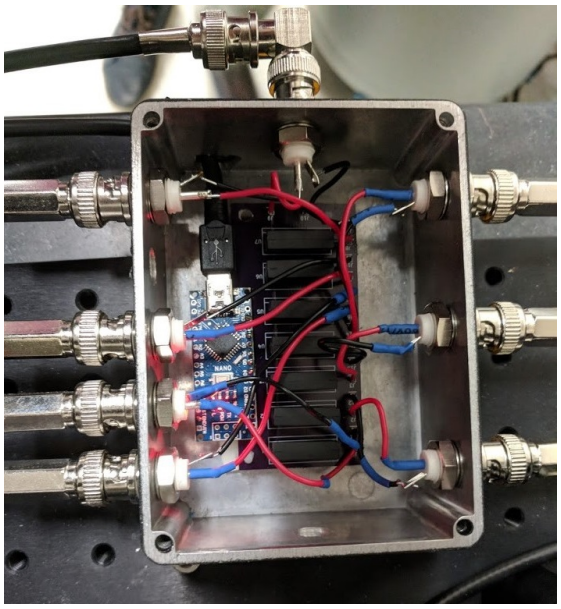

Fig. G.5. Relay-based channel switcher including a custom printed circuit board with seven relays, and arduino nano, and a simple enclosure with BNC connections.

```
// Python will send the int pinOn, which is between 1-7
// The conversion to pins 4-10 is due to which pins were soldered on the
 ↪  arduino nano
int pinOn = 0;
bool sent = 0;
```

```
void setup() {
  Serial.begin(9600);
  // Setup digital pins 4-10
  for (int i = 4; i < 11; i++){
    pinMode(i, OUTPUT);
  }
  Serial.setTimeout(100);
}
void loop() {
  while (Serial.available()>0){
    pinOn=Serial.parseInt();
    sent = 0;
  }
  if(!sent){
    selectChannel(pinOn);
    sent = 1;
  }
}
void selectChannel(int pinOn)
{
    for (int i = 1; i < 8; i++){
      if(i==pinOn)/
      {
        Serial.println(i);
        digitalWrite(i+3, HIGH);
      }
      else
      {
        digitalWrite(i+3, LOW);
      }
    }
  }
```